

Dissertation zur Erlangung des Doktorgrades
der Fakultät für Chemie und Pharmazie
der Ludwig-Maximilians-Universität München

Structural Studies of Eukaryotic Ribosome Biogenesis and the Sec and Bcs1 Protein Translocation Systems



Lukas Jonas Kater
aus
Bad Waldsee, Deutschland

2020

Erklärung

Diese Dissertation wurde im Sinne von § 7 der Promotionsordnung vom 28. November 2011 von Herrn Prof. Dr. Roland Beckmann betreut.

Eidesstattliche Versicherung

Diese Dissertation wurde eigenständig und ohne unerlaubte Hilfe erarbeitet.

München, 19.05.2020

Lukas Kater

Dissertation eingereicht am: 20.05.2020

1. Gutachter: Prof. Dr. Roland Beckmann

2. Gutachter: Prof. Dr. Karl-Peter Hopfner

Mündliche Prüfung am: 10.07.2020

List of Publications

Visualizing the Assembly Pathway of Nucleolar Pre-60S Ribosomes.

Kater L, Thoms M, Barrio-Garcia C, Cheng J, Ismail S, Ahmed YL, Bange G, Kressler D, Berninghausen O, Sinning I, Hurt E, and Beckmann R
Cell 171, 1599-1610.e1514 (2017), doi: 10.1016/j.cell.2017.11.0390

Suppressor mutations in Rpf2-Rrs1 or Rpl5 bypass the Cgr1 function for pre-ribosomal 5S RNP-rotation.

Thoms M, Mitterer V, Kater L, Falquet L, Beckmann R, Kressler D, and Hurt E
Nat Commun 9, 4094 (2018), doi:10.1038/s41467-018-06660-w

Partially inserted nascent chain unzips the lateral gate of the Sec translocon.

Kater L, Frieg B, Berninghausen O, Gohlke H, Beckmann R and Kedrov A
EMBO Reports 20: e48191 (2019), doi: 10.15252/embr.201948191

Structure of the Bcs1 AAA-ATPase suggests an airlock-like translocation mechanism for folded proteins.

Kater L, Wagener N, Berninghausen O, Becker T, Neupert W, and Beckmann R
Nat Struct Mol Biol 27, 142-149 (2020), doi: 10.1038/s41594-019-0364-1

Construction of the Central Protuberance and L1-stalk during 60S Subunit Biogenesis.

Kater L, Mitterer V, Thoms M, Cheng J, Berninghausen O, Beckmann R, and Hurt E
Mol Cell, in press (2020), doi: 10.1016/j.molcel.2020.06.032

Contribution Report

This dissertation contains my PhD research, which was conducted between January 2016 and April 2020. All my work was performed in the Lab of Prof. Dr. Roland Beckmann at the Genecenter, Ludwig-Maximilians-University of Munich (Munich, Germany). Multiple collaborations supported this work. Ribosome biogenesis projects (publication 1, 2 and 5) were conducted in collaboration with the groups of Prof. Dr. Ed Hurt (Heidelberg, Germany), Prof. Dr. Irmgard Sinning (Heidelberg, Germany), Prof. Dr. Gert Bange (Marburg, Germany), and Dr. Dieter Kressler (Fribourg, Switzerland). Work on the SecYEG translocation (publication 3) was performed in collaboration with the groups of Prof. Dr. Holger Gohlke (Düsseldorf, Germany) and Prof. Dr. Alexej Kedrov (Düsseldorf, Germany). Work on the Rip1 translocation factor Bcs1 (publication 4) was performed in collaboration with Prof. Dr. Walter Neupert (Munich, Germany) and Dr. Nikola Wagener (Munich, Germany).

Publication 1 | Kater et al. (2017)

This study reports the structures of five nucleolar assembly intermediates of the large ribosomal subunit. It shows how the rRNA of the large subunit is incorporated stepwise but not following the transcriptional 5' - 3' sequence, first forming the solvent exposed back side, and later the peptide exit tunnel and intersubunit surface. I performed the cryo-electron microscopy (cryo-EM) data processing as well as molecular model building and refinement. Furthermore, I contributed to the structural analysis and interpretation. Also, I prepared the figures for the manuscript and contributed to its writing.

Publication 2 | Thoms et al. (2018)

This study reports on suppressor mutants that bypass Cgr1 function, thereby elucidating the role of this protein in a central maturation event during the assembly of the large ribosomal subunit: rotation of the central protuberance (CP). Cgr1 is required for stabilization of the CP after this rotation, as the *cgr1* Δ mutation causes

an arrest prior to this central maturation step. Using cryo-EM we showed a partial reversion of this phenotype by an *rrs1* E102D suppressor mutation. Here, I performed the cryo-EM data processing and as well as analysis and interpretation of the structural data. Also, I prepared figures and contributed to writing the manuscript.

Publication 3 | Kater et al. (2019)

In this publication we present the structure of the Sec translocon in a lipid nanodisc bound to a translationally stalled 70S ribosome. The reported structure shows how binding of the ribosome nascent chain complex to SecYEG leads to an unzipping-like opening of the lateral gate of the translocon. Molecular dynamics simulations of this system were performed to corroborate the structural findings. I supported this publication by performing the cryo-EM data processing as well as the model building and refinement. Furthermore, I contributed to the analysis and interpretation of the structural data. I supported the manuscript with figures and writing.

Publication 4 | Kater et al. (2020b)

Here we present the structure of the AAA-protein (ATPases associated with diverse cellular activities) Bcs1 in different conformational states. The presented structures allowed us to propose an airlock-like mechanism for the folded protein translocation through the inner mitochondrial membrane (IM) by Bcs1. For this study I performed the cryo-EM grid preparation and contributed to the microscopic screening and cryo-EM data collection. I furthermore performed the processing of the cryo-EM data and built and refined the molecular structures. Additionally, I supported analysis and interpretation of the structural models as well as writing of the manuscript, to which I contributed the figures.

Publication 5 | Kater et al. (2020a)

In this publication we present three structures of ribosomal large subunit biogenesis intermediates. These structures provide insight into two major restructuring events occurring during 60S biogenesis in the nucleoplasm: assembly of the mature-like L1-stalk and rotation and maturation of the CP. For this study I performed the cryo-EM grid preparation and contributed to the microscopic screening and cryo-

EM data collection. Furthermore, I performed the cryo-EM data evaluation and processing as well as building and refinement of the molecular models. Also, I prepared the figures for publication and contributed to writing the manuscript.

Summary

Three publications of this cumulative dissertation use cryo-electron microscopy (cryo-EM) to dissect the assembly pathway of the eukaryotic large ribosomal subunit (LSU). This pathway commences with freshly transcribed and initially unfolded rRNA in the nucleolus, which folds and incorporates ribosomal proteins while traveling to the cytoplasm, ultimately culminating in the mature LSU. During this highly complex pathway, the yeast cell must assemble four rRNAs and 79 ribosomal proteins with the help of over 200 assembly factors (AFs). Using cryo-EM, structures of nucleoplasmic and cytoplasmic assembly intermediates of the LSU could be solved in recent years, thus shedding light on the later stages of LSU formation. Early assembly steps remain enigmatic, as nucleolar LSU assembly intermediates have been biochemically but not structurally characterized.

Taken together, we solved the structure of seven nucleolar or early nucleoplasmic intermediates at resolutions ranging from 3.3 to 4.5 Å, showing a linear assembly sequence. The first five structures show how the rRNA of the LSU is incorporated stepwise, in a non-transcriptional sequence, first forming the solvent exposed back side, and later the peptide exit tunnel and parts of the intersubunit surface (ISS). At the late nucleolar stage, the L1-stalk rRNA of domain V blocks the site of central protuberance (CP) assembly and is stabilized in a premature conformation by a range of AFs associated with the meandering, long N-terminal tail of Erb1.

Two further structures show progression from this stage after release of the Erb1-Ytm1 complex by the Rea1 remodeling machinery. These intermediates, purified via Nop53, show dissociation of many early AFs from the premature ISS and destabilization of the L1-stalk. After subsequent release of the Spb1 methyltransferase, the L1-stalk rRNA can be accommodated in its mature conformation. This allows the premature CP to form, leading to a previously characterized nucleoplasmic intermediate, with a formed but premature CP. This particle is the substrate for the second Rea1 mediated structural remodeling, an intermediate of which we resolved to molecular resolution revealing Ipi1 as a central integrator for the Rix1-Ipi1-Ipi3 complex on this pre-60S particle.

The binding of the Rix1-Rea1 remodeling machinery at this nucleoplasmic stage progresses maturation by inducing a 180° rotation of the 5S ribonucleoprotein par-

ticle (5S RNP) and CP. Using a combination of yeast genetics and cryo-EM we investigated the function of the AF Cgr1 in this maturation step. We showed that Cgr1 is required for CP rotation to take place, likely by stabilizing the rotated conformation. The Cgr1 function can be bypassed by introducing suppressor mutations in Rpf2 and Rrs1, two factors stabilizing the CP prior to rotation.

Apart from ribosome biogenesis, two additional publications of this dissertation address protein translocation machinery, required for transport of proteins across or into membranes. The Sec translocon allows co- and posttranslational translocation of mostly unfolded substrates across the bacterial plasma and the eukaryotic endoplasmic reticulum (ER) membrane. We solved the structure of a stalled 70S ribosome-nascent chain complex (RNC) bound to the SecYEG translocon in a native like environment provided by a large lipid nanodisc. The structure shows all three subunits of the bacterial SecYEG complex and displays the lateral gate at a defined, early stage of opening or unzipping on the cytoplasmic side upon insertion of the signal anchor domain of the nascent chain.

Specific pathways, such as the assembly of the mitochondrial bc1 respiratory chain complex, require folding of proteins in one compartment before translocation across a membrane to allow the protein to be active in another compartment. The bc1-complex component Rip1 folds in the mitochondrial matrix and assembles a 2Fe-2S cluster before being translocated across the inner mitochondrial membrane (IM) by the AAA-protein Bcs1. We solved the structure of Bcs1 in an ADP-bound state and two apo states, displaying a heptameric ring of Bcs1 protomers. Bcs1 forms two large aqueous vestibules separated by a seal forming middle domain. One vestibule is accessible from the matrix side and one lies within the inner mitochondrial membrane. The architecture and structural dynamics between the three states suggest an airlock like mechanism, allowing transport of folded Rip1 while maintaining the permeability barrier of the membrane.

List of Abbreviations

AAA	ATPases associated with diverse cellular activities
AAA+	extended family of AAA-proteins
AF	assembly factor
A-site	aminoacyl-tRNA site
ADP	adenosine diphosphate
ASCE	additional strand conserved E (domain)
ATP	adenosine triphosphate
ATPγS	adenosine [γ -thio]triphosphate
CP	central protuberance
cryo-EM	cryo-electron microscopy
DNA	deoxyribonucleic acid
rDNA	ribosomal DNA
<i>E. coli</i>	<i>Escherichia coli</i>
E-site	exit site
ER	endoplasmic reticulum
ES	expansion segment
ETS	external transcribed spacer
Fe-S	iron-sulfur (cofactor)
GAC	GTPase-associated center
GTP	guanosine triphosphate
H, h	helix number of the large and small subunit, respectively
IM	inner (mitochondrial) membrane
IMS	intermembrane space
ISS	intersubunit surface
ITS	internal transcribed spacer
LSU	large subunit
LD	large domain (of the AAA cassette)
MIDAS	metal ion dependent adhesion site
Ni-Fe	nickle-iron (cofactor)
NPC	nuclear pore complex
PMF	proton motive force

P-site	peptidyl-tRNA site
PTC	peptidyl transferase center
RNA	ribonucleic acid
mRNA	messenger RNA
rRNA	ribosomal RNA
snoRNA	small nucleolar RNA
tRNA	transfer RNA
RNC	ribosome-nascent chain complex
RNP	ribonucleoprotein particle
snoRNP	small nucleolar RNA containing RNPs
S	Svedberg, sedimentation constant
<i>S. cerevisiae</i>	<i>Saccharomyces cerevisiae</i>
SD	small domain (of the AAA cassette)
SRP	signal recognition particle
SRH	second region of homology
SSU	small subunit
Tat	twin-arginine translocase
TMH	transmembrane α -helix
UBL	ubiquitin like (domain)
UTP	U3 small nucleolar RNA-associated protein

Contents

List of Publications	iii
Contribution Report	iv
Summary	vii
List of Abbreviations	ix
Contents	xii
List of Figures	xiii
1 Introduction	1
1.1 The Structure and Function of the Ribosome	1
1.2 Eukaryotic Ribosome Biogenesis	4
1.2.1 Formation of the Small Ribosomal Subunit	7
1.2.2 Formation of the Large Ribosomal Subunit	10
1.3 Protein Translocation	17
1.3.1 The Sec Translocation Pathway	18
1.3.2 Folded Protein Translocation	22
1.4 AAA-Proteins: a Versatile Clade of Molecular Machines	25
2 Aims of this Thesis	29
2.1 Publications 1, 2 and 5 Structural Analysis of Eukaryotic Large Ribosomal Subunit Biogenesis	29
2.2 Publication 3 Partially Inserted Nascent Chain Unzips the Lateral Gate of the Sec Translocon.	30
2.3 Publication 4 Structure of the Bcs1 AAA-ATPase Suggests an Airlock-like Translocation Mechanism for Folded Proteins.	30
3 Discussion and Outlook	32
3.1 Biogenesis of the Large Ribosomal Subunit	32
3.2 Early Steps in SecYEG Mediated Protein Insertion	36
3.3 Folded Protein Translocation by the Heptameric Bcs1 AAA-ATPase	38
4 Acknowledgments	42
References	44

5	Publications of this Dissertation	74
5.1	Kater et al. 2017	75
5.2	Thoms et al. 2018	101
5.3	Kater et al. 2019	114
5.4	Kater et al. 2020b	127
5.5	Kater et al. 2020a	141

List of Figures

1	Overview of the Eukaryotic 80S Ribosome	2
2	Schematic of 35S pre-rRNA, its Processing and Secondary Structure of the Products	5
3	The Nucleoplasmic Restructuring Step of the Rix1-Rea1 Remodeling Machinery	13
4	Architecture of the SecYEG Translocon	19
5	Assembly Scheme of the Rieske Protein	24
6	Structural Overview of the AAA Cassette and the Hand-Over-Hand Translocation Mechanism	26
7	Schematic of Early, Nucleolar Steps of pre-60S Assembly.	33
8	Schematic of CP Formation in the Nucleoplasm.	35
9	Structure of the RNC:SecYEG:Nanodisc Complex	37
10	Model for translocation of folded Rip1 protein by Bcs1.	39

1 Introduction

Ribosomes are the cellular machinery for the synthesis of proteins. They fulfill this task by translating mRNA into polypeptide chains with the help of aminoacylated tRNAs. Ribosomes themselves consist of rRNA and ribosomal proteins, which must in turn be synthesized and assembled in a highly orchestrated fashion to form this complex machinery. Once matured and active, they are a hub for various cellular processes, such as mRNA turnover, regulation of gene expression, and protein targeting. This dissertation covers two ribosome associated pathways: the formation of the large ribosomal 60S subunit, as well as cotranslational protein translocation via the universally conserved Sec translocation system. Finally, it covers an exceptional, non-ribosome driven pathway of folded protein translocation in the mitochondria, enabled by the AAA-protein Bcs1.

1.1 The Structure and Function of the Ribosome

A hallmark of all cells is that translation of genetic information, protein biosynthesis, is conducted by large molecular machines, the ribosomes. The principal architecture, the functional sites and the catalytic mechanism are conserved over all kingdoms of life: bacteria, archaea and eukaryotes. Historically, the dimensions of ribosomes, and the small and large subunit (SSU and LSU) as their major subcomplexes, have been reported based on their sedimentation coefficients (S: Svedberg). The eukaryotic cytoplasmic ribosome is thus referred to as the 80S ribosome, consisting of the 40S (SSU) and 60S (LSU) subunit, whereas the 70S prokaryotic ribosome consists of the 30S (SSU) and 50S (LSU) subunit. The building blocks of all ribosomes are rRNA and ribosomal proteins. In the yeast *Saccharomyces cerevisiae* the LSU consists of the 25S, 5.8S and 5S rRNA moieties and 46 ribosomal proteins, whereas the SSU is composed of the 18S rRNA and 33 ribosomal proteins. As indicated by the sedimentation coefficients, eukaryotic ribosomes are larger than their prokaryotic counterparts, comprising additional rRNA expansion segments (ES) and ribosomal proteins.

To perform the task of protein biosynthesis, the two subunits act together in decoding the mRNA and translating it into proteins (Crick, 1958). The mRNA

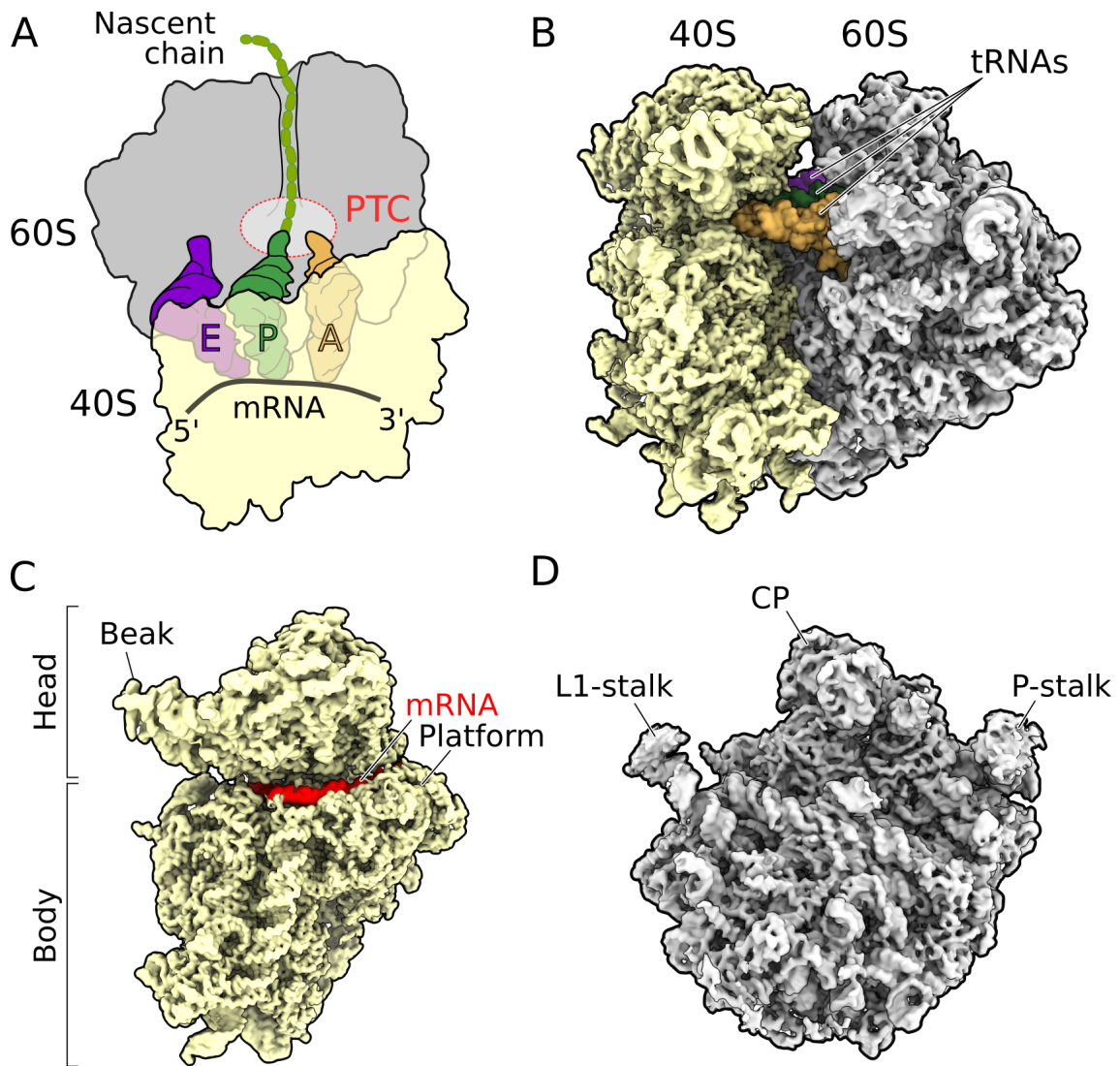


Figure 1: Overview of the Eukaryotic 80S Ribosome

A) Schematic of the ribosome showing the SSU and LSU, mRNA, three tRNAs, the peptidyl-transfer center (PTC) and the nascent polypeptide chain in the peptide exit tunnel.

B) Side view of the *Saccharomyces cerevisiae* 80S ribosome (EMD-4474, Tesina et al., 2019).

C) and D) views on the intersubunit surface (ISS) of the SSU and LSU respectively.

consists of non-overlapping, adjacent trinucleotide codons, that each code for one amino acid (Crick et al., 1961). With the exception of the three stop codons, there is a 3'-aminoacylated tRNA with a matching anti-codon for every codon of the mRNA (Nirenberg et al., 1965). Complementarity of codons and anti-codons is ensured through base pairing and non-perfect wobble base-pairing, allowing a single tRNA to match multiple codons (Crick, 1966). The translational process has been extensively reviewed (Frank and Gonzalez, 2010; Ramakrishnan, 2002; Schmeing and Ramakrishnan, 2009) and it can be briefly summarized in three phases: i) initiation, when the two ribosomal subunits are joined on the mRNA and find the translation start site. ii) Elongation, during which the ribosome reads along the mRNA and translates it via tRNAs into a polypeptide chain and iii) Termination and recycling, where translation is completed by release of the newly formed polypeptide chain and the ribosomal subunits are recovered for reuse. All of these steps are associated with the activity of a plethora of additional factors.

The assembled ribosome displays a globular shape with a cleft between both subunits, which harbors three distinct tRNA binding sites: the A-, P-, and E- site (see Figure 1A, 1B and Agrawal et al., 1996). The SSU shows an elongated shape with a head, containing a protrusion called the beak, and a body. During translation, the 5' end of the mRNA threads through the entry tunnel, passes through a groove between head and body and leaves the SSU at the mRNA exit site between SSU platform and head (Schlueder et al., 2000). During translation, the mRNA that passes through the groove between head and body (Figure 1C) exposes nucleotides towards the ISS, where these can be matched with corresponding tRNAs in the mRNA decoding center (Ogle et al., 2001). The fidelity of this decoding process is supervised by the rRNA of the decoding center of the SSU (Carter et al., 2000; Ogle et al., 2001). During initiation, the SSU serves as an assembly platform to form the initiation complex, consisting of an initiator tRNA, initiation factors, the mRNA and the SSU (Aitken and Lorsch, 2012).

The LSU has a flattened spherical shape with three structural protrusions at the ISS: the L1-stalk, CP and P-stalk. This results in the characteristic crown shape, when viewed from the ISS (Figure 1D). The L1-stalk, consisting of rRNA helices 75–78 and the ribosomal protein uL1 is required for efficient release of tRNA from the E-site (Cornish et al., 2009; Trabuco et al., 2010) but also serves as a binding site for factors such as eIF5A (Schmidt et al., 2016). The CP consists of rRNA helices 80–88, the 5S rRNA and ribosomal proteins uL5 and uL18. It provides an intersubunit bridge connecting the LSU to the SSU (Frank et al., 1991) with

key functionalities in binding of tRNAs (Agrawal et al., 1996) and the elongation factor eEF3 in fungi (Andersen et al., 2006). The P-stalk consists of the ribosomal proteins uL11, P1 and P2 and together with the sarcin-ricin-loop forms the GTPase-associated center (GAC), a region essential for the interaction with translational GTPases (Diaconu et al., 2005; Huang et al., 2010; Nomura et al., 2012). The central feature of the ribosome, the peptidyl transferase center (PTC) is also located on the LSU (see Figure 1A and Traut and Monro, 1964). Here, formation of the peptide bond takes place by transferring the nascent peptide chain from the P-site tRNA onto the aminoacylated A-site tRNA, thus elongating it by one amino acid (Frank and Gonzalez, 2010). The PTC marks the beginning of the the peptide exit tunnel which spans the entire LSU. The N-terminal end of the nascent chain exits the catalytic site and later the ribosome through this tunnel. The peptide tunnel exit site, located on the solvent exposed backside of the LSU, is an important interaction hub for various factors involved in cotranslational targeting, folding or modification of the nascent chain. For example chaperones like RAC (Gautschi et al., 2001), nascent chain modifying enzymes (metAPs and NATs, Gautschi et al., 2003; Giglione et al., 2015; Knorr et al., 2019) as well as co-translational protein targeting and translocation factors (e.g SRP and the Sec translocon, Beckmann et al., 1997; Görlich et al., 1992; Halic et al., 2004) bind in close proximity to the peptide exit tunnel.

1.2 Eukaryotic Ribosome Biogenesis

The investigation of ribosome assembly began with the reconstitution of bacterial ribosomes from their individual components: rRNA and ribosomal proteins (Held et al., 1973; Nierhaus and Dohme, 1974). Since then, more elaborate techniques have enabled the study of this process in eukaryotes, especially using the yeast *Saccharomyces cerevisiae* as a model organism. As such, genetic screening and biochemical approaches have revealed numerous auxiliary proteins required for ribosome assembly and have provided insights into pre-rRNA processing. Affinity purification combined with mass spectrometry analysis has been used to characterize distinct assembly intermediates (Woolford and Baserga, 2013). Regarding the economics of ribosome production: a typical yeast cell harbors approximately 200,000 cytoplasmic ribosomes. Under ideal conditions, such a cell can reproduce every 90-100 minutes, thus requiring the production of circa 130,000 ribosomes per hour or equivalently 10 million ribosomal proteins and around one billion nucleotides of rRNA

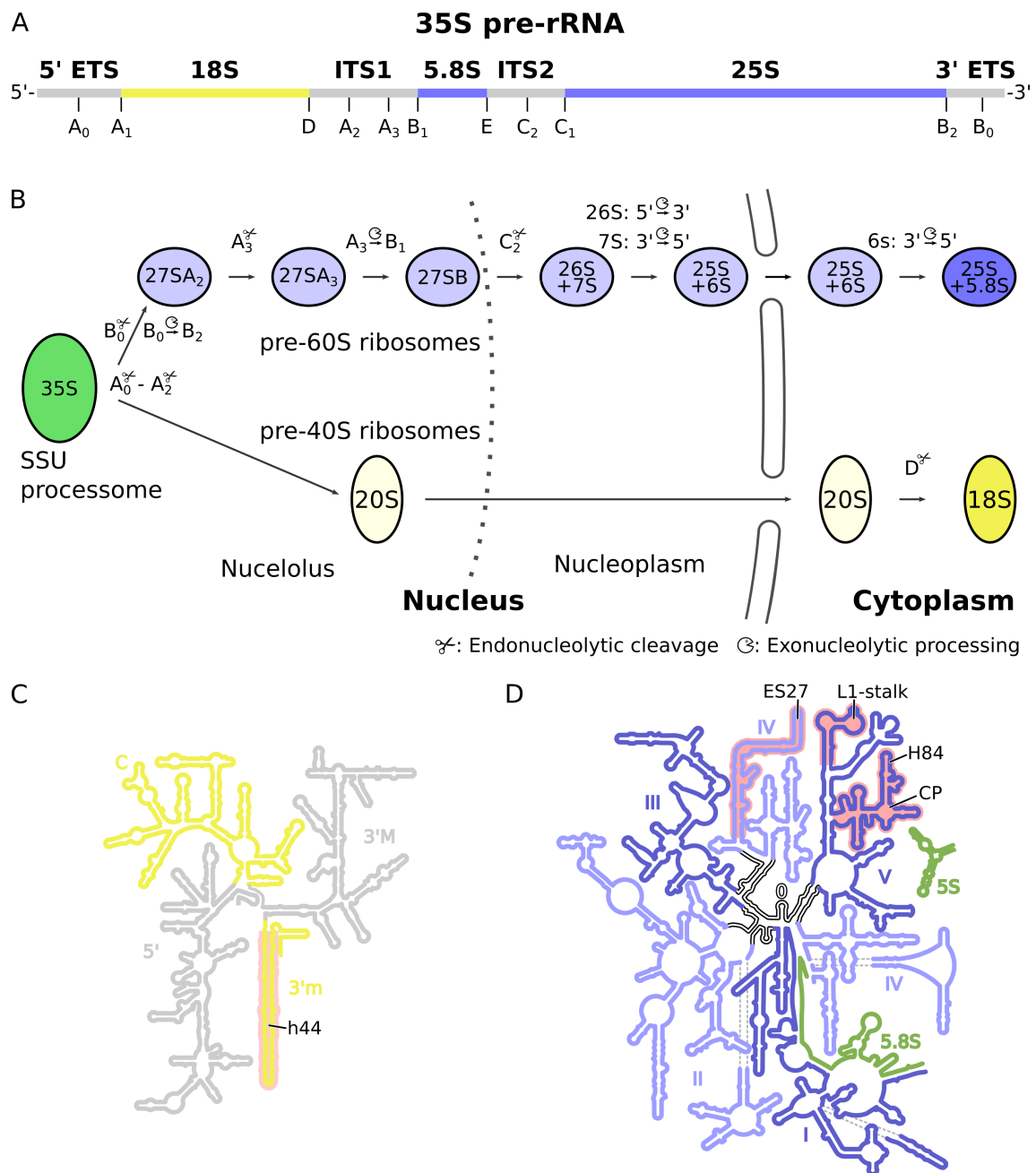


Figure 2: Schematic of 35S pre-rRNA, its Processing and Secondary Structure of the Products

A) Schematic of the 35S pre-rRNA, the encompassed rRNA moieties, processing and cleavage sites (Henras et al., 2015).

B) Schematic of the pre-rRNA processing pathway through the eukaryotic cell (Henras et al., 2015).

C) and D) secondary structure diagrams of the SSU and LSU rRNA, colored by domain (Petrov et al., 2014). Important regions are highlighted with a red outline. 3'm: 3' minor domain ; 3'M: 3' major domain; C: central domain; CP: central protuberance; ES: expansion segment; H, h: helix of the LSU and SSU, respectively.

(Warner, 1999). This process consumes the major part of the cellular energy and thus presents an enormous logistic feat for the cell (Warner, 1999). Consequently, production of ribosomes is tightly regulated and involves a plethora of more than 200 AFs guiding and supporting this assembly process, providing directionality, as well as guaranteeing efficiency and accuracy (Kressler et al., 2010; Thomson et al., 2013; Woolford and Baserga, 2013).

Starting point for eukaryotic ribosome biogenesis is the nucleolus, a sub-compartment of the nucleus and the transcription site of the bulk of rDNA (Perry, 1962). Here, the RNA polymerase I (Pol I) transcribes a polycistronic precursor, the 35S pre-rRNA in yeast (47S pre-rRNA in higher eukaryotes) (see Figure 2A and Nogi et al., 1991). This precursor RNA harbors the 18S rRNA of the SSU, as well as the 5.8S and 25S rRNA moieties of the LSU (Udem and Warner, 1972). These RNA species are connected via the internal transcribed spacer 1 and 2 (ITS1 and ITS2) and flanked by the 5' and 3' external transcribed spacers (5' ETS and 3' ETS) (Johnston et al., 1997). Thus, to obtain the final rRNA species, a series of rRNA processing steps is required. While Pol I transcription appears to be strictly localized to the nucleolus, the location of 5S rRNA transcription by RNA polymerase III (Pol III) varies by organism, cell and tissue type and is not necessarily nucleolar (Haeusler and Engelke, 2006; Highett et al., 1993; Pardue et al., 1973). Once transcribed, the pre-rRNA must be processed and, together with ribosomal proteins, assembled to form the previously described complex tertiary structure (Figure 1B, 2C and 2D). Electron microscopy of nucleolar chromatin spreads has revealed that assembly of the ribosomal particles starts parallel to transcription (Miller and Beatty, 1969; Mougey et al., 1993; Osheim et al., 2004). These spreads show “christmas tree”-like structures where the rDNA corresponds to the stem of the tree. Numerous actively transcribing polymerases sit at branching points along the rDNA with the rRNA transcripts forming the branches of the tree. The branches terminate in knob-like structures, which are a result of the compaction of the transcribed rRNA and thus assembly of early pre-ribosomal particles (Mougey et al., 1993; Osheim et al., 2004).

Apart from processing events leading to the removal of the ETS and ITS sequences, the pre-rRNA also undergoes a high number of RNA modification events. The bulk of rRNA modifications are introduced by small nucleolar RNA (snoRNA) containing RNPs (snoRNPs), of which there are several types: box H/ACA snoRNPs catalyze pseudouridylation at 44 known sites in yeast, while the box C/D snoRNPs catalyze 2'-O-ribose methylation at 67 known sites (Balakin et al., 1996; Ganot et al., 1997; Kiss-László et al., 1996; Liang et al., 2009; Watkins and Bohnsack,

2012). These RNPs are guided to their respective target sites via base complementarity between the rRNA and their snoRNA component (Nicoloso et al., 1996; Qu et al., 1995). Apart from snoRNPs, additional modifications are introduced by enzymatic AFs such as the methyltransferases Bud23, Nop2 or Spb1 (Kressler, 1999; Lapeyre and Purushothaman, 2004; Sharma et al., 2013; White et al., 2008).

1.2.1 Formation of the Small Ribosomal Subunit

Early Nucleolar Steps of SSU Assembly

Determined by the sequence of rRNAs encoded on the 35S pre-rRNA, assembly of ribosomal particles starts with the SSU, as its 18S rRNA is transcribed first (Figure 2A). The first assembly intermediates purified containing the 35S precursor rRNA is the 90S particle, which, apart from RNA also contains ribosomal proteins, AFs and snoRNAs (Dragon et al., 2002; Grandi et al., 2002; Trapman et al., 1975). Strikingly, while these particles contain the 35S precursor rRNA, they are only associated with ribosomal proteins of the SSU, thus giving it the name SSU processome (Dragon et al., 2002; Grandi et al., 2002). Key components of this particle are a set of structurally autonomous complexes: the U3 snoRNP, as well as the U3 small nucleolar RNA-associated protein modules A, B and C (UTP-A, -B and -C), the Mpp10-Imp3-Imp4 module and the Bms1-Rcl1 module (Chaker-Margot et al., 2015; Pérez-Fernández et al., 2011; Zhang et al., 2016). Binding of the UTP-A module to the 5' ETS initiates assembly of the SSU processome and is followed by subsequent incorporation of the UTP-B module and the U3 snoRNP (Chaker-Margot et al., 2015; Dutca et al., 2011; Hunziker et al., 2016). The U3 snoRNP plays a significant role in early folding events of the 5' ETS and 18S rRNA, as it prevents premature formation of the central pseudo knot structure found in mature SSU (Dutca et al., 2011; Kudla et al., 2011; Marmier-Gourrier et al., 2011). It is aided by the Mpp10-Imp3-Imp4 module, which has been shown to stimulate the formation of RNA duplexes between the U3 snoRNA and 5' ETS and 18S sequences of the 35S precursor *in vitro* (Gerczei et al., 2009). By arresting the assembly of the SSU processome at different time points of rRNA transcription, the association of these modules could be mapped to different rRNA regions, showing that after the association of the UTP-A, UTP-B, U3 snoRNP and Mpp10-Imp3-Imp4 modules to the forming 5' ETS domain, the UTP-C module associates to later transcripts harboring both the 5' and central domain of the 18S rRNA (see also Figure 2C and Chaker-Margot et al., 2015; Zhang et al., 2016). The following domains of the SSU rRNA

are all associated with distinct sets of ribosomal AFs. Several cryo-EM structures have revealed the architecture of the SSU processome (Chaker-Margot et al., 2017; Cheng et al., 2017; Kornprobst et al., 2016; Sun et al., 2017). These structures show how the 5' ETS together with the UTP-A and UTP-B modules act as a mold or a scaffold to allow for a separate, sequential and seemingly independent maturation of the 18S rRNA domains, with the U3 snoRNP acting as a central organizing element. Proceeding from 90S SSU processome particle to mature SSU particles requires processing of the 35S pre-rRNA at sites A_0 and A_1 in the 5' ETS and at site A_2 in the ITS1, where both Rcl1 and Utp24 have been implied as required endonucleases (Horn et al., 2011; Tomecki et al., 2015). Nucleolytic cleavage of the rRNA at these sites results in the separation of the rRNA into the 5' ETS, the 20S pre-rRNA and the 27S pre-rRNA (Figure 2A and 2B). While the 5' ETS is degraded by the nuclear exosome and 5' exonucleases (Allmang et al., 2000; Petfalski et al., 1998), the 20S and 27S pre-rRNA moieties continue to separately mature into the SSU and LSU.

Late Steps of SSU Assembly

Proceeding from the large SSU processome state to pre-40S particles requires dismantling of the 90S particle, removing the UTP modules, the U3 snoRNP and the 5' ETS RNA (Schäfer et al., 2003; Grandi et al., 2002). The ATP dependent helicase Dhr1 plays a key role in this disassembly process, facilitating the removal of the U3 snoRNP (Sardana et al., 2015). Biochemical data indicate that this dismantling step occurs as a fast, transient process, quickly leading from the complex 90S SSU processome to a much less complex 20S pre-rRNA containing particle (Schäfer et al., 2003). Structural data depicting this dismantling remains to be published. While a large part of the early AFs is removed and recycled, a set of AFs including Dim1, Enp1, Rrp12 and Hrr25 further accompany the maturing pre-40S particle (Schäfer et al., 2003). Kinetic and ultrastructural analysis combined with localization studies of pre-40S associated AFs indicates that once the nascent SSU has passed the 90S stage, pre-40S particles are rapidly exported into the cytoplasm where final maturation takes place (Gleizes et al., 2001; Schäfer et al., 2003; Udem and Warner, 1973). Nevertheless, to achieve nuclear export competency, pre-40S particles must complete a series of steps, among these is the incorporation of ribosomal proteins eS17 and uS19 (Ferreira-Cerca et al., 2005; Léger-Silvestre et al., 2004; O'Donohue et al., 2010). A series of high resolution cryo-EM structures provide insight into these late nuclear and early cytoplasmic yeast and human pre-40S assembly inter-

mediates (Ameismeier et al., 2018; Heuer et al., 2017; Scaiola et al., 2018). These structures reveal that while the 40S body is mostly in a close to mature conformation, the head and thus the 3' major and 3' minor domains of the 18S rRNA (Figure 2C) are yet to form and mature (Ameismeier et al., 2018; Heuer et al., 2017; Scaiola et al., 2018). Structures of the assembling human pre-40S indicate that assembly of the head starts in the nucleus (Ameismeier et al., 2018). Here Rrp12, a remnant of the SSU processome (Cheng et al., 2019), plays a major role, initially stabilizing rRNA in premature conformations and potentially acting as a quality control factor (Ameismeier et al., 2018).

Finally, export through the nuclear pore complex (NPC) is dependent on a set of nuclear export sequence containing proteins (Rio2, Pno1 and Ltv1) and the export adaptors Rrp12 and Slx9, of which the latter was indicated to bind both Rio2 and Gsp1/Ran-GTP and furthermore facilitates recruitment of the transport receptor Crm1 (Fischer et al., 2015; Hurt et al., 1999; Oeffinger et al., 2004; Seiser et al., 2006; Vanrobays et al., 2008; Zemp et al., 2009). During the final maturation steps in the cytoplasm, the remaining AFs, including the nuclear export factors are removed, remaining ribosomal proteins are incorporated and final rRNA maturation occurs. As many of the remaining AFs could be located to functionally important sites on the SSU, it was proposed that these factors prevent premature association of unfinished pre-40S with the active translation machinery (Strunk et al., 2011). Release of Ltv1 and Enp1 from the maturing head allows binding of a cluster of ribosomal proteins, eS10, uS3, uS10 and uS14, resulting in a mature-like beak on the head of the pre-40S (Mitterer et al., 2016; Ameismeier et al., 2018). To enable finalization of the A- and P-site as well as the decoding center, Tsr1 and Rio2 must dissociate, allowing helix 44 to assume its mature conformation (Ameismeier et al., 2018; Heuer et al., 2017; Scaiola et al., 2018). Finally, a cleavage step at site D of the SSU pre-rRNA via Nob1 is required to produce mature 18S rRNA (Fatica et al., 2004; Lamanna and Karbstein, 2009; Lebaron et al., 2012). In yeast, these finishing steps appear to include a translation like step, where Nob1 containing pre-40S particles associate with mature 60S particles and the GTPase Fun12 perform a final proof-reading step resulting in mature and translationally competent SSU particles (Lebaron et al., 2012; Strunk et al., 2012).

1.2.2 Formation of the Large Ribosomal Subunit

As mentioned above (see 1.2.1: Early Nucleolar Steps of SSU Assembly), nucleolytic cleavage at site A₂ sets both SSU and LSU maturation on independent tracks and thereby paves the way for the formation of the LSU. From there on, LSU biogenesis can be subdivided into three main phases defined by three different cellular compartments. In the first phase, initial formation of the pre-60S particle occurs in a series of steps in the nucleolus (de la Cruz et al., 2015; Kressler et al., 2017). In the nucleoplasmic phase, large parts of the pre-60S have already reached a mature like state (Barrio-Garcia et al., 2016; Bradatsch et al., 2012; Leidig et al., 2014; Wu et al., 2016). While progressing further, large scale restructuring events take place, including processing of the ITS2 (Fromm et al., 2017; Gasse et al., 2015) and maturation of the CP (Barrio-Garcia et al., 2016; Leidig et al., 2014; Wu et al., 2016). Upon licensing for export, the pre-60S particles pass the NPCs and enter the final phase in the cytoplasm where maturation completes and translational competency is achieved (Greber, 2016; Kressler et al., 2017). Similar to formation of the 40S, this process is accompanied by a large number of AFs, which transiently bind the forming pre-particles, aid in the assembly process, perform regulatory tasks and consume energy to provide directionality (Greber, 2016; Kressler et al., 2017; Woolford and Baserga, 2013). While in the SSU process some of the individual rRNA domains mature mostly in an independent fashion (Chaker-Margot et al., 2017; Cheng et al., 2017; Kornprobst et al., 2016; Sun et al., 2017), the mature LSU forms a more monolithic structure, with the rRNA domains intertwined (Ben-Shem et al., 2010), hinting at differences in assembly and folding between SSU and LSU.

Early Nucleolar Steps of Large Subunit Assembly

Similar to the SSU processome, formation of the LSU commences with complex assembly intermediates bearing many different AFs, which decrease in complexity during the course of their maturation (Nissan et al., 2002; Wu et al., 2016). Using the AF Npa1 as bait, a pre-60S particle bearing mainly the early 27SA₂ pre-rRNA intermediate can be isolated (Figure 2A and 2B and Dez et al., 2004). As it is also the only particle known to contain a number of the early acting snoRNPs, this particle represents one of the earliest assembly intermediates of the LSU (Dez et al., 2004). Furthermore, this particle also enriches a number of RNA helicases, including Dbp3, Dbp6, Dbp7, Dbp9, Drs1 and Has1, indicating ongoing folding and assembly of the pre-rRNA. While the 27SA₂ pre-rRNA is already associated with many LSU

ribosomal proteins (Dez et al., 2004; Fatica et al., 2002), systematic studies of LSU assembly phenotypes caused by depletion of ribosomal proteins indicate that assembly of the LSU happens in hierarchical steps, with groups of ribosomal proteins essential for early, intermediate and late assembly (Gamalinda et al., 2014). The clustering of the ribosomal proteins of these groups within the structure of the LSU indicates that the solvent exposed back of the LSU is among the first structures to assemble, followed by the peptide exit tunnel region, and finally the CP and ISS. Integration of ribosomal protein uL3, a member of the group of ribosomal proteins essential during early assembly, is thought to be among the earliest LSU assembly steps and was shown to be required for correct and efficient processing of 27SA₂ pre-rRNA (Gamalinda et al., 2014; Kruiswijk et al., 1978; Rosado et al., 2007b). This protein connects the 5' (domain II) and the 3' (domain VI) portion of the 25S rRNA (Ben-Shem et al., 2010). Its assembly into the maturing LSU requires a specific complex of AFs consisting of Dbp6, Npa1/Urb1, Npa2/Urb2, Nop8 and Rsa3 (Rosado et al., 2007a). Thus, both 5' terminal and 3' terminal segments of the 27S pre-rRNA are required for these early folding and assembly steps.

Via Ssf1, a later nucleolar intermediate of the assembling LSU can be isolated which co-purifies 27SA₂ and 27SA₃ and 27SB pre-rRNA (Dez et al., 2004; Fatica et al., 2002; Kressler et al., 2008). Both the Npa1 and the Ssf1 particle show AFs known to bind the ITS2 organizing structure termed the foot, indicating that this structure already forms during these early steps of LSU assembly (Dez et al., 2004; Fatica et al., 2002; Kressler et al., 2008; Wu et al., 2016). A particle further downstream can be purified via Nsa1 (Kressler et al., 2008). Nsa1 is mainly associated with 27SB pre-rRNA, where processing of residual ITS1 at the 5' end has fully taken place (see Figure 2B and Kressler et al., 2008). Furthermore, at this stage, incorporation of the 5S rRNA has also occurred. This involves a set of five proteins, the two ribosomal proteins uL5 and uL18, the AFs Rpf2 and Rrs1 and the auxiliary protein Syo1 (Calviño et al., 2015; Kharde et al., 2015; Madru et al., 2015; Zhang et al., 2007). Syo1 is a nuclear import adaptor, synchronizing import of the ribosomal proteins uL5 and uL18 (Kressler et al., 2012). It was furthermore indicated to act as a chaperone for assembly of the 5S RNP consisting of the 5S rRNA, uL5 and uL18, as well as the AFs Rpf2 and Rrs1 (Calviño et al., 2015; Kharde et al., 2015). Moreover, Syo1 was proposed to aid in the subsequent integration of the 5S RNP into the LSU precursor, where it binds to H84 in domain V of the 25S rRNA (see also Figure 2D, Ben-Shem et al., 2010; Calviño et al., 2015; Kharde et al., 2015; Leidig et al., 2014). The Nsa1 particle is also characterized by the presence

of the ITS2 organizing factors Cic1/Nsa3, Nop7, Rlp7 and Nop15, which form the previously mentioned foot structure (Kressler et al., 2008; Wu et al., 2016), as well as Erb1 and Ytm1, a heterodimer of β -propellers known to interact with Nop7 of the foot (Kressler et al., 2008; Miles et al., 2005; Tang et al., 2008; Thoms et al., 2016; Wegrecki et al., 2015). Both Nsa1 and Ytm1 are dependent on the activity of the AAA-proteins Rix7 and Rea1, respectively, to be dissociated from the maturing pre-60S particles (see also 1.4: AAA-Proteins: a Versatile Clade of Molecular Machines and Bassler et al., 2010; Kressler et al., 2008). The motor protein Rix7, required for stripping Nsa1 from pre-60S particles, is a type II AAA-protein and shows similarities to the hexameric unfoldase Cdc48 (Gadal et al., 2001b; Kressler et al., 2008; Xia et al., 2016). Rea1, on the other hand, is a large dynein related protein, which harbors six AAA+ modules, as well as a long N-terminal tail bearing a metal ion dependent adhesion domain (MIDAS) (Garbarino and Gibbons, 2002). MIDAS domains are homologous to the I-domain of integrins, which mediate tensile force resistant substrate binding via a coordinated metal ion (Arnaout et al., 2005; Craig et al., 2004; Garbarino and Gibbons, 2002). It was demonstrated that Rea1 is required for two subsequent steps of pre-60S remodeling: release of the Erb1-Ytm1 subcomplex, which is thought to occur at the transition between nucleolus and nucleoplasm and release of the Rsa4 AF in the nucleoplasm (Bassler et al., 2010; Ulbrich et al., 2009). To do so, the MIDAS domain binds the ubiquitin like (UBL) domain of its substrate proteins, Rsa4 and Ytm1. Based on immuno-labeled negative stain electron microscopy images, the MIDAS domain was thought to be localized at the tip of the long, structured tail protruding from the ring of AAA+ domains, putatively enabling Rea1 to act like a mechano-chemical spring (Ulbrich et al., 2009). Removal of the Erb1-Ytm1 subcomplex via Rea1 precedes a large restructuring event, during which many early acting AFs are lost and is linked to the nucleolar to nucleoplasmic transition of pre-60S particles. Disruption of this release step via overexpression of the dominant-negative Ytm1 E80A mutant, rendering it incapable of binding the Rea1 MIDAS domain, retains and accumulates pre-60S particles in the nucleolus (Bassler et al., 2010). Thus, this release step is a necessary requirement for progression of the maturing LSU into the nucleoplasm.

Nucleoplasmic Restructuring Events Leading to Export Competency

Multiple nucleoplasmic intermediates have been structurally characterized via cryo-EM, the earliest of which is the Arx1/Nog2 particle that can be purified via Alb1,

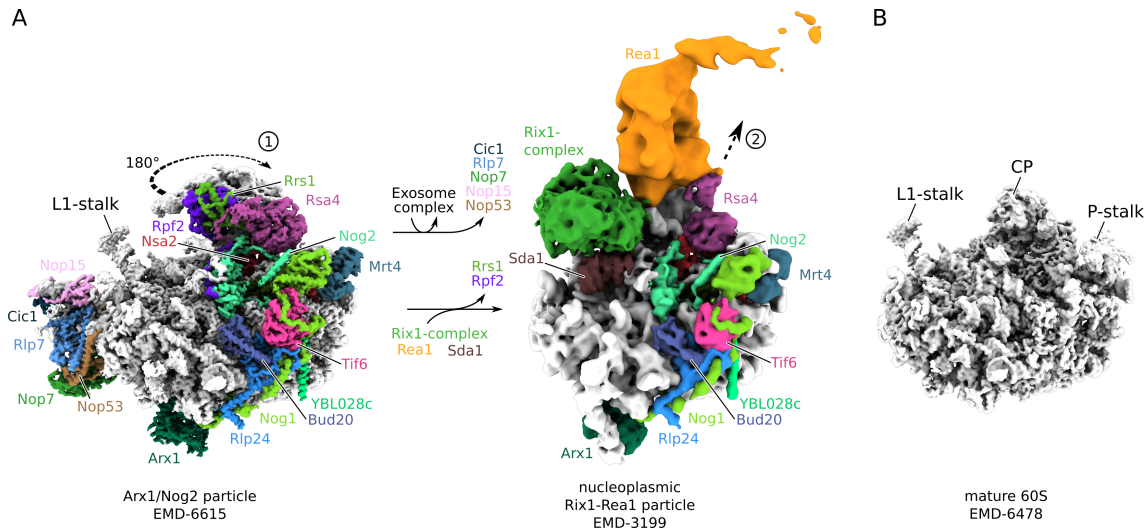


Figure 3: The Nucleoplasmic Restructuring Step of the Rix1-Rea1 Remodeling Machinery

A) Transition from the Arx1/Nog2 particle (EMD-6615, Wu et al., 2016) to the Rix1-Rea1 particle (EMD: 3199, Barrio-Garcia et al., 2016) showing ITS2 processing and maturation of the central protuberance. Step 1: rotation of the CP and 5S RNP requiring binding of the Rix1-complex and Rea1. Step 2: Release of Rsa4 by Rea1 causing dissociation of Rea1, the Rix1-complex and Sda1. rRNA and ribosomal proteins are depicted in gray, assembly factors are depicted in color.

B) For comparison, a mature LSU viewed in the same orientation as (A) with central hallmarks indicated (EMD-6478 Passmore and Russo, 2016).

a binding partner of Arx1, and via Nog2 (Bradatsch et al., 2012; Leidig et al., 2014; Wu et al., 2016). Overall, this particle bears 19 AFs and 36 of the 46 LSU ribosomal proteins (Wu et al., 2016). Most of the rRNA of this particle is already stably folded. Particularly the early-forming solvent side is largely in a mature state (Bradatsch et al., 2012; Leidig et al., 2014; Wu et al., 2016). AFs cluster at functionally important sites. Arx1 and Alb1 are bound at the peptide exit tunnel (Bradatsch et al., 2012). A series of AFs decorate the immature ISS and CP, covering an arch-like section of the LSU precursor, reaching from the CP along the edge of the ISS and the P-stalk region towards the peptide exit tunnel (Leidig et al., 2014; Wu et al., 2016). Apart from the characteristic ITS2-bearing foot structure (see 1.2.2: Early Nucleolar Steps of Large Subunit Assembly), the hallmark of this particle is the configuration of the CP, showing the 5S RNP stabilized in a premature state. To reach its final cytoplasmic conformation it requires a 180° rotation (Figure 3). The 5S RNP and CP are anchored and stabilized in this premature configuration

by the AFs Cgr1, Rsa4 and the Rpf2-Rrs1 heterodimer.

Notably, a reoccurring theme in ribosomal biogenesis are AFs with long meandering extensions that act as a connection and interaction hub. In this case the GTPases Nog1 and Nog2 and also the 5S RNP factors Rpf2 and Rrs1 show such extensions (Wu et al., 2016). Nog1 forms an N-terminal tripod like helical bundle blocking the premature A- and P-sites, with its GTPase domain in close proximity to the AF Tif6 and the sarcin-ricin loop of the LSU (Leidig et al., 2014; Wu et al., 2016). Its long C-terminal tail stretches along the side of the ISS past Tif6, making contacts with Rlp24. It then crosses the solvent exposed back side of the LSU, where it interacts with Arx1 and finally threads into the forming peptide exit tunnel (Wu et al., 2016). Nog2 sits at the base of the premature ISS, contacting multiple rRNA segments of 25S rRNA domain IV and making multiple interactions with its C-terminal tail with the AFs Nog1, Nsa2, Rpf2, Rrs1 and Rsa4 (Wu et al., 2016).

As indicated above, Rsa4, the second substrate of the AAA-protein Rea1 is present in these early nucleoplasmic particles (Ulbrich et al., 2009; Wu et al., 2016). Binding of the Rea1 remodeling machinery, consisting of the Rix1-Ipi1-Ipi3 subcomplex (in short: Rix1-complex), Sda1 and the Rea1 AAA protein, is the onset of a large restructuring event of the CP and ISS of the maturing 60S particle (Barrio-Garcia et al., 2016; Bassler et al., 2014; Ulbrich et al., 2009). In a cryo-EM study, particles purified via Rix1 and Rea1 show Sda1 binding on the premature ISS between the L1-stalk and the CP. Here, it acts as an adapter or as a binding platform for a globular protein density, which was previously assigned to the Rix1-complex (Barrio-Garcia et al., 2016; Wu et al., 2016). The approximately 280 Å long Rea1 protein is attached with its ring of AAA+ motor domains to three binding sites: the CP, H38 and Rsa4. Its long and structured N-terminal tail protrudes away from the LSU (Barrio-Garcia et al., 2016). In contrast to the Arx1/Nog2 particle, this particle shows the 5S RNP and CP in a conformation close to its mature state, indicating a significant previous remodeling event, resulting in the 180° rotation of the 5S RNP (Barrio-Garcia et al., 2016; Leidig et al., 2014; Wu et al., 2016). It was shown that binding of Rea1, but not ATP hydrolysis is required for this restructuring to take place (Barrio-Garcia et al., 2016). Apart from rotation of the 5S RNP, the restructuring of the CP goes hand in hand with a repositioning of H38, a shift in the interaction with Rsa4, both of which are binding sites of Rea1, as well as a conformational change in Cgr1 (Barrio-Garcia et al., 2016; Wu et al., 2016). The observed Rix1-Rea1 particle appears to be in a pre-release state, with the Rea1 ATPase bound to its substrate Rsa4, even though the MIDAS domain, critical to

the release reaction, could not be identified (Barrio-Garcia et al., 2016). It was proposed that the placement of the Rix1-complex and Rea1 at the CP allows sensing its maturation. The observed Rix1-Rea1 particle thus would serve as a checkpoint, which then would allow unidirectional progression of the LSU precursor along the maturation pathway through release of Rsa4.

A further notable process taking place in the transition between the Arx1/Nog2 particle and the later Rix1-Rea1 defined particle is the processing of the ITS2 and thus removal of the foot structure (see Figure 3A and Barrio-Garcia et al., 2016; Wu et al., 2016). First, the 27SB pre-rRNA bearing the full ITS2 is cleaved at site C₂ by the Las1 endonuclease, which forms a stable complex with the polynucleotide kinase Grc3, the 5' - 3' exonuclease Rat1 and its activating cofactor Rai1 (Braglia et al., 2010; Castle et al., 2013; Fromm et al., 2017; Gasse et al., 2015; Geerlings et al., 2000; Xiang et al., 2009). The result of this cleavage reaction is the 2',3'-cyclic phosphate bearing 7S and the 5' OH bearing 26S pre-rRNA (Gasse et al., 2015). The 7S pre-rRNA is processed to 6S pre-rRNA by the nuclear exosome, in combination with the Mtr4 helicase, responsible for unwinding the ITS2 rRNA and dismantling the foot structure (Fromm et al., 2017). Nop53, a component of the foot in nucleoplasmic pre-60S particles acts as an exosome adapter by specifically binding the Mtr4 helicase, thus targeting the 3' - 5' RNA processing machinery to the pre-ribosome (Thoms et al., 2015; Wu et al., 2016). The 26S pre-rRNA on the other hand is first phosphorylated by Grc3, facilitating subsequent processing via the Rat1-Rai1 module, resulting in 25S pre-rRNA (Gasse et al., 2015). Maturation of 6S pre-rRNA to 5.8S rRNA takes place later, after nuclear export of the LSU precursors to the cytoplasm (Thomson and Tollervey, 2010). While rotation of the 5S RNP and CP and the processing of the ITS2 appear as independent events *in vitro* (Fromm et al., 2017), the exact mechanisms governing the timing and coordination of these events remain unclear. The fact that the human ortholog of Las1 (LAS1L) is a part of the human Rix1-complex (PELP1-complex in humans) indicates that the Rix1-complex might be a central coordinator between CP maturation and ITS2 processing (Castle et al., 2012, 2013).

Similar to the SSU, export of the large ribosomal precursor particles is dependent on the presence of an array of export adaptors and auxiliary export factors, which are required to pass the hydrophobic phenylalanine-glycine-repeat (FG-repeat) mesh of the NPCs (Adams et al., 2010; Gerhardy et al., 2014). These factors shield the hydrophilic patches of the ribosomal particles and mediate interactions with the hydrophobic FG-repeats (Tran and Wentz, 2006). The Ran-GTP system additionally

provides directionality in the export process (Güttler and Görlich, 2011). Thus, export into the cytoplasm marks a critical, because non-reversible checkpoint in ribosome biogenesis (Gerhardy et al., 2014; Kressler et al., 2017). To obtain export competence, release of Rsa4 by Rea1 coincides with the release of the Rix1-Rea1 remodeling machinery from the pre-60S particle (Matsuo et al., 2014; Ulbrich et al., 2009). Concomitant GTP hydrolysis-dependent release of the Nog2 GTPase requires Rea1 action and frees the binding site of the export adaptor Nmd3 (Ma et al., 2017; Malyutin et al., 2017; Matsuo et al., 2014). Binding of the nuclear export sequence containing adaptor Nmd3 is a key step in establishing export competence. It recruits the Ran-GTP dependent Crm1, thus contributing to export of the particle through the NPC (Gadal et al., 2001a; Ho et al., 2000). A further role of Nmd3 appears to be compaction of the pre-60S particle by stabilizing the L1-stalk in an inward facing conformation and by binding H38 of the 25S rRNA, perhaps thereby facilitating passage through the NPC (Ma et al., 2017; Malyutin et al., 2017). Furthermore, the heterodimeric export adapter Mex67-Mtr2 is required for the cytoplasmic export of the LSU precursor (Lo and Johnson, 2009; Yao et al., 2007). It shows two distinct binding sites on pre-60S particles, at the 5.8S rRNA and at the site of the premature P0-stalk, apparently coupling export with maturation of the P-stalk (Sarkar et al., 2016). Arx1, already present in early nucleoplasmic LSU precursor particles also interacts with FG-repeats and is thus involved in conferring export competence (Bradatsch et al., 2007; Hung et al., 2008). Similar to Nmd3, Arx1 also helps compact the pre-60S particle by binding the long and flexible expansion segment ES27 (Bradatsch et al., 2012). Taken together, export competence relies on key maturation steps at the CP, ISS and P-stalk, allowing export adapters to bind which facilitate traversal of the NPCs to reach the cytoplasm.

Final Maturation Checkpoints in the Cytoplasm

LSU precursors are exported to the cytoplasm in a functionally inactive state requiring final rRNA processing and completion of assembly by release of AFs and coordinated incorporation of the remaining LSU ribosomal proteins (Kressler et al., 2017; Konikkat and Woolford, 2017). With respect to rRNA processing, the LSU undergoes a final cytoplasmic exonucleolytic maturation step: 3' - 5' trimming of the 6S pre-rRNA via the non-essential exonucleases Ngl2, Rex1 and Rex2 to form the final 5.8S rRNA (van Hoof et al., 2000; Thomson and Tollervey, 2010). The remaining assembly steps focus on the functionally most important sites of the LSU:

the catalytic PTC, the GAC and the tRNA binding sites on the ISS and finally the peptide exit tunnel (Figure 1). These steps constitute a series of checkpoints and proofreading processes validating the assembly of the LSU (Kressler et al., 2017; Konikkat and Woolford, 2017). Release of the GTPase Nog1 and the ribosomal protein placeholder Rlp24 requires a further AAA-protein, Drg1 (Lo et al., 2010; Pertschy et al., 2007). While Rlp24, which recruits and activates Drg1, is replaced by its paralog, ribosomal protein eL24, the peptide exit tunnel probing C-terminus of Nog1 is replaced by another AF, Rei1 (Greber et al., 2016; Lo et al., 2010; Pertschy et al., 2007). Rei1 in turn, together with Jjj1 and the Hsp70 protein Ssa1 are required for recycling of the export adapter Arx1 and its binding partner Alb1 (Greber et al., 2012; Lo et al., 2010; Meyer et al., 2007, 2010). Surprisingly, after release of Rei1 during Arx1 dissociation, AF Reh1 inserts into the tunnel, further blocking this functionally important site (Greber et al., 2016; Ma et al., 2017). On the ISS, several maturation steps are required for completion of the PTC and P-stalk. Release of the helicase Mrt4 at the site of the yet to form P-stalk requires binding of the Yvh1 phosphatase, which in turn is replaced by the Mrt4 paralog uL10 (Kemmler et al., 2009; Lo et al., 2010; Sarkar et al., 2016). Release and recycling of the export adapter Nmd3 requires the GTPase Lsg1 and is coupled to assembly of the ribosomal protein uL16 at the CP and PTC (Hedges et al., 2005; Hofer et al., 2007; West et al., 2005). Finally, only Tif6, a component of the pre-60S particles since the nucleolus stage, inhibits translational engagement of the quasi complete LSU with the SSU, implying that Tif6 dissociation via Sdo1 and Efl1 is the ultimate step in the assembly pathway of the LSU (Finch et al., 2011; Gartmann et al., 2010; Menne et al., 2007; Senger et al., 2001). The human ortholog of Sdo1, SBDS, was shown to probe multiple functional sites including the P-site and the P-stalk prior to inducing Tif6 release by stimulating GTP hydrolysis of Efl1, thus completing a final checkpoint in the assembly of the LSU (Weis et al., 2015).

1.3 Protein Translocation

One of the core tasks of cells is to ensure the correct transport of newly synthesized proteins from the cytosol to their final cellular destination (Berks, 2015; Christie, 2019; Green and Mecsas, 2016; Rapoport et al., 2017). In prokaryotes, possible target sites are the plasma membrane, the extracellular space and, in gram-negative bacteria, also the periplasmic space and the outer membrane. In eukaryotes, possible targets also include the ER membrane and lumen and the various organelles.

To do so, proteins encode signal sequences, stretches within the polypeptide, that encode a designated cellular localization signal to allow efficient sorting (Blobel, 1980). Prokaryotes have evolved a large number of different and specialized secretory pathways for protein translocation (Christie, 2019; Green and Meccas, 2016). While some of these have homologous counterparts in the mitochondria and plastids of eukaryotic cells (Bonney et al., 1994; Celedon and Cline, 2013; Kozjak et al., 2003; Schuenemann et al., 1998; Tu et al., 1999), the Sec translocation system stands out as the main prokaryotic and eukaryotic translocation and secretion pathway (Elvekrog and Walter, 2015; Rapoport et al., 2017; Zimmermann et al., 2011). Protein targeting and translocation into and within the mitochondria and chloroplasts is more complex, yielding a plethora of different pathways to target the individual sub-organellar compartments and membranes (Bölter, 2018; Celedon and Cline, 2012; Wiedemann and Pfanner, 2017).

1.3.1 The Sec Translocation Pathway

The SecYEG/Sec61 protein conducting channel—also called the Sec translocon—is a membrane protein complex required for translocation of unfolded proteins across, or insertion of proteins into membranes (Rapoport et al., 2017). This complex is highly conserved and present in all kingdoms of life. It is located in the plasma membrane of bacteria and archaea and in the ER-membrane of eukaryotes (Pohlschroder et al., 1997; Stephenson, 2005). Additionally, chloroplasts and also a few mitochondria make use of this system (Burger et al., 2013; Celedon and Cline, 2013). Substrates of this pathway are targeted to the Sec translocon by a signal sequence. This sequence typically contains a stretch of hydrophobic residues at the N-terminus and can be either cleavable or form an integral transmembrane α -helix (TMH) (Walter et al., 1981). As indicated above, the Sec translocon supports two different modes: translocation through the membrane via an aqueous central pore or lateral insertion of an integral TMH into the lipid phase of the membrane via a lateral gate (Rapoport et al., 2017). The distinction between lateral insertion into the membrane and translocation across the membrane is likely based on biophysical properties of the peptide sequence, such as length, hydrophobicity and nature of flanking residues (Hessa et al., 2005, 2007).

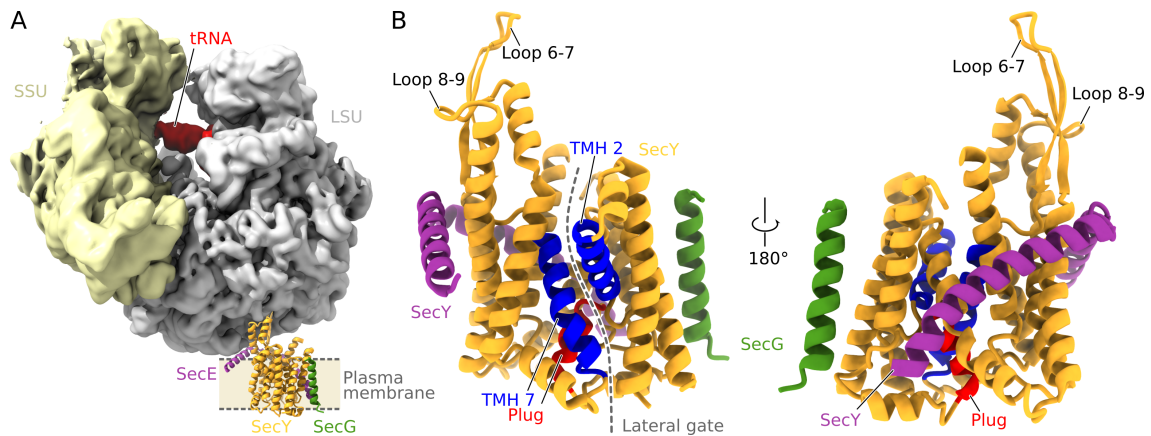


Figure 4: Architecture of the SecYEG Translocon

A) Overview of the bacterial ribosome bound to SecYEG.

B) Architecture of the SecYEG translocon showing the lateral gate (blue helices and dashed line), as well as the plug (red) and the ribosome interacting loops between TMH 6 and 7 (Loop 6-7) and between TMH 8 and 9 (Loop 8-9).

All structures based on PDB 5GAE and EMD-8001 (Jomaa et al., 2016).

Architecture of the Sec Translocon

Multiple structures of the Sec translocon have been solved from bacteria, archaea and eukaryotes, reflecting different conformational states and portraying various steps of the translocation pathway (e.g. Van den Berg et al., 2004; Egea and Stroud, 2010; Gogala et al., 2014; Tsukazaki et al., 2008). Neglecting variations in the auxiliary subunits, the overall architecture and mechanism appears to be universally conserved (Rapoport et al., 2017). The Sec translocon itself is a complex of α -helical, integral membrane proteins called SecY, SecE and SecG in bacteria and Sec61 α , Sec61 γ and Sec61 β in eukaryotes, respectively (Figure 4). The crystal structure of the archaeal SecY-SecE complex from *Methanocaldococcus jannaschii* reveals the translocon in a closed or idle state and gives detailed insight on its core features (Van den Berg et al., 2004). It reveals SecY as the pore-forming subunit, consisting of 10 TMH separated into two linked halves, TMH 1–5 and 6–10, which form a clam-like arrangement. Viewed from the side, it resembles an hourglass, with aqueous funnel-like openings on both sides of the membrane, separated by a central constriction site. This constriction is lined with a ring of six hydrophobic residues with their side chains pointing into the pore. In the closed, resting state, TMH 2A forms a plug at the constriction site in the extracellular funnel-like cavity, blocking passage of proteins or small molecules (Van den Berg et al., 2004; Park and Rapoport, 2011). TMH 2 and TMH 7 form a seam along the central channel, which is

is also called the lateral gate, through which TMHs can insert into the hydrophobic membrane phase (Van den Berg et al., 2004; Egea et al., 2004; Tsukazaki et al., 2008). SecE consists of two alpha-helices, an N-terminal interfacial amphipathic alpha helix and a TMH, which together act like a clamp, stabilizing the two halves of SecY (Van den Berg et al., 2004; Tsukazaki et al., 2008). SecE subunits of gram-negative bacteria show two additional, non-essential N-terminal helices providing further stability (Nishiyama et al., 2000). The auxiliary and non-essential SecG subunit is not conserved and consists of one or two TMH near the N-terminus of SecY, contributing to SecY-SecE complex stability and performing a stimulatory role during translocation (Belin et al., 2015; Nishiyama et al., 1993; Tanaka et al., 2015). Furthermore, in a peptide bound crystal structure of *Thermus thermophilus* SecYEG, the loop connecting the two TMH of SecG caps the cytoplasmic SecY funnel opening (Tanaka et al., 2015). Nevertheless, while SecY and SecE form a stable complex, SecG appears to be less stably bound (Joly et al., 1994).

Targeting of Translocation Substrates

Targeting of proteins to the Sec translocon follows two different pathways: cotranslational and posttranslational targeting (Rapoport et al., 2017). While integral membrane proteins are usually targeted cotranslationally, many secretory proteins in yeast and bacteria are targeted in a posttranslational manner (Ast et al., 2013; Ng et al., 1996; Schibich et al., 2016). To be able to pass the narrow central pore of the translocon, these posttranslational substrates must be kept in a loosely folded or unfolded state, which is usually maintained by cytosolic chaperones (Ast et al., 2013; Huber et al., 2005; Schierle et al., 2003). Targeting of these fully translated proteins to the translocon is not completely understood (Rapoport et al., 2017). In yeast, Sec72, a component of the posttranslational translocon, is capable of binding chaperones and may serve as a substrate receptor (Tripathi et al., 2017). Posttranslational targeting in bacteria relies on cytosolic chaperones such as SecB and the ATPase SecA to transfer the substrates to the translocon (Hartl et al., 1990). The driving force of this translocation type is provided by the cytosolic ATPase SecA and an electrochemical gradient at the inner membrane called the proton motive force (PMF). The import machinery in eukaryotes is located in the ER-lumen and usually consists of the DnaK-like Hsp70 chaperone BiP, which acts in concert with its J-domain containing partner Sec63 in the ER membrane. Together they prevent back-sliding of the translocating peptide and thus provide directionality (Chatzi

et al., 2014; Matlack et al., 1999).

To date, cotranslational translocation is much better understood. It typically involves the signal recognition particle SRP and its receptor, SRP receptor (SR, or FtsY in bacteria). Both factors are required for targeting translating ribosomes to the Sec translocon (Elvekrog and Walter, 2015). The SRP is an RNP consisting of six proteins and a 7S RNA in eukaryotes and a single protein, Ffh, bound to a 4.5S or 6S RNA in bacteria (Poritz et al., 1990; Rosenblad et al., 2009; Walter and Blobel, 1980, 1982). SRP binds to hydrophobic signal sequences in nascent chains as they emerge from the ribosomal peptide exit tunnel with the methionine-rich M domain of SRP54 and to the ribosome via its N-terminal and GTPase (NG) domain (Janda et al., 2010; Voorhees and Hegde, 2015). When the SRP has engaged an RNC, it can be delivered to the translocon via an interaction of the SRP with the SR (Gilmore et al., 1982). Once targeted to the SR, the NG-domain of the SRP and the homologous NG domain of the SR co-activate, triggering GTP hydrolysis resulting in a handover of the RNC to the translocon where translation continues parallel to translocation or membrane insertion (Egea et al., 2004; Focia et al., 2004; Valent et al., 1998).

Dynamics of the Translocon during Cotranslational Translocation

In the idle state, the Sec translocon shows the central pore plugged and the gate in a closed conformation (Van den Berg et al., 2004; Tsukazaki et al., 2008). For protein translocation or membrane insertion, the translocon can undergo a series of conformational changes. First, the translocon is primed, followed by an opening of the channel, the insertion of the signal sequence and subsequent translocation of hydrophilic stretches or membrane insertion of hydrophobic stretches (Rapoport et al., 2017). In the cotranslational pathway, the Sec translocon is primed by binding of the ribosome to the cytosolic loops between TMH 6 and TMH 7, as well as between TMH 8 and TMH 9 of the C-terminal half of the SecY channel (Becker et al., 2009; Gogala et al., 2014; Voorhees et al., 2014). Binding of the ribosome causes conformational changes in these loops, which are transmitted to the adjacent helices, causing this slight opening of the cytosolic side of the gate, while the plug remains closed (Gogala et al., 2014; Voorhees et al., 2014). In the case of a secretory protein, the signal sequence engages Sec at its lateral gate, whereby the translocating peptide passes through the central pore. In many secretory proteins, as well as for certain types of membrane proteins, the N-terminus is consequently oriented towards

the cytosol and the helical signal sequence supplanting TMH 2 of the gate, leading to a loop-insertion of the nascent peptide. This is commonly accompanied by a displacement of the plug, as well as a further opening of the engaged lateral gate (Voorhees and Hegde, 2016). Accommodation of a TMH likely follows the same mechanism as signal sequence recognition in the lateral gate. Subsequent release of the TMH is thought to occur by partitioning of the THM into the lipid phase of the membrane, at least for single-spanning transmembrane proteins (Gogala et al., 2014; Heinrich et al., 2000; Li et al., 2016; Voorhees and Hegde, 2016). In combination with cleavage of the signal sequence, this mechanism would provide the correct topology for the nascent chain to translocate through the protein conducting channel (Rapoport et al., 2017). Further translocation of the hydrophilic nascent chain can occur with an essentially closed gate and only a slightly rearranged central channel (Gogala et al., 2014).

1.3.2 Folded Protein Translocation

Typically, transmembrane transport is mediated by translocators dealing with unfolded proteins. These are, for example, the previously described Sec translocon or the general import machinery of mitochondria consisting of the TOM and TIM23 complexes (Rapoport et al., 2017; Wiedemann and Pfanner, 2017). This allows them to handle a plethora of different substrates with a small protein conducting pore. Yet, a limited set of proteins require translocation across a membrane in a folded state. So far, a set of scenarios necessitating folded protein translocation have been identified. For instance, certain proteins require insertion of complex cofactors such as Fe-S, Ni-Fe or molybdopterin clusters via enzymatic Afs prior to translocation (Berks, 1996; Santini et al., 1998; Sargent et al., 1998; Wagener et al., 2011). Furthermore, the lack of specific metal ions in the extracellular milieu requires some enzymes to bind these ions to their folded active site prior to export (Monteferrante et al., 2012; Tottey et al., 2008). Additionally, multimeric complexes have been identified that require assembly prior to translocation (Rodrigue et al., 1999). Finally, as an adaptation to extreme environmental conditions, specific proteins have been found to fold very rapidly after translation, thus requiring translocation in a folded state (Rose et al., 2002). For such cases, a specialized translocation pathway exists, called the twin-arginine translocase pathway (Tat-pathway). Moreover, for a unique case of the Fe-S cluster bearing Rieske protein, a dedicated system evolved in mitochondria, involving the unusual AAA-ATPase Bcs1, which replaced the Tat

system for this specific substrate.

The Twin-Arginine Folded Proteins Translocation System

The primary pathway associated with the translocation of folded proteins is the Tat system. This system plays a key role in a number of processes, such as phosphate and iron acquisition (Letoffe et al., 2009; Ize et al., 2004), symbiotic nitrogen fixation (Basile et al., 2018; Meloni et al., 2003), as well as photosynthetic and respiratory pathways (Aldridge et al., 2008; Bachmann et al., 2006; Molik et al., 2001; Rodrigue et al., 1999; Santini et al., 1998; Sargent et al., 2002). Homologues of the Tat system are present in many bacteria, archaea and in chloroplasts (Berks, 2015; Patel et al., 2014). While mitochondrial Tat systems are present in some eukaryotic lineages, including plants, jakobid protists and a number of sponges (Burger et al., 2013; Carrie et al., 2016; Pett and Lavrov, 2013), most mitochondria appear to have lost this translocation pathway. The minimal working Tat systems utilizes only two subunits: TatA (Tha4 in chloroplasts) and TatC (Jongbloed et al., 2004). Nevertheless, the thylakoid Tat systems and many other bacterial Tat systems such as that of the *E. coli* model organism require a third subunit, TatB (Hcf106 in chloroplasts), to function (Sargent et al., 1998). While TatB is a functionally distinct paralog of TatA, bacteria often possess further, functionally equivalent paralogs of TatA, such as TatE. In the trimeric Tat system, TatB and TatC form an oligomeric membrane complex (TatBC) of so far unclear stoichiometry (Celedon and Cline, 2012). Substrate recognition and engagement occurs when the name-giving, N-terminal twin-arginine containing signal sequence of the substrate protein binds to the TatBC complex (Alami et al., 2003; Cline and Mori, 2001). Initial binding of the substrate causes recruitment of free TatA subunits, a process that is driven by the PMF (Alami et al., 2003; Mori and Cline, 2002). While TatBC is required for substrate recognition and TatA recruitment, TatA appears to transiently form the protein conducting pore (Alcock et al., 2013; Rose et al., 2013; Rodríguez-Galán et al., 2013). This relatively small subunit forms only one TMH and an amphipathic alpha-helix, thus requiring the concerted action of many subunits to transiently form the protein conducting pore (Rodríguez-Galán et al., 2013). The undefined oligomerization and transient assembly explain the flexibility of the system with respect to substrate size. It may also explain, why acquisition of high-resolution structural data depicting the active translocation process or the pore is difficult. Thus, mechanistic insights into the modes of action of Tat proteins remained largely elusive so far.

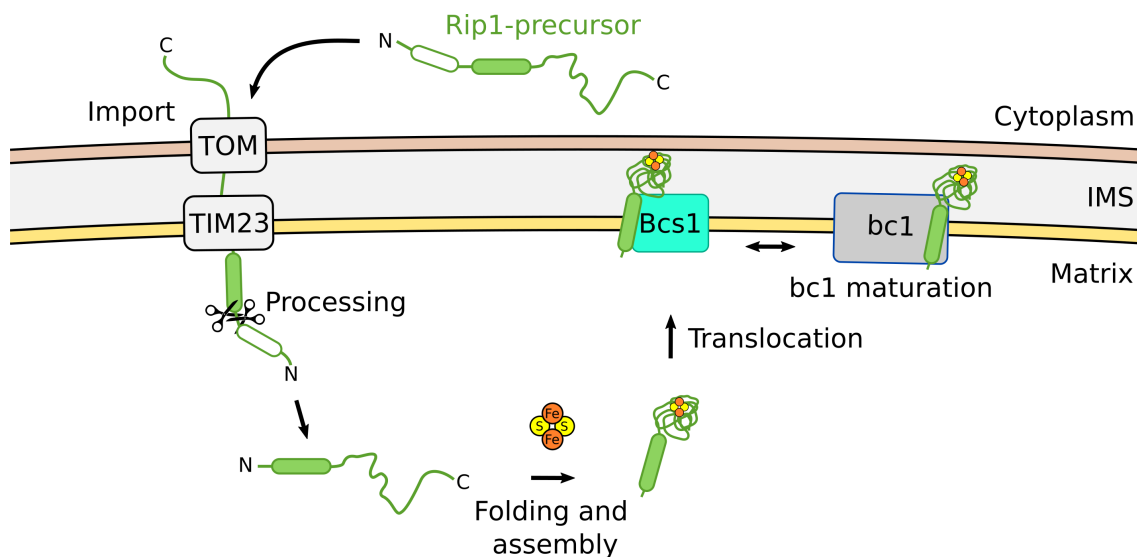


Figure 5: Assembly Scheme of the Rieske Protein

Translocation and assembly scheme of the *S. cerevisiae* Rieske protein Rip1 showing import of the unfolded precursor into the mitochondrial matrix, folding of the C-terminal domain, assembly of the 2Fe-2S cluster, and finally translocation across the inner mitochondrial membrane by Bcs1 (Wagener et al., 2011).

Translocation of the Rieske Protein by Bcs1

The Rieske protein, Rip1 in *S. cerevisiae*, is a small, Fe-S cluster containing protein. It was for the first time isolated from bovine mitochondria as part of the bc1 respiratory chain complex, which is also known as complex III (Rieske et al., 1964). Bc-1 is a complex of the inner mitochondrial membrane (IM) and constitutes a key component of the mitochondrial respiratory chain. Essentially, it is responsible for oxidation of the membrane pool of ubiquinol and reduction of cytochrome c in the mitochondrial intermembrane space (IMS) (Crofts, 2004; Xia et al., 2013). It uses energy derived from these redox reactions to act as a proton pump, thus helping to create the pH gradient across the IM used for ATP synthesis (Crofts, 2004; Reid et al., 1966; Xia et al., 2013). Functionally, the Rieske protein constitutes one of the electron-conducting centers of the bc1-complex. Its Fe-S center is one of the two initial electron acceptors in the quinol oxidation reaction (Link, 1997; Trumpower and Edwards, 1979). Apart from mitochondrial bc1-complexes, Rieske proteins are also found in other electron transport chains such as bacterial bc-1 complexes, the cytochrome b₆f complex in chloroplasts and photosynthetic bacteria (Malkin and Bearden, 1978) and bacterial dioxygenases (Mason and Cammack, 1992). It is a small integral membrane protein with an N-terminal TMH and the 2Fe-2S cluster

bearing C-terminal domain, which is exposed to the IMS (Harnisch et al., 1985). While iron atoms in 2Fe-2S clusters are commonly coordinated by four cysteine residues, the Rieske proteins show coordination by two cysteine and two histidine residues (Gurbiel et al., 1989; Iwata et al., 1996).

Mitochondrial assembly of Rip1 and its insertion into the bc1-complex is a complicated process (Figure 5). After cytoplasmic translation of the Rip1 precursor, which contains a mitochondrial localization signal, it is initially imported into the mitochondria via the TOM and Tim23 complexes (Hartl et al., 1986; van Loon and Schatz, 1987). Once in the matrix, the 30 amino acid long mitochondrial targeting pre-sequence is removed in two processing steps (Graham and Trumpower, 1991) and the C-terminal domain folds and acquires its 2Fe-2S cluster (Kispal et al., 1999; Wagener et al., 2011). To prevent aggregation and proteolytic decay while in the matrix, Rip1 is associated with the small chaperone Mzm1 for stabilization (Cui et al., 2012). Considering that folding of Rip1 takes place in the matrix and its final localization is in the inner membrane with the folded C-terminus located in the IMS, Rip1 is a target for folded protein translocation (Wagener et al., 2011). While in bacteria and chloroplasts, the Rieske protein is a substrate for the previously described Tat translocation system (Aldridge et al., 2008; Bachmann et al., 2006; De Buck et al., 2007), most mitochondria have lost this pathway (see 1.3.2: The Twin-Arginine Folded Proteins Translocation System). Instead, Bcs1, the name-giving representative of an outlying clade of AAA-proteins (Frickey and Lupas, 2004) was found to mediate the selective back-translocation of Rip1 in the yeast *S. cerevisiae* (Wagener et al., 2011). Rip1 integration into bc1-precomplexes via Bcs1 is a prerequisite for the final maturation and the formation of bc1-complex dimers and supercomplexes (Cruciat et al., 1999).

1.4 AAA-Proteins: a Versatile Clade of Molecular Machines

AAA-proteins—the ATPases associated with diverse cellular activities—are a large family of ATPases sharing a conserved, common ATPase module (Erdmann et al., 1991; Tomoyasu et al., 1993). As the name implies, these molecular machines are involved in a wide range of processes such as membrane fusion (Woodman, 1997), protein degradation (Yedidi et al., 2017) or peroxisome biogenesis (Grimm et al., 2016). A core feature of these proteins is the highly conserved P-loop NTPase

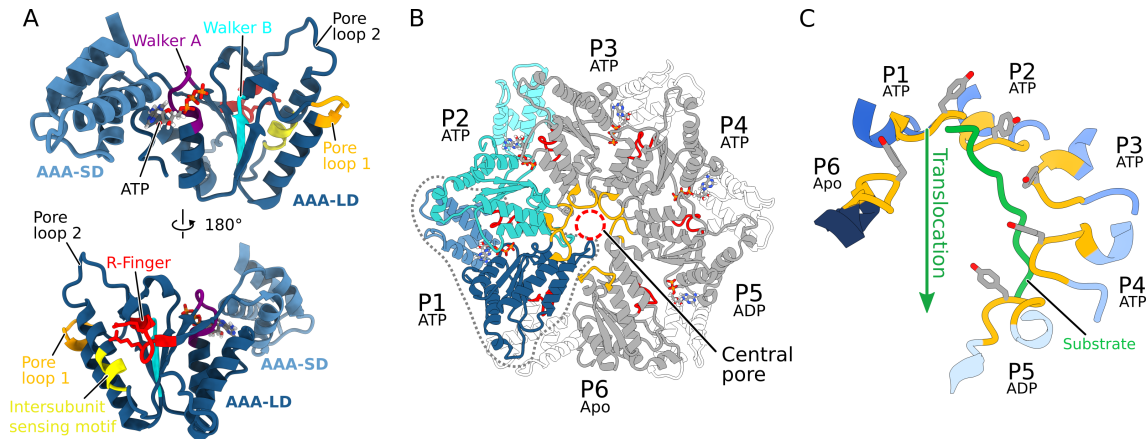


Figure 6: Structural Overview of the AAA Cassette and the Hand-Over-Hand Translocation Mechanism

A) Overview of the AAA cassette showing the AAA large domain (LD) and small domain (SD), the Walker A/B and intersubunit sensing motifs, the arginin fingers (R-fingers) and pore loops 1 and 2.

B) Hexameric assembly of AAA cassettes, with two protomers highlighted. Dashed gray line delineates the protomer 1, the dashed red line indicates the location of the central pore.

C) Spirale staircase like arrangement of the pore loops of all six protomers (orange) with substrate polypeptide that is translocated through the central pore. P1–P6: Protomers 1–6. All structures based on PDB: 6AZ0 (Puchades et al., 2017).

domain, featuring around 220–250 amino acids (Wendler et al., 2012). Structurally the AAA cassette consists of two subdomains, the AAA-large domain (also called additional strand conserved E, in short ASCE domain) and small domain, henceforth referred to as LD and SD (Figure 6A and Lupas and Martin, 2002; Wendler et al., 2012). A core feature of the LD is the central five stranded parallel β -sheet, following a 5-1-4-3-2 order of the individual strands (Iyer et al., 2004; Wendler et al., 2012). This sheet is sandwiched between α -helices and bears the Walker A and B motifs required for ATP binding and hydrolysis at the tips of β -strands 1 and 3, respectively (Walker et al., 1982; Wendler et al., 2012). It furthermore harbors the intersubunit sensing region involved in communication between individual protomers when in multimeric assemblies, as well as the second region of homology (SRH), which can contain one or more catalytically important arginine fingers (Augustin et al., 2009; Tomoyasu et al., 1993). The SD, on the other hand, consists of a bundle of 3–5 α -helices (Lupas and Martin, 2002; Wendler et al., 2012). The nucleotide binding pocket lies in close proximity to the Walker A motif, and is formed by the LD and SD

of one protomer and the LD of a further protomer in oligomeric assemblies (Wendler et al., 2012).

AAA-proteins and the encompassing superfamily of AAA+ or extended AAA-proteins are constructed in a modular fashion combining one (Type I), two (Type II) or more AAA cassettes often with additional enzymatic, regulatory, binding or transmembrane domains within a single polypeptide (Grimm et al., 2016). As such, Rea1, a AAA+ protein required for LSU biogenesis (see 1.2.2: Formation of the Large Ribosomal Subunit) combines six AAA cassettes and additional functional domains such as the MIDAS domain (Garbarino and Gibbons, 2002). Rix7, a further AAA+ protein involved in LSU biogenesis is a Type II AAA+ protein showing two AAA (D1 and D2) domains (Kressler et al., 2008). The FtsH family of proteins including Yme1 and AFG3L2, specialized in protein quality control of membrane proteins, consist of an N-terminal domain, a transmembrane domain, a AAA cassette, and a metalloprotease domain (Janska et al., 2013). Virtually all studied AAA+ proteins are known to form ring-like structures, typically as homohexamers (see Figure 6B and Iyer et al., 2004; Vale, 2000). Notable exceptions are for instance the AAA+ clade of clamp loaders, which are known to form pentameric rings (Yao et al., 2003) and the σ 54 activator, which forms heptameric and hexameric rings (Batchelor et al., 2009). A slight deviation from this rule is also presented by Rea1 and Dynein: these form rings of six AAA cassettes, yet all are encoded on a single polypeptide chain (Garbarino and Gibbons, 2002; Neuwald et al., 1999). Complexes bearing two AAA cassettes, such as type II AAA+ proteins Rix7 or Cdc48, or AAA+ proteins containing extra domains, such as Yme1, result in structures of stacked rings (Lo et al., 2019; Puchades et al., 2017; Twomey et al., 2019). These assemblies all have a central pore and the SRH of one subunit is located in such a way that one or more arginines in the SRH can reach towards the γ -phosphate of the ATP bound to the adjacent subunit, thus resembling the arginine fingers found in some small GTPases (see Figure 6A, 6B and Ogura et al., 2004; Scheffzek et al., 1997; Wendler et al., 2012). The intersubunit sensing region shows a similar arrangement as the SRH and allows one subunit to sense the presence of ATP in the adjacent, a feature vital to coordinated ATP-hydrolysis (Augustin et al., 2009; Puchades et al., 2017).

Many of the so far characterized AAA+ proteins use ATP hydrolysis for substrate unfolding and translocation through the central pore of their ring-like assembly (Gates and Martin, 2020; Niwa et al., 2002; Ortega et al., 2000; Reid et al., 2001). They possess specialized loops within the AAA cassette, called pore loops,

that line the central pore and engage with the substrate via conserved aromatic residues in an ATP dependent manner (Graef and Langer, 2006; Martin et al., 2008; Niwa et al., 2002; Wang et al., 2001). Initial structures have shown planar and symmetric hexameric rings, displaying all six protomers trapped in the same state of the ATP hydrolysis cycle (Bieniossek et al., 2006; Huyton et al., 2003; Stinson et al., 2013). In contrast, more recent structural analysis of substrate-engaging AAA+ complexes have revealed an asymmetric assembly, showing a common mechanism for these machines, which is referred to as a spiral staircase or hand-over-hand mechanism (see Figure 6C and Gates and Martin, 2020; Puchades et al., 2017; Twomey et al., 2019). These structures show asymmetric assemblies with different co-existing nucleotide states. They typically display multiple ATP bound subunits, an ADP bound and/or an apo-subunit. Binding of ATP coincides with substrate engagement via the conserved pore loops, whereas ATP hydrolysis occurs with substrate release. Four successive subunits are typically bound to ATP, whereas the fifth subunit can be either ADP bound or in an apo state, placing the ATP hydrolysis event between the fourth and fifth subunit. The presence of different nucleotide states in a single assembly results in the individual subunits not forming a planar ring but a split washer- or right handed spiral staircase-like assembly with the apo-subunit at the top and the ADP bound subunit at the bottom of the “staircase” (Figure 6B and 6C). Thus, ATP hydrolysis occurs in a coordinated around-the-ring fashion, resulting in a stepwise substrate translocation. In the sixth subunit, after ATP hydrolysis, release of the phosphate and opening of the nucleotide binding pocket results in a disengagement from the bottom subunit of the spiral and its transition towards the top of the spiral, thus completing one translocation cycle. For reviews of this mechanism see Gates and Martin (2020) and Puchades et al. (2019).

2 Aims of this Thesis

2.1 Publications 1, 2 and 5 | Structural Analysis of Eukaryotic Large Ribosomal Subunit Biogenesis

Eukaryotic ribosomal subunits must be built from their base components, the 5S, 5.8S, 18S and 25S rRNA and 79 ribosomal proteins in yeast (Kressler et al., 2017). This highly complex assembly process, which spans the nucleolus, nucleoplasm and cytoplasm, requires the coordinated action of over 200 AFs (Woolford and Baserga, 2013). Cryo-EM structures of pre-60S particles have provided insight into intermediate and late stages of the LSU assembly pathway, showing large parts of the LSU fully constructed (Barrio-Garcia et al., 2016; Bradatsch et al., 2012; Leidig et al., 2014; Ma et al., 2017; Wu et al., 2016). Conversely, the early steps of LSU biogenesis, involving initial rRNA folding, assembly of ribosomal proteins, and the function of early AFs remained largely enigmatic. Therefore, the aim of publication 1 (Kater et al., 2017) was to address these open questions by structurally characterizing heterogeneous, nucleolar, and thus early stage pre-60S intermediates obtained by affinity purifications targeting early acting 60S AFs.

In publication 2 (Thoms et al., 2018) we aimed to investigate the function of the nucleoplasmic AF Cgr1. This protein is involved in a large-scale remodeling of intermediate, nucleoplasmic pre-60S particles, the rotation of the 5S RNP and maturation of the CP (Barrio-Garcia et al., 2016; Wu et al., 2016). Nevertheless, its exact function in this process remained unclear. We aimed to find suppressor mutants which bypass the function of Cgr1. By structurally characterizing pre-60S intermediates depleted of Cgr1 and intermediates rescued by such a suppressor mutation, we intended to dissect the role of Cgr1 in rotation of the 5S RNP.

The aim of Publication 5 (Kater et al., 2020a) was to analyze the transition between late nucleolar particles presented in publication 1 and the nucleoplasmic Arx1 particle by investigating the two large-scale remodeling steps associated with the Rix1-Rea1 remodeling machinery. This machinery is required for two key dissociation events, release of the nucleolar Erb1-Ytm1 complex and the nucleoplasmic Rsa4 AF (Bassler et al., 2010; Ulbrich et al., 2009). Using cryo-EM, we aimed to solve high resolution structures of this remodeling machinery and gain insight into

the transition triggered by Rea1 mediated Erb1-Ytm1 release.

2.2 Publication 3 | Partially Inserted Nascent Chain Unzips the Lateral Gate of the Sec Translocon.

The Sec-pathway is universally conserved and can be found in all kingdoms of life (Pohlschroder et al., 1997; Stephenson, 2005). It allows translocation of secretory proteins across and integration of integral membrane proteins into the cytoplasmic membrane in bacteria and the ER membrane in eukaryotes (Rapoport et al., 2017). In the cotranslational translocation pathway, ribosomes directly associate with the Sec translocon to couple protein synthesis with protein translocation. The vast majority of ribosome bound translocon structures are based on detergent solubilized complexes. Notably, some of these studies have yielded contradictory results with respect to the dynamics of this complex (Egea and Stroud, 2010; Gogala et al., 2014; Voorhees and Hegde, 2016), possibly a result of the translocon subjected to a non-native detergent environment. In publication 3 (Kater et al., 2019) we aimed to solve the complete structure of the *E. coli* RNC bound Sec translocon in a lipid nanodisc at a defined, early stage of translocation. By reconstituting SecYEG in a lipid nanodisc, our goal was to obtain the structure of this complex in a close to native environment. Using a combination of cryo-EM, biochemical crosslinking and molecular dynamics simulation, our intention was to gain insight into the conformational dynamics of the SecYEG lateral gate during this early stage of translocation.

2.3 Publication 4 | Structure of the Bcs1 AAA-ATPase Suggests an Airlock-like Translocation Mechanism for Folded Proteins.

Some proteins require completion of folding before translocation across a membrane into another cellular compartment. Rip1, a subunit of the bc1 respiratory chain complex is imported from the cytosol into the mitochondrial matrix via the Tom and Tim23 complexes, where it folds and incorporates an Fe-S cluster (Kispal et al., 1999; Wagener et al., 2011). To assemble the bc1-complex, the folded C-terminal domain of Rip1 must be translocated across, while its N-terminal TMH is inserted into the inner mitochondrial membrane. This process was shown to require the

AAA-ATPase Bcs1 (Wagener2011). In publication 4 (Kater et al., 2020b) we aimed to solve cryo-EM structures of Bcs1 oligomers to understand how an AAA-protein can perform the task of translocating a folded protein across a membrane while maintaining its permeability barrier.

3 Discussion and Outlook

3.1 Biogenesis of the Large Ribosomal Subunit

After separation of the 90S SSU precursor, assembly, folding and maturation of the large ribosomal subunit can be divided into three phases: i) initial compaction of the rRNA, associated ribosomal proteins and early acting AFs in the nucleolus (Kater et al., 2017; Sanghai et al., 2018; Zhou et al., 2019a), ii) formation and maturation of the L1-stalk and CP in the nucleoplasm (Barrio-Garcia et al., 2016; Kater et al., 2017; Wu et al., 2016) and iii) nuclear export of the pre-60S and finalization of the ISS in the cytoplasm (Greber et al., 2012, 2016; Kargas et al., 2019; Ma et al., 2017; Weis et al., 2015; Zhou et al., 2019b).

Cryo-EM structures presented in the publications associated with this dissertation provide seven distinct snapshots in the early formation of the LSU, starting in the nucleolus and leading up to the well-studied Arx1/Nog2 particle (Kater et al., 2017, 2020a). With structures published by others supporting these findings (Sanghai et al., 2018; Zhou et al., 2019a), the steps of phase (i) can be summarized as follows (Figure 7): Initial compaction of the LSU commences with the solvent exposed shell. Folding of additional segments of rRNA and associated proteins into a stable core occurs in sequential steps. First the solvent exposed back is completed and then the peptide exit tunnel is closed (Kater et al., 2017). Thereby, rRNA compaction and maturation does not follow a transcriptional 5' - 3' sequence, but rather a sequence from scaffold to function, allowing structural elements to form first as a support for the later completion of functionally important sites (Kater et al., 2017; Sanghai et al., 2018; Zhou et al., 2019a). Phase (i) is then completed by the release of the Nsa1 module.

At the late nucleolar stage, a plethora of AFs occupies the ISS and stabilizes the L1-stalk in a premature conformation, blocking access to the later site of CP formation (see states D and E in Kater et al., 2017, and Figure 8). Progression from this stage, in phase (ii), requires the first action of the Rix1-Real remodeling machinery, which removes the Erb1-Ytm1 complex from these early particles (Bassler et al., 2010; Kater et al., 2017). Upon removal of this complex, many of the factors associated with the long meandering N-terminal tail of Erb1 dissociate (Kater et al.,

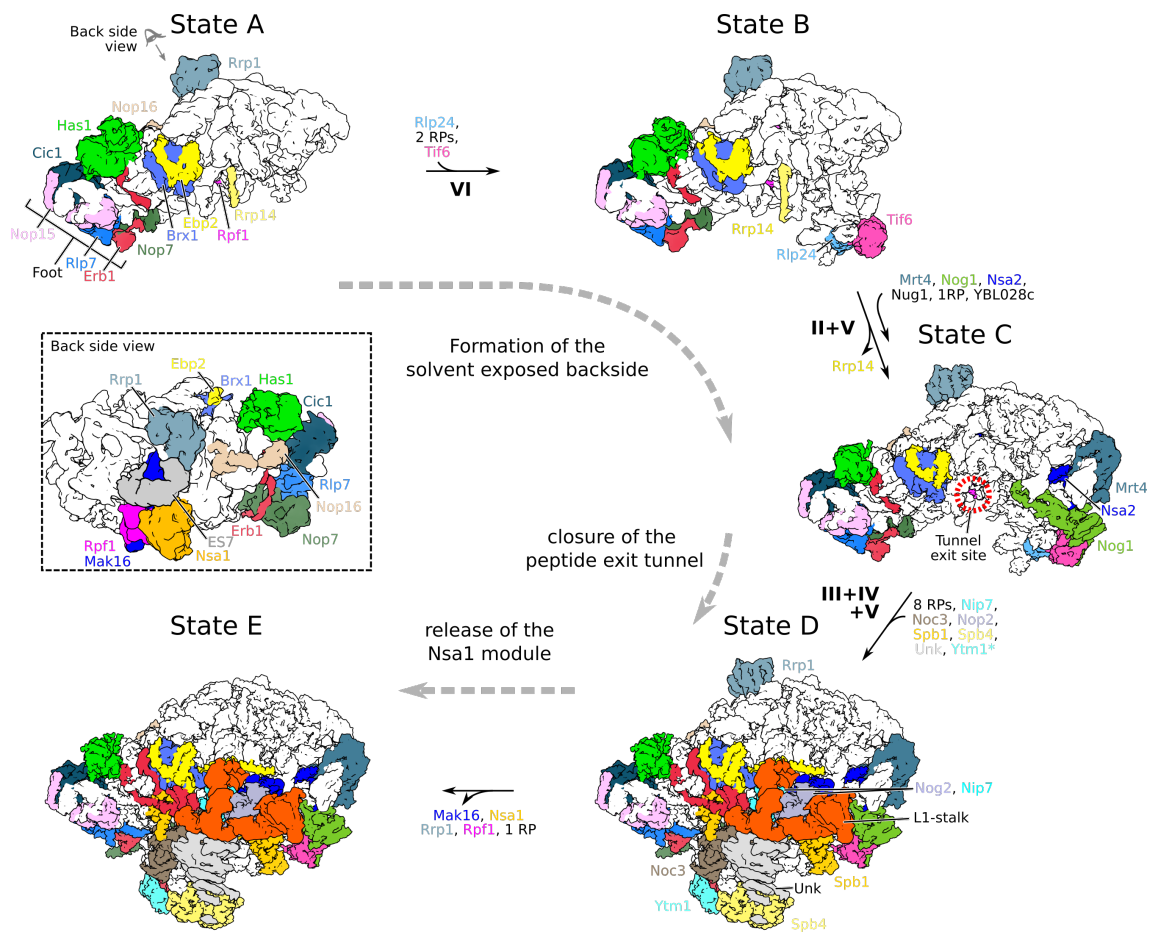


Figure 7: Schematic of Early, Nucleolar Steps of pre-60S Assembly. Maturation of the pre-60S particle from state A to state E (Kater et al., 2017), shown as top views. Dashed gray arrows indicate the three main steps of this early phase: formation of the solvent exposed back side, closure of the peptide exit tunnel and release of the Nsa1 module consisting of Mak16, Nsa1, Rpf1 and Rrp1 (see dashed box). Assembly factors and the L1-stalk rRNA are displayed in color, other rRNA and ribosomal proteins in light gray. Roman numerals indicate which parts of 25S rRNA domains are incorporated in the transition between two states. The dashed box shows the back side of state A, the viewing direction is as indicated by the eye symbol. RP: ribosomal protein. Ytm1*: Ytm1 becomes visible in state E, but is previously flexibly attached to the unresolved C-terminus of Erb1. Unk: unidentified assembly factor(s). Assignment of Rrp14 and Spb4 as suggested by Sanghai et al. (2018).

2020a). As a result, the L1-stalk rRNA is at first destabilized, but ultimately accommodates in its mature position after additional release of Spb1, Nog2 and Nip7. This lays the ground for assembly and maturation of the ISS and CP. Incorporation of the CP and 5S RNP initially occurs in a premature configuration, requiring

a 180° rotation triggered by binding of the Rix1-Real complex via Sda1 and Ipi1 (Barrio-Garcia et al., 2016; Kater et al., 2020a; Leidig et al., 2014; Wu et al., 2016). In this context, the pentameric Rix1-complex, targeted to the pre-60S with the help of Ipi1, appears to be a link connecting processing of the ITS2 via the Grc3-Las1 endonuclease complex and rotation of the CP and 5S RNP via Real (Barrio-Garcia et al., 2016; Castle et al., 2012, 2013; Kater et al., 2020a). Surprisingly, the versatile Rix1-Real remodeling machinery fulfills multiple roles during maturation of nucleolar and nucleoplasmic stages of LSU assembly, but also as a central component in regulation of heterochromatin (Bassler et al., 2010; Kater et al., 2017, 2020a; Shipkovenska et al., 2019; Ulbrich et al., 2009).

A reoccurring concept in both LSU and SSU biogenesis is the initial assembly of rRNA structures in a premature conformation, usually requiring energy intensive restructuring at a later point to reach a more mature state. This is often the case on a small scale, where individual AFs induce or stabilize non-mature conformations in the rRNA. Brx1 for instance, blocks formation of a three-way interaction between the tips of helices H22, H68 and H88 of the 25S rRNA in the nucleolus (Kater et al., 2017). Similarly, presence of Sda1 coincides with distortion of helices H68 and H81 in the nucleoplasm (Kater et al., 2020a). In the SSU, Tsr1 prevents maturation of helix h44 of the 18S rRNA via its N-terminal helix (Heuer et al., 2017; Scaiola et al., 2018). On a larger scale, assembly of the LSU shows two stages where big segments of the rRNA are first stabilized in a premature conformation by the concerted action of multiple AFs: the L1-stalk in late nucleolar particles and the 5S RNP and CP in nucleoplasmic particles (Kater et al., 2017; Leidig et al., 2014; Wu et al., 2016). The restructuring events necessary to remodel these premature rRNA structures represent checkpoints in the assembly process, where progression occurs only after fulfilling certain criteria. The passing of these points typically requires the expenditure of energy, and thus drives the assembly forward. During construction of the LSU, they mark important transitions in terms of cellular localization and particle composition. The first checkpoint is thought to coincide with the transition from nucleolus to nucleoplasm, whereas the second checkpoint is a key step for gaining nuclear export competency (Barrio-Garcia et al., 2016; Kater et al., 2017, 2020a; Matsuo et al., 2014). Interestingly, a conceptually similar situation is present in the 90S particle prior to Utp24 mediated cleavage at the A₁ site (Cheng et al., 2017). An RNA conformational change triggered by the formation of helix h1 of the 18S rRNA is required to bring the A₁ cleavage site into proximity of the Utp24 endonuclease, allowing separation of the 5' ETS from the maturing SSU and thus maturation to

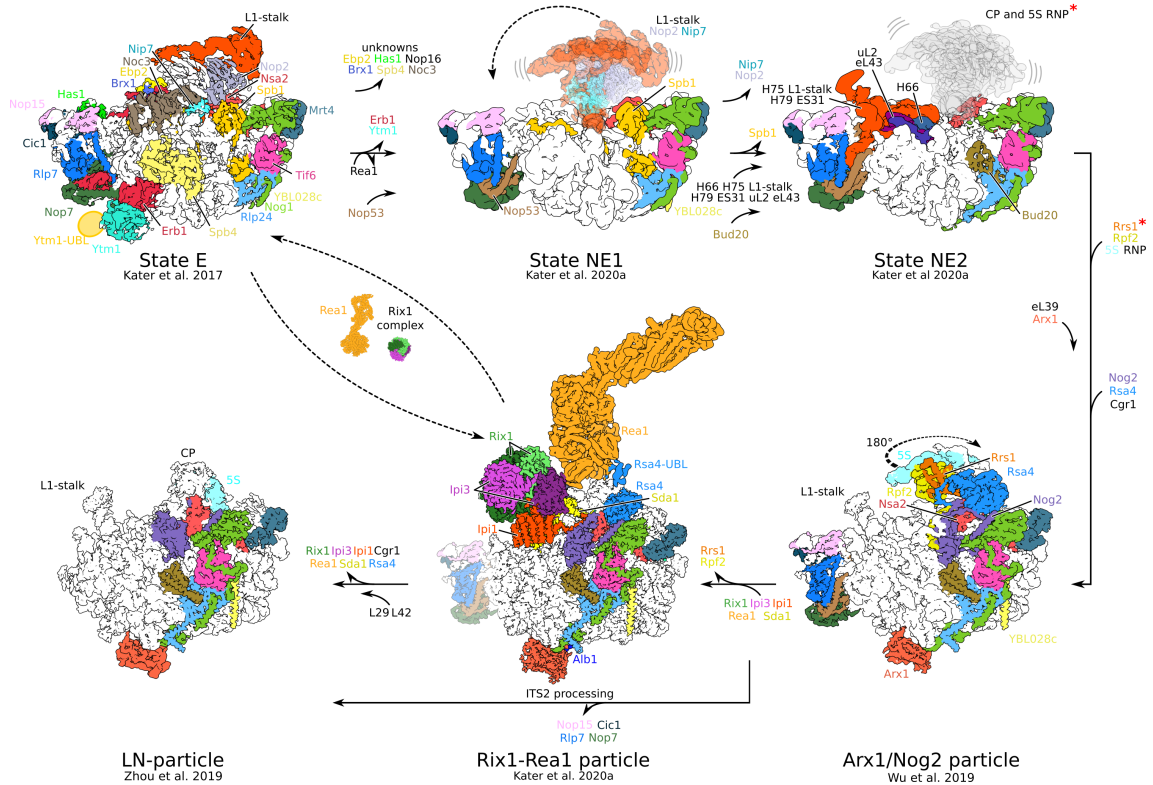


Figure 8: Schematic of CP Formation in the Nucleoplasm.

Starting with late nucleolar state E (Kater et al., 2017), the formation of the CP is depicted in five steps. In brief, triggered by release of the Erb1-Ytm1 complex via Rea1 in the nucleolus, the prematurely stabilized L1-stalk is released in state NE1 and takes a mature-like conformation in state NE2 (Kater et al., 2020a). This enables formation of the premature CP in the Arx1/Nog2 particle, which is further matured by the Rix1-Rea1 remodelling machinery. Assembly factors, important rRNA segments and ribosomal proteins are highlighted in color, other rRNA and ribosomal proteins are displayed in light gray. *: the 5S RNP including Rpf2 and Rrs1 becomes stably integrated in the Arx1/Nog2 particle, yet it is already associated to flexible portions of the pre-60S particle in earlier stages. Figure adapted from Kater et al. (2020a).

progress (Cheng et al., 2017, Cheng et al. 2020 in press).

While both of the above-mentioned LSU checkpoints require the Rix1-Rea1 remodeling machinery (Bassler et al., 2010; Kater et al., 2017, 2020a; Ulbrich et al., 2009), so far, the mechanisms or triggers determining when to activate Rea1 and thus overcome these checkpoints remain unclear. Nevertheless, structural data of the nucleolar intermediate state E (see Kater et al., 2017) allow speculation on how energy expenditure of Rea1 is communicated to trigger a large-scale structural remodeling of the nascent LSU. Rea1 interacts with state E particles by binding the

Ytm1-UBL via its MIDAS domain, allowing it to dissociate the Erb1-Ytm1 complex (Bassler et al., 2010; Kater et al., 2017). As mentioned above, Erb1 possesses a long and essential N-terminal tail that wraps around half of the maturing pre-60S particle, thereby connecting numerous AFs (Kater et al., 2017; Konikkat et al., 2017). As progression from state E requires dissociation of many of these factors, the Erb1 N-terminal extension may be the entity that links Rea1 ATP hydrolysis to this large-scale dissociation and restructuring event (Kater et al., 2017, 2020a). The second checkpoint requires the coupled action of Rea1 and the Nog2 GTPase to license the LSU precursor for nuclear export (Barrio-Garcia et al., 2016; Matsuo et al., 2014; Ulbrich et al., 2009). As mentioned above, Nog2 also has a long meandering C-terminal tail, which makes interactions with both Rsa4 and Nsa2 (Kater et al., 2017; Wu et al., 2016). Thus, similar to Erb1 in the first Rea1 step, this C-terminal tail could potentially act as a sensor coupling Rea1 mediated Rsa4 release to Nog2 GTP hydrolysis.

In conclusion, the structural and biochemical data presented in the publications 1, 2 and 5 of this dissertation (Kater et al., 2017; Thoms et al., 2018; Kater et al., 2020a, respectively) provide an important cornerstone to understand early and intermediate events of LSU formation, including the mechanisms governing initial compaction and remodeling of the rRNA. In addition, the structures presented in these publications provide a wealth of data on dozens of AFs, guiding further characterization of these proteins and thus enabling hybrid approaches to dissect their function. In this manner, we used yeast genetics coupled with structural biology to analyze the function of Cgr1, revealing its role in stabilizing the CP after its 180° rotation upon binding of Rea1 (Thoms et al., 2018). Furthermore, these data constitute important groundwork both for the analysis of LSU formation in higher eukaryotes such as humans, but also provide the foundation to investigate the ribosomal assembly process *in situ* through methods such as cellular cryo-electron tomography.

3.2 Early Steps in SecYEG Mediated Protein Insertion

The Sec pathway is the main pathway to target and translocate secretory and membrane proteins in bacteria and eukaryotes (Rapoport et al., 2017). While cotranslational protein translocation and membrane insertion has been structurally inves-

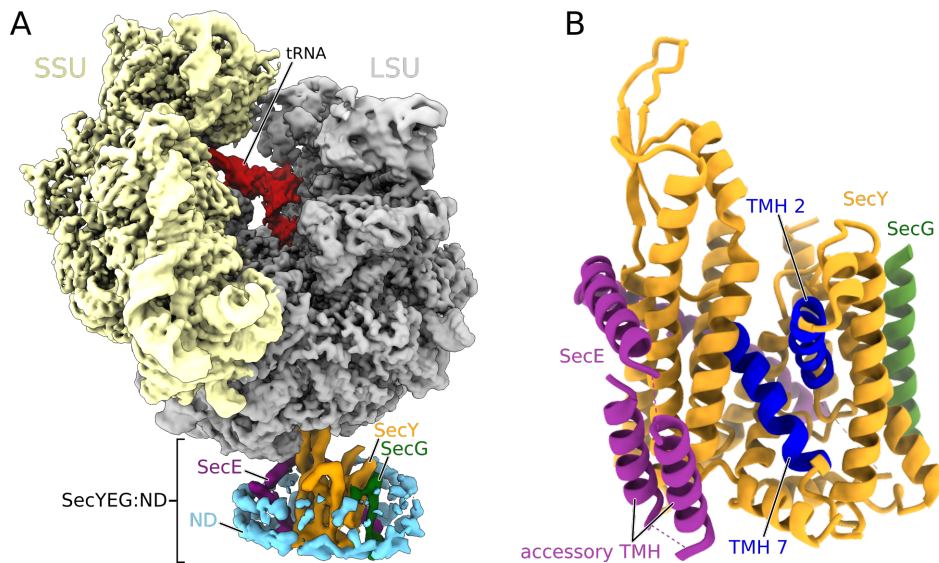


Figure 9: Structure of the RNC:SecYEG:Nanodisc Complex

(A) Overview of the cryo-EM structure showing the ribosomal subunits and the SecYEG:nanodisc, independently refined using multi body refinement (Kater et al., 2019).

(B) Model of the *E. coli* SecYEG complex showing the accessory helices of SecE in proximity to the lateral gate (blue helices), which is in an early stage of unzipping on the cytoplasmic side.

ND: nanodisc.

tigated in both eukaryotes and bacteria (Gogala et al., 2014; Jomaa et al., 2016; Voorhees et al., 2014), many details of the underlying mechanism of TMH and signal sequence insertion, especially the dynamics of the lateral gate, are yet to be fully understood. Publication 3 of this dissertation (Kater et al., 2019) presents the to date most complete structure of the bacterial SecYEG complex, bound to a translationally stalled 70S ribosome (Figure 9). For the first time, this structure shows the accessory TMHs of SecE interacting with the lateral gate, possibly modulating the gate dynamics and assisting in membrane insertion. The lateral gate itself is slightly opened, induced by binding of the RNC to the cytoplasmic loops as indicated by molecular dynamics simulations. Previous analysis of the lateral gate dynamics yielded controversial results (Egea and Stroud, 2010; Gogala et al., 2014; Voorhees and Hegde, 2016), with conformational changes through a non-native environment and detergent solubilization being a plausible cause (Cross et al., 2013). In this study, SecYEG was prepared in a large nanodisc, which allows it to be surrounded by phospholipids and providing sufficient space to mimic a native environment, enabling native conformations and dynamics (Kater et al., 2019). This

structure highlights an early step in the insertion of the signal sequence, contributing to our understanding of cotranslational insertion of TMH. To achieve this, the nascent chain was designed to be long enough to interact with the lateral gate but of insufficient length to form a TMH in the correct topology. While crosslinking could confirm the presence of the signal sequence at the lateral gate, density for the nascent chain outside of the ribosomal exit tunnel could not be traced readily, suggesting conformational heterogeneity. Compared to previous structures, the SecY lateral gate shows a conformation between the “primed” state, where the gate is slightly opened and the “inserting” state, where the signal sequence has displaced TMH 2 of the lateral gate (Kater et al., 2019; Voorhees et al., 2014; Voorhees and Hegde, 2016).

While this structure presents an important step towards understanding the conformational dynamics of SecYEG in a native environment, it also illustrates the difficulties of this undertaking. The absence of nascent chain density at the lateral gate could indicate a high degree of flexibility at this stage. Surprisingly, even with the onset of direct electron detectors routinely enabling high resolution structure determination, well resolved structures of SecYEG bound to the ribosome remain elusive. While the ribosome itself can typically be resolved to high resolution, SecYEG, placed at the periphery of the structure shows a prominent drop in local resolution (see for example: Gogala et al., 2014; Jomaa et al., 2016; Kater et al., 2019; Voorhees and Hegde, 2016). Considering the small size of SecYEG (approximately 75 kDa) and the inherently heterogeneous lipid or detergent environment surrounding this small complex, this sample still presents a challenge for cryo-EM methods such as multi body refinement. It thus highlights the importance of hybrid approaches combining structural biology with biochemical data and molecular dynamics simulations.

3.3 Folded Protein Translocation by the Heptameric Bcs1 AAA-ATPase

Assembly of the bc1 respiratory chain complex requires translocation of the folded, Fe-S cluster bearing Rip1 protein from the mitochondrial matrix into the IMS and inner membrane (Wagener and Neupert, 2012). This act of folded protein translocation requires Bcs1, an outlier of the AAA family of ATPases (Wagener et al., 2011). In Publication 4 of this dissertation we solved the oligomeric structure of yeast Bcs1

by cryo-EM in two apo states and one ADP bound state (Kater et al., 2020b). These structures reveal that the Bcs1 monomer consists of three domains, an N-terminal TMH, a β -sheet containing middle domain and a C-terminal AAA cassette (Kater et al., 2020b). Unlike classical hexameric AAA-proteins like Yme1 or Cdc48, Bcs1 forms an unusual homo-heptameric assembly, resulting in two large aqueous vestibules, one on the matrix side formed by the seven AAA cassettes and one in the inner membrane formed by the seven TMHs (Kater et al., 2020b). The middle domain forms a seal-like structure separating the two vestibules that can transiently open up through conformational changes. The architecture of the heptameric assembly, combined with the structural transitions reflecting different nucleotide states of the ATPase, suggest an airlock-like mechanism for the translocation of Rip1 (see Figure 10).

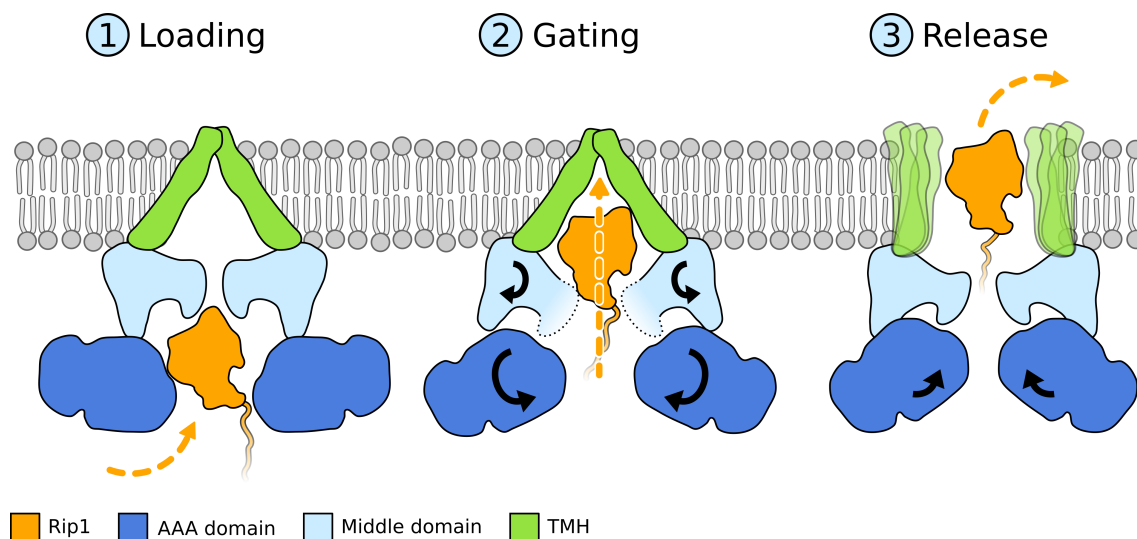


Figure 10: Model for translocation of folded Rip1 protein by Bcs1.

The different structures of Bcs1, either bound to ATP γ S, ADP or in a nucleotide free state suggest an airlock like translocation mechanism. Simplified, this model comprises three steps:

- (1) a loading step, where Rip1 is accommodated into the matrix vestibule of the Bcs1 heptamer
- (2) a gating step, where the seal pore opens to allow passage of Rip1 from the matrix vestibule into the IM vestibule and
- (3) a release step, where the globular domain of Rip1 is released into the IMS, and the N-terminal TMH is laterally integrated into the IM. This likely coincides with closing of the seal pore and is probably enabled by opening of the bundle of TMH of Bcs1.

Figure adapted from Kater et al. (2020b).

A recent publication presenting structures of the mouse ortholog of Bcs1 cor-

roborate our findings and propose a similar translocation mechanism (Tang et al., 2020). These structures also show C7 symmetric heptameric assemblies and, in addition to an apo and ADP-bound state, an ATP γ S state is presented. While the two published ADP structures show highly similar conformations of the AAA ring and the middle domain, the mouse structure resolves only the C-terminal 19 amino acids of the TMH, resulting in a flattened basket and indicating higher flexibility in the mouse TMH (Kater et al., 2020b; Tang et al., 2020). Surprisingly, the overall conformation of the mouse ADP state corresponds to that of the mouse apo state, showing only minor differences around the nucleotide binding pockets (Tang et al., 2020). This presents a strong contrast to our structures in yeast, where a transition between the ADP and both apo states results in the inward rolling of the AAA cassettes and thus the narrowing of the central pore (Kater et al., 2020b). The reasons for these discrepancies remain unclear at this point. They may be a result of differences in sample preparation or perhaps caused by a lack of substrate protein.

Inward rolling of the AAA cassettes, similar to what we observed in the yeast apo states, is observed in the mouse ATP γ S state (Tang et al., 2020). This state shows a stronger similarity to the yeast Apo 2 state, where a long β -hairpin termed the connector haipin is flipped outward, away from the central symmetry axis. This coincides with an opening of the seal domain as the middle domain is rotated away from the membrane plane (Kater et al., 2020b; Tang et al., 2020). While the yeast Apo 2 and mouse ATP γ S show a similar conformation, the ATP γ S state shows a more compacted form, with the matrix vestibule significantly contracted and thus reduced in size (Tang et al., 2020). In this state, the matrix vestibule is too small to harbour the Rip1 folded domain. Coincidentally, while the TMH of the yeast Apo 2 state are less well resolved, the TMH of the mouse ATP γ S are entirely delocalized, indicating that this change in conformation results in a destabilization of the IM basket of TMHs (Kater et al., 2020b; Tang et al., 2020). This delocalization of the TMHs could reflect the opening of the IM vestibule towards the IMS, necessary for release of the Rip1 cargo. Thus, this state could be similar to the release state during Rip1 translocation (see step 3 in Figure 10).

Taken together, these studies cover the three different nucleotide states and show how nucleotide-driven conformational changes are translated from the AAA cassettes to the middle domains and TMHs (Kater et al., 2020b; Tang et al., 2020). All of these structures support the proposed airlock-like mechanism for Rip1 translocation (Figure 10). Furthermore, they suggest a concerted mechanism of action, as opposed to the spiral staircase, hand-over-hand translocation mechanism performed by clas-

sical AAA proteins. This is supported by several findings, including the phylogenetic placement of Bcs1 in an outlying clade of AAA proteins with unique features, such as a seven stranded central β -sheet in its AAA cassette and the lack of pore loops (Frickey and Lupas, 2004; Kater et al., 2020b; Tang et al., 2020). In addition, the Bcs1 AAA cassette was found to be more similar to domain D2 in type II AAA proteins, which, during substrate translocation remain in a planar configuration (Tang et al., 2020). On the other hand, initial structures of classical AAA proteins solved without substrate and with defined nucleotide conditions resulted in symmetric assemblies (Bieniossek et al., 2006; Huyton et al., 2003; Stinson et al., 2013). Such structures are now thought to represent inactive ground states, resulting from a lack of bound substrate (Puchades et al., 2019). Thus, solving structures of Bcs1 in complex with the Rip1 substrate protein will be key to a full understanding of the details of its translocation mechanism.

4 Acknowledgments

It has been a long journey, starting with a short practical course to learn about structural biology during my master program and now ending with my PhD defense some 6 years later. There are many people to thank for their contributions, their support and help and for all the fun over these years. Thank you Roland for inviting me to your lab, for motivating me to go into structural biology and study ribosomes. I would also like to say thanks to Prof. Karl-Peter Hopfner, Prof. Klaus Förstemann, Dr. Gregor Witte, Dr. Dietmar Martin, and Prof. Johannes Stigler for being part of my thesis committee and for their part in my defense.

I want to thank all the people that have contributed to my projects and with whom I worked on papers, especially Alexej, Nikola, Matthias, Valentin, and Ed. Numerous people have supported my projects with biochemical data, sample preps, wisdom on model building and refinement (master builder Jingdong!), snacks, food and drink! Thanks to all of you and to all past (André!!) and present members of the Beckmann Supergroup. You have provided a fantastic atmosphere and a fun environment for the last few years! The many parties, retreats (including 7AM train / bus brunches), video seminars and Christmas time Star Wars events will be missed in the future!

Special thanks is due to the Garlics, my partners in crime, those responsible for the smell of fried garlic and onions emanating from the kitchen (sorry Klaus). Michi, Kathi and Hanna: it has been a blast with you! Not just cooking but all the things we did together, from coffee breaks on the roof to whiskey dates in far out Eching, and from late night pool parties in Großhadern to distilling Gin at work.

Thomas: thank you for the numerous spontaneous car rides to and from work! Thank you for all your scientific wisdom, for enduring our silliness in the office, for the great ski trips, the whiskey evenings and all the fun things we got to enjoy together. You truly are one of the cornerstones of the Beckmann lab.

To CPO Otto (chief plumbing officer) and his cryo-queens: thank you for all your support, thanks for collecting data and handling samples, fixing all things microscope. And special thanks to Susi: thank you for bergundsteigen, for always letting me borrow the shovel and pieps. And for selflessly sacrificing your own leg to save my grids and of course thanks for my birthday present!

Finally, Lydi: Thank you for putting up with this PhD and all it entailed and

whatever comes after it. Thank you for all your support!

I remember the day when I first knocked on that door. The sign next to it suggested: “come join the dark side!”. The intention was to join the group for only a few weeks, to do one of the practicals of my master program. I wanted to learn some things about cryo-EM, do some SPIDER scripting, just some old school processing but then quickly move on. Because, who would want to do ribosome blobology all day? And hadn't the structure of a ribosome already been solved years ago? Then why still always look at the same complex? And why would anybody want to work with a complex consisting of some 80 components all with names like eL42 or uL1, including illogical species differences and nomenclature mix-ups?! That dreaded thought of looking at yet another ribosome + factor X. But my goal was puzzling together this incredible machine from its individual components. I was to look at the birth of the cellular 3D-printer, seeing baby ribosomes for the first time and then realizing that they look nothing like the grown up 80S! And the timing was perfect. The almighty Resolution Revolution was overthrowing the field of structural biology and we had to keep up. We had to push the limits of what we could do with our data analysis, explore new grounds and look beyond the SPIDER horizon. And so dogmas were overthrown (As André once heatedly proclaimed: We **are** and always **will be** a SPIDER group!!11elf) and new frontiers were explored. Much has happened since then in the Beckmann Lab but I will always look back fondly on my time spent here.

References

- Adams PD, Afonine PV, Bunk'oczi G, Chen VB, Davis IW, Echols N, Headd JJ, Hung LW, Kapral GJ, Grosse-Kunstleve RW, et al. PHENIX: a comprehensive Python-based system for macromolecular structure solution. *Acta Crystallographica Section D: Biological Crystallography* 2010;66(2):213–21. doi:10.1107/s0907444909052925.
- Agrawal RK, Penczek P, Grassucci RA, Li Y, Leith A, Nierhaus KH, Frank J. Direct visualization of A-, P-, and E-site transfer RNAs in the *Escherichia coli* ribosome. *Science (New York, NY)* 1996;271:1000–2. doi:10.1126/science.271.5251.1000.
- Aitken CE, Lorsch JR. A mechanistic overview of translation initiation in eukaryotes. *Nature structural & molecular biology* 2012;19:568–76. doi:10.1038/nsmb.2303.
- Alami M, Luke I, Deitermann S, Eisner G, Koch HG, Brunner J, Muller M. Differential interactions between a twin-arginine signal peptide and its translocase in *Escherichia coli*. *Molecular cell* 2003;12:937–46. doi:10.1016/s1097-2765(03)00398-8.
- Alcock F, Baker MAB, Greene NP, Palmer T, Wallace MI, Berks BC. Live cell imaging shows reversible assembly of the TatA component of the twin-arginine protein transport system. *Proceedings of the National Academy of Sciences of the United States of America* 2013;110(24003141):E3650–9. doi:10.1073/pnas.1306738110.
- Aldridge C, Spence E, Kirkilionis MA, Frigerio L, Robinson C. Tat-dependent targeting of Rieske iron-sulphur proteins to both the plasma and thylakoid membranes in the cyanobacterium *Synechocystis* PCC6803. *Molecular microbiology* 2008;70:140–50. doi:10.1111/j.1365-2958.2008.06401.x.
- Allmang C, Mitchell P, Petfalski E, Tollervey D. Degradation of ribosomal RNA precursors by the exosome. *Nucleic acids research* 2000;28:1684–91. doi:10.1093/nar/28.8.1684.
- Ameismeier M, Cheng J, Berninghausen O, Beckmann R. Visualizing late states of human 40S ribosomal subunit maturation. *Nature* 2018;558:249–53. doi:10.1038/s41586-018-0193-0.
- Andersen CB, Becker T, Blau M, Anand M, Halic M, Balar B, Mielke T, Boesen T, Pedersen JS, Spahn CM, et al. Structure of eEF3 and the mechanism of transfer RNA release from the E-site. *Nature* 2006;443(7112):663. doi:10.1038/nature05126.

- Arnaout MA, Mahalingam B, Xiong JP. Integrin structure, allostery, and bidirectional signaling. *Annual review of cell and developmental biology* 2005;21:381–410. doi:10.1146/annurev.cellbio.21.090704.151217.
- Ast T, Cohen G, Schuldiner M. A network of cytosolic factors targets SRP-independent proteins to the endoplasmic reticulum. *Cell* 2013;152:1134–45. doi:10.1016/j.cell.2013.02.003.
- Augustin S, Gerdes F, Lee S, Tsai FTF, Langer T, Tatsuta T. An intersubunit signaling network coordinates ATP hydrolysis by m-AAA proteases. *Molecular cell* 2009;35:574–85. doi:10.1016/j.molcel.2009.07.018.
- Bachmann J, Bauer B, Zwicker K, Ludwig B, Anderka O. The Rieske protein from *Paracoccus denitrificans* is inserted into the cytoplasmic membrane by the twin-arginine translocase. *The FEBS journal* 2006;273:4817–30. doi:10.1111/j.1742-4658.2006.05480.x.
- Balakin AG, Smith L, Fournier MJ. The RNA world of the nucleolus: two major families of small RNAs defined by different box elements with related functions. *Cell* 1996;86:823–34. doi:10.1016/s0092-8674(00)80156-7.
- Barrio-Garcia C, Thoms M, Flemming D, Kater L, Berninghausen O, Baßler J, Beckmann R, Hurt E. Architecture of the Rix1-Real checkpoint machinery during pre-60S-ribosome remodeling. *Nature structural & molecular biology* 2016;23(1):37–44. doi:10.1038/nsmb.3132.
- Basile LA, Zalguizuri A, Briones G, Lepék VC. Two Rieske Fe/S Proteins and TAT System in *Mesorhizobium loti* MAFF303099: Differential Regulation and Roles on Nodulation. *Frontiers in plant science* 2018;9(30515183):1686–. doi:10.3389/fpls.2018.01686.
- Bassler J, Kallas M, Pertschy B, Ulbrich C, Thoms M, Hurt E. The AAA-ATPase Real drives removal of biogenesis factors during multiple stages of 60S ribosome assembly. *Molecular cell* 2010;38(5):712–21. doi:10.1016/j.molcel.2010.05.024.
- Bassler J, Paternoga H, Holdermann I, Thoms M, Granneman S, Barrio-Garcia C, Nyarko A, Lee W, Stier G, Clark SA, Schraivogel D, Kallas M, Beckmann R, Tollervey D, Barbar E, Sinning I, Hurt E. A network of assembly factors is involved in remodeling rRNA elements during preribosome maturation. *J Cell Biol* 2014;207(4):481–98. doi:10.1083/jcb.201408111.
- Batchelor JD, Sterling HJ, Hong E, Williams ER, Wemmer DE. Receiver domains control the active-state stoichiometry of *Aquifex aeolicus* sigma54 activator NtrC4, as revealed by electrospray ionization mass spectrometry. *Journal of molecular biology* 2009;393:634–43. doi:10.1016/j.jmb.2009.08.033.

- Becker T, Bhushan S, Jarasch A, Armache JP, Funes S, Jossinet F, Gumbart J, Mielke T, Berninghausen O, Schulten K, Westhof E, Gilmore R, Mandon EC, Beckmann R. Structure of monomeric yeast and mammalian Sec61 complexes interacting with the translating ribosome. *Science (New York, NY)* 2009;326:1369–73. doi:10.1126/science.1178535.
- Beckmann R, Bubeck D, Grassucci R, Penczek P, Verschoor A, Blobel G, Frank J. Alignment of conduits for the nascent polypeptide chain in the ribosome-Sec61 complex. *Science (New York, NY)* 1997;278:2123–6. doi:10.1126/science.278.5346.2123.
- Belin D, Plaia G, Boulfekhar Y, Silva F. Escherichia coli SecG is required for residual export mediated by mutant signal sequences and for SecY-SecE complex stability. *Journal of bacteriology* 2015;197:542–52. doi:10.1128/JB.02136-14.
- Ben-Shem A, Jenner L, Yusupova G, Yusupov M. Crystal Structure of the Eukaryotic Ribosome. *Science* 2010;330(6008):1203–9. doi:10.1126/science.1194294.
- Van den Berg B, Clemons WM, Collinson I, Modis Y, Hartmann E, Harrison SC, Rapoport TA. X-ray structure of a protein-conducting channel. *Nature* 2004;427:36–44. doi:10.1038/nature02218.
- Berks BC. A common export pathway for proteins binding complex redox cofactors? *Molecular microbiology* 1996;22:393–404. doi:10.1046/j.1365-2958.1996.00114.x.
- Berks BC. The twin-arginine protein translocation pathway. *Annual review of biochemistry* 2015;84:843–64. doi:10.1146/annurev-biochem-060614-034251.
- Bieniossek C, Schalch T, Bumann M, Meister M, Meier R, Baumann U. The molecular architecture of the metalloprotease FtsH. *Proceedings of the National Academy of Sciences of the United States of America* 2006;103:3066–71. doi:10.1073/pnas.0600031103.
- Blobel G. Intracellular protein topogenesis. *Proceedings of the National Academy of Sciences of the United States of America* 1980;77:1496–500. doi:10.1073/pnas.77.3.1496.
- Bonnefoy N, Chalvet F, Hamel P, Slonimski PP, Dujardin G. OXA1, a *Saccharomyces cerevisiae* nuclear gene whose sequence is conserved from prokaryotes to eukaryotes controls cytochrome oxidase biogenesis. *Journal of molecular biology* 1994;239:201–12. doi:10.1006/jmbi.1994.1363.
- Bradatsch B, Katahira J, Kowalinski E, Bange G, Yao W, Sekimoto T, Baumgartel V, Boese G, Bassler J, Wild K, Peters R, Yoneda Y, Sinning I, Hurt E. Arx1 functions as an unorthodox nuclear export receptor for the 60S preribosomal subunit. *Molecular cell* 2007;27:767–79. doi:10.1016/j.molcel.2007.06.034.

- Bradatsch B, Leidig C, Granneman S, Gnädig M, Tollervey D, Böttcher B, Beckmann R, Hurt E. Structure of the pre-60S ribosomal subunit with nuclear export factor Arx1 bound at the exit tunnel. *Nature structural & molecular biology* 2012;19(12):1234–41. doi:10.1038/nsmb.2438.
- Braglia P, Heindl K, Schleiffer A, Martinez J, Proudfoot NJ. Role of the RNA/DNA kinase Grc3 in transcription termination by RNA polymerase I. *EMBO reports* 2010;11:758–64. doi:10.1038/embor.2010.130.
- Burger G, Gray MW, Forget L, Lang BF. Strikingly bacteria-like and gene-rich mitochondrial genomes throughout jakobid protists. *Genome biology and evolution* 2013;5:418–38. doi:10.1093/gbe/evt008.
- Bölter B. En route into chloroplasts: preproteins' way home. *Photosynthesis research* 2018;138:263–75. doi:10.1007/s11120-018-0542-8.
- Calviño FR, Kharde S, Ori A, Hendricks A, Wild K, Kressler D, Bange G, Hurt E, Beck M, Sinning I. Symportin 1 chaperones 5S RNP assembly during ribosome biogenesis by occupying an essential rRNA-binding site. *Nature communications* 2015;6:6510. doi:10.1038/ncomms7510.
- Carrie C, Weissenberger S, Soll J. Plant mitochondria contain the protein translocase subunits TatB and TatC. *Journal of cell science* 2016;129:3935–47.
- Carter AP, Clemons WM, Brodersen DE, Morgan-Warren RJ, Wimberly BT, Ramakrishnan V. Functional insights from the structure of the 30S ribosomal subunit and its interactions with antibiotics. *Nature* 2000;407:340–8. doi:10.1038/35030019.
- Castle CD, Cassimere EK, Denicourt C. LAS1L interacts with the mammalian Rix1 complex to regulate ribosome biogenesis. *Molecular biology of the cell* 2012;23:716–28. doi:10.1091/mbc.E11-06-0530.
- Castle CD, Sardana R, Dandekar V, Borgianini V, Johnson AW, Denicourt C. Las1 interacts with Grc3 polynucleotide kinase and is required for ribosome synthesis in *Saccharomyces cerevisiae*. *Nucleic acids research* 2013;41(2):1135–50. doi:10.1093/nar/gks1086.
- Celedon JM, Cline K. Stoichiometry for binding and transport by the twin arginine translocation system. *The Journal of cell biology* 2012;197(22564412):523–34. doi:10.1083/jcb.201201096.
- Celedon JM, Cline K. Intra-plastid protein trafficking: how plant cells adapted prokaryotic mechanisms to the eukaryotic condition. *Biochimica et biophysica acta* 2013;1833:341–51. doi:10.1016/j.bbamcr.2012.06.028.
- Chaker-Margot M, Barandun J, Hunziker M, Klinge S. Architecture of the yeast small subunit processome. *Science (New York, NY)* 2017;355. doi:10.1126/science.aal1880.

- Chaker-Margot M, Hunziker M, Barandun J, Dill BD, Klinge S. Stage-specific assembly events of the 6-MDa small-subunit processome initiate eukaryotic ribosome biogenesis. *Nature structural & molecular biology* 2015;22:920–3. doi:10.1038/nsmb.3111.
- Chatzi KE, Sardis MF, Economou A, Karamanou S. SecA-mediated targeting and translocation of secretory proteins. *Biochimica et biophysica acta* 2014;1843:1466–74. doi:10.1016/j.bbamcr.2014.02.014.
- Cheng J, Baßler J, Fischer P, Lau B, Kellner N, Kunze R, Griesel S, Kallas M, Berninghausen O, Strauss D, Beckmann R, Hurt E. Thermophile 90S Pre-ribosome Structures Reveal the Reverse Order of Co-transcriptional 18S rRNA Subdomain Integration. *Molecular cell* 2019;doi:10.1016/j.molcel.2019.06.032.
- Cheng J, Kellner N, Berninghausen O, Hurt E, Beckmann R. 3.2-Å-resolution structure of the 90S preribosome before A1 pre-rRNA cleavage. *Nature structural & molecular biology* 2017;24:954–64. doi:10.1038/nsmb.3476.
- Christie PJ. The Rich Tapestry of Bacterial Protein Translocation Systems. *The protein journal* 2019;38:389–408. doi:10.1007/s10930-019-09862-3.
- Cline K, Mori H. Thylakoid DeltapH-dependent precursor proteins bind to a cpTatC-Hcf106 complex before Tha4-dependent transport. *The Journal of cell biology* 2001;154:719–29. doi:10.1083/jcb.200105149.
- Cornish PV, Ermolenko DN, Staple DW, Hoang L, Hickerson RP, Noller HF, Ha T. Following movement of the L1 stalk between three functional states in single ribosomes. *Proceedings of the National Academy of Sciences of the United States of America* 2009;106:2571–6. doi:10.1073/pnas.0813180106.
- Craig D, Gao M, Schulten K, Vogel V. Structural insights into how the MIDAS ion stabilizes integrin binding to an RGD peptide under force. *Structure (London, England : 1993)* 2004;12:2049–58. doi:10.1016/j.str.2004.09.009.
- Crick FH. On protein synthesis. *Symposia of the Society for Experimental Biology* 1958;12:138–63.
- Crick FH. Codon–anticodon pairing: the wobble hypothesis. *Journal of molecular biology* 1966;19:548–55. doi:10.1016/s0022-2836(66)80022-0.
- Crick FH, Barnett L, Brenner S, Watts-Tobin RJ. General nature of the genetic code for proteins. *Nature* 1961;192:1227–32. doi:10.1038/1921227a0.
- Crofts AR. The cytochrome bc1 complex: function in the context of structure. *Annual review of physiology* 2004;66:689–733. doi:10.1146/annurev.physiol.66.032102.150251.

- Cross TA, Murray DT, Watts A. Helical membrane protein conformations and their environment. *European biophysics journal* : EBJ 2013;42:731–55. doi:10.1007/s00249-013-0925-x.
- Cruciat CM, Hell K, Fölsch H, Neupert W, Stuart RA. Bcs1p, an AAA-family member, is a chaperone for the assembly of the cytochrome bc(1) complex. *The EMBO journal* 1999;18:5226–33. doi:10.1093/emboj/18.19.5226.
- de la Cruz J, Karbstein K, Woolford JL. Functions of Ribosomal Proteins in Assembly of Eukaryotic Ribosomes In Vivo. *Annu Rev Biochem* 2015;84(1):93–129. doi:10.1146/annurev-biochem-060614-033917.
- Cui TZ, Smith PM, Fox JL, Khalimonchuk O, Winge DR. Late-stage maturation of the Rieske Fe/S protein: Mzm1 stabilizes Rip1 but does not facilitate its translocation by the AAA ATPase Bcs1. *Molecular and cellular biology* 2012;32:4400–9. doi:10.1128/MCB.00441-12.
- De Buck E, Vranckx L, Meyen E, Maes L, Vandersmissen L, Anne J, Lammertyn E. The twin-arginine translocation pathway is necessary for correct membrane insertion of the Rieske Fe/S protein in *Legionella pneumophila*. *FEBS letters* 2007;581:259–64. doi:10.1016/j.febslet.2006.12.022.
- Dez C, Froment C, Noaillac-Depeyre J, Monsarrat B, Caizergues-Ferrer M, Henry Y. Npa1p, a component of very early pre-60S ribosomal particles, associates with a subset of small nucleolar RNPs required for peptidyl transferase center modification. *Molecular and cellular biology* 2004;24(14):6324–37. doi:10.1128/MCB.24.14.6324-6337.2004.
- Diaconu M, Kothe U, Schlünzen F, Fischer N, Harms JM, Tonevitsky AG, Stark H, Rodnina MV, Wahl MC. Structural basis for the function of the ribosomal L7/12 stalk in factor binding and GTPase activation. *Cell* 2005;121:991–1004. doi:10.1016/j.cell.2005.04.015.
- Dragon F, Gallagher JEG, Compagnone-Post PA, Mitchell BM, Porwancher KA, Wehner KA, Wormsley S, Settlage RE, Shabanowitz J, Osheim Y, Beyer AL, Hunt DF, Baserga SJ. A large nucleolar U3 ribonucleoprotein required for 18S ribosomal RNA biogenesis. *Nature* 2002;417:967–70. doi:10.1038/nature00769.
- Dutca LM, Gallagher JEG, Baserga SJ. The initial U3 snoRNA:pre-rRNA base pairing interaction required for pre-18S rRNA folding revealed by in vivo chemical probing. *Nucleic acids research* 2011;39:5164–80. doi:10.1093/nar/gkr044.
- Egea PF, Shan SO, Napetschnig J, Savage DF, Walter P, Stroud RM. Substrate twinning activates the signal recognition particle and its receptor. *Nature* 2004;427:215–21. doi:10.1038/nature02250.
- Egea PF, Stroud RM. Lateral opening of a translocon upon entry of protein suggests the mechanism of insertion into membranes. *Proceedings of the National Academy*

- of Sciences of the United States of America 2010;107:17182–7. doi:10.1073/pnas.1012556107.
- Elvekrog MM, Walter P. Dynamics of co-translational protein targeting. *Current opinion in chemical biology* 2015;29:79–86. doi:10.1016/j.cbpa.2015.09.016.
- Erdmann R, Wiebel FF, Flessau A, Rytka J, Beyer A, Frohlich KU, Kunau WH. PAS1, a yeast gene required for peroxisome biogenesis, encodes a member of a novel family of putative ATPases. *Cell* 1991;64:499–510. doi:10.1016/0092-8674(91)90234-p.
- Fatica A, Cronshaw AD, Dlakić M, Tollervey D. Ssf1p prevents premature processing of an early pre-60S ribosomal particle. *Molecular cell* 2002;9(2):341–51. doi:10.1016/s1097-2765(02)00458-6.
- Fatica A, Tollervey D, Dlakić M. PIN domain of Nob1p is required for D-site cleavage in 20S pre-rRNA. *RNA (New York, NY)* 2004;10:1698–701. doi:10.1261/rna.7123504.
- Ferreira-Cerca S, Poll G, Gleizes PE, Tschochner H, Milkereit P. Roles of eukaryotic ribosomal proteins in maturation and transport of pre-18S rRNA and ribosome function. *Molecular cell* 2005;20:263–75. doi:10.1016/j.molcel.2005.09.005.
- Finch AJ, Hilcenko C, Basse N, Drynan LF, Goyenechea B, Menne TF, Gonzalez Fernandez A, Simpson P, D’Santos CS, Arends MJ, Donadieu J, Bellanne-Chantelot C, Costanzo M, Boone C, McKenzie AN, Freund SMV, Warren AJ. Uncoupling of GTP hydrolysis from eIF6 release on the ribosome causes Shwachman-Diamond syndrome. *Genes & development* 2011;25:917–29. doi:10.1101/gad.623011.
- Fischer U, Schäuble N, Schütz S, Altvater M, Chang Y, Faza MB, Panse VG. A non-canonical mechanism for Crm1-export cargo complex assembly. *eLife* 2015;4. doi:10.7554/eLife.05745.
- Focia PJ, Shepotinovskaya IV, Seidler JA, Freymann DM. Heterodimeric GTPase core of the SRP targeting complex. *Science (New York, NY)* 2004;303:373–7. doi:10.1126/science.1090827.
- Frank J, Gonzalez RL. Structure and dynamics of a processive Brownian motor: the translating ribosome. *Annual review of biochemistry* 2010;79:381–412. doi:10.1146/annurev-biochem-060408-173330.
- Frank J, Penczek P, Grassucci R, Srivastava S. Three-dimensional reconstruction of the 70S Escherichia coli ribosome in ice: the distribution of ribosomal RNA. *The Journal of cell biology* 1991;115:597–605. doi:10.1083/jcb.115.3.597.
- Frickey T, Lupas AN. Phylogenetic analysis of AAA proteins. *Journal of structural biology* 2004;146:2–10. doi:10.1016/j.jsb.2003.11.020.

- Fromm L, Falk S, Flemming D, Schuller JM, Thoms M, Conti E, Hurt E. Reconstitution of the complete pathway of ITS2 processing at the pre-ribosome. *Nature communications* 2017;8(1):1787. doi:10.1038/s41467-017-01786-9.
- Gadal O, Strauss D, Kessl J, Trumpower B, Tollervey D, Hurt E. Nuclear export of 60s ribosomal subunits depends on Xpo1p and requires a nuclear export sequence-containing factor, Nmd3p, that associates with the large subunit protein Rpl10p. *Molecular and cellular biology* 2001a;21:3405–15. doi:10.1128/MCB.21.10.3405-3415.2001.
- Gadal O, Strauß D, Braspenning J, Hoepfner D, Petfalski E, Philippsen P, Tollervey D, Hurt E. A nuclear AAA-type ATPase (Rix7p) is required for biogenesis and nuclear export of 60S ribosomal subunits. *The EMBO Journal* 2001b;20(14):3695–704. doi:10.1093/emboj/20.14.3695.
- Gamalinda M, Ohmayer U, Jakovljevic J, Kumcuoglu B, Woolford J, Mbom B, Lin L, Woolford JL. A hierarchical model for assembly of eukaryotic 60S ribosomal subunit domains. *Genes & Development* 2014;28(2):198–210. doi:10.1101/gad.228825.113.
- Ganot P, Caizergues-Ferrer M, Kiss T. The family of box ACA small nucleolar RNAs is defined by an evolutionarily conserved secondary structure and ubiquitous sequence elements essential for RNA accumulation. *Genes and development* 1997;11:941–56. doi:10.1101/gad.11.7.941. arXiv:10.1101/gad.11.7.941.
- Garbarino JE, Gibbons IR. Expression and genomic analysis of midasin, a novel and highly conserved AAA protein distantly related to dynein. *BMC genomics* 2002;3:18. doi:10.1186/1471-2164-3-18.
- Gartmann M, Blau M, Armache JP, Mielke T, Topf M, Beckmann R. Mechanism of eIF6-mediated inhibition of ribosomal subunit joining. *The Journal of biological chemistry* 2010;285:14848–51. doi:10.1074/jbc.C109.096057.
- Gasse L, Flemming D, Hurt E. Coordinated ribosomal ITS2 RNA processing by the Las1 complex integrating endonuclease, polynucleotide kinase, and exonuclease activities. *Molecular cell* 2015;60(5):808–15. doi:10.1016/j.molcel.2015.10.021.
- Gates SN, Martin A. Stairway to translocation: AAA+ motor structures reveal the mechanisms of ATP-dependent substrate translocation. *Protein Science* 2020;29(2):407–19. doi:10.1002/pro.3743.
- Gautschi M, Just S, Mun A, Ross S, Rücknagel P, Dubaquié Y, Ehrenhofer-Murray A, Rospert S. The yeast N(alpha)-acetyltransferase NatA is quantitatively anchored to the ribosome and interacts with nascent polypeptides. *Molecular and cellular biology* 2003;23:7403–14. doi:10.1128/mcb.23.20.7403-7414.2003.

- Gautschi M, Lilie H, Funfschilling U, Mun A, Ross S, Lithgow T, Rucknagel P, Rospert S. RAC, a stable ribosome-associated complex in yeast formed by the DnaK-DnaJ homologs Ssz1p and zuotin. *Proceedings of the National Academy of Sciences of the United States of America* 2001;98:3762–7. doi:10.1073/pnas.071057198.
- Geerlings TH, Vos JC, Raue HA. The final step in the formation of 25S rRNA in *Saccharomyces cerevisiae* is performed by 5'→3' exonucleases. *RNA (New York, NY)* 2000;6:1698–703. doi:10.1017/s1355838200001540.
- Gerczei T, Shah BN, Manzo AJ, Walter NG, Correll CC. RNA chaperones stimulate formation and yield of the U3 snoRNA-Pre-rRNA duplexes needed for eukaryotic ribosome biogenesis. *Journal of molecular biology* 2009;390:991–1006. doi:10.1016/j.jmb.2009.05.072.
- Gerhardy S, Menet AM, Pena C, Petkowski JJ, Panse VG. Assembly and nuclear export of pre-ribosomal particles in budding yeast. *Chromosoma* 2014;123(4):327–44. doi:10.1007/s00412-014-0463-z.
- Giglione C, Fieulaine S, Meinnel T. N-terminal protein modifications: Bringing back into play the ribosome. *Biochimie* 2015;114:134–46. doi:10.1016/j.biochi.2014.11.008.
- Gilmore R, Blobel G, Walter P. Protein translocation across the endoplasmic reticulum. I. Detection in the microsomal membrane of a receptor for the signal recognition particle. *The Journal of cell biology* 1982;95:463–9. doi:10.1083/jcb.95.2.463.
- Gleizes PE, Noaillac-Depeyre J, Léger-Silvestre I, Teulières F, Dauxois JY, Pommet D, Azum-Gelade MC, Gas N. Ultrastructural localization of rRNA shows defective nuclear export of preribosomes in mutants of the Nup82p complex. *The Journal of cell biology* 2001;155:923–36. doi:10.1083/jcb.200108142.
- Gogala M, Becker T, Beatrix B, Armache JP, Barrio-Garcia C, Berninghausen O, Beckmann R. Structures of the Sec61 complex engaged in nascent peptide translocation or membrane insertion. *Nature* 2014;506(7486):107–10. doi:10.1038/nature12950.
- Graef M, Langer T. Substrate specific consequences of central pore mutations in the i-AAA protease Yme1 on substrate engagement. *Journal of structural biology* 2006;156(1):101–8. doi:10.1016/j.jsb.2006.01.009.
- Graham LA, Trumpower B. Mutational analysis of the mitochondrial Rieske iron-sulfur protein of *Saccharomyces cerevisiae*. III. Import, protease processing, and assembly into the cytochrome bc1 complex of iron-sulfur protein lacking the iron-sulfur cluster. *Journal of Biological Chemistry* 1991;266(33):22485–92.

- Grandi P, Rybin V, Baßler J, Petfalski E, Strauss D, Marzioch M, Schäfer T, Kuster B, Tschochner H, Tollervey D, Gavin AC, Hurt E. 90S pre-ribosomes include the 35S pre-rRNA, the U3 snoRNP, and 40S subunit processing factors but predominantly lack 60S synthesis factors. *Molecular cell* 2002;10:105–15. doi:10.1016/s1097-2765(02)00579-8.
- Greber BJ. Mechanistic insight into eukaryotic 60S ribosomal subunit biogenesis by cryo-electron microscopy. *RNA* 2016;22(11):1643–62. doi:10.1261/rna.057927.116.
- Greber BJ, Boehringer D, Montellese C, Ban N. Cryo-EM structures of Arx1 and maturation factors Rei1 and Jjj1 bound to the 60S ribosomal subunit. *Nature structural & molecular biology* 2012;19(12):1228–33. doi:10.1038/nsmb.2425.
- Greber BJ, Gerhardy S, Leitner A, Leibundgut M, Salem M, Boehringer D, Leulliot N, Aebersold R, Panse VG, Ban N. Insertion of the biogenesis factor Rei1 probes the ribosomal tunnel during 60S maturation. *Cell* 2016;164(1):91–102. doi:10.1016/j.cell.2015.11.027.
- Green ER, Mecsas J. Bacterial Secretion Systems: An Overview. *Microbiology spectrum* 2016;4. doi:10.1128/microbiolspec.VMBF-0012-2015.
- Grimm I, Erdmann R, Girzalsky W. Role of AAA(+)-proteins in peroxisome biogenesis and function. *Biochimica et biophysica acta* 2016;1863:828–37. doi:10.1016/j.bbamcr.2015.10.001.
- Gurbiel RJ, Batie CJ, Sivaraja M, True AE, Fee JA, Hoffman BM, Ballou DP. Electron-nuclear double resonance spectroscopy of nitrogen-15-enriched phthalate dioxygenase from *Pseudomonas cepacia* proves that two histidines are coordinated to the [2Fe-2S] Rieske-type clusters. *Biochemistry* 1989;28(11):4861–71. doi:10.1021/bi00437a051.
- Görlich D, Prehn S, Hartmann E, Kalies KU, Rapoport TA. A mammalian homolog of SEC61p and SecYp is associated with ribosomes and nascent polypeptides during translocation. *Cell* 1992;71(3):489–503. doi:10.1016/0092-8674(92)90517-G.
- Güttler T, Görlich D. Ran-dependent nuclear export mediators: a structural perspective. *The EMBO journal* 2011;30:3457–74. doi:10.1038/emboj.2011.287.
- Haeusler RA, Engelke DR. Spatial organization of transcription by RNA polymerase III. *Nucleic acids research* 2006;34:4826–36. doi:10.1093/nar/gkl1656.
- Halic M, Becker T, Pool MR, Spahn CMT, Grassucci RA, Frank J, Beckmann R. Structure of the signal recognition particle interacting with the elongation-arrested ribosome. *Nature* 2004;427:808–14. doi:10.1038/nature02342.
- Harnisch U, Weiss H, Sebald W. The primary structure of the iron-sulfur subunit of ubiquinol—cytochrome c reductase from *Neurospora*, determined by cDNA and

- gene sequencing. *European journal of biochemistry* 1985;149(1):95–9. doi:10.1111/j.1432-1033.1985.tb08898.x.
- Hartl FU, Lecker S, Schiebel E, Hendrick JP, Wickner W. The binding cascade of SecB to SecA to SecY/E mediates preprotein targeting to the *E. coli* plasma membrane. *Cell* 1990;63:269–79. doi:10.1016/0092-8674(90)90160-G.
- Hartl FU, Schmidt B, Wachter E, Weiss H, Neupert W. Transport into mitochondria and intramitochondrial sorting of the Fe/S protein of ubiquinol-cytochrome c reductase. *Cell* 1986;47:939–51. doi:10.1016/0092-8674(86)90809-3.
- Hedges J, West M, Johnson AW. Release of the export adapter, Nmd3p, from the 60S ribosomal subunit requires Rpl10p and the cytoplasmic GTPase Lsg1p. *The EMBO journal* 2005;24:567–79. doi:10.1038/sj.emboj.7600547.
- Heinrich SU, Mothes W, Brunner J, Rapoport TA. The Sec61p complex mediates the integration of a membrane protein by allowing lipid partitioning of the transmembrane domain. *Cell* 2000;102(2):233–44. doi:10.1016/s0092-8674(00)00028-3.
- Held WA, Mizushima S, Nomura M. Reconstitution of *Escherichia coli* 30S ribosomal subunits from purified molecular components. *Journal of Biological Chemistry* 1973;248(16):5720–30.
- Henras AK, Plisson-Chastang C, O’Donohue MF, Chakraborty A, Gleizes PE. An overview of pre-ribosomal RNA processing in eukaryotes. *Wiley Interdisciplinary Reviews: RNA* 2015;6(2):225–42. doi:10.1002/wrna.1269.
- Hessa T, Kim H, Bihlmaier K, Lundin C, Boekel J, Andersson H, Nilsson I, White SH, von Heijne G. Recognition of transmembrane helices by the endoplasmic reticulum translocon. *Nature* 2005;433:377–81. doi:10.1038/nature03216.
- Hessa T, Meindl-Beinker NM, Bernsel A, Kim H, Sato Y, Lerch-Bader M, Nilsson I, White SH, von Heijne G. Molecular code for transmembrane-helix recognition by the Sec61 translocon. *Nature* 2007;450:1026–30. doi:10.1038/nature06387.
- Heuer A, Thomson E, Schmidt C, Berninghausen O, Becker T, Hurt E, Beckmann R. Cryo-EM structure of a late pre-40S ribosomal subunit from *Saccharomyces cerevisiae*. *eLife* 2017;6. doi:10.7554/eLife.30189.
- Hightett MI, Beven AF, Shaw PJ. Localization of 5S genes and transcripts in *Pisum sativum* nuclei. *Journal of cell science* 1993;105 (Pt 4):1151–8.
- Ho JH, Kallstrom G, Johnson AW. Nmd3p is a Crm1p-dependent adapter protein for nuclear export of the large ribosomal subunit. *The Journal of cell biology* 2000;151(11086007):1057–66. doi:10.1083/jcb.151.5.1057.
- Hofer A, Bussiere C, Johnson AW. Mutational analysis of the ribosomal protein Rpl10 from yeast. *The Journal of biological chemistry* 2007;282:32630–9. doi:10.1074/jbc.M705057200.

- van Hoof A, Lennertz P, Parker R. Three conserved members of the RNase D family have unique and overlapping functions in the processing of 5S, 5.8S, U4, U5, RNase MRP and RNase P RNAs in yeast. *The EMBO journal* 2000;19:1357–65. doi:10.1093/emboj/19.6.1357.
- Horn DM, Mason SL, Karbstein K. Rcl1 protein, a novel nuclease for 18 S ribosomal RNA production. *The Journal of biological chemistry* 2011;286:34082–7. doi:10.1074/jbc.M111.268649. arXiv:10.1074/jbc.M111.268649.
- Huang C, Mandava CS, Sanyal S. The ribosomal stalk plays a key role in IF2-mediated association of the ribosomal subunits. *Journal of molecular biology* 2010;399(1):145–53. doi:10.1016/j.jmb.2010.04.009.
- Huber D, Boyd D, Xia Y, Olma MH, Gerstein M, Beckwith J. Use of thioredoxin as a reporter to identify a subset of *Escherichia coli* signal sequences that promote signal recognition particle-dependent translocation. *Journal of bacteriology* 2005;187:2983–91. doi:10.1128/JB.187.9.2983-2991.2005.
- Hung NJ, Lo KY, Patel SS, Helmke K, Johnson AW. Arx1 is a nuclear export receptor for the 60S ribosomal subunit in yeast. *Molecular biology of the cell* 2008;19:735–44. doi:10.1091/mbc.e07-09-0968.
- Hunziker M, Barandun J, Petfalski E, Tan D, Delan-Forino C, Molloy KR, Kim KH, Dunn-Davies H, Shi Y, Chaker-Margot M, Chait BT, Walz T, Tollervey D, Klinge S. UtpA and UtpB chaperone nascent pre-ribosomal RNA and U3 snoRNA to initiate eukaryotic ribosome assembly. *Nature communications* 2016;7:12090. doi:10.1038/ncomms12090.
- Hurt E, Hannus S, Schmelzl B, Lau D, Tollervey D, Simos G. A novel in vivo assay reveals inhibition of ribosomal nuclear export in ran-cycle and nucleoporin mutants. *The Journal of cell biology* 1999;144:389–401. doi:10.1083/jcb.144.3.389.
- Huyton T, Pye VE, Briggs LC, Flynn TC, Beuron F, Kondo H, Ma J, Zhang X, Freemont PS. The crystal structure of murine p97/VCP at 3.6Å. *Journal of structural biology* 2003;144:337–48. doi:10.1016/j.jsb.2003.10.007.
- Iwata S, Saynovits M, Link TA, Michel H. Structure of a water soluble fragment of the ‘Rieske’iron–sulfur protein of the bovine heart mitochondrial cytochrome bc1 complex determined by MAD phasing at 1.5 Å resolution. *Structure* 1996;4(5):567–79. doi:10.1016/s0969-2126(96)00062-7.
- Iyer LM, Leipe DD, Koonin EV, Aravind L. Evolutionary history and higher order classification of AAA+ ATPases. *Journal of structural biology* 2004;146:11–31. doi:10.1016/j.jsb.2003.10.010.
- Ize B, Porcelli I, Lucchini S, Hinton JC, Berks BC, Palmer T. Novel phenotypes of *Escherichia coli* tat mutants revealed by global gene expression and phenotypic

- analysis. *The Journal of biological chemistry* 2004;279:47543–54. doi:10.1074/jbc.M406910200.
- Janda CY, Li J, Oubridge C, Hernandez H, Robinson CV, Nagai K. Recognition of a signal peptide by the signal recognition particle. *Nature* 2010;465:507–10. doi:10.1038/nature08870.
- Janska H, Kwasniak M, Szczepanowska J. Protein quality control in organelles - AAA/FtsH story. *Biochimica et biophysica acta* 2013;1833:381–7. doi:10.1016/j.bbamcr.2012.03.016.
- Johnston M, Hillier L, Riles L, Albermann K, André B, Ansorge W, Benes V, Brückner M, Delius H, Dubois E, Düsterhöft A, Entian KD, Floeth M, Goffeau A, Hebling U, Heumann K, Heuss-Neitzel D, Hilbert H, Hilger F, Kleine K, Kötter P, Louis EJ, Messenguy F, Mewes HW, Hoheisel JD. The nucleotide sequence of *Saccharomyces cerevisiae* chromosome XII. *Nature* 1997;387:87–90. doi:10.1038/387s087.
- Joly JC, Leonard MR, Wickner WT. Subunit dynamics in *Escherichia coli* preprotein translocase. *Proceedings of the National Academy of Sciences of the United States of America* 1994;91:4703–7. doi:10.1073/pnas.91.11.4703.
- Jomaa A, Boehringer D, Leibundgut M, Ban N. Structures of the *E. coli* translating ribosome with SRP and its receptor and with the translocon. *Nature communications* 2016;7:10471. doi:10.1038/ncomms10471.
- Jongbloed JDH, Grieger U, Antelmann H, Hecker M, Nijland R, Bron S, Van Dijl JM. Two minimal Tat translocases in *Bacillus*. *Molecular Microbiology* 2004;54(5):1319–25. doi:10.1111/j.1365-2958.2004.04341.x.
- Kargas V, Castro-Hartmann P, Escudero-Urquijo N, Dent K, Hilcenko C, Sailer C, Zisser G, Marques-Carvalho MJ, Pellegrino S, Wawiórka L, Freund SM, Wagstaff JL, Andreeva A, Faille A, Chen E, Stengel F, Bergler H, Warren AJ. Mechanism of completion of peptidyltransferase centre assembly in eukaryotes. *eLife* 2019;8. doi:10.7554/eLife.44904.
- Kater L, Frieg B, Berninghausen O, Gohlke H, Beckmann R, Kedrov A. Partially inserted nascent chain unzips the lateral gate of the Sec translocon. *EMBO reports* 2019;20:e48191. doi:10.15252/embr.201948191.
- Kater L, Mitterer V, Thoms M, Cheng J, Berninghausen O, Beckmann R, Hurt E. Construction of the Central Protuberance and L1 Stalk during 60S Subunit Biogenesis. *Molecular cell* 2020a;doi:10.1016/j.molcel.2020.06.032.
- Kater L, Thoms M, Barrio-Garcia C, Cheng J, Ismail S, Ahmed YL, Bange G, Kressler D, Berninghausen O, Sinning I, Hurt E, Beckmann R. Visualizing the Assembly Pathway of Nucleolar Pre-60S Ribosomes. *Cell* 2017;171(7):1599–1610.e14. doi:10.1016/j.cell.2017.11.039.

- Kater L, Wagener N, Berninghausen O, Becker T, Neupert W, Beckmann R. Structure of the Bcs1 AAA-ATPase suggests an airlock-like translocation mechanism for folded proteins. *Nature structural & molecular biology* 2020b;27:142–9. doi:10.1038/s41594-019-0364-1.
- Kemmler S, Occhipinti L, Veisu M, Panse VG. Yvh1 is required for a late maturation step in the 60S biogenesis pathway. *The Journal of cell biology* 2009;186:863–80. doi:10.1083/jcb.200904111.
- Kharde S, Calviño FR, Gumiero A, Wild K, Sinning I. The structure of Rpf2-Rrs1 explains its role in ribosome biogenesis. *Nucleic acids research* 2015;43(14):7083–95. doi:10.1093/nar/gkv640.
- Kispal G, Csere P, Prohl C, Lill R. The mitochondrial proteins Atm1p and Nfs1p are essential for biogenesis of cytosolic Fe/S proteins. *The EMBO journal* 1999;18:3981–9. doi:10.1093/emboj/18.14.3981.
- Kiss-László Z, Henry Y, Bachellerie JP, Caizergues-Ferrer M, Kiss T. Site-specific ribose methylation of preribosomal RNA: a novel function for small nucleolar RNAs. *Cell* 1996;85:1077–88. doi:10.1016/s0092-8674(00)81308-2.
- Knorr AG, Schmidt C, Tesina P, Berninghausen O, Becker T, Beatrix B, Beckmann R. Ribosome-NatA architecture reveals that rRNA expansion segments coordinate N-terminal acetylation. *Nature structural & molecular biology* 2019;26:35–9. doi:10.1038/s41594-018-0165-y.
- Konikkat S, Biedka S, Woolford JL. The assembly factor Erb1 functions in multiple remodeling events during 60S ribosomal subunit assembly in *S. cerevisiae*. *Nucleic Acids Research* 2017;;gkw1361doi:10.1093/nar/gkw1361.
- Konikkat S, Woolford JL. Principles of 60S ribosomal subunit assembly emerging from recent studies in yeast. *Biochemical Journal* 2017;474(2):195–214. doi:10.1042/bcj20160516.
- Kornprobst M, Turk M, Kellner N, Cheng J, Flemming D, Koš-Braun I, Koš M, Thoms M, Berninghausen O, Beckmann R, Hurt E. Architecture of the 90S Pre-ribosome: A Structural View on the Birth of the Eukaryotic Ribosome. *Cell* 2016;166(2):380–93. doi:10.1016/j.cell.2016.06.014.
- Kozjak V, Wiedemann N, Milenkovic D, Lohaus C, Meyer HE, Guiard B, Meisinger C, Pfanner N. An essential role of Sam50 in the protein sorting and assembly machinery of the mitochondrial outer membrane. *The Journal of biological chemistry* 2003;278:48520–3. doi:10.1074/jbc.C300442200.
- Kressler D. Spb1p is a putative methyltransferase required for 60S ribosomal subunit biogenesis in *Saccharomyces cerevisiae*. *Nucleic Acids Research* 1999;27(23):4598–608. doi:10.1093/nar/27.23.4598.

- Kressler D, Bange G, Ogawa Y, Stjepanovic G, Bradatsch B, Pratte D, Amlacher S, Strauss D, Yoneda Y, Katahira J, Sinning I, Hurt E. Synchronizing nuclear import of ribosomal proteins with ribosome assembly. *Science (New York, NY)* 2012;338(6107):666–71. doi:10.1126/science.1226960.
- Kressler D, Hurt E, Bassler J. A Puzzle of Life: Crafting Ribosomal Subunits. *Trends in Biochemical Sciences* 2017;doi:10.1016/j.tibs.2017.05.005.
- Kressler D, Hurt E, Baßler J. Driving ribosome assembly. *Biochimica et biophysica acta* 2010;1803(6):673–83. doi:10.1016/j.bbamcr.2009.10.009.
- Kressler D, Roser D, Pertschy B, Hurt E. The AAA ATPase Rix7 powers progression of ribosome biogenesis by stripping Nsa1 from pre-60S particles. *The Journal of cell biology* 2008;181(6):935–44. doi:10.1083/jcb.200801181.
- Kruiswijk T, Planta RJ, Krop JM. The course of the assembly of ribosomal subunits in yeast. *Biochimica et biophysica acta* 1978;517:378–89. doi:10.1016/0005-2787(78)90204-6.
- Kudla G, Granneman S, Hahn D, Beggs JD, Tollervy D. Cross-linking, ligation, and sequencing of hybrids reveals RNA-RNA interactions in yeast. *Proceedings of the National Academy of Sciences of the United States of America* 2011;108:10010–5. doi:10.1073/pnas.1017386108.
- Lamanna AC, Karbstein K. Nob1 binds the single-stranded cleavage site D at the 3'-end of 18S rRNA with its PIN domain. *Proceedings of the National Academy of Sciences of the United States of America* 2009;106:14259–64. doi:10.1073/pnas.0905403106.
- Lapeyre B, Purushothaman SK. Spb1p-Directed Formation of Gm2922 in the Ribosome Catalytic Center Occurs at a Late Processing Stage. *Molecular Cell* 2004;16(4):663–9. doi:10.1016/j.molcel.2004.10.022.
- Lebaron S, Schneider C, van Nues RW, Swiatkowska A, Walsh D, Böttcher B, Granneman S, Watkins NJ, Tollervy D. Proofreading of pre-40S ribosome maturation by a translation initiation factor and 60S subunits. *Nature structural & molecular biology* 2012;19:744–53. doi:10.1038/nsmb.2308.
- Leidig C, Thoms M, Holdermann I, Bradatsch B, Berninghausen O, Bange G, Sinning I, Hurt E, Beckmann R. 60S ribosome biogenesis requires rotation of the 5S ribonucleoprotein particle. *Nature communications* 2014;5:3491. doi:10.1038/ncomms4491.
- Letoffe S, Heuck G, Delepelaire P, Lange N, Wandersman C. Bacteria capture iron from heme by keeping tetrapyrrol skeleton intact. *Proceedings of the National Academy of Sciences of the United States of America* 2009;106:11719–24. doi:10.1073/pnas.0903842106.

- Li L, Park E, Ling J, Ingram J, Ploegh H, Rapoport TA. Crystal structure of a substrate-engaged SecY protein-translocation channel. *Nature* 2016;531:395–9. doi:10.1038/nature17163.
- Liang B, Zhou J, Kahen E, Terns RM, Terns MP, Li H. Structure of a functional ribonucleoprotein pseudouridine synthase bound to a substrate RNA. *Nature structural & molecular biology* 2009;16:740–6. doi:10.1038/nsmb.1624.
- Link TA. The role of the ‘Rieske’ iron sulfur protein in the hydroquinone oxidation (QP) site of the cytochrome bc 1 complex. *FEBS Letters* 1997;412(2):257–64. doi:10.1016/S0014-5793(97)00772-2.
- Lo KY, Johnson AW. Reengineering ribosome export. *Molecular biology of the cell* 2009;20:1545–54. doi:10.1091/mbc.e08-10-1000.
- Lo KY, Li Z, Bussiere C, Bresson S, Marcotte EM, Johnson AW. Defining the pathway of cytoplasmic maturation of the 60S ribosomal subunit. *Molecular cell* 2010;39(2):196–208. doi:10.1016/j.molcel.2010.06.018.
- Lo YH, Sobhany M, Hsu AL, Ford BL, Krahn JM, Borgnia MJ, Stanley RE. Cryo-EM structure of the essential ribosome assembly AAA-ATPase Rix7. *Nature communications* 2019;10(1):513. doi:10.1038/s41467-019-08373-0.
- van Loon AP, Schatz G. Transport of proteins to the mitochondrial intermembrane space: the ‘sorting’ domain of the cytochrome c1 presequence is a stop-transfer sequence specific for the mitochondrial inner membrane. *The EMBO journal* 1987;6(2822393):2441–8. doi:10.1002/j.1460-2075.1987.tb02523.x.
- Lupas AN, Martin J. AAA proteins. *Current opinion in structural biology* 2002;12(6):746–53. doi:10.1016/s0959-440x(02)00388-3.
- Léger-Silvestre I, Milkereit P, Ferreira-Cerca S, Saveanu C, Rousselle JC, Choesmel V, Guinefoleau C, Gas N, Gleizes PE. The ribosomal protein Rps15p is required for nuclear exit of the 40S subunit precursors in yeast. *The EMBO journal* 2004;23:2336–47. doi:10.1038/sj.emboj.7600252.
- Ma C, Wu S, Li N, Chen Y, Yan K, Li Z, Zheng L, Lei J, Woolford JL, Gao N. Structural snapshot of cytoplasmic pre-60S ribosomal particles bound by Nmd3, Lsg1, Tif6 and Reh1. *Nature Structural & Molecular Biology* 2017;doi:10.1038/nsmb.3364.
- Madru C, Lebaron S, Blaud M, Delbos L, Pipoli J, Pasmant E, Réty S, Leulliot N. Chaperoning 5S RNA assembly. *Genes & development* 2015;29:1432–46. doi:10.1101/gad.260349.115.
- Malkin R, Bearden AJ. Membrane-bound iron-sulfur centers in photosynthetic systems. *Biochimica et biophysica acta* 1978;505:147–81. doi:10.1016/0304-4173(78)90011-3.

- Malyutin AG, Musalgaonkar S, Patchett S, Frank J, Johnson AW. Nmd3 is a structural mimic of eIF5A, and activates the cpGTPase Lsg1 during 60S ribosome biogenesis. *The EMBO journal* 2017;36(7):854–68. doi:10.15252/embj.201696012.
- Marmier-Gourrier N, Cléry A, Schlotter F, Senty-Ségault V, Branlant C. A second base pair interaction between U3 small nucleolar RNA and the 5'-ETS region is required for early cleavage of the yeast pre-ribosomal RNA. *Nucleic acids research* 2011;39:9731–45. doi:10.1093/nar/gkr675.
- Martin A, Baker TA, Sauer RT. Pore loops of the AAA+ ClpX machine grip substrates to drive translocation and unfolding. *Nature structural & molecular biology* 2008;15(11):1147. doi:10.1038/nsmb.1503.
- Mason JR, Cammack R. The electron-transport proteins of hydroxylating bacterial dioxygenases. *Annual review of microbiology* 1992;46:277–305. doi:10.1146/annurev.mi.46.100192.001425.
- Matlack KE, Misselwitz B, Plath K, Rapoport TA. BiP acts as a molecular ratchet during posttranslational transport of prepro-*alpha* factor across the ER membrane. *Cell* 1999;97(5):553–64. doi:10.1016/S0092-8674(00)80767-9.
- Matsuo Y, Granneman S, Thoms M, Manikas RG, Tollervey D, Hurt E. Coupled GTPase and remodelling ATPase activities form a checkpoint for ribosome export. *Nature* 2014;505(7481):112–6. doi:10.1038/nature12731.
- Meloni S, Rey L, Sidler S, Imperial J, Ruiz-Argueso T, Palacios JM. The twin-arginine translocation (Tat) system is essential for *Rhizobium-legume* symbiosis. *Molecular microbiology* 2003;48:1195–207. doi:10.1046/j.1365-2958.2003.03510.x.
- Menne TF, Goyenechea B, Sanchez-Puig N, Wong CC, Tonkin LM, Ancliff PJ, Brost RL, Costanzo M, Boone C, Warren AJ. The Shwachman-Bodian-Diamond syndrome protein mediates translational activation of ribosomes in yeast. *Nature genetics* 2007;39:486–95. doi:10.1038/ng1994.
- Meyer AE, Hoover LA, Craig EA. The cytosolic J-protein, Jjj1, and Rei1 function in the removal of the pre-60 S subunit factor Arx1. *The Journal of biological chemistry* 2010;285:961–8. doi:10.1074/jbc.M109.038349.
- Meyer AE, Hung NJ, Yang P, Johnson AW, Craig EA. The specialized cytosolic J-protein, Jjj1, functions in 60S ribosomal subunit biogenesis. *Proceedings of the National Academy of Sciences of the United States of America* 2007;104:1558–63. doi:10.1073/pnas.0610704104.
- Miles TD, Jakovljevic J, Horsey EW, Harnpicharnchai P, Tang L, Woolford JL. Ytm1, Nop7, and Erb1 form a complex necessary for maturation of yeast 66S preribosomes. *Molecular and cellular biology* 2005;25(23):10419–32. doi:10.1128/MCB.25.23.10419-10432.2005.

- Miller O, Beatty BR. Visualization of nucleolar genes. *Science* 1969;164(3882):955–7. doi:10.1126/science.164.3882.955.
- Mitterer V, Gantenbein N, Birner-Gruenberger R, Murat G, Bergler H, Kressler D, Pertschy B. Nuclear import of dimerized ribosomal protein Rps3 in complex with its chaperone Yar1. *Scientific reports* 2016;6:36714. doi:10.1038/srep36714.
- Molik S, Karnauchoy I, Weidlich C, Herrmann RG, Klosgen RB. The Rieske Fe/S protein of the cytochrome b6/f complex in chloroplasts: missing link in the evolution of protein transport pathways in chloroplasts? *The Journal of biological chemistry* 2001;276:42761–6. doi:10.1074/jbc.M106690200.
- Monteferrante CG, Miethke M, van der Ploeg R, Glasner C, van Dijl JM. Specific targeting of the metallophosphoesterase YkuE to the bacillus cell wall requires the twin-arginine translocation system. *The Journal of biological chemistry* 2012;287:29789–800. doi:10.1074/jbc.M112.378190.
- Mori H, Cline K. A twin arginine signal peptide and the pH gradient trigger reversible assembly of the thylakoid [Delta]pH/Tat translocase. *The Journal of cell biology* 2002;157:205–10. doi:10.1083/jcb.200202048.
- Mougey EB, O'Reilly M, Osheim Y, Miller OL, Beyer A, Sollner-Webb B. The terminal balls characteristic of eukaryotic rRNA transcription units in chromatin spreads are rRNA processing complexes. *Genes & development* 1993;7(8):1609–19. doi:10.1101/gad.7.8.1609.
- Neuwald A, Aravind L, Spouge J, Neuwald A, Aravind L, Spouge J, et al. Assembly, Operation, and Disassembly of Protein Complexes AAA+: A Class of Chaperone-Like ATPases Associated with the Assembly, Operation, and Disassembly of Protein Complexes. *Genome Res* 1999;9:27–43. doi:10.1101/gr.9.1.27.
- Ng DT, Brown JD, Walter P. Signal sequences specify the targeting route to the endoplasmic reticulum membrane. *The Journal of cell biology* 1996;134:269–78. doi:10.1083/jcb.134.2.269.
- Nicoloso M, Qu LH, Michot B, Bachellerie JP. Intron-encoded, antisense small nucleolar RNAs: the characterization of nine novel species points to their direct role as guides for the 2'-O-ribose methylation of rRNAs. *Journal of molecular biology* 1996;260(2):178–95. doi:10.1006/jmbi.1996.0391.
- Nierhaus KH, Dohme F. Total reconstitution of functionally active 50S ribosomal subunits from *Escherichia coli*. *Proceedings of the National Academy of Sciences* 1974;71(12):4713–7. doi:10.1073/pnas.71.12.4713.
- Nirenberg M, Leder P, Bernfield M, Brimacombe R, Trupin J, Rottman F, O'Neal C. RNA codewords and protein synthesis, VII. On the general nature of the RNA code. *Proceedings of the National Academy of Sciences of the United States of America* 1965;53:1161–8. doi:10.1073/pnas.53.5.1161.

- Nishiyama K, Mizushima S, Tokuda H. A novel membrane protein involved in protein translocation across the cytoplasmic membrane of *Escherichia coli*. *The EMBO journal* 1993;12:3409–15. doi:10.1002/j.1460-2075.1993.tb06015.x.
- Nishiyama K, Suzuki H, Tokuda H. Role of the non-essential region encompassing the N-terminal two transmembrane stretches of *Escherichia coli* SecE. *Bioscience, biotechnology, and biochemistry* 2000;64:2121–7. doi:10.1271/bbb.64.2121.
- Nissan TA, Bassler J, Petfalski E, Tollervey D, Hurt E. 60S pre-ribosome formation viewed from assembly in the nucleolus until export to the cytoplasm. *The EMBO journal* 2002;21(20):5539–47. doi:10.1093/emboj/cdf547.
- Niwa H, Tsuchiya D, Makyio H, Yoshida M, Morikawa K. Hexameric ring structure of the ATPase domain of the membrane-integrated metalloprotease FtsH from *Thermus thermophilus* HB8. *Structure (London, England : 1993)* 2002;10:1415–23. doi:10.1016/s0969-2126(02)00855-9.
- Nogi Y, Yano R, Nomura M. Synthesis of large rRNAs by RNA polymerase II in mutants of *Saccharomyces cerevisiae* defective in RNA polymerase I. *Proceedings of the National Academy of Sciences* 1991;88(9):3962–6. doi:10.1073/pnas.88.9.3962.
- Nomura N, Honda T, Baba K, Naganuma T, Tanzawa T, Arisaka F, Noda M, Uchiyama S, Tanaka I, Yao M, et al. Archaeal ribosomal stalk protein interacts with translation factors in a nucleotide-independent manner via its conserved C terminus. *Proceedings of the National Academy of Sciences* 2012;109(10):3748–53. doi:10.1073/pnas.1112934109.
- O'Donohue MF, Choismel V, Faubladiet M, Fichant G, Gleizes PE. Functional dichotomy of ribosomal proteins during the synthesis of mammalian 40S ribosomal subunits. *The Journal of cell biology* 2010;190:853–66. doi:10.1083/jcb.201005117.
- Oeffinger M, Dlakic M, Tollervey D. A pre-ribosome-associated HEAT-repeat protein is required for export of both ribosomal subunits. *Genes & development* 2004;18:196–209. doi:10.1101/gad.285604.
- Ogle JM, Brodersen DE, Clemons WM, Tarry MJ, Carter AP, Ramakrishnan V. Recognition of cognate transfer RNA by the 30S ribosomal subunit. *Science (New York, NY)* 2001;292:897–902. doi:10.1126/science.1060612.
- Ogura T, Whiteheart SW, Wilkinson AJ. Conserved arginine residues implicated in ATP hydrolysis, nucleotide-sensing, and inter-subunit interactions in AAA and AAA+ ATPases. *Journal of structural biology* 2004;146(1-2):106–12. doi:10.1016/j.jsb.2003.11.008.

- Ortega J, Singh SK, Ishikawa T, Maurizi MR, Steven AC. Visualization of substrate binding and translocation by the ATP-dependent protease, ClpXP. *Molecular cell* 2000;6:1515–21. doi:10.1016/s1097-2765(00)00148-9.
- Osheim YN, French SL, Keck KM, Champion EA, Spasov K, Dragon F, Baserga SJ, Beyer AL. Pre-18S ribosomal RNA is structurally compacted into the SSU processome prior to being cleaved from nascent transcripts in *Saccharomyces cerevisiae*. *Molecular cell* 2004;16:943–54. doi:10.1016/j.molcel.2004.11.031.
- Pardue ML, Brown DD, Birnstiel ML. Location of the genes for 5S ribosomal RNA in *Xenopus laevis*. *Chromosoma* 1973;42:191–203. doi:10.1007/bf00320940.
- Park E, Rapoport TA. Preserving the membrane barrier for small molecules during bacterial protein translocation. *Nature* 2011;473:239–42. doi:10.1038/nature10014.
- Passmore L, Russo C. Specimen Preparation for High-Resolution Cryo-EM. In: *Methods in Enzymology*. Elsevier BV; 2016. p. 51–86. doi:10.1016/bs.mie.2016.04.011.
- Patel R, Smith SM, Robinson C. Protein transport by the bacterial Tat pathway. *Biochimica et biophysica acta* 2014;1843:1620–8. doi:10.1016/j.bbamcr.2014.02.013.
- Perry RP. The Cellular Sites of Synthesis of Ribosomal and 4S RNA. *Proceedings of the National Academy of Sciences of the United States of America* 1962;48:2179–86. doi:10.1073/pnas.48.12.2179.
- Pertschy B, Saveanu C, Zisser G, Lebreton A, Tengg M, Jacquier A, Liebming E, Nobis B, Kappel L, van der Klei I, Högenauer G, Fromont-Racine M, Bergler H. Cytoplasmic recycling of 60S preribosomal factors depends on the AAA protein Drg1. *Molecular and cellular biology* 2007;27(19):6581–92. doi:10.1128/MCB.00668-07.
- Petfalski E, Dandekar T, Henry Y, Tollervey D. Processing of the precursors to small nucleolar RNAs and rRNAs requires common components. *Molecular and cellular biology* 1998;18:1181–9. doi:10.1128/mcb.18.3.1181.
- Petrov AS, Bernier CR, Gulen B, Waterbury CC, Hershkovits E, Hsiao C, Harvey SC, Hud NV, Fox GE, Wartell RM, Williams LD. Secondary structures of rRNAs from all three domains of life. *PloS one* 2014;9:e88222. doi:10.1371/journal.pone.0088222.
- Pett W, Lavrov DV. The twin-arginine subunit C in *Oscarella*: origin, evolution, and potential functional significance. *Integrative and comparative biology* 2013;53:495–502. doi:10.1093/icb/ict079.

- Pohlschroder M, Prinz WA, Hartmann E, Beckwith J. Protein translocation in the three domains of life: variations on a theme. *Cell* 1997;91:563–6. doi:10.1016/s0092-8674(00)80443-2.
- Poritz MA, Bernstein HD, Strub K, Zopf D, Wilhelm H, Walter P. An *E. coli* ribonucleoprotein containing 4.5S RNA resembles mammalian signal recognition particle. *Science* (New York, NY) 1990;250:1111–7. doi:10.1126/science.1701272.
- Puchades C, Rampello AJ, Shin M, Giuliano CJ, Wiseman RL, Glynn SE, Lander GC. Structure of the mitochondrial inner membrane AAA+ protease YME1 gives insight into substrate processing. *Science* 2017;358(6363):eaao0464. doi:10.1126/science.aao0464.
- Puchades C, Sandate CR, Lander GC. The molecular principles governing the activity and functional diversity of AAA+ proteins. *Nature reviews Molecular cell biology* 2019;doi:10.1038/s41580-019-0183-6.
- Pérez-Fernández J, Martín-Marcos P, Dosil M. Elucidation of the assembly events required for the recruitment of Utp20, Imp4 and Bms1 onto nascent pre-ribosomes. *Nucleic acids research* 2011;39:8105–21. doi:10.1093/nar/gkr508.
- Qu LH, Henry Y, Nicoloso M, Michot B, Azum MC, Renalier MH, Caizergues-Ferrer M, Bachellerie JP. U24, a novel intron-encoded small nucleolar RNA with two 12 nt long, phylogenetically conserved complementarities to 28S rRNA. *Nucleic acids research* 1995;23(14):2669–76. doi:10.1093/nar/23.14.2669.
- Ramakrishnan V. Ribosome structure and the mechanism of translation. *Cell* 2002;108:557–72. doi:10.1016/s0092-8674(02)00619-0.
- Rapoport TA, Li L, Park E. Structural and Mechanistic Insights into Protein Translocation. *Annual review of cell and developmental biology* 2017;33:369–90. doi:10.1146/annurev-cellbio-100616-060439.
- Reid BG, Fenton WA, Horwich AL, Weber-Ban EU. ClpA mediates directional translocation of substrate proteins into the ClpP protease. *Proceedings of the National Academy of Sciences of the United States of America* 2001;98:3768–72. doi:10.1073/pnas.071043698.
- Reid RA, Moyle J, Mitchell P. Synthesis of adenosine triphosphate by a proton-motive force in rat liver mitochondria. *Nature* 1966;212:257–8. doi:10.1038/212257a0.
- Rieske JS, MacLennan DH, Coleman R. Isolation and properties of an iron-protein from the (reduced coenzyme Q)-cytochrome C reductase complex of the respiratory chain. *Biochemical and Biophysical Research Communications* 1964;15(4):338–44. doi:10.1016/0006-291x(64)90171-8.

- Rodrigue A, Chanal A, Beck K, Müller M, Wu LF. Co-translocation of a periplasmic enzyme complex by a hitchhiker mechanism through the bacterial tat pathway. *The Journal of biological chemistry* 1999;274:13223–8. doi:10.1074/jbc.274.19.13223.
- Rodríguez-Galán O, García-Gómez JJ, de la Cruz J. Yeast and human RNA helicases involved in ribosome biogenesis: current status and perspectives. *Biochimica et biophysica acta* 2013;1829:775–90. doi:10.1016/j.bbagr.2013.01.007.
- Rosado IV, Dez C, Lebaron S, Caizergues-Ferrer M, Henry Y, de la Cruz J. Characterization of *Saccharomyces cerevisiae* Npa2p (Urb2p) reveals a low-molecular-mass complex containing Dbp6p, Npa1p (Urb1p), Nop8p, and Rsa3p involved in early steps of 60S ribosomal subunit biogenesis. *Molecular and cellular biology* 2007a;27:1207–21. doi:10.1128/MCB.01523-06.
- Rosado IV, Kressler D, de la Cruz J. Functional analysis of *Saccharomyces cerevisiae* ribosomal protein Rpl3p in ribosome synthesis. *Nucleic acids research* 2007b;35(12):4203–13. doi:10.1093/nar/gkm388.
- Rose P, Fröbel J, Graumann PL, Müller M. Substrate-dependent assembly of the Tat translocase as observed in live *Escherichia coli* cells. *PloS one* 2013;8(23936332):e69488–. doi:10.1371/journal.pone.0069488.
- Rose RW, Brüser T, Kissinger JC, Pohlschröder M. Adaptation of protein secretion to extremely high-salt conditions by extensive use of the twin-arginine translocation pathway. *Molecular microbiology* 2002;45:943–50. doi:10.1046/j.1365-2958.2002.03090.x.
- Rosenblad MA, Larsen N, Samuelsson T, Zwieb C. Kinship in the SRP RNA family. *RNA biology* 2009;6(5):508–16. doi:10.4161/rna.6.5.9753.
- Sanghai ZA, Miller L, Molloy KR, Barandun J, Hunziker M, Chaker-Margot M, Wang J, Chait BT, Klinge S. Modular assembly of the nucleolar pre-60S ribosomal subunit. *Nature* 2018;556(7699):126. doi:10.1038/nature26156.
- Santini CL, Ize B, Chanal A, Müller M, Giordano G, Wu LF. A novel sec-independent periplasmic protein translocation pathway in *Escherichia coli*. *The EMBO journal* 1998;17:101–12. doi:10.1093/emboj/17.1.101.
- Sardana R, Liu X, Granneman S, Zhu J, Gill M, Papoulas O, Marcotte EM, Tollervey D, Correll CC, Johnson AW. The DEAH-box helicase Dhr1 dissociates U3 from the pre-rRNA to promote formation of the central pseudoknot. *PLoS biology* 2015;13:e1002083. doi:10.1371/journal.pbio.1002083.
- Sargent F, Berks BC, Palmer T. Assembly of membrane-bound respiratory complexes by the Tat protein-transport system. *Archives of microbiology* 2002;178:77–84. doi:10.1007/s00203-002-0434-2.

- Sargent F, Bogsch EG, Stanley NR, Wexler M, Robinson C, Berks BC, Palmer T. Overlapping functions of components of a bacterial Sec-independent protein export pathway. *The EMBO journal* 1998;17(9649434):3640–50. doi:10.1093/emboj/17.13.3640.
- Sarkar A, Pech M, Thoms M, Beckmann R, Hurt E. Ribosome-stalk biogenesis is coupled with recruitment of nuclear-export factor to the nascent 60S subunit. *Nat Struct Mol Biol* 2016;23(12):1074–82. doi:10.1038/nsmb.3312.
- Scaiola A, Peña C, Weisser M, Böhringer D, Leibundgut M, Klingauf-Nerurkar P, Gerhardy S, Panse VG, Ban N. Structure of a eukaryotic cytoplasmic pre-40S ribosomal subunit. *The EMBO journal* 2018;37. doi:10.15252/emj.201798499.
- Scheffzek K, Ahmadian MR, Kabsch W, Wiesmuller L, Lautwein A, Schmitz F, Wittinghofer A. The Ras-RasGAP complex: structural basis for GTPase activation and its loss in oncogenic Ras mutants. *Science (New York, NY)* 1997;277:333–8. doi:10.1126/science.277.5324.333.
- Schibich D, Gloge F, Pöhner I, Björkholm P, Wade RC, von Heijne G, Bukau B, Kramer G. Global profiling of SRP interaction with nascent polypeptides. *Nature* 2016;536:219–23. doi:10.1038/nature19070.
- Schierle CF, Berkmen M, Huber D, Kumamoto C, Boyd D, Beckwith J. The DsbA signal sequence directs efficient, cotranslational export of passenger proteins to the *Escherichia coli* periplasm via the signal recognition particle pathway. *Journal of bacteriology* 2003;185:5706–13. doi:10.1128/jb.185.19.5706–5713.2003.
- Schlutzen F, Tocilj A, Zarivach R, Harms J, Gluehmann M, Janell D, Bashan A, Bartels H, Agmon I, Franceschi F, Yonath A. Structure of functionally activated small ribosomal subunit at 3.3 angstroms resolution. *Cell* 2000;102:615–23. doi:10.1016/s0092-8674(00)00084-2.
- Schmeing TM, Ramakrishnan V. What recent ribosome structures have revealed about the mechanism of translation. *Nature* 2009;461:1234–42. doi:10.1038/nature08403.
- Schmidt C, Kowalinski E, Shanmuganathan V, Defenouill'ere Q, Braunger K, Heuer A, Pech M, Namane A, Berninghausen O, Fromont-Racine M, Jacquier A, Conti E, Becker T, Beckmann R. The cryo-EM structure of a ribosometextendashSki2mbox-Ski3mbox-Ski8 helicase complex. *Science* 2016;354(6318):1431–3. doi:10.1126/science.aaf7520.
- Schuenemann D, Gupta S, Persello-Cartieaux F, Klimyuk VI, Jones JD, Nussaume L, Hoffman NE. A novel signal recognition particle targets light-harvesting proteins to the thylakoid membranes. *Proceedings of the National Academy of Sciences of the United States of America* 1998;95:10312–6. doi:10.1073/pnas.95.17.10312.

- Schäfer T, Strauss D, Petfalski E, Tollervey D, Hurt E. The path from nucleolar 90S to cytoplasmic 40S pre-ribosomes. *The EMBO journal* 2003;22:1370–80. doi:10.1093/emboj/cdg121.
- Seiser RM, Sundberg AE, Wollam BJ, Zobel-Thropp P, Baldwin K, Spector MD, Lycan DE. Ltv1 is required for efficient nuclear export of the ribosomal small subunit in *Saccharomyces cerevisiae*. *Genetics* 2006;174:679–91. doi:10.1534/genetics.106.062117.
- Senger B, Lafontaine DL, Graindorge JS, Gadai O, Camasses A, Sanni A, Garnier JM, Breitenbach M, Hurt E, Fasiolo F. The nucle(ol)ar Tif6p and Efl1p are required for a late cytoplasmic step of ribosome synthesis. *Molecular cell* 2001;8:1363–73. doi:10.1016/s1097-2765(01)00403-8.
- Sharma S, Yang J, Watzinger P, Kötter P, Entian KD. Yeast Nop2 and Rcm1 methylate C2870 and C2278 of the 25S rRNA, respectively. *Nucleic acids research* 2013;41(19):9062–76. doi:10.1093/nar/gkt679.
- Shipkovenska G, Durango A, Kalocsay M, Gygi SP, Moazed D. An RNA Degradation Complex Required for Spreading and Epigenetic Inheritance of Heterochromatin. *bioRxiv* 2019;:870766doi:10.1101/870766.
- Stephenson K. Sec-dependent protein translocation across biological membranes: evolutionary conservation of an essential protein transport pathway (review). *Molecular membrane biology* 2005;22:17–28. doi:10.1080/09687860500063308.
- Stinson BM, Nager AR, Glynn SE, Schmitz KR, Baker TA, Sauer RT. Nucleotide binding and conformational switching in the hexameric ring of a AAA+ machine. *Cell* 2013;153:628–39. doi:10.1016/j.cell.2013.03.029.
- Strunk BS, Loucks CR, Su M, Vashisth H, Cheng S, Schilling J, Brooks CL, Karbstein K, Skiniotis G. Ribosome assembly factors prevent premature translation initiation by 40S assembly intermediates. *Science (New York, NY)* 2011;333:1449–53. doi:10.1126/science.1208245.
- Strunk BS, Novak MN, Young CL, Karbstein K. A translation-like cycle is a quality control checkpoint for maturing 40S ribosome subunits. *Cell* 2012;150:111–21. doi:10.1016/j.cell.2012.04.044.
- Sun Q, Zhu X, Qi J, An W, Lan P, Tan D, Chen R, Wang B, Zheng S, Zhang C, et al. Molecular architecture of the 90S small subunit pre-ribosome. *Elife* 2017;6:e22086. doi:10.7554/elife.22086.
- Tanaka Y, Sugano Y, Takemoto M, Mori T, Furukawa A, Kusakizako T, Kumazaki K, Kashima A, Ishitani R, Sugita Y, Nureki O, Tsukazaki T. Crystal Structures of SecYEG in Lipidic Cubic Phase Elucidate a Precise Resting and a Peptide-Bound State. *Cell reports* 2015;13:1561–8. doi:10.1016/j.celrep.2015.10.025.

- Tang L, Sahasranaman A, Jakovljevic J, Schleifman E, Woolford JL. Interactions among Ytm1, Erb1, and Nop7 required for assembly of the Nop7mbox-subcomplex in yeast preribosomes. *Molecular biology of the cell* 2008;19(7):2844–56. doi:10.1091/mbc.E07-12-1281.
- Tang WK, Borgnia MJ, Hsu AL, Esser L, Fox T, de Val N, Xia D. Structures of AAA protein translocase Bcs1 suggest translocation mechanism of a folded protein. *Nature structural & molecular biology* 2020;27:202–9. doi:10.1038/s41594-020-0373-0.
- Tesina P, Heckel E, Cheng J, Fromont-Racine M, Buschauer R, Kater L, Beatrix B, Berninghausen O, Jacquier A, Becker T, et al. Structure of the 80S ribosome–Xrn1 nuclease complex. *Nature structural & molecular biology* 2019;26(4):275. doi:10.1038/s41594-019-0202-5.
- Thoms M, Ahmed YL, Maddi K, Hurt E, Sinning I. Concerted removal of the Erb1–Ytm1 complex in ribosome biogenesis relies on an elaborate interface. *Nucleic acids research* 2016;44(2):926–39. doi:10.1093/nar/gkv1365.
- Thoms M, Mitterer V, Kater L, Falquet L, Beckmann R, Kressler D, Hurt E. Suppressor mutations in Rpf2–Rrs1 or Rpl5 bypass the Cgr1 function for pre-ribosomal 5S RNP-rotation. *Nature communications* 2018;9:4094. doi:10.1038/s41467-018-06660-w.
- Thoms M, Thomson E, Bassler J, Gnädig M, Griesel S, Hurt E. The Exosome Is Recruited to RNA Substrates through Specific Adaptor Proteins. *Cell* 2015;162(5):1029–38. doi:10.1016/j.cell.2015.07.060.
- Thomson E, Ferreira-Cerca S, Hurt E. Eukaryotic ribosome biogenesis at a glance. *Journal of cell science* 2013;126(Pt 21):4815–21. doi:10.1242/jcs.111948.
- Thomson E, Tollervey D. The final step in 5.8S rRNA processing is cytoplasmic in *Saccharomyces cerevisiae*. *Molecular and cellular biology* 2010;30:976–84. doi:10.1128/MCB.01359-09.
- Tomecki R, Labno A, Drazkowska K, Cysewski D, Dziembowski A. hUTP24 is essential for processing of the human rRNA precursor at site A1, but not at site A0. *RNA biology* 2015;12:1010–29. doi:10.1080/15476286.2015.1073437.
- Tomoyasu T, Yuki T, Morimura S, Mori H, Yamanaka K, Niki H, Hiraga S, Ogura T. The *Escherichia coli* FtsH protein is a prokaryotic member of a protein family of putative ATPases involved in membrane functions, cell cycle control, and gene expression. *Journal of bacteriology* 1993;175:1344–51. doi:10.1128/jb.175.5.1344-1351.1993.
- Tottey S, Waldron KJ, Firbank SJ, Reale B, Bessant C, Sato K, Cheek TR, Gray J, Banfield MJ, Dennison C, Robinson NJ. Protein-folding location can regulate manganese-binding versus copper- or zinc-binding. *Nature* 2008;455:1138–42. doi:10.1038/nature07340.

- Trabuco LG, Schreiner E, Eargle J, Cornish P, Ha T, Luthey-Schulten Z, Schulten K. The role of L1 stalk-tRNA interaction in the ribosome elongation cycle. *Journal of molecular biology* 2010;402:741–60. doi:10.1016/j.jmb.2010.07.056.
- Tran EJ, Wentz SR. Dynamic nuclear pore complexes: life on the edge. *Cell* 2006;125:1041–53. doi:10.1016/j.cell.2006.05.027.
- Trapman J, Retèl J, Planta RJ. Ribosomal precursor particles from yeast. *Experimental cell research* 1975;90:95–104. doi:10.1016/0014-4827(75)90361-4.
- Traut RR, Monro RE. The Puromycin Reaction and its Relation to Protein Synthesis. *Journal of molecular biology* 1964;10:63–72. doi:10.1016/s0022-2836(64)80028-0.
- Tripathi A, Mandon EC, Gilmore R, Rapoport TA. Two alternative binding mechanisms connect the protein translocation Sec71-Sec72 complex with heat shock proteins. *The Journal of biological chemistry* 2017;292:8007–18. doi:10.1074/jbc.M116.761122.
- Trumpower BL, Edwards CA. Identification of oxidation factor as a reconstitutively active form of the iron-sulfur protein of the cytochrome b-c1 segment of the respiratory chain. *FEBS letters* 1979;100:13–6. doi:10.1016/0014-5793(79)81121-7.
- Tsukazaki T, Mori H, Fukai S, Ishitani R, Mori T, Dohmae N, Perederina A, Sugita Y, Vassilyev DG, Ito K, Nureki O. Conformational transition of Sec machinery inferred from bacterial SecYE structures. *Nature* 2008;455(7215):988–91. doi:10.1038/nature07421.
- Tu CJ, Schuenemann D, Hoffman NE. Chloroplast FtsY, chloroplast signal recognition particle, and GTP are required to reconstitute the soluble phase of light-harvesting chlorophyll protein transport into thylakoid membranes. *The Journal of biological chemistry* 1999;274:27219–24. doi:10.1074/jbc.274.38.27219.
- Twomey EC, Ji Z, Wales TE, Bodnar NO, Ficarro SB, Marto JA, Engen JR, Rapoport TA. Substrate processing by the Cdc48 ATPase complex is initiated by ubiquitin unfolding. *Science (New York, NY)* 2019;365. doi:10.1126/science.aax1033.
- Udem SA, Warner JR. Ribosomal RNA synthesis in *Saccharomyces cerevisiae*. *Journal of molecular biology* 1972;65:227–42. doi:10.1016/0022-2836(72)90279-3.
- Udem SA, Warner JR. The cytoplasmic maturation of a ribosomal precursor ribonucleic acid in yeast. *The Journal of biological chemistry* 1973;248:1412–6.
- Ulbrich C, Diepholz M, Baßler J, Kressler D, Pertschy B, Galani K, Böttcher B, Hurt E. Mechanochemical removal of ribosome biogenesis factors from nascent 60S ribosomal subunits. *Cell* 2009;138(5):911–22. doi:10.1016/j.cell.2009.06.045.

- Vale RD. AAA proteins. Lords of the ring. *The Journal of cell biology* 2000;150:F13–9. doi:10.1083/jcb.150.1.f13.
- Valent QA, Scotti PA, High S, de Gier JW, von Heijne G, Lentzen G, Wintermeyer W, Oudega B, Luirink J. The Escherichia coli SRP and SecB targeting pathways converge at the translocon. *The EMBO journal* 1998;17:2504–12. doi:10.1093/emboj/17.9.2504.
- Vanrobays E, Leplus A, Osheim YN, Beyer AL, Wacheul L, Lafontaine DLJ. TOR regulates the subcellular distribution of DIM2, a KH domain protein required for cotranscriptional ribosome assembly and pre-40S ribosome export. *RNA (New York, NY)* 2008;14:2061–73. doi:10.1261/rna.1176708.
- Voorhees RM, Fernández IS, Scheres SHW, Hegde RS. Structure of the mammalian ribosome-Sec61 complex to 3.4 Å resolution. *Cell* 2014;157:1632–43. doi:10.1016/j.cell.2014.05.024.
- Voorhees RM, Hegde RS. Structures of the scanning and engaged states of the mammalian SRP-ribosome complex. *eLife* 2015;4. doi:10.7554/eLife.07975.
- Voorhees RM, Hegde RS. Structure of the Sec61 channel opened by a signal sequence. *Science (New York, NY)* 2016;351:88–91. doi:10.1126/science.aad4992.
- Wagener N, Ackermann M, Funes S, Neupert W. A pathway of protein translocation in mitochondria mediated by the AAA-ATPase Bcs1. *Molecular cell* 2011;44(2):191–202. doi:10.1016/j.molcel.2011.07.036.
- Wagener N, Neupert W. Bcs1, a AAA protein of the mitochondria with a role in the biogenesis of the respiratory chain. *Journal of structural biology* 2012;179(2):121–5. doi:10.1016/j.jsb.2012.04.019.
- Walker JE, Saraste M, Runswick MJ, Gay NJ. Distantly related sequences in the alpha- and beta-subunits of ATP synthase, myosin, kinases and other ATP-requiring enzymes and a common nucleotide binding fold. *The EMBO journal* 1982;1:945–51. doi:10.1002/j.1460-2075.1982.tb01276.x.
- Walter P, Blobel G. Purification of a membrane-associated protein complex required for protein translocation across the endoplasmic reticulum. *Proceedings of the National Academy of Sciences of the United States of America* 1980;77:7112–6. doi:10.1073/pnas.77.12.7112.
- Walter P, Blobel G. Signal recognition particle contains a 7S RNA essential for protein translocation across the endoplasmic reticulum. *Nature* 1982;299:691–8. doi:10.1038/299691a0.
- Walter P, Ibrahimi I, Blobel G. Translocation of proteins across the endoplasmic reticulum. I. Signal recognition protein (SRP) binds to in-vitro-assembled polysomes synthesizing secretory protein. *The Journal of cell biology* 1981;91:545–50. doi:10.1083/jcb.91.2.545.

- Wang J, Song JJ, Franklin M, Kamtekar S, Im Y, Rho S, Seong IS, Lee C, Chung CH, Eom SH. Crystal structures of the HslVU peptidase–ATPase complex reveal an ATP-dependent proteolysis mechanism. *Structure* 2001;9(2):177–84. doi:10.1016/S0969-2126(01)00570-6.
- Warner JR. The economics of ribosome biosynthesis in yeast. *Trends in biochemical sciences* 1999;24:437–40. doi:10.1016/s0968-0004(99)01460-7.
- Watkins NJ, Bohnsack MT. The box C/D and H/ACA snoRNPs: key players in the modification, processing and the dynamic folding of ribosomal RNA. *Wiley interdisciplinary reviews RNA* 2012;3:397–414. doi:10.1002/wrna.117.
- Wegrecki M, Rodríguez-Galán O, de la Cruz J, Bravo J. The structure of Erb1-Ytm1 complex reveals the functional importance of a high-affinity binding between two */beta*-propellers during the assembly of large ribosomal subunits in eukaryotes. *Nucleic acids research* 2015;43(22):11017–30. doi:10.1093/nar/gkv1043.
- Weis F, Giudice E, Churcher M, Jin L, Hilcenko C, Wong CC, Traynor D, Kay RR, Warren AJ. Mechanism of eIF6 release from the nascent 60S ribosomal subunit. *Nature structural & molecular biology* 2015;22(11):914–9. doi:10.1038/nsmb.3112.
- Wendler P, Ciniawsky S, Kock M, Kube S. Structure and function of the AAA+ nucleotide binding pocket. *Biochimica et biophysica acta* 2012;1823:2–14. doi:10.1016/j.bbamcr.2011.06.014.
- West M, Hedges JB, Chen A, Johnson AW. Defining the order in which Nmd3p and Rpl10p load onto nascent 60S ribosomal subunits. *Molecular and cellular biology* 2005;25:3802–13. doi:10.1128/MCB.25.9.3802-3813.2005.
- White J, Li Z, Sardana R, Bujnicki JM, Marcotte EM, Johnson AW. Bud23 methylates G1575 of 18S rRNA and is required for efficient nuclear export of pre-40S subunits. *Molecular and cellular biology* 2008;28:3151–61. doi:10.1128/MCB.01674-07.
- Wiedemann N, Pfanner N. Mitochondrial Machineries for Protein Import and Assembly. *Annual review of biochemistry* 2017;86:685–714. doi:10.1146/annurev-biochem-060815-014352.
- Woodman PG. The roles of NSF, SNAPs and SNAREs during membrane fusion. *Biochimica et Biophysica Acta (BBA)-Molecular Cell Research* 1997;1357(2):155–72. doi:10.1016/s0167-4889(97)00039-6.
- Woolford JL, Baserga SJ. Ribosome biogenesis in the yeast *Saccharomyces cerevisiae*. *Genetics* 2013;195(3):643–81. doi:10.1534/genetics.113.153197.
- Wu S, Tutuncuoglu B, Yan K, Brown H, Zhang Y, Tan D, Gamalinda M, Yuan Y, Li Z, Jakovljevic J, Ma C, Lei J, Dong MQ, Woolford JL, Gao N. Diverse roles of

- assembly factors revealed by structures of late nuclear pre-60S ribosomes. *Nature* 2016;doi:10.1038/nature17942.
- Xia D, Esser L, Tang WK, Zhou F, Zhou Y, Yu L, Yu CA. Structural analysis of cytochrome bc₁ complexes: implications to the mechanism of function. *Biochimica et biophysica acta* 2013;1827(23201476):1278–94. doi:10.1016/j.bbabi.2012.11.008.
- Xia D, Tang WK, Ye Y. Structure and function of the AAA+ ATPase p97/Cdc48p. *Gene* 2016;583:64–77. doi:10.1016/j.gene.2016.02.042.
- Xiang S, Cooper-Morgan A, Jiao X, Kiledjian M, Manley JL, Tong L. Structure and function of the 5'→3' exoribonuclease Rat1 and its activating partner Rai1. *Nature* 2009;458:784–8. doi:10.1038/nature07731.
- Yao N, Coryell L, Zhang D, Georgescu RE, Finkelstein J, Coman MM, Hingorani MM, O'Donnell M. Replication factor C clamp loader subunit arrangement within the circular pentamer and its attachment points to proliferating cell nuclear antigen. *The Journal of biological chemistry* 2003;278:50744–53. doi:10.1074/jbc.M309206200.
- Yao W, Roser D, Köhler A, Bradatsch B, Baßler J, Hurt E. Nuclear export of ribosomal 60S subunits by the general mRNA export receptor Mex67-Mtr2. *Molecular cell* 2007;26(1):51–62. doi:10.1016/j.molcel.2007.02.018.
- Yedidi RS, Wendler P, Enenkel C. AAA-ATPases in Protein Degradation. *Frontiers in molecular biosciences* 2017;4:42. doi:10.3389/fmolb.2017.00042.
- Zemp I, Wild T, O'Donohue MF, Wandrey F, Widmann B, Gleizes PE, Kutay U. Distinct cytoplasmic maturation steps of 40S ribosomal subunit precursors require hRio2. *The Journal of cell biology* 2009;185:1167–80. doi:10.1083/jcb.200904048.
- Zhang J, Harnpicharnchai P, Jakovljevic J, Tang L, Guo Y, Oeffinger M, Rout MP, Hiley SL, Hughes T, Woolford JL. Assembly factors Rpf2 and Rrs1 recruit 5S rRNA and ribosomal proteins rpL5 and rpL11 into nascent ribosomes. *Genes & development* 2007;21(20):2580–92. doi:10.1101/gad.1569307.
- Zhang L, Wu C, Cai G, Chen S, Ye K. Stepwise and dynamic assembly of the earliest precursors of small ribosomal subunits in yeast. *Genes & development* 2016;30:718–32. doi:10.1101/gad.274688.115.
- Zhou D, Zhu X, Zheng S, Tan D, Dong MQ, Ye K. Cryo-EM structure of an early precursor of large ribosomal subunit reveals a half-assembled intermediate. *Protein & cell* 2019a;10:120–30. doi:10.1007/s13238-018-0526-7.
- Zhou Y, Musalgaonkar S, Johnson AW, Taylor DW. Tightly-orchestrated rearrangements govern catalytic center assembly of the ribosome. *Nature communications* 2019b;10(1):958. doi:10.1038/s41467-019-08880-0.

Zimmermann R, Eyrisch S, Ahmad M, Helms V. Protein translocation across the ER membrane. *Biochimica et biophysica acta* 2011;1808:912–24. doi:10.1016/j.bbamem.2010.06.015.

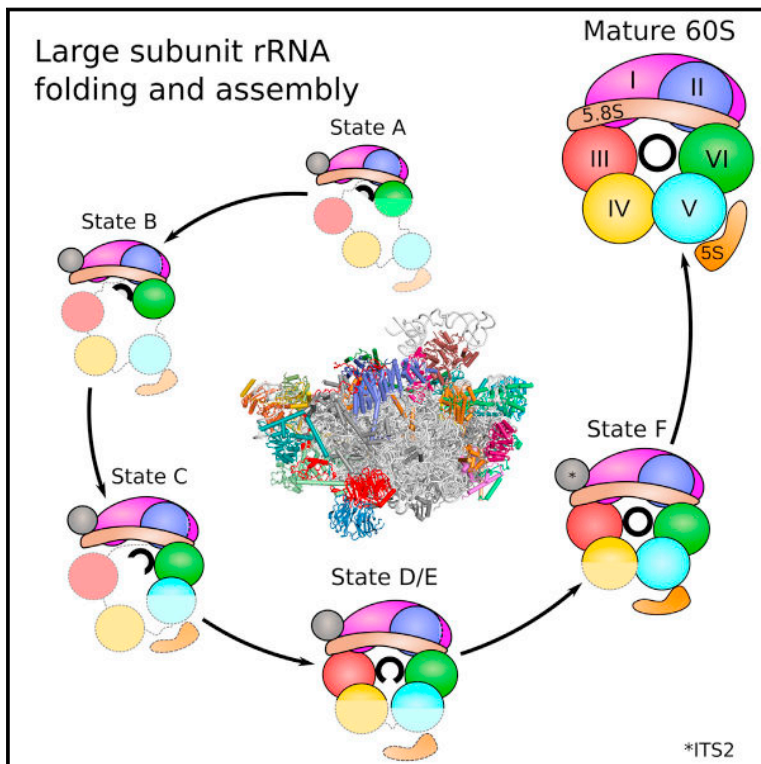
5 Publications of this Dissertation

The following pages contain the 5 publications of this dissertation:

- Kater et al. (2017)
- Thoms et al. (2018)
- Kater et al. (2019)
- Kater et al. (2020b)
- Kater et al. (2020a)

Visualizing the Assembly Pathway of Nucleolar Pre-60S Ribosomes

Graphical Abstract



Authors

Lukas Kater, Matthias Thoms, Clara Barrio-Garcia, ..., Irmgard Sinning, Ed Hurt, Roland Beckmann

Correspondence

beckmann@lmb.uni-muenchen.de

In Brief

Cryo-EM analysis of the architecture of pre-60S ribosomes provides insights into the sequential events and intermediate states critical for ribosome assembly, as well as the functions of many associated factors.

Highlights

- Structures of five nucleolar pre-60S intermediates by cryo-EM
- Assembly factors Nsa1, Mak16, Rpf1, and Rrp1 form a module at the solvent side
- Erb1 acts as a central coordinator at the intersubunit side
- A sequential assembly pathway follows after the 5' to 3' circular formation of pre-rRNA



Visualizing the Assembly Pathway of Nucleolar Pre-60S Ribosomes

Lukas Kater,¹ Matthias Thoms,² Clara Barrio-Garcia,¹ Jingdong Cheng,¹ Sherif Ismail,² Yasar Luqman Ahmed,² Gert Bange,^{2,3,4} Dieter Kressler,^{2,5} Otto Berninghausen,¹ Irmgard Sinning,² Ed Hurt,² and Roland Beckmann^{1,6,*}

¹Gene Center Munich and Center of Integrated Protein Science-Munich (CiPS-M), Department of Biochemistry, Feodor-Lynen-Str. 25, University of Munich, 81377 Munich, Germany

²Biochemie-Zentrum der Universität Heidelberg, 69120 Heidelberg, Germany

³Present address: LOEWE Center for Synthetic Microbiology (SYNMIKRO), 35043 Marburg, Germany

⁴Present address: Department of Chemistry, Philipps-University-Marburg, Hans-Meerwein-Straße, 35043 Marburg, Germany

⁵Present address: Department of Biology, Unit of Biochemistry, University of Fribourg, 1700 Fribourg, Switzerland

⁶Lead Contact

*Correspondence: beckmann@lmb.uni-muenchen.de

<https://doi.org/10.1016/j.cell.2017.11.039>

SUMMARY

Eukaryotic 60S ribosomal subunits are comprised of three rRNAs and ~50 ribosomal proteins. The initial steps of their formation take place in the nucleolus, but, owing to a lack of structural information, this process is poorly understood. Using cryo-EM, we solved structures of early 60S biogenesis intermediates at 3.3 Å to 4.5 Å resolution, thereby providing insights into their sequential folding and assembly pathway. Besides revealing distinct immature rRNA conformations, we map 25 assembly factors in six different assembly states. Notably, the Nsa1-Rpf1-Mak16 module stabilizes the solvent side of the 60S subunit, and the Erb1-Ytm1-Nop7 complex organizes and connects through Erb1's meandering N-terminal extension, eight assembly factors, three ribosomal proteins, and three 25S rRNA domains. Our structural snapshots reveal the order of integration and compaction of the six major 60S domains within early nucleolar 60S particles developing stepwise from the solvent side around the exit tunnel to the central protuberance.

INTRODUCTION

Eukaryotic ribosomes, the protein-synthesizing molecular machines, consist of a small subunit (SSU) (40S) and a large subunit (LSU) (60S), which comprise four ribosomal RNAs (18S, 5S, 5.8S, and 25S/28S) and around 80 ribosomal proteins (RPs). The assembly of ribosomal subunits starts in the nucleolus, where RNA polymerase I transcribes the rRNA precursor (35S pre-rRNA in yeast), from which, after processing and removal of the external and internal transcribed spacers (ETS and ITS), the mature 18S, 5.8S, and 25S rRNAs are generated (Woolford and Baserga, 2013). The pre-rRNA is modified during transcription by small nucleolar ribonucleoproteins (snoRNPs), processed by RNA nucleases, and

assembled with numerous RPs (Turowski and Tollervey, 2015). After endonucleolytic cleavage of the rRNA precursor at site A₂ in yeast, the pre-40S and pre-60S subunits follow separate biogenesis routes.

Co-transcriptional folding and assembly intermediates of pre-ribosomes were first visualized as compact knobs on rDNA-chromatin spreads, representing the 90S pre-ribosome or SSU processome (Grandi et al., 2002; Miller and Beatty, 1969). Here, the modular assembly of the 90S particle provides a scaffold for the domain-wise folding of the 18S precursor rRNA (Chaker-Margot et al., 2017; Kornprobst et al., 2016; Sun et al., 2017). In contrast to the 40S subunit, the architecture of the 60S subunit is more complex with its six highly intertwined domains of the 25S rRNA (Ben-Shem et al., 2011). Around 90 assembly factors (AFs) have been associated with 60S biogenesis (Woolford and Baserga, 2013). Proteomic analysis has revealed that early nucleolar intermediates show a high degree of complexity with respect to AF association and that the number of AFs generally decreases throughout the maturation pathway (Nissan et al., 2002; Wu et al., 2016). During this development, it is thought that the incorporation of RPs occurs hierarchically via the sequential integration of early-, middle-, and late-acting groups of RPs (Gamalinda et al., 2014).

Complex early pre-60S intermediates containing the 27SB pre-rRNA and the 5S rRNA could be isolated by affinity purification methods based on tagged assembly factors, among which Nsa1 yielded a nucleolar pre-60S particle of distinct protein and rRNA composition (Kressler et al., 2008). Notably, these particles contained numerous early-acting AFs, including the conserved Erb1-Ytm1 complex (Kressler et al., 2008). Release of Nsa1 and the Erb1-Ytm1 complex from these particles is mediated through the action of the remodeling AAA-ATPases Rix7 and Rea1, respectively (Bassler et al., 2010; Kressler et al., 2008). To date, however, nothing is known about the structure of such early biogenesis intermediates, and, accordingly, it remains to be determined how pre-60S subunits form and evolve during the first steps of their nucleolar assembly. Major structural transitions are expected to occur during this early phase, as indicated by the finding that the release of the Erb1-Ytm1 complex is linked to the exit of the particle



from the nucleolus to the nucleoplasm (Bassler et al., 2010). Here, another set of AFs associates with these intermediate pre-60S particles, including the Arx1-Alb1 dimer that binds at the already formed ribosomal tunnel exit site (Bradatsch et al., 2012; Leidig et al., 2014; Wu et al., 2016). As there is no structural characterization of any nucleolar intermediate, this nucleoplasmic Arx1-containing particle (also referred to as Arx1 or Nog2 particle) represents the earliest observed pre-60S structure at present. In addition to Arx1, this pre-60S particle is associated with further AFs, including Rsa4, Nog2, and the Rpf2-Rrs1 complex, in the area of the unrotated 5S RNP (Bradatsch et al., 2012; Leidig et al., 2014; Nissan et al., 2002; Ulbrich et al., 2009; Wu et al., 2016) and typically exhibits a landmark structure, called “foot,” consisting of five biogenesis factors (Nop15, Cic1, Nop7, Rlp7, and Nop53) and partially processed ITS2 (Wu et al., 2016). Surprisingly, in this intermediate, the central protuberance (CP) together with the bound 5S RNP (5S rRNA and RPs uL18 and uL5) is stabilized in an immature, 180°-rotated state (Leidig et al., 2014; Wu et al., 2016). However, apart from the CP, several helices on the inter-subunit side and the ITS2, the rRNA within the Arx1 particle has acquired a close-to-mature globular conformation. Prior to nuclear export, the Rix1-Rea1 complex exerts a further remodeling step, likely releasing the Rpf2-Rrs1 complex and resulting in the rotation of the 5S RNP, as well as the release of Rsa4 (Barrio-Garcia et al., 2016; Ulbrich et al., 2009; Wu et al., 2016). Export competence of the particle is achieved in two steps, release of the guanosine triphosphatase (GTPase) Nog2 allows recruitment of the export adaptor Nmd3, whereas Yvh1-binding-mediated release of Mrt4 allows binding of the export receptor Mex67-Mtr2 (Matsuo et al., 2014; Sarkar et al., 2016). Upon exit into the cytoplasm, the pre-60S particle undergoes final maturation, which is mostly dedicated to AF removal and incorporation of the last remaining RPs (Lo et al., 2010). Here, Drg1, a further AAA-type ATPase, is required for the recycling of the assembly factors Rlp24 and Nog1, resulting in an ordered cascade of assembly factor release events (Kappel et al., 2012; Lo et al., 2010; Pertschy et al., 2007). The removal of the export factor Nmd3 is enabled through incorporation of the RP uL16 and the action of the GTPase Lsg1 (Ma et al., 2017; Malyutin et al., 2017). It is thought that in a final step, removal of the anti-association factor Tif6 by the combined action of the Shwachman-Bodian-Diamond syndrome homolog Sdo1 and the elongation factor G homolog Efl1 leads to translationally competent LSU (Menne et al., 2007; Weis et al., 2015).

The known pre-60S structures depict the rRNA to a large extent already in a mature state. As even the nucleoplasmic Arx1 or Nog2 particle only show rRNA at the intersubunit side and the central protuberance in a pre-mature state, the question arises of how the majority of the rRNA folds in preceding nucleolar pre-60S intermediates to adopt a monolithic and intertwined conformation. To elucidate the order of these folding events and the underlying mechanisms, we have performed a cryoelectron microscopy (cryo-EM) analysis of nucleolar pre-60S particles isolated from yeast. This analysis provided insight into the nucleolar pre-60S assembly steps, which allowed us to assign roles to the multiple biogenesis

factors and deduce the principles of rRNA folding during 60S biogenesis.

RESULTS

Cryo-EM Analysis of Stage-Ordered Nucleolar Pre-60S Particles

We selected several biogenesis factors that allow isolation of nucleolar pre-60S particles upon affinity purification following two different strategies. First, we applied the split-tag affinity purification method (based on two different bait proteins, each labeled with a different affinity tag followed by two subsequent affinity purifications) to restrict the pool of assembly intermediates. Second, we aimed to isolate early pre-60S particles via a single bait protein from yeast mutants arresting at, and thus accumulating, a distinct stage during early pre-60S biogenesis.

Following the first strategy, we affinity purified bona fide pre-60S particles from wild-type yeast cells using combinations of tagged early pre-60S assembly factors, the first pair consisting of Nsa1 and Ytm1 (Nsa1-TAP, Flag-Ytm1) and expected to enrich nucleolar pre-60S assembly intermediates, and the second pair of Rix1 and Rpf2 (Rix1-TAP, Rpf2-Flag), which could enrich further progressed pre-60S particles (Figures S1A and S1B). Regarding the mutant approach, we selected the dominant-lethal TAP-tagged Ytm1 E80A allele (Figures S1C and S1D), which allows affinity purification of a distinct pre-60S particle. It harbors a single amino-acid substitution in the N-terminal ubiquitin-like (UBL) domain of Ytm1, and, similar to the complete deletion of the UBL domain, this mutant is impaired in the interaction with the AAA-type ATPase Rea1. Consequently, Rea1 cannot remove the Erb1-Ytm1 complex, thereby blocking further maturation (Bassler et al., 2010). When all these different affinity purified pre-60S particles were analyzed by single-particle cryo-EM and 3D classification, six distinct and stable pre-60S maturation states could be obtained, which in the following will be referred to as states A to F (Figures 1A, S2, and S3). These intermediates were put into a consecutive order (from states A to F), based on the increase of structured rRNA and incorporation of RPs, which are thought to follow a hierarchical assembly pathway (Gamalinda et al., 2014) (Figures 1A and S4). Consistent with our experimental design, the four earliest intermediates (A to D) were isolated via the Nsa1-Ytm1 baits, whereas the Rix1-Rpf2 pair yielded the intermediates of the two later states (E and F). Importantly, only state F pre-60S particles displayed a clearly visible and stably incorporated 5S RNP module. This state represents the previously observed nucleoplasmic pre-60S particle, which can be affinity purified with either Arx1 or Nog2 as bait (Leidig et al., 2014; Wu et al., 2016). Therefore, we used the Arx1/Nog2 particle model as basis for the interpretation of the State F map (Wu et al., 2016). Using the dominant-lethal Ytm1 E80A mutant to affinity purify pre-60S subunits, we indeed observed an enrichment of particles, which are structurally indistinguishable from type E particles derived from wild-type cells (Rix1-TAP/Rpf2-Flag), with only a minor portion of particles resembling earlier intermediates similar to states A–C. Importantly, the state E pre-60S population yielded the highest resolved structure at 3.3 Å average resolution (Figures 1A, S2, and S3).

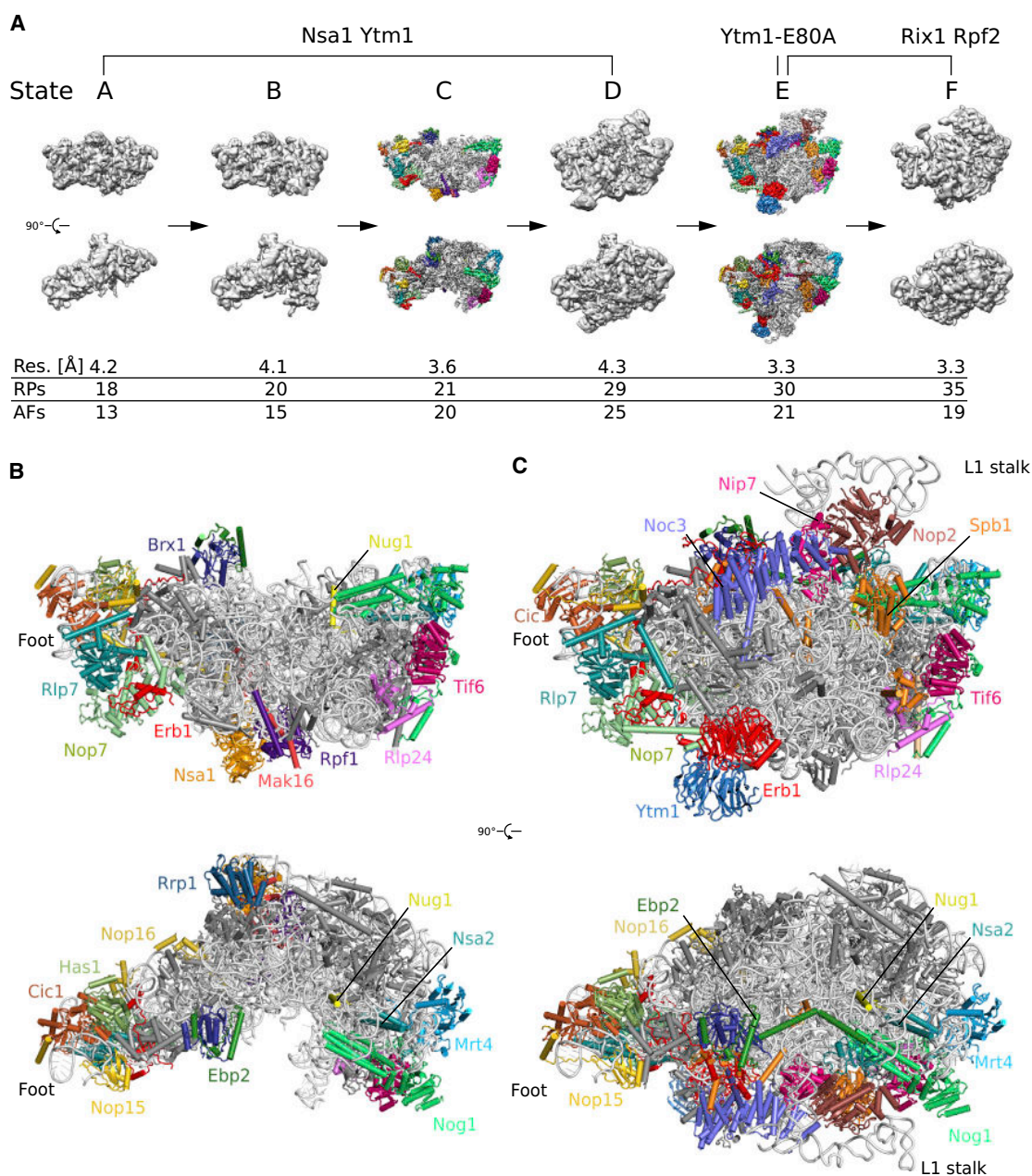


Figure 1. Cryo-EM Structures of Nucleolar Pre-60S Assembly Intermediates

(A) Cryo-EM densities filtered to 10 Å in the case of states A, B, D, and F. Maps of states C and E are filtered to 3.6 Å with the identified biogenesis factors highlighted in color. Below each map, the overall resolution (res.), the number ribosomal proteins (RPs), and assembly factors (AFs), which are stably associated with the core particle and thus are resolved in the cryo-EM structures, are shown. The resolution of state E corresponds to the Ytm1-E80A particle-derived map. (B and C) Front and top views of the model of state C (B) and state E (C). rRNA and RPs are colored in light and dark gray, respectively. Biogenesis factors are highlighted in color. Helices 76–79 of the L1 stalk (C) are shown as backbone only and not included in the deposited model. See also [Figures S2 and S4](#).

Atomic Structure of Early States C and E Pre-60S Particles

We built atomic structures for the two highest resolved pre-60S particles, states C and E, with average resolutions of 3.6 Å and 3.3 Å, respectively. These models comprise a total

of 25 localized ribosome assembly factors, of which 13 were built *de novo*, including Nsa1, Rrp1, Rpf1, Mak16, Erb1, Has1, Nop16, Ebp2, Brx1, Noc3, Nop2, Nip7, and Spb1 ([Figures 1B and S5](#)). The models for Nsa1 and Rrp1 agree nicely with the respective crystal structures, indicating that both

behave as rigid bodies in the pre-60S particles (Figures S6B and S6C).

The nucleolar pre-60S particles in states A–C show a characteristic arch-like morphology. This strongly deviates from the later D, E, and F state particles, which already display a globular shape similar to the mature 60S (Figure S2A). However, states A–C already contain a hallmark structure typically seen on Arx1 or Nog2 particles, termed the “foot,” which is formed by ITS2 rRNA and its associated “A3” cluster factors Cic1/Nsa3, Nop7, Nop15, and Rlp7 (Bradatsch et al., 2012; Leidig et al., 2014; Wu et al., 2016). In contrast to the “foot” in the Arx1 particle, the A–C state particles contain a part of the Erb1 N terminus (amino acid residues 328–400) instead of Nop53 (Figure 1B). More importantly, however, adjacent to the foot, the 5.8S portion of the pre-rRNA and the 25S rRNA domains I and II and the increasing parts of domain VI complete, together with eventually 21 RPs (in state C), the solvent-exposed back side of these pre-60S particles. Strikingly, in state C the polypeptide exit tunnel (PET) and the entire inter-subunit side, including the CP, the peptidyl transferase center, and the L1 stalk, are not yet formed, since domains III and IV and most of domain V of the 25S rRNA are not stably incorporated into the core particle (Figures 1A–1C). Notably, these domains are inevitably tethered to the particle (linked between domains II and VI); however, they are not yet rigidly oriented with respect to the developing core particle. Therefore, we cannot draw any conclusion regarding their intra-domain folding state and association mode of ribosomal and non-ribosomal proteins. However, we can clearly observe how the core particle develops, which apparently starts with the formation of the solvent side of the 60S subunit. Here, a cluster of four AFs—the Nsa1 module—is positioned; it consists of the β -propeller protein Nsa1 (used as a bait), the α -helical protein Rrp1, and the Brix-fold protein Rpf1 with its known interaction partner Mak16 (Baßler et al., 2017; McCann et al., 2015). The Nsa1 module binds the rRNA expansion segment (ES) 7a, which adopts a distinct L-shaped conformation, and thereby interacts with and clamps together rRNA domains I and II (Figure 2). This solvent-side location of Nsa1 explains why failure of its removal during 60S biogenesis, due to an N-terminal deletion in the Rix7 AAA ATPase, still allows the formation of functional 80S ribosomes and polysomes (Kressler et al., 2008). The loop between the fourth and fifth β -blade of Nsa1 (Loop 4D-5A) (Figure 2A) was described to mediate the interaction between the human homologs of Nsa1 (WDR74) and Rix7 (NVL2) (Lo et al., 2017). Yet in yeast, we found that the Nsa1 loop 4D-5A is involved in interactions with ES7a and Mak16; it is therefore not readily accessible for interaction with Rix7 (Figure 2A). Thus, a conformational rearrangement may be required for Rix7-mediated dissociation of Nsa1 from the pre-60S particle.

Another assembly factor of the Nsa1 module, prominently seen in our pre-60S particle, is the Brix protein Rpf1 (Wehner and Baserga, 2002). Notably, its N terminus extends from the solvent side of the particle to a location where later the PET will form and, moreover, binds close to helix H24 of the 25S rRNA and the RP uL24 (Figure 2B). This N-terminal helix remains in place during the further construction of the tunnel until state D, thus it may act as a “place marker” for where the PET will be constructed. After dissociation of the Nsa1 module from the pre-60S

particle, likely triggered by Rix7, the tunnel is seen unoccupied in state E, but becomes filled with the C-terminal extension of Nog1 in state F, where typically Arx1-Alb1 decorate the exit site (Figure 2B) (Bradatsch et al., 2012; Wu et al., 2016). In addition to the aforementioned assembly factors, state C particles already contain a subset of the so-called B-factors: Nog1, Mrt4, Tif6, and Rlp24, which are essential for the later separation of the 27SB precursor into 26S and 7S pre-rRNA (Talkish et al., 2012). These B-factors, together with the N-terminal anchor helices of Nsa2 and Nug1, bind to the side of the pre-60S particle opposing the “foot” (Figure 1B). Notably, although present from state C onward, Nog1’s C-terminal extension, which can reach toward and into the peptide exit tunnel, is not localized at states C–E.

Erb1 Functions as a Multivalent Interaction Hub

In the further matured states D and E, the rRNA domain III with parts of domain IV and additional stretches of domain V of the 25S rRNA become visible after incorporation into the core particle, resulting in the lateral closure and, thus, completion of exit tunnel formation. This correlates with the stable incorporation of nine additional RPs (Figure S4) and five AFs (Nip7, Noc3, Nop2, Spb1, and Ytm1) at the maturing inter-subunit interface of state E, which are not seen in state C (Figure 1). Notably, state E pre-60S particles are very similar to state D particles, except that in state E the Nsa1 module is absent and RP uL15 has been acquired. This suggests that E-type pre-60S particles have undergone the AAA-type ATPase Rix7-mediated dissociation of Nsa1.

A central assembly factor already present on the earliest pre-60S particles is Erb1, for which a large number of biochemical, structural, and genetic data have been obtained in previous studies (Konikkat et al., 2017; Miles et al., 2005; Thoms et al., 2016; Wegrecki et al., 2015). It is composed of an N-terminal region containing the nuclear localization signal, a long N-terminal stretch, and a C-terminal β -propeller domain (Konikkat et al., 2017; Pestov et al., 2001; Thoms et al., 2016; Wegrecki et al., 2015). Whereas part of its N terminus is already visible in states A–C, most of Erb1 (amino acids 125 to 807 of 807) can only be seen in the states D and E particles (Figure 3A). Here, the Erb1 β -propeller binds at the edge of the maturing inter-subunit side, in close proximity to the RPs eL27 and eL38, rRNA helix H58, and ES20a and ES27 (Figure 3). Notably, Erb1 contacts its nearby interaction partner Ytm1, as previously observed in the crystal structure of the *Chaetomium thermophilum* Erb1-Ytm1 complex (Thoms et al., 2016; Wegrecki et al., 2015). Ytm1 contains an N-terminal domain, called MIDO (MIDAS-interacting domain) or UBL domain, which binds the MIDAS (metal ion-dependent adhesion site) domain of Rea1 during the first Rea1 remodeling step (Bassler et al., 2010). However, due to flexibility the MIDO is not well resolved in state D and E. Based on the crystal structure of Ytm1 (Thoms et al., 2016; Wegrecki et al., 2015), the Ytm1-UBL domain is strategically located at the distal edge of the pre-60S particle, thus allowing access for the Rea1 MIDAS-domain and enabling the Rea1-mediated removal of the Ytm1-Erb1 heterodimer from the pre-ribosomal particle.

Following the Erb1 N-terminal tail meandering over the pre-60S particle reveals a number of different AFs contacts on the early pre-60S particles (states A–E). In state D and E, it

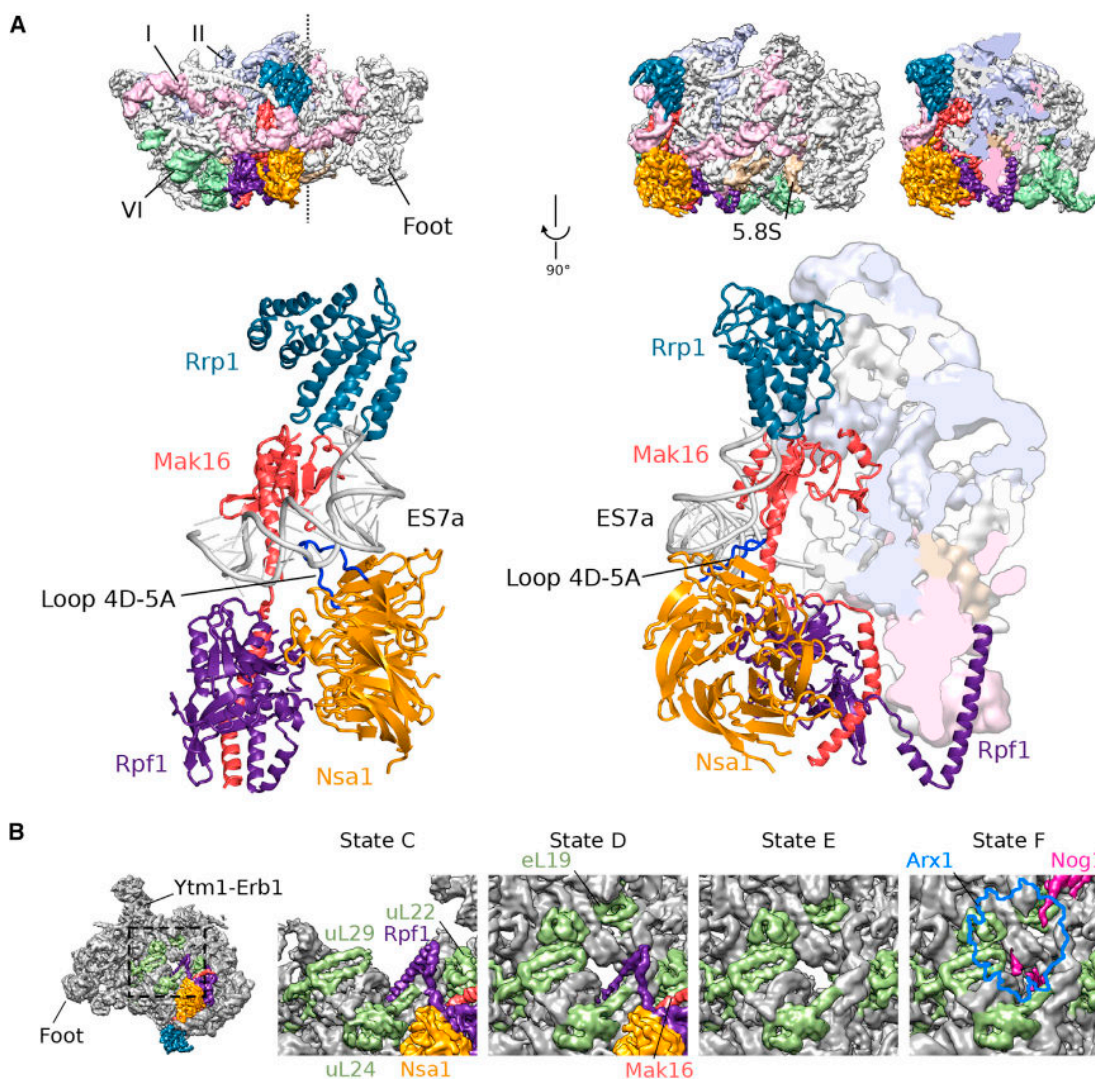


Figure 2. Nsa1 Module and Formation of the PET

(A) Binding site of the Nsa1 module consisting of Mak16 (red), Nsa1 (orange), Rpf1 (purple), and Rrp1 (dark blue) bound to ES7a (light gray). A back and side view of the particle is shown. Densities for rRNA domains I, II, and VI as well as the 5.8S rRNA are, respectively, colored in light pink, purple, green, and beige. The vertical dashed line through the particle in the upper left view indicates the clipping plane for the cropped density. Loop 4D-5A, suggested to interact with the AAA-ATPase Rix7, is indicated in blue.

(B) Maturation of the PET from states C–F. The N terminus of Rpf1 occupies the tunnel in states A–D; state E shows a free tunnel; and state F displays the C terminus of Nog1 residing in the tunnel.

extends toward the base of the foot, where it interacts with Nop7 and forms a short two-stranded intermolecular β sheet with the N terminus of Rlp7. The Erb1 tail then wraps along the back side of the “foot” to the top of the pre-60S particle, where it comes in contact with Nop16, the helicase Has1, and RP eL36. From there, it proceeds to the rather immature inter-subunit side, where it interacts with further four AFs: the C terminus of the Spb1 methyltransferase (Kressler et al., 1999; Lapeyre and Purushothaman, 2004), Noc3, Ebp2 and its binding partner Brx1. In this way, the Erb1 N-terminal extension coordinates three 25S rRNA domains (I, III, and IV), three ribosomal L-proteins, and nine different biogenesis factors, in total reaching

around half of the pre-60S particle (Figures 3A–3C). Thus, our cryo-EM structures explain at molecular level many of the described *in vivo* effects of the A3-factor Erb1 and its partner Ytm1, and clarify its key role as coordination hub in the early nucleolar pre-60S particles of states D and E.

Notably, although the state E pre-60S particle is well on its way toward maturation by compaction of domains III, IV, and V, it is striking to see that the CP (i.e., the area around 5S RNP in the mature 60S) has not developed at all, and that the L1-stalk (rRNA H74–H79) exhibits a strong displacement from its mature position in the 60S subunit to a stable immature conformation in the pre-60S particle. Specifically, a rotation of the L1 stalk at

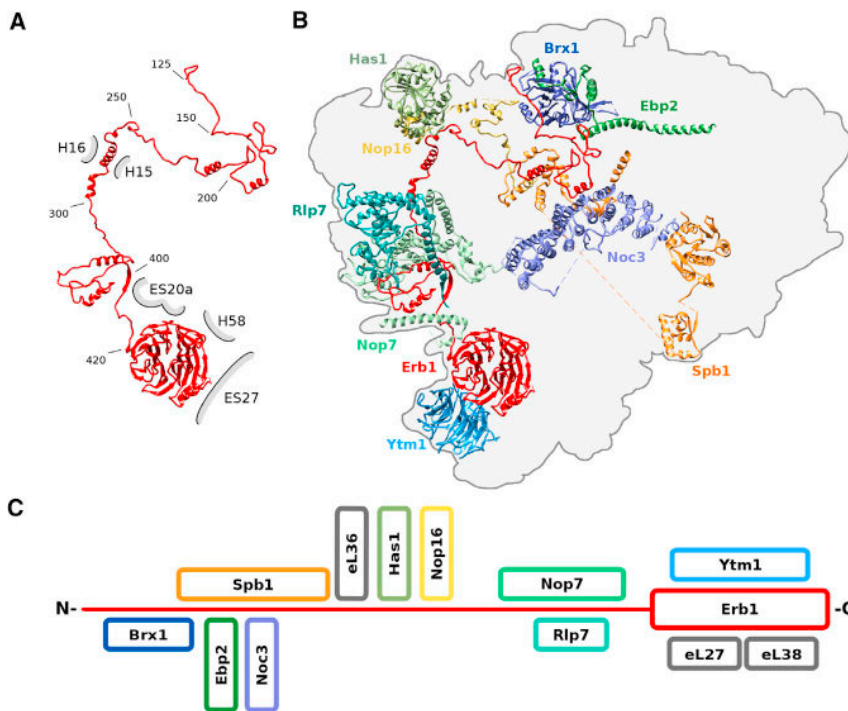


Figure 3. Erb1 Functions as a Multivalent Interaction Hub

(A) Overview of the Erb1 domain architecture showing the extended N terminus and the doughnut-shaped WD40 repeat domain. Interactions with rRNA are indicated in gray.

(B) Localization of Erb1 in the state E particle (gray silhouette) with interacting AFs.

(C) Schematic overview of protein contacts between Erb1 and other AFs and RPs.

Sequential Incorporation of the Six 25S rRNA Domains into the Developing Pre-60S Core Particle

The 25S rRNA can be divided into six domains (I–VI) that assemble into a monolithic compact mature 60S subunit (Ben-Shem et al., 2011). We analyzed the immature pre-60S states A–F to derive the most plausible order of 25S rRNA domain folding and compaction, when transiting from state A to F (Figure 5).

The very early state A pre-60S particle shows density only for 5.8S rRNA, ITS2, and 25S rRNA domain I, whereas 25S rRNA domains II and VI are only partly

visible and domains III to V are not at all visible. Structure-wise, this corresponds to the “foot” and the adjacent portion of the solvent-exposed (back) side of the pre-60S particle. Upon progression to state B, the solvent side becomes enlarged with the full incorporation of domain VI. Upon further progression to state C, the additional folding of helices H42–H44 of domain II and of helices H89–H91 of domain V can be seen. As maturation progresses further to state D, the PET and the tunnel exit site are formed, with the stable folding of domain III and stabilization of the L1 stalk in its premature state. States D and E show very similar rRNA conformation, except for the 50-nt-long ES7a, which is only rigidly incorporated up to state D particles, stabilized by the Nsa1 module. As the L1 stalk moves into a mature-like position in state F, domains IV and V and the rotated 5S RNP form additional domains at the inter-subunit face and the immature CP (Leidig et al., 2014; Wu et al., 2016). Notably, the 5S RNP, comprising 5S rRNA, uL5, and uL18, and its assembly factors Rpf2 and Rrs1 are all present in nucleolar pre-60S particles affinity purified via the Nsa1 bait (Kressler et al., 2008) or in our early pre-60S particles (corresponding to states A–D), obtained via the Nsa1-Ytm1 split-tag approach (see above) (Figure S1). This suggests that the 5S RNP associates from very early on with the nucleolar pre-60S particles, before it becomes stably incorporated as domain V into the developing pre-60S core particle, which is prior to formation of the CP.

the base of helix H74 is required to bring this hallmark structure of the large subunit from its outward conformation to the mature position. Interestingly, the immature position of rRNA helices H76 to H79 is similar to the immature non-rotated location of the 5S rRNP in the later Arx1 particle (Leidig et al., 2014) (Figures 1 and 4). The L1 stalk RNA is chaperoned and kept in this unusual conformation by a set of five AFs, consisting of the C terminus of Ebp2, Noc3, the methyltransferase domain of Nop2 (Sharma et al., 2013) its binding partner Nip7 (Talkish et al., 2012), and the C-terminal β -barrel domain of Nsa2. As a consequence, accommodation of the entire rRNA segment, later forming the L1 stalk, into the conformation observed in the further progressed F state particles (also Arx1 particles) is prevented (Bradatsch et al., 2012; Leidig et al., 2014; Wu et al., 2016). Thus, a set of factors, including Nip7, Nop2, Noc3, and Ebp2, has to dissociate from the developing pre-60S particle before the L1 stalk domain can adopt its mature position. Importantly, the E state structure reveals how the rearrangement of the L1-stalk toward a more mature conformation as seen in state F particles is linked to distinct changes in the “foot” structure (Figures 4C and 4D). Removal of Erb1-Ytm1 from the pre-60S particle by Rea1 will also disrupt a small antiparallel β sheet between Erb1 and Rlp7, which in turn allows the adjoining C-terminal α helix of Rlp7 to rotate toward the “foot.” One long distance effect of this β sheet splitting is that the rotation of the entire L1 stalk becomes possible, which otherwise would clash with Rlp7 via its rRNA ES31. Another consequence is that the exosome recruiting factor Nop53 (Thoms et al., 2015; Wu et al., 2016) can be recruited to the position previously occupied by Erb1 (Figures 4C and 4D), explaining why 7S pre-rRNA processing by the nuclear exosome can only occur after the first Rea1 remodeling step.

Finally, our structures agree with the postulated hierarchical incorporation of ribosomal L-proteins into the newly forming 60S subunit (Gamalinda et al., 2014). We observe that many new RPs become stably incorporated into the core particle upon rRNA compaction, from 18 in the earliest particle (state A)

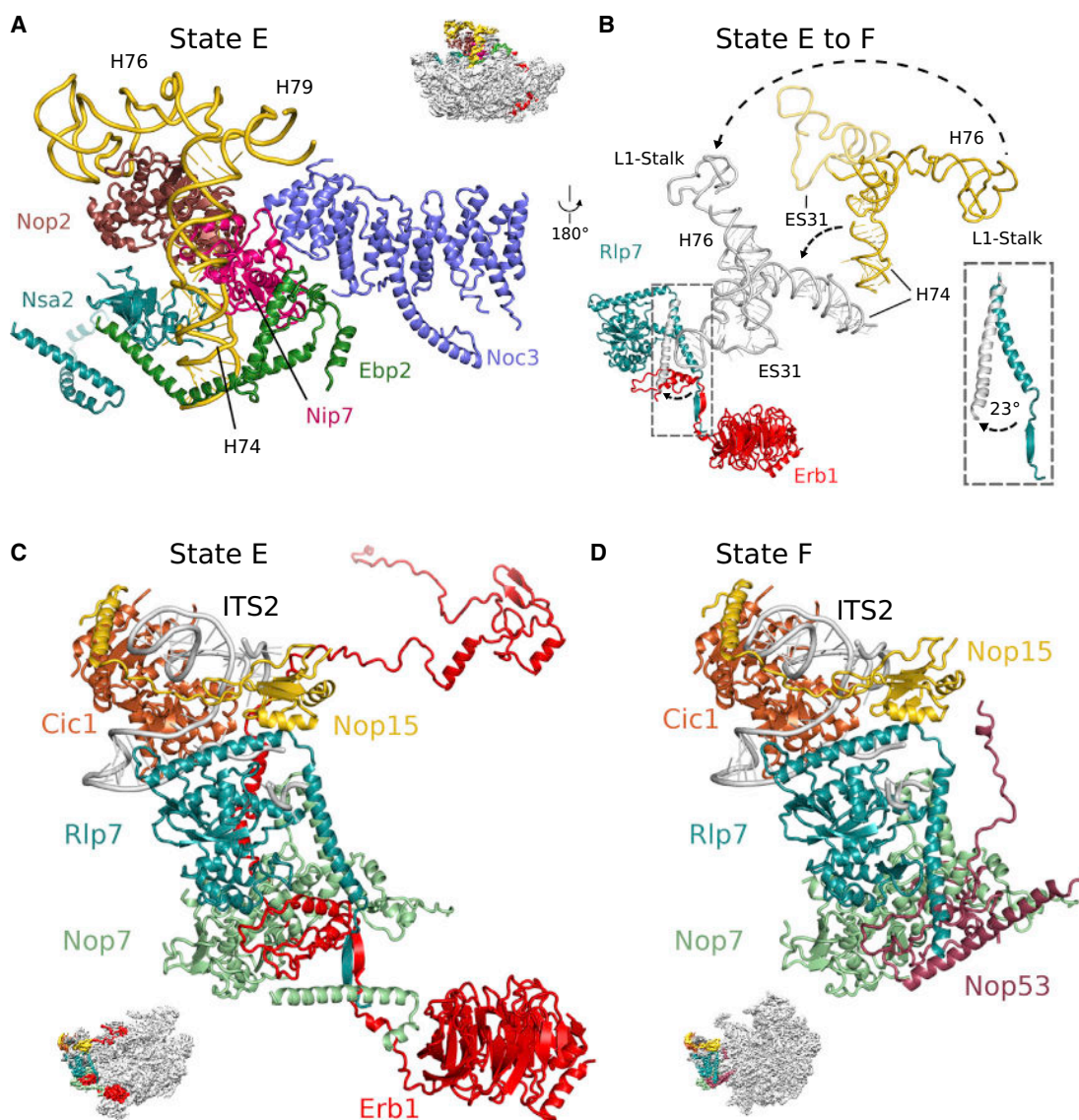


Figure 4. Maturation of the L1-Stalk Segment Is Linked to “Foot” Remodeling

(A) The L1 segment (rRNA helices H74–H79, gold) is stabilized in a pre-mature conformation by a set of AFs, including Ebp2 (green), Nip7 (magenta), Noc3 (purple), Nop2 (brown), and Nsa2 (turquoise).

(B) The L1 segment undergoes large-scale conformational changes during maturation, which requires an outward rotation of the Rlp7 N-terminal α helix. The conformations as observed in states D and E of the L1 segment and Rlp7 are colored in gold and turquoise. Gray denotes their conformation as observed in state F.

(A and B) Helices H76–H79 are displayed as backbone only and are not included in the provided model. In states D and E, the position of ES31 (gold, semi-transparent, backbone only) is indicated based on connectivity to helix H79, but not observed in the respective maps because of flexibility.

(C and D) Structure of the “foot” in states E (C) and F (D). In state F, Nop53 takes the place of Erb1, resulting in a conformational change in the N terminus of Rlp7. The molecular interpretation of state F is based on the Arx1/Nog2 particle model (PDB: 3JCT) (Wu et al., 2016).

to the 35 in the latest particle (state F) (Figure S4). Along the maturation trajectory, the AF composition varies in complexity, with distinct sets of AFs, such as the Nsa1 module, being present only for a certain assembly interval in a subset of states (Figure 5C). Altogether, these data indicate that folding and stable integration of rRNA domains into the developing 60S core particle proceeds in a non-transcriptional yet linear series of steps by first forming the solvent-exposed side like an exoskeleton, fol-

lowed by formation of the exit tunnel and the inter-subunit interface at last.

DISCUSSION

Function of Assembly Factors Nsa1, Erb1, and Rea1

The Nsa1 module was identified on the early pre-60S particles (states A–D) at a position where it clamps the early-forming

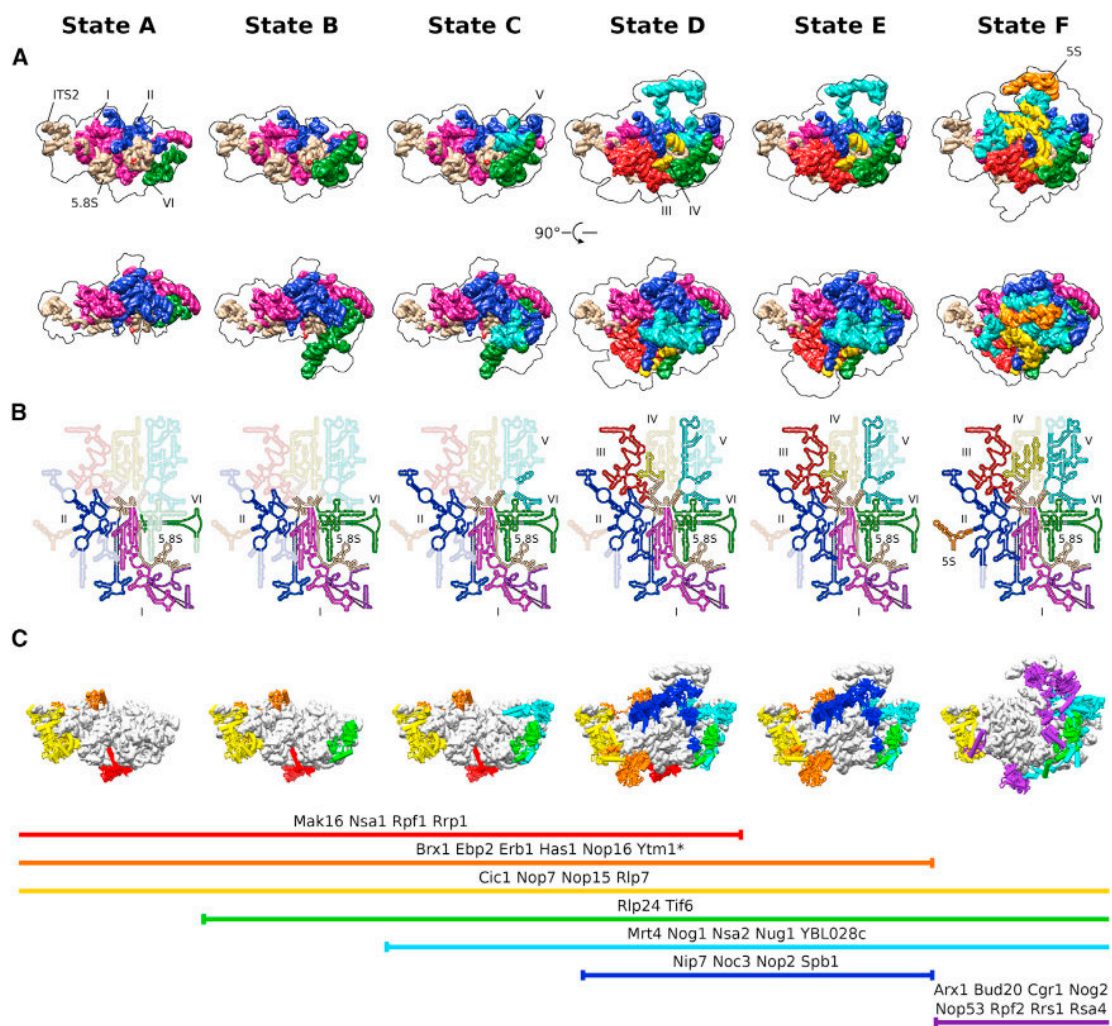


Figure 5. Sequential Incorporation of the rRNA Domains into a Developing Pre-60S Core Particle

(A) Front and top views of structural rRNA representations based on Chimera molmaps for states A–F. The molmaps are color-coded by the rRNA domains: domain 0, ITS2, and the 5.8S rRNA portions are displayed in light brown; the 5S rRNA is in orange; domains I–VI are in magenta, blue, red, yellow, cyan, and green, respectively.

(B) Secondary structure plots indicating folded rRNA for each state following the same color-code used in (A).

(C) Schematic representation of AFs associated with all states. Clustering and coloration is based on the time point of stable association and dissociation from the maturing particle as indicated by the horizontal lines. (*) Ytm1 was clustered with Erb1, as the two proteins form a tight complex (Thoms et al., 2016; Wegrecki et al., 2015), and it was used as a bait protein to purify states A–D. It is therefore clear that Ytm1 is present in these states (A–D), but not yet stably localized in the core particle.

The molecular interpretation of state F is based on the Arx1/Nog2 particle model (PDB: 3JCT) (Wu et al., 2016).

rRNA domains I and II and marks the future PET construction site, explaining why the Nsa1 module has a key role in the early steps of 60S assembly. Many interactions involving the Nsa1 module are clustered at the rRNA expansion segment ES7a. Besides ES7a, ES27 also has been observed to interact with AFs, namely with the Erb1-Ytm1 complex in the nucleolus and Arx1 during later stages of 60S assembly (Bradatsch et al., 2012; Greber et al., 2012; Leidig et al., 2014; Wu et al., 2016). Therefore, our findings support the importance of ES in eukaryotic rRNA for ribosomal assembly (Ramesh and Woolford, 2016), likely by acting as a binding hub for assembly factors and eukaryote-specific exten-

sions of RPs (Bradatsch et al., 2012; Granneman et al., 2011; Greber et al., 2012; Leidig et al., 2014; Wu et al., 2016).

In addition to the Nsa1 module, we identified Erb1 as a key connector, which wraps around the maturing 60S subunit with its long N-terminal extension, thereby establishing a multitude of interactions with different rRNA domains, AFs, and RPs (Figure 3). Our structural data explain why deletions in the Erb1 N-terminal extension caused many different *in vivo* defects in 60S biogenesis (Konikkat et al., 2017).

The C-terminal β -propeller domain of Erb1 forms a tight complex with Ytm1 and removal of the Erb1-Ytm1 heterodimer from

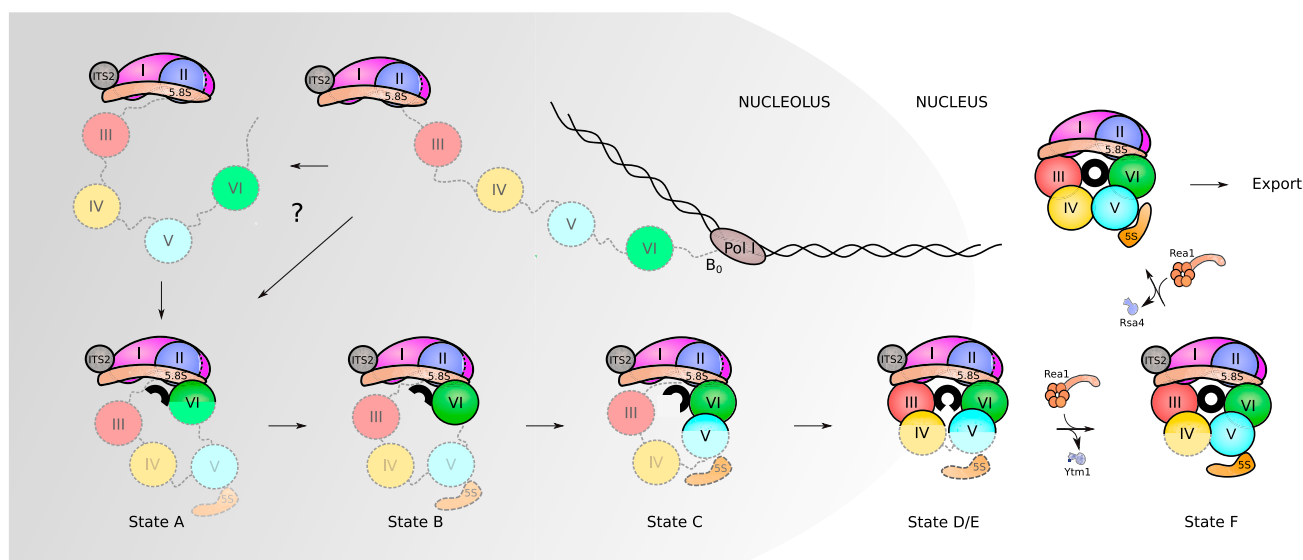


Figure 6. Assembly Sequence of the Pre-rRNA Domains

Assembly of RPs and AFs to the nascent 35S rRNA precursor starts co-transcriptionally. Very early, the pre-rRNA is circularized as domain VI binds to domains I and II and the 5.8S portion of the precursor rRNA. The formation of the PET (displayed here as a black circle) starts with this circularization. Its maturation progresses as rRNA domains fold following this order: VI, V, III, and IV. Full assembly of the PET is only achieved when domain V is completely folded as observed in state F. After that, only few nucleoplasmic steps need to occur before the particles are exported to the cytoplasm, where they undergo final maturation.

the early pre-60S particles by Rea1 is an essential remodeling step to induce the transition from the nucleolus to the nucleoplasm (Bassler et al., 2010). While investigating the structure of the pre-60S particle isolated from the dominant-lethal Ytm1 E80A mutant accumulating in state E, we found that this intermediate is identical to wild-type pre-60S particles split-tag affinity purified via Rix1-TAP/Rpf2-Flag (state E), indicating that the impaired release of the Erb1-Ytm1 complex blocks further maturation, with the L1-stalk domain stabilized by several AFs in its pre-translocation conformation. To overcome this immature state and allow rRNA helices H74-H79 to properly rearrange, dissociation of multiple factors (Ebp2, Noc3, the Nop2-Nip7 sub-complex, and the C terminus of Spb1) and remodeling of Rlp7 are required (Figure 4). As many of these factors directly interact with Erb1, we suggest that the timely release of Erb1-Ytm1 is the trigger for the observed large-scale rearrangement at the inter-subunit face that eventually leads to the stabilization of rRNA domains IV and V (as observed in state F). Notably, a related restructuring step from a stabilized immature rRNA conformation occurs during the 180° rotation of the 5S rRNA on a later pre-60S particle, which was suggested to be part of a checkpoint control (Barrio-Garcia et al., 2016; Wu et al., 2016). Thus, it is intriguing that these two large-scale rRNA reorganization steps during 60S biogenesis rely on Rea1 AAA-type ATPase, which apparently facilitates the transition from one state characterized by a stabilized immature rRNA conformation (of the L1 domain and 5S RNP, respectively) to the next, more mature state. For the remodeling step allowing 5S RNP rearrangement, the Rix1-Rea1 complex was found to bind at the inter-subunit surface and the CP (Barrio-Garcia et al., 2016). Interestingly, the structural landscape of this area is completely different in the nucleolar pre-60S particles. Nevertheless, Rix1

as a bait can be used to purify nucleolar state E particles (Figures 1 and S1). This suggests that Rix1 might also be involved in the nucleolar Rea1 remodeling step. Taken together and considering the distinct positions of the Rea1 target proteins Ytm1 and Rsa4, Rea1 appears to employ two distinct interaction modes with pre-60S particles.

Early 60S Assembly Employs a Sequential rRNA Folding Pathway

The diverse structural states observed in the nucleolar pre-60S particles are likely to be of physiological relevance since they were affinity purified via functional bait proteins from wild-type-like yeast cells (Figures S1A and S1B). Analyzing these states provided mechanistic insight into how the six rRNA domains (I to VI) are compacted and subsequently decorated with a number of ribosomal L-proteins, finally leading to monolithic 60S core particles. Our structural data do not point to parallel 60S assembly pathways, as suggested for bacterial 50S subunits (Davis et al., 2016). However, this previous study was based on 50S assembly intermediates obtained from bacterial cells, in which the early RP bL17 was depleted, causing a severe growth defect and a 20-fold reduced ribosome assembly rate. Hence, the isolated 50S assembly intermediates may have used alternative assembly pathways for compensation. Importantly, however, there are major kingdom-specific differences between eukaryotic and bacterial ribosome assembly, which is illustrated by the almost complete lack of ribosomal AFs in the observed bacterial pre-50S intermediates (Davis et al., 2016).

During the earliest steps of 60S assembly, the different rRNA domains may already have folded into their secondary structures and recruited the earliest ribosomal L-proteins to these sites, which in consequence may stabilize first tertiary folds. For

example, nucleolar pre-60S particles purified via Nsa1 contain already the 5S RNP, but it can only be seen as a structurally distinct entity in the 60S core when reaching state F (Arx1/Nog2 particle). Therefore, when analyzing and interpreting ribosomal assembly intermediates, one has to distinguish between initial rRNA secondary structure formation, partial tertiary structure construction, ordered incorporation into the core particle, and, eventually, condensation into a fully mature conformation. Similarly, RPs may already bind early during the assembly process, but become part of the core particle only later, and when absent could prevent further maturation. In the past, different approaches have been used to follow the consecutive steps in 60S assembly, e.g., by using truncated rDNA transcripts (Chen et al., 2017) or by depletion of specific RPs (Davis et al., 2016; Gamalinda et al., 2014). However, blocking formation of full-length rRNA particles, as in the first case, may lead to kinetic off-path intermediates, and the absence of a given RP, as in the second case, can identify its rate limiting role during 60S assembly, but without a clear connection to its initial or later interaction characteristics in the evolving particle.

On the basis of these considerations, we propose a model for the early structural assembly of the 60S subunit. A hallmark of this model is that in the nucleolus, after circularization of rRNA domains, early 60S assembly into a growing core particle is carried out in a sequential fashion (Figure 6): as RNA-polymerase-I-driven transcription of the 35S pre-rRNA proceeds, fast secondary structure formation and assembly of first AFs and RPs is thought to begin co-transcriptionally. However, instead of following the transcriptional sequence, circularization of the pre-rRNA is one of the first steps in the formation of a rigid core structure, as only the 5.8S portion, ITS2, and domains I and II and partially domain VI are folded in the earliest observed intermediate (state A). Thus, initially the solvent-exposed back side of the LSU forms like an exoskeleton and construction proceeds by formation of the exit tunnel, which is in agreement with a previously suggested model of hierarchical folding based on RP depletion phenotypes (Gamalinda et al., 2014). Although the very late-folding peptidyl transferase center is the evolutionary oldest part of the ribosome, it is likely that folding the solvent side first brings the advantage of providing a stable scaffold for the developing 60S subunit.

STAR★METHODS

Detailed methods are provided in the online version of this paper and include the following:

- **KEY RESOURCES TABLE**
- **CONTACT FOR REAGENT AND RESOURCE SHARING**
- **EXPERIMENTAL MODEL AND SUBJECT DETAILS**
 - Plasmid constructs and yeast strains
- **METHOD DETAILS**
 - Affinity purifications from *S. cerevisiae*
 - Protein production, crystallization and structure determination
 - CRAC analysis
 - Cryo-electron microscopy
 - Image processing
 - Model building and refinements

- **QUANTIFICATION AND STATISTICAL ANALYSES**
- **DATA AND SOFTWARE AVAILABILITY**
 - Accession codes

SUPPLEMENTAL INFORMATION

Supplemental Information includes six figures and five tables and can be found with this article online at <https://doi.org/10.1016/j.cell.2017.11.039>.

ACKNOWLEDGMENTS

We thank S. Rieder for preparation of Cryo-EM grids; T. Becker for critical input on the manuscript; A. Heuer and the Leibniz Rechenzentrum for support with HPC infrastructure; and J. Kopp and C. Siegmann from the BZH/CellNetworks crystallization platform. This work was supported by grants from the German Research Council (QBM, GRK 1721, FOR 1805, and SFB646 to R.B.; HU363/10-5 and HU363/12-1 to E.H.; SFB638, the Leibniz Programme and the Cluster of Excellence/CellNetworks Ectop1 to I.S.; and GRK1188 to M.T.). This work was also supported by CellNetworks Ectop1 and the Leibniz Programme (to I.S.). I.S. and E.H. are investigators of the Cluster of Excellence/CellNetworks. R.B. acknowledges support from the Center for Integrated Protein Science (CIPS-M) and the European Research Council (advanced grant CRYOTRANSLATION). L.K. was supported by a DFG fellowship through the Graduate School of Quantitative Biosciences Munich (QBM).

AUTHOR CONTRIBUTIONS

R.B., E.H., M.T., and L.K. designed this study and the experiments. Preparation of cryo-EM samples was performed by M.T. Cryo-EM data were collected by O.B. and processed by L.K. Model building was performed by L.K. and J.C. and C.B.-G. assisted. Crystal structure determination of Nsa1 and Rrp1 was performed by G.B., D.K., Y.L.A., and I.S. CRAC analysis was performed by S.I., E.H., R.B., and M.T., and L.K. interpreted the results. E.H., R.B., M.T., C.B.-G., and L.K. wrote the manuscript. All authors discussed the results and commented on the manuscript.

DECLARATION OF INTERESTS

All authors declare no competing interests.

Received: June 23, 2017

Revised: October 13, 2017

Accepted: November 20, 2017

Published: December 14, 2017

REFERENCES

- Afonine, P.V., Grosse-Kunstleve, R.W., Echols, N., Headd, J.J., Moriarty, N.W., Mustyakimov, M., Terwilliger, T.C., Urzhumtsev, A., Zwart, P.H., and Adams, P.D. (2012). Towards automated crystallographic structure refinement with phenix.refine. *Acta Crystallogr. D Biol. Crystallogr.* **68**, 352–367.
- Amunts, A., Brown, A., Bai, X.C., Ll acer, J.L., Hussain, T., Emsley, P., Long, F., Murshudov, G., Scheres, S.H.W., and Ramakrishnan, V. (2014). Structure of the yeast mitochondrial large ribosomal subunit. *Science* **343**, 1485–1489.
- Bai, X.C., Fernandez, I.S., McMullan, G., and Scheres, S.H. (2013). Ribosome structures to near-atomic resolution from thirty thousand cryo-EM particles. *eLife* **2**, e00461.
- Barrio-Garcia, C., Thoms, M., Flemming, D., Kater, L., Berninghausen, O., Ba ler, J., Beckmann, R., and Hurt, E. (2016). Architecture of the Rix1-Rea1 checkpoint machinery during pre-60S-ribosome remodeling. *Nat. Struct. Mol. Biol.* **23**, 37–44.
- Bassler, J., Kallas, M., Pertschy, B., Ulbrich, C., Thoms, M., and Hurt, E. (2010). The AAA-ATPase Rea1 drives removal of biogenesis factors during multiple stages of 60S ribosome assembly. *Mol. Cell* **38**, 712–721.

- Baßler, J., Ahmed, Y.L., Kallas, M., Kornprobst, M., Calviño, F.R., Gnädig, M., Thoms, M., Stier, G., Ismail, S., Kharde, S., et al. (2017). Interaction network of the ribosome assembly machinery from a eukaryotic thermophile. *Protein Sci.* **26**, 327–342.
- Ben-Shem, A., Garreau de Loubresse, N., Melnikov, S., Jenner, L., Yusupova, G., and Yusupov, M. (2011). The structure of the eukaryotic ribosome at 3.0 Å resolution. *Science* **334**, 1524–1529.
- Bradatsch, B., Leidig, C., Granneman, S., Gnädig, M., Tollervey, D., Böttcher, B., Beckmann, R., and Hurt, E. (2012). Structure of the pre-60S ribosomal subunit with nuclear export factor Arx1 bound at the exit tunnel. *Nat. Struct. Mol. Biol.* **19**, 1234–1241.
- Brown, A., Long, F., Nicholls, R.A., Toots, J., Emsley, P., and Murshudov, G. (2015). Tools for macromolecular model building and refinement into electron cryo-microscopy reconstructions. *Acta Crystallogr. D Biol. Crystallogr.* **71**, 136–153.
- Chaker-Margot, M., Barandun, J., Hunziker, M., and Klinge, S. (2017). Architecture of the yeast small subunit processome. *Science* **355**, 355.
- Chen, V.B., Arendall, W.B., 3rd, Headd, J.J., Keedy, D.A., Immormino, R.M., Kapral, G.J., Murray, L.W., Richardson, J.S., and Richardson, D.C. (2010). MolProbity: all-atom structure validation for macromolecular crystallography. *Acta Crystallogr. D Biol. Crystallogr.* **66**, 12–21.
- Chen, W., Xie, Z., Yang, F., and Ye, K. (2017). Stepwise assembly of the earliest precursors of large ribosomal subunits in yeast. *Nucleic Acids Res.* **45**, 6837–6847.
- Cowtan, K. (2006). The Buccaneer software for automated model building. 1. Tracing protein chains. *Acta Crystallogr. D Biol. Crystallogr.* **62**, 1002–1011.
- Davis, J.H., Tan, Y.Z., Carragher, B., Potter, C.S., Lyumkis, D., and Williamson, J.R. (2016). Modular assembly of the bacterial large ribosomal subunit. *Cell* **167**, 1610–1622.e15.
- de Sanctis, D., Beteva, A., Caserotto, H., Dobias, F., Gabadinho, J., Giraud, T., Gobbo, A., Guijarro, M., Lentini, M., Lavault, B., et al. (2012). ID29: a high-intensity highly automated ESRF beamline for macromolecular crystallography experiments exploiting anomalous scattering. *J. Synchrotron Radiat.* **19**, 455–461.
- Emsley, P., Lohkamp, B., Scott, W.G., and Cowtan, K. (2010). Features and development of Coot. *Acta Crystallogr. D Biol. Crystallogr.* **66**, 486–501.
- Evans, P.R., and Murshudov, G.N. (2013). How good are my data and what is the resolution? *Acta Crystallogr. D Biol. Crystallogr.* **69**, 1204–1214.
- Gamalinda, M., Ohmayer, U., Jakovljevic, J., Kumcuoglu, B., Woolford, J., Mbom, B., Lin, L., and Woolford, J.L., Jr. (2014). A hierarchical model for assembly of eukaryotic 60S ribosomal subunit domains. *Genes Dev.* **28**, 198–210.
- Grandi, P., Rybin, V., Bassler, J., Petfalski, E., Strauss, D., Marzoch, M., Schäfer, T., Kuster, B., Tschöchner, H., Tollervey, D., et al. (2002). 90S pre-ribosomes include the 35S pre-rRNA, the U3 snoRNP, and 40S subunit processing factors but predominantly lack 60S synthesis factors. *Mol. Cell* **10**, 105–115.
- Granneman, S., Kudla, G., Petfalski, E., and Tollervey, D. (2009). Identification of protein binding sites on U3 snoRNA and pre-rRNA by UV cross-linking and high-throughput analysis of cDNAs. *Proc. Natl. Acad. Sci. USA* **106**, 9613–9618.
- Granneman, S., Petfalski, E., and Tollervey, D. (2011). A cluster of ribosome synthesis factors regulate pre-rRNA folding and 5.8S rRNA maturation by the Rat1 exonuclease. *EMBO J.* **30**, 4006–4019.
- Greber, B.J., Boehringer, D., Monteliese, C., and Ban, N. (2012). Cryo-EM structures of Arx1 and maturation factors Rei1 and Jji1 bound to the 60S ribosomal subunit. *Nat. Struct. Mol. Biol.* **19**, 1228–1233.
- Janke, C., Magiera, M.M., Rathfelder, N., Taxis, C., Reber, S., Maekawa, H., Moreno-Borchart, A., Doenges, G., Schwob, E., Schiebel, E., and Knop, M. (2004). A versatile toolbox for PCR-based tagging of yeast genes: new fluorescent proteins, more markers and promoter substitution cassettes. *Yeast* **21**, 947–962.
- Kabsch, W. (2014). Processing of X-ray snapshots from crystals in random orientations. *Acta Crystallogr. D Biol. Crystallogr.* **70**, 2204–2216.
- Kappel, L., Loibl, M., Zisser, G., Klein, I., Fruhmann, G., Gruber, C., Unterweger, S., Rechberger, G., Pertschy, B., and Bergler, H. (2012). Rlp24 activates the AAA-ATPase Drg1 to initiate cytoplasmic pre-60S maturation. *J. Cell Biol.* **199**, 771–782.
- Kelley, L.A., Mezulis, S., Yates, C.M., Wass, M.N., and Sternberg, M.J.E. (2015). The Phyre2 web portal for protein modeling, prediction and analysis. *Nat. Protoc.* **10**, 845–858.
- Kimanius, D., Forsberg, B.O., Scheres, S.H.W., and Lindahl, E. (2016). Accelerated cryo-EM structure determination with parallelisation using GPUs in RELION-2. *eLife* **5**, 5.
- Konikkat, S., Biedka, S., and Woolford, J.L., Jr. (2017). The assembly factor Erb1 functions in multiple remodeling events during 60S ribosomal subunit assembly in *S. cerevisiae*. *Nucleic Acids Res.* **45**, 4853–4865.
- Kornprobst, M., Turk, M., Kellner, N., Cheng, J., Flemming, D., Koš-Braun, I., Koš, M., Thoms, M., Berninghausen, O., Beckmann, R., and Hurt, E. (2016). Architecture of the 90S Pre-ribosome: a structural view on the birth of the eukaryotic ribosome. *Cell* **166**, 380–393.
- Kressler, D., Rojo, M., Linder, P., and Cruz, J. (1999). Spb1p is a putative methyltransferase required for 60S ribosomal subunit biogenesis in *Saccharomyces cerevisiae*. *Nucleic Acids Res.* **27**, 4598–4608.
- Kressler, D., Roser, D., Pertschy, B., and Hurt, E. (2008). The AAA ATPase Rix7 powers progression of ribosome biogenesis by stripping Nsa1 from pre-60S particles. *J. Cell Biol.* **181**, 935–944.
- Lapeyre, B., and Purushothaman, S.K. (2004). Spb1p-directed formation of Gm2922 in the ribosome catalytic center occurs at a late processing stage. *Mol. Cell* **16**, 663–669.
- Leidig, C., Thoms, M., Holdermann, I., Bradatsch, B., Berninghausen, O., Bange, G., Sinning, I., Hurt, E., and Beckmann, R. (2014). 60S ribosome biogenesis requires rotation of the 5S ribonucleoprotein particle. *Nat. Commun.* **5**, 3491.
- Li, X., Mooney, P., Zheng, S., Booth, C.R., Braunschweig, M.B., Gubbens, S., Agard, D.A., and Cheng, Y. (2013). Electron counting and beam-induced motion correction enable near-atomic-resolution single-particle cryo-EM. *Nat. Methods* **10**, 584–590.
- Lo, K.Y., Li, Z., Bussièrè, C., Bresson, S., Marcotte, E.M., and Johnson, A.W. (2010). Defining the pathway of cytoplasmic maturation of the 60S ribosomal subunit. *Mol. Cell* **39**, 196–208.
- Lo, Y.-H., Romes, E.M., Pillon, M.C., Sobhany, M., and Stanley, R.E. (2017). Structural analysis reveals features of ribosome assembly factor Nsa1/WDR174 important for localization and interaction with Rix7/NVL2. *Structure* **25**, 762–772.e4.
- Longtine, M.S., McKenzie, A., 3rd, Demarini, D.J., Shah, N.G., Wach, A., Brachat, A., Philippsen, P., and Pringle, J.R. (1998). Additional modules for versatile and economical PCR-based gene deletion and modification in *Saccharomyces cerevisiae*. *Yeast* **14**, 953–961.
- Ma, C., Wu, S., Li, N., Chen, Y., Yan, K., Li, Z., Zheng, L., Lei, J., Woolford, J.L., Jr., and Gao, N. (2017). Structural snapshot of cytoplasmic pre-60S ribosomal particles bound by Nmd3, Lsg1, Tif6 and Reh1. *Nat. Struct. Mol. Biol.* **24**, 214–220.
- Malyutin, A.G., Musalgaonkar, S., Patchett, S., Frank, J., and Johnson, A.W. (2017). Nmd3 is a structural mimic of eIF5A, and activates the cpGTPase Lsg1 during 60S ribosome biogenesis. *EMBO J.* **36**, 854–868.
- Matsuo, Y., Granneman, S., Thoms, M., Manikas, R.G., Tollervey, D., and Hurt, E. (2014). Coupled GTPase and remodelling ATPase activities form a checkpoint for ribosome export. *Nature* **505**, 112–116.
- McCann, K.L., Charette, J.M., Vincent, N.G., and Baserga, S.J. (2015). A protein interaction map of the LSU processome. *Genes Dev.* **29**, 862–875.
- McCoy, A.J., Grosse-Kunstleve, R.W., Adams, P.D., Winn, M.D., Storoni, L.C., and Read, R.J. (2007). Phaser crystallographic software. *J. Appl. Cryst.* **40**, 658–674.
- Meier, A., and Söding, J. (2015). Automatic prediction of protein 3D structures by probabilistic multi-template homology modeling. *PLoS Comput. Biol.* **11**, e1004343.

- Menne, T.F., Goyenechea, B., Sánchez-Puig, N., Wong, C.C., Tonkin, L.M., Ancliff, P.J., Brost, R.L., Costanzo, M., Boone, C., and Warren, A.J. (2007). The Shwachman-Bodian-Diamond syndrome protein mediates translational activation of ribosomes in yeast. *Nat. Genet.* **39**, 486–495.
- Miles, T.D., Jakovljevic, J., Horsey, E.W., Hampicharnchai, P., Tang, L., and Woolford, J.L., Jr. (2005). Ytm1, Nop7, and Erb1 form a complex necessary for maturation of yeast 66S preribosomes. *Mol. Cell. Biol.* **25**, 10419–10432.
- Miller, O.L., Jr., and Beatty, B.R. (1969). Visualization of nucleolar genes. *Science* **164**, 955–957.
- Murshudov, G.N., Skubák, P., Lebedev, A.A., Pannu, N.S., Steiner, R.A., Nicholls, R.A., Winn, M.D., Long, F., and Vagin, A.A. (2011). REFMAC5 for the refinement of macromolecular crystal structures. *Acta Crystallogr. D Biol. Crystallogr.* **67**, 355–367.
- Nissan, T.A., Bassler, J., Petfalski, E., Tollervey, D., and Hurt, E. (2002). 60S pre-ribosome formation viewed from assembly in the nucleolus until export to the cytoplasm. *EMBO J.* **21**, 5539–5547.
- Pape, T., and Schneider, T.R. (2004). HKL2MAP: a graphical user interface for macromolecular phasing with SHELX programs. *J. Appl. Cryst.* **37**, 843–844.
- Passos, D.O., and Lyumkis, D. (2015). Single-particle cryoEM analysis at near-atomic resolution from several thousand asymmetric subunits. *J. Struct. Biol.* **192**, 235–244.
- Pertschy, B., Saveanu, C., Zisser, G., Lebreton, A., Tengg, M., Jacquier, A., Liebminger, E., Nobis, B., Kappel, L., van der Klei, I., et al. (2007). Cytoplasmic recycling of 60S preribosomal factors depends on the AAA protein Drg1. *Mol. Cell. Biol.* **27**, 6581–6592.
- Pestov, D.G., Stockelman, M.G., Strezoska, Z., and Lau, L.F. (2001). ERB1, the yeast homolog of mammalian Bop1, is an essential gene required for maturation of the 25S and 5.8S ribosomal RNAs. *Nucleic Acids Res.* **29**, 3621–3630.
- Pettersen, E.F., Goddard, T.D., Huang, C.C., Couch, G.S., Greenblatt, D.M., Meng, E.C., and Ferrin, T.E. (2004). UCSF Chimera—a visualization system for exploratory research and analysis. *J. Comput. Chem.* **25**, 1605–1612.
- Ramesh, M., and Woolford, J.L., Jr. (2016). Eukaryote-specific rRNA expansion segments function in ribosome biogenesis. *RNA* **22**, 1153–1162.
- Sarkar, A., Pech, M., Thoms, M., Beckmann, R., and Hurt, E. (2016). Ribosome-stalk biogenesis is coupled with recruitment of nuclear-export factor to the nascent 60S subunit. *Nat. Struct. Mol. Biol.* **23**, 1074–1082.
- Scheres, S.H. (2014). Beam-induced motion correction for sub-megadalton cryo-EM particles. *eLife* **3**, e03665.
- Sharma, S., Yang, J., Watzinger, P., Kötter, P., and Entian, K.D. (2013). Yeast Nop2 and Rcm1 methylate C2870 and C2278 of the 25S rRNA, respectively. *Nucleic Acids Res.* **41**, 9062–9076.
- Sheldrick, G.M. (2008). A short history of SHELX. *Acta Crystallogr. A* **64**, 112–122.
- Sun, Q., Zhu, X., Qi, J., An, W., Lan, P., Tan, D., Chen, R., Wang, B., Zheng, S., Zhang, C., et al. (2017). Molecular architecture of the 90S small subunit pre-ribosome. *eLife* **6**, pii: e22086.
- Talkish, J., Zhang, J., Jakovljevic, J., Horsey, E.W., and Woolford, J.L., Jr. (2012). Hierarchical recruitment into nascent ribosomes of assembly factors required for 27SB pre-rRNA processing in *Saccharomyces cerevisiae*. *Nucleic Acids Res.* **40**, 8646–8661.
- Thomas, B.J., and Rothstein, R. (1989). Elevated recombination rates in transcriptionally active DNA. *Cell* **56**, 619–630.
- Thoms, M., Thomson, E., Baßler, J., Gnädig, M., Griesel, S., and Hurt, E. (2015). The exosome is recruited to RNA substrates through specific adaptor proteins. *Cell* **162**, 1029–1038.
- Thoms, M., Ahmed, Y.L., Maddi, K., Hurt, E., and Sinning, I. (2016). Concerted removal of the Erb1-Ytm1 complex in ribosome biogenesis relies on an elaborate interface. *Nucleic Acids Res.* **44**, 926–939.
- Turowski, T.W., and Tollervey, D. (2015). Cotranscriptional events in eukaryotic ribosome synthesis. *Wiley Interdiscip. Rev. RNA* **6**, 129–139.
- Ulbrich, C., Diepholz, M., Bassler, J., Kressler, D., Pertschy, B., Galani, K., Böttcher, B., and Hurt, E. (2009). Mechanochemical removal of ribosome biogenesis factors from nascent 60S ribosomal subunits. *Cell* **138**, 911–922.
- Wang, Z., Hryc, C.F., Bammes, B., Afonine, P.V., Jakana, J., Chen, D.H., Liu, X., Baker, M.L., Kao, C., Ludtke, S.J., et al. (2014). An atomic model of bromo mosaic virus using direct electron detection and real-space optimization. *Nat. Commun.* **5**, 4808.
- Wegrecki, M., Rodríguez-Galán, O., de la Cruz, J., and Bravo, J. (2015). The structure of Erb1-Ytm1 complex reveals the functional importance of a high-affinity binding between two β -propellers during the assembly of large ribosomal subunits in eukaryotes. *Nucleic Acids Res.* **43**, 11017–11030.
- Wehner, K.A., and Baserga, S.J. (2002). The sigma(70)-like motif: a eukaryotic RNA binding domain unique to a superfamily of proteins required for ribosome biogenesis. *Mol. Cell* **9**, 329–339.
- Weis, F., Giudice, E., Churcher, M., Jin, L., Hilcenko, C., Wong, C.C., Traynor, D., Kay, R.R., and Warren, A.J. (2015). Mechanism of eIF6 release from the nascent 60S ribosomal subunit. *Nat. Struct. Mol. Biol.* **22**, 914–919.
- Winn, M.D., Ashton, A.W., Briggs, P.J., Ballard, C.C., and Patel, P. (2002). Ongoing developments in CCP4 for high-throughput structure determination. *Acta Crystallogr. D Biol. Crystallogr.* **58**, 1929–1936.
- Woolford, J.L., Jr., and Baserga, S.J. (2013). Ribosome biogenesis in the yeast *Saccharomyces cerevisiae*. *Genetics* **195**, 643–681.
- Wu, S., Tutuncuoglu, B., Yan, K., Brown, H., Zhang, Y., Tan, D., Gamalinda, M., Yuan, Y., Li, Z., Jakovljevic, J., et al. (2016). Diverse roles of assembly factors revealed by structures of late nuclear pre-60S ribosomes. *Nature* **534**, 133–137.
- Zhang, K. (2016). Gctf: Real-time CTF determination and correction. *J. Struct. Biol.* **193**, 1–12.
- Zheng, S.Q., Palovcak, E., Armache, J.P., Verba, K.A., Cheng, Y., and Agard, D.A. (2017). MotionCor2: anisotropic correction of beam-induced motion for improved cryo-electron microscopy. *Nat. Methods* **14**, 331–332.

STAR★METHODS

KEY RESOURCES TABLE

REAGENT or RESOURCE	SOURCE	IDENTIFIER
Bacterial and Virus Strains		
<i>E. coli</i> BL21(DE3)	Merck	69450
Deposited Data		
Cryo-EM density map: State A	This paper	EMD-3888
Cryo-EM density map: State B	This paper	EMD-3889
Cryo-EM density map: State C	This paper	EMD-3893
Cryo-EM density map: State D	This paper	EMD-3890
Cryo-EM density map: State E	This paper	EMD-3891
Cryo-EM density map: State F	This paper	EMD-3892
Atomic model: Rrp1 (Spacegroup C2)	This paper	PDB: 6EMF
Atomic model: Rrp1 (Spacegroup P6322)	This paper	PDB: 6EMG
Atomic model: Nsa1	This paper	PDB: 6EN7
Atomic model: State C	This paper	PDB: 6EM1
Atomic model: State E	This paper	PDB: 6ELZ
Architectural model: State A	This paper	PDB: 6EM3
Architectural model: State B	This paper	PDB: 6EM4
Architectural model: State D	This paper	PDB: 6EM5
Experimental Models: Organisms/Strains		
Yeast: W303	Thomas and Rothstein, 1989	N/A
Yeast: DS1-2b	Nissan et al., 2002	N/A
Yeast: NSA1-TAP Flag-YTM1	This paper	N/A
Yeast: RIX1-TAP RPF2-Flag	This paper	N/A
Yeast: BRX1-HTpA	This paper	N/A
Yeast: pA-TEV-(His) ₆ -RPF1	This paper	N/A
Recombinant DNA		
pFA6a-Flag-natNT2	This paper	N/A
pFA6a-TAP-klURA3	This paper	N/A
pnatNT2 P _{YTM1} Flag	This paper	N/A
YCplac111-TAP-Flag-YTM1	Thoms et al., 2016	N/A
YCplac111-TAP-Flag-ytm1 ΔUBL	This paper	N/A
YCplac111-TAP-Flag-ytm1 E80A	This paper	N/A
YCplac111-pA-TEV-(His) ₆ -RPF1	This paper	N/A
pET15b-CtRrp1-(His) ₆	Baßler et al., 2017	N/A
pET15b-Nsa1-(His) ₆	This paper	N/A
Software and Algorithms		
EM-TOOLS	TVIPS GmbH	http://www.tvips.com/imaging-software/em-tools/
MotionCorr2.1	Li et al., 2013	http://cryoem.ucsf.edu/software/driftcorr.html
GCTF	Zhang, 2016	http://www.mrc-lmb.cam.ac.uk/kzhang
Motioncor2	Zheng et al., 2017	http://msg.ucsf.edu/em/software/motioncor2.html
Gautomatch	Jack Kai Zhang, Division of structural studies, MRC Laboratory of Molecular Biology	http://www.mrc-lmb.cam.ac.uk/kzhang
Relion-2	Kimanius et al., 2016	http://www2.mrc-lmb.cam.ac.uk/relion/index.php/Main_Page

(Continued on next page)

Continued

REAGENT or RESOURCE	SOURCE	IDENTIFIER
Phenix suite (phenix.real_space_refine, molprobity)	Afonine et al., 2012; Chen et al., 2010; Wang et al., 2014	https://www.phenix-online.org/
PSIPRED	UCL Department Of Computer Science	http://bioinf.cs.ucl.ac.uk/psipred/
HHpred / Modeler	Meier and Söding, 2015	https://toolkit.tuebingen.mpg.de/#/tools/hhpred
Phyre2	Kelley et al., 2015	http://www.sbg.bio.ic.ac.uk/~phyre2
CCP4 (LIBG, ProSMART, Refmac5, Buccaneer, AIMLESS, XDS, Phaser, COOT, SHELXC/D/E)	Amunts et al., 2014; Brown et al., 2015; Cowtan, 2006; Emsley et al., 2010; Evans and Murshudov, 2013; Kabsch, 2014; McCoy et al., 2007; Murshudov et al., 2011; Winn et al., 2002; Sheldrick, 2008	http://www.ccp4.ac.uk/
ClustalOMEGA	EMBL-EBI	https://www.ebi.ac.uk/Tools/msa/clustalo
RNAcomposer	Institute of Computing Science, Poznan University of Technology	http://rnacomposer.ibch.poznan.pl/
Chimera	UCSF Resource for Biocomputing, Visualization, and Bioinformatics	http://www.cgl.ucsf.edu/chimera/
Pymol	PyMOL Molecular Graphics System, Schrödinger, LLC	https://pymol.org/2/
HKL2MAP	Pape and Schneider, 2004	http://webapps.embl-hamburg.de/hkl2map/
Other		
Carbon coated holey grids (2nm) R 3/3 Copper	Quantifoil	N/A

CONTACT FOR REAGENT AND RESOURCE SHARING

Further information and requests for resources and reagents should be directed to and will be fulfilled by the Lead Contact, Roland Beckmann (beckmann@imb.uni-muenchen.de).

EXPERIMENTAL MODEL AND SUBJECT DETAILS**Plasmid constructs and yeast strains**

Recombinant DNA techniques were performed using standard procedures. Cloning and plasmid propagation was carried out with *E. coli* DH5 α . Cloned DNA fragments obtained by PCR amplification were verified through sequencing. Plasmids used in this study are listed in [Table S1](#). *S. cerevisiae* strains used and generated in this study are listed in [Table S2](#). Genomic tagging was performed as previously described according to standard procedures (Janke et al., 2004; Longtine et al., 1998).

METHOD DETAILS**Affinity purifications from *S. cerevisiae***

The *NSA1*-TAP Flag-*YTM1* and the *RIX1*-TAP *RPF2*-Flag strains were grown in YPD medium and harvested at an OD₆₀₀ of 2.0-2.5. For the *YTM1* wild-type, *ytm1* Δ UBL and *ytm1* E80A alleles plasmids were generated harboring the respective coding sequences fused to an N-terminal TAP-Flag tag under control of the endogenous *PYTM1* promoter. The plasmids were transformed into a wild-type strain (W303) (Thomas and Rothstein, 1989) and selected on SDC-Leu. Cultures were grown over-night in SDC-Leu medium and shifted to YPD for additional 6-7 h until the cultures reached an OD₆₀₀ of 2.0-2.5. Cell pellets were harvested by centrifugation, flash frozen in liquid nitrogen and stored at -20°C .

The affinity purifications were performed as described previously (Barrio-Garcia et al., 2016). Cells were disrupted by cryogenic grinding with a Retch grinding mill (MM 400) and the cell powder was incubated with lysis buffer containing 50 mM Tris pH 7.5, 100 mM NaCl, 5 mM MgCl₂, 5% (v/v) glycerol, 1 mM DTT and 0.1% (w/v) NP40 supplemented with protease inhibitors (SIGMAFAST, Sigma Aldrich). The lysate was cleared by centrifugation and incubated with IgG Sepharose 6 Fast Flow (GE Healthcare) for 90 min at 4°C to enrich for the TAP tagged bait protein. Beads were collected and washed once with 25 mL lysis buffer (batch wash) and additionally with 10 mL lysis buffer by gravity flow. The IgG beads were collected and incubated with lysis buffer supplemented with TEV protease to release the sample from the beads. The eluate was incubated with Anti-Flag M2 Affinity gel (Sigma Aldrich) for additional 90 min at 4°C to enrich for the Flag tagged protein. The remaining steps were performed in buffer containing 50 mM

Tris pH 7.5, 100 mM NaCl, 5 mM MgCl₂ and 1 mM DTT. The Flag agarose beads were extensively washed and samples were eluted with ca. 60 µl buffer supplemented with Flag peptide.

Protein production, crystallization and structure determination

ScNsa1

For expression of *Saccharomyces cerevisiae* (Sc) Nsa1-(His)₆, *E. coli* BL21(DE3) cells, grown in lysogeny broth (LB) medium, were used. Protein expression was induced with 1.8% (w/v) lactose, and cells were harvested after overnight growth at 30°C and stored at –80°C. Cells pellets were resuspended in 10 mL buffer A (20mM HEPES (pH 8.0), 250mM NaCl, 20mM KCl, 20mM MgCl₂ and 40mM imidazole) per gram of cells and lysed with a M-110L Microfluidizer (Microfluidics). Lysate was cleared at 20,000 r.p.m and Nsa1 was enriched by Ni-NTA chromatography. Nsa1 was eluted from Ni-NTA by buffer B (20mM HEPES (pH 8.0), 250mM NaCl, 20mM KCl, 20mM MgCl₂, 500mM imidazole) and further purified by size-exclusion chromatography (HiLoad 26/60 Superdex 200) equilibrated in buffer C (20mM HEPES (pH 8), 200mM NaCl, 20mM KCl and 20mM MgCl₂). Protein was concentrated to approximately 30 mg/ml and crystallization screens were performed at 291K by the sitting-drop vapor-diffusion method upon mixing equal volumes (0.5 µl) of protein solution and crystallization buffer with a reservoir volume of 100 µl. Nsa1 crystallized in a wide range of polyethyleneglycol (PEG)-containing conditions (e.g., 0.1 M MES pH 6.5, 25% w/v PEG-1000). Prior data collection, crystals were flash-frozen in liquid nitrogen after cryo-protection by transfer into cryo-solution containing mother liquor and 20% (v/v) glycerol. Diffraction data were measured under cryogenic conditions (100 K; Oxford Cryosystems Cryostream) at the European Synchrotron Radiation Facility (ESRF; Grenoble). Data were processed with XDS (Kabsch, 2014). The Nsa1 structure was determined by molecular replacement using PHASER and PDB: 5SUM as search model. The structure was manually corrected with Coot (Emsley et al., 2010) and refined with REFMAC5 (Murshudov et al., 2011) and PHENIX (Afonine et al., 2012). Data collection and refinement statistics are summarized in Table S3.

CtRrp1

Rrp1 from *Chaetomium thermophilum* (Ct) was expressed in Rosetta 2 (DE3) T1R cells transformed with the pET15b-CtRrp1-(His)₆ plasmid (Baßler et al., 2017). Briefly, cells were grown until an OD₆₀₀ of 0.8 was reached and then transferred to 18°C. Protein expression was induced by the addition of 0.5 mM IPTG and cells were further grown overnight. Harvested cells were lysed in buffer L (30 mM HEPES pH7.5, 30 mM imidazole, 500 mM NaCl) using a Microfluidizer (Microfluidics). Cell debris and insoluble proteins were removed by centrifugation for 35 minutes at 35000 × g and 4°C. The cleared lysate was filtered with 0.45 µm filter and applied to 2 mL NiNTA column. After washing with 30 column volumes with buffer L the protein was eluted using buffer H (buffer L plus 400 mM Imidazol). Further purification was done using a Superdex 75 26/60 column equilibrated with buffer S (20 mM HEPES pH 7.5, 400 mM NaCl, 5 mM MgCl₂, 2 mM DTT). CtRrp1 containing fractions were pooled, concentrated to 20–40 mg/ml and used for crystallization trials. CtRrp1 crystallized in two conditions, giving rod-shaped crystals in PEG-3350 based condition (200 mM Proline, 100 mM HEPES pH 7.5, 10% PEG3350) and thick hexagonal shaped crystals in a phosphate-containing condition (0.8M K-H₂PO₄, 0.8M Na-H₂PO₄). For data-collection crystals from both conditions were harvested into reservoir solution supplemented with 20% glycerol or ethylene-glycol and flash cooled in liquid nitrogen. Data were collected at ESRF beamline ID 29 (de Sanctis et al., 2012). For phasing, a crystal from the phosphate condition was soaked in reservoir solution supplemented with 1 mM K₂PtCl₄ for 1 hour and cryo-protected as described above. Data were collected at ESRF beamline ID29. Data were processed with XDS (Kabsch, 2014) and AIMLESS (Evans and Murshudov, 2013) from the CCP4 package (Winn et al., 2002). The structure was solved with SHELXC/D/E (Sheldrick, 2008) navigated with HKL2MAP (Pape and Schneider, 2004). The initial map was readily interpretable and Buccaneer (Cowtan, 2006) could place the majority of the residues automatically. Remaining residues were built with Coot (Emsley et al., 2010) and the structure was refined with REFMAC5 (Murshudov et al., 2011) and PHENIX (Afonine et al., 2012). The C2-dataset was solved by molecular replacement as implemented in PHASER (McCoy et al., 2007), using the previously determined structure as search model. The final structures contain 2 molecules per ASU in both space-groups, arranged in different way to each other. Data collection and refinement statistics are summarized in Table S4.

CRAC analysis

The CRAC experiments for Brx1 and Rpf1 were done as described in Granneman et al. (2009) and Thoms et al. (2015) with a modification in case of Rpf1. Brx1 was tagged at the C terminus with (HIS)₆-TEV-protA (HTpA). Rpf1 was tagged at the N terminus on a plasmid (YCplac111- pA-TEV-(HIS)₆-RPF1). Untagged W303 was used as a background control. The yeast cultures were grown to OD 0.6–0.7 and UV-irradiated (*in vivo*) using a Megatron chamber (1.6 J/cm²). Brx1 and Rpf1 were purified as described in Granneman et al. (2009) including high salt (1M NaCl) wash after IgG purification. For Brx1, the sample was transferred to nitrocellulose membrane and RNA was extracted from the membrane as described in Granneman et al. (2009). In case of Rpf1, RNA was extracted directly from the imidazole eluate. For both proteins, the cDNAs obtained were sequenced using the Illumina MiSeq sequencing platform. Analysis of the sequencing results was done as described in Thoms et al. (2015). The 5' and 3' linkers, RT and PCR oligos are listed in Table S6 (Thoms et al., 2015). The experiments were performed twice for both proteins and the results were reproducible.

Cryo-electron microscopy

Carbon coated holey grids (2nm, Quantifoil) were glow discharged at 2.2x10⁻¹ mbar for 30 s. For each grid, 3.5µl of sample were applied to the grids at a concentration of 1.8 A₂₆₀ml⁻¹ for the Nsa1-TAP Flag-Ytm1 sample, 1.5 A₂₆₀ml⁻¹ for the TAP-Flag-Ytm1

E80A sample and $1.3 \text{ A}_{260} \text{ ml}^{-1}$ for the Rix1-TAP Rpf2-Flag sample. Subsequent vitrification was performed by plunge freezing in liquid ethane using a Vitrobot mark IV (FEI Company, Netherlands) with a blotting time of 3 s at 4°C .

Cryo-EM data were collected semi-automatically using the acquisition software EM-TOOLS (TVIPS, Germany) on a Titan Krios transmission electron microscope (FEI Company) at a defocus range between 0.9 and $3.5 \mu\text{m}$. All data for the Nsa1-TAP Flag-Ytm1 sample and the Rix1-TAP Rpf2-Flag sample were recorded on a Falcon II detector under low dose conditions with a nominal pixel size of $1.084 \text{ \AA}/\text{pixel}$ on the object scale. For the Nsa1-TAP Flag-Ytm1 sample, a total of four datasets comprising 2547, 689, 1196 and 1046 micrographs were collected. All micrographs experienced a total exposure of $\sim 27 \text{ e}^-/\text{\AA}^2$ fractionated into 6 frames for the first dataset and 10 for all subsequent datasets. For the Rix1-TAP Rpf2-Flag sample 4447 micrographs dose fractionated into 10 frames were collected. Micrographs of the TAP-Flag-Ytm1 E80A sample were recorded using a Falcon II upgraded with a Falcon III detector chip also operating with a pixel size of $1.084 \text{ \AA}/\text{pixel}$ on the object scale. For this dataset 5812 micrographs were collected with an accumulated dose of $27 \text{ e}^-/\text{\AA}^2$ fractionated into 10 frames.

Image processing

Dose-fractionation movies were initially aligned and summed up using MotionCorr2.1 (Li et al., 2013). Determination of the contrast transfer function parameters was performed via GCTF (Zhang, 2016). For further processing, the original movies were re-aligned with Motioncor2 with anisotropic motion correction (Zheng et al., 2017) using 5×5 patches. Gautomatch (<http://www.mrc-lmb.cam.ac.uk/kzhang>) was used to pick particles. All further image processing (classifications, refinements, and particle polishing) was performed using Relion-2.0 (Kimanius et al., 2016).

Nsa1-TAP Flag-Ytm1 dataset

First, all picked particles were subjected to two-dimensional reference free classification into 150 classes. Based on the resulting class averages, 90 classes with a total of 306732 particles were selected for further processing. An initial round of 3D classification was performed using the Arx1 particle (EMDB: 2528) as a reference allowing rotational and translational alignment. Classes with similar map features were combined, subjected to 3D refinement and second rounds of 3D-classifications. After the final classification step, similar maps classes were joined and 3D-refinements using a wide soft edge mask and solvent flattened FSC calculation were performed. Particles of the highest resolved state C (3.7 \AA) were then subjected to movie refinement of individual particle stacks using a running average window of 3 frames and a standard deviation of 1 pixel as a prior for the translations (Bai et al., 2013). Particle polishing (Scheres, 2014) was performed using default parameters, followed by a final round of 3D refinement. All final reconstructions were subjected to post processing using a wide soft edge mask. In this fashion, four distinct states were recovered from the dataset, State A at a resolution of 4.2 \AA , State B at 4.1 \AA , State C at 3.6 \AA and State D at 4.3 \AA . All resolutions are supplied according to the $\text{FSC}_{0.143}$ criterion following the Relion gold-standard refinement (Figure S2).

Rix1-TAP Rpf2-Flag dataset

Reference free two dimensional classification into 150 classes yielded in 60 classes with 320144 good (ribosomal) particles. These were subjected to 3D refinement and classified into 10 classes. Based on visual inspection of the map features, classes were combined and further refined. Movie processing and particle polishing was performed as described above. Another round of 3D classification followed by a final 3D refinement and post-processing yields in State E with a nominal resolution of 3.7 \AA . The remaining 7 classes of the initial 3D classification were all joined and refined, resulting in state F with an average resolution of 3.3 \AA after post processing with a wide soft edge mask (Figure S2).

TAP-Flag-YtmE80A dataset

All particles were subjected to reference free 2D classification into 200 classes, yielding 78 classes with 297516 good ribosomal particles. After an initial round of 3D refinement, 3D classification of the particles into 8 classes was performed. The 5 classes representing the state E of the Rix1-TAP Rpf2-Flag sample were joined. Movie processing and particle polishing was performed as described above. A further round of 3D classification was performed followed by a final round of 3D refinement yielding a 3.3 \AA reconstruction of state E after post processing with a wide soft edge mask (Figure S2).

Model building and refinements

Based on the proteins identified in the purification (Figure S1), a model was built for the Ytm1 E80A state E map. Therefore, the model of the Nog2 particle (PDB: 3jct) was first fitted as a rigid body into the State E density using UCSF Chimera (Pettersen et al., 2004). This served as a starting model for fitting the ribosomal RNA, the RPs as well as the biogenesis factors Cic1, Mrt4, Nog1, Nop7, Nop15, Nsa2, Nug1, Rlp24, Rlp7 and Tif6. Chains of factors not represented by density in this map were deleted, the rRNA stretches that were not represented by the density were pruned. The results were then manually inspected and adjusted in COOT (Emsley et al., 2010). Nucleotides 2404-2818 were independently fitted with COOT based on the crystal structure of the yeast 80S ribosome (PDB: 4V7R). For target proteins with existing homologies, secondary structure predictions were calculated by PSIPRED and homology models were created via HHpred/Modeler (Meier and Söding, 2015) and Phyre2 (Kelley et al., 2015). The homology models then served as a starting model for de-novo building in COOT. Assignments of the proteins were confirmed by side chain density and secondary structure patterns. Assignments of the structurally similar Brix proteins were verified using CRAC analysis (Figure S6).

All models were combined and subsequently refined using phenix.real_space_refine (Wang et al., 2014). Refmac5 reciprocal space refinement using restraints generated via LIBG and ProSMART was then performed as previously shown (Amunts et al., 2014; Brown et al., 2015).

The model for Nsa1-TAP Flag-Ytm1 state C was created as previously described, the final model of state E was used as a starting model. The crystal structure of Nsa1 (this study) (Figure S6B) was used as a starting model and modified in COOT. An *S. cerevisiae* homology model of Rrp1 was created using MODELER with the *C. thermophilum* crystal structure (also this study) (Figure S6C) and the respective sequence alignment from ClustalOMEGA as input. For modeling the RNA of ES7a, an RNA tertiary structure prediction by RNAComposer (<http://rnacomposer.ibch.poznan.pl/>) was used as an initial reference. Refinement of the model was performed as described for Ytm1 E80A state E, with the exception that the chains of the less well resolved “foot” region (ITS2 RNA, Cic1/Nsa3, Erb1, Has1, Nop7, Nop15 and Rlp7) were not subjected to refinement in Refmac5 but docked as a rigid body using chimera.

Architectural models of states A, B and D were created on the basis of the refined state C and E models. First a general model was created by clipping segments not represented by the respective density map using chimera, the chains of the resulting model were then rigid body fitted using phenix.real_space_refine and finally sidechains were removed using phenix.pdbtools (Pettersen et al., 2004; Wang et al., 2014).

Values of the final refinements and model validation for both models are provided in Table S5.

Molecular interpretation of State F was based on the Arx1/Nog2 particle model (PDB: 3JCT) (Wu et al., 2016). Figures were created using UCSF chimera and PyMOL Molecular Graphics System (Version 1.7.4, Schrödinger, LLC).

QUANTIFICATION AND STATISTICAL ANALYSES

See [Methods Details](#) for details on image processing and model building and refinements.

DATA AND SOFTWARE AVAILABILITY

All maps are deposited at EMDB as noted in the [Key Resources Table](#). Atomic models and architectural models are deposited at PDB as noted in the [Key Resources Table](#).

Accession codes

Cryo-EM density map State A-F: EMDB: EMD-3888; EMDB: EMD-3889; EMDB: EMD-3893; EMDB: EMD-3890; EMDB: EMD-3891; EMDB: EMD-3892

Atomic model (PDB) Rrp1 (Spacegroup C2, P6322): PDB: 6EMF, PDB: 6EMG

Atomic model (PDB) Nsa1: PDB: 6EN7

Atomic model (PDB) State C, E: PDB: 6EM1, PDB: 6ELZ

Architectural model (PDB) state A, B, D: PDB: 6EM3, PDB: 6EM4, PDB: 6EM5

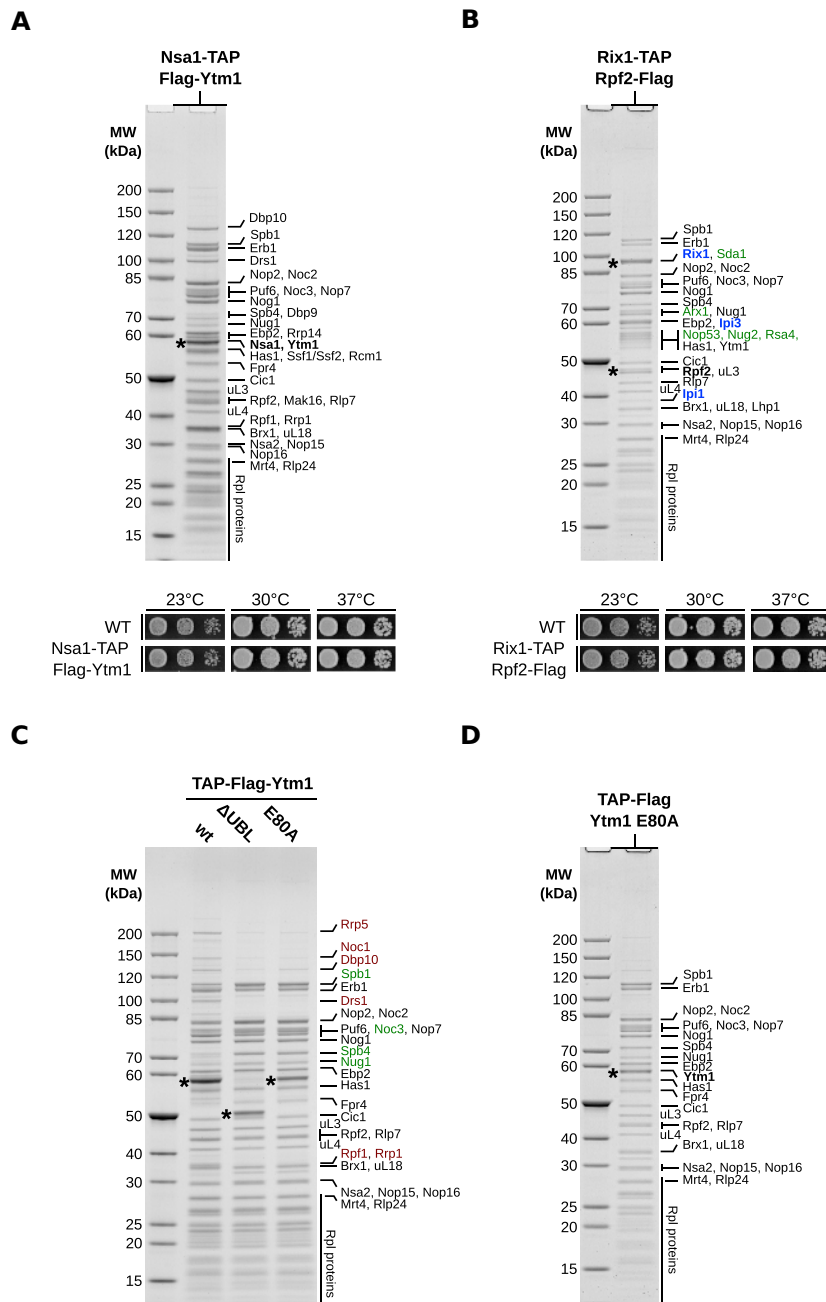


Figure S1. Affinity Purification of Nucleolar Pre-60S Particles for Cryo-EM Analysis, Related to Figure 1

(A and B) Split affinity purifications of pre-60S intermediates (upper panels) purified through Nsa1-TAP Flag-Ytm1 (A) and Rix1-TAP Rpf2-Flag (B). Final eluates were used for cryo-EM and analyzed by SDS-PAGE and Coomassie staining. Major protein bands were identified by mass-spectrometry and are labeled on the right side of the gels. The bait proteins are shown in bold and indicated by asterisks. The Rix1-TAP Rpf2-Flag purification purifies nucleolar (state E) and nucleoplasmic (state F) pre-60S particles (B). Nucleoplasmic assembly factors are indicated in green and the Rix1 subcomplex members (Rix1, Ipi3, Ipi1) in blue. Growth analysis (lower panels) of the Nsa1-TAP Flag-Ytm1 (A) and the Rix1-TAP Rpf2-Flag (B) strains in comparison to the untagged wild-type strain (DS1-2b). Cells were spotted in 10-fold serial dilution on YPD medium and cell growth at the indicated temperatures was monitored after 2 days.

(C) Affinity purifications of the indicated plasmid-encoded Ytm1 variants fused to an N-terminal TAP-Flag tag and expressed from the endogenous promoter. The plasmids were transformed into a wild-type strain (W303). Final eluates of the purifications were analyzed by SDS-PAGE and Coomassie staining and co-purifying proteins are indicated on the right side of the gel and bands corresponding to the Ytm1 bait proteins are marked with an asterisk. Proteins decreased in the Ytm1 Δ UBL/E80A purifications compared to the Ytm1 wild-type particle are shown in red and factors increased on the mutant particles are indicated in green.

(D) Affinity purification of the Ytm1 E80A particle used for cryo-EM analyzed by SDS-PAGE. Proteins bands were identified by mass-spectrometry and are labeled on the right side of the Coomassie stained gel.

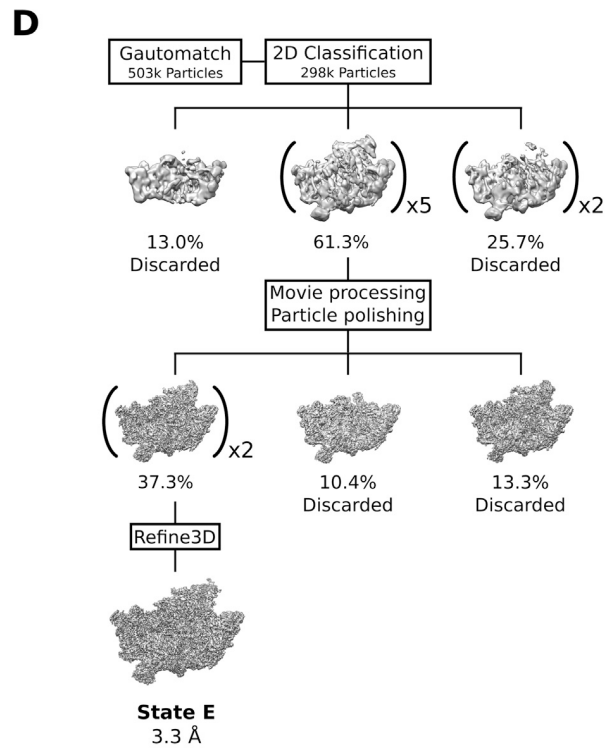
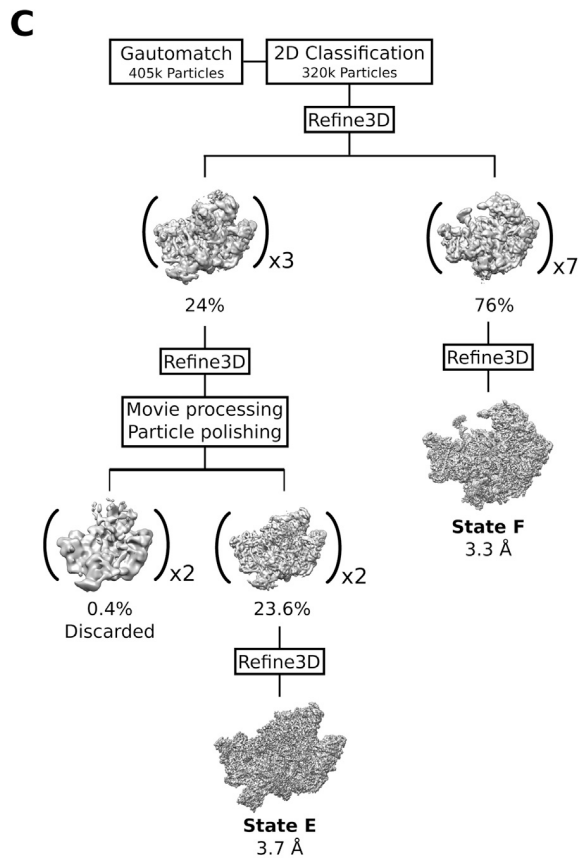
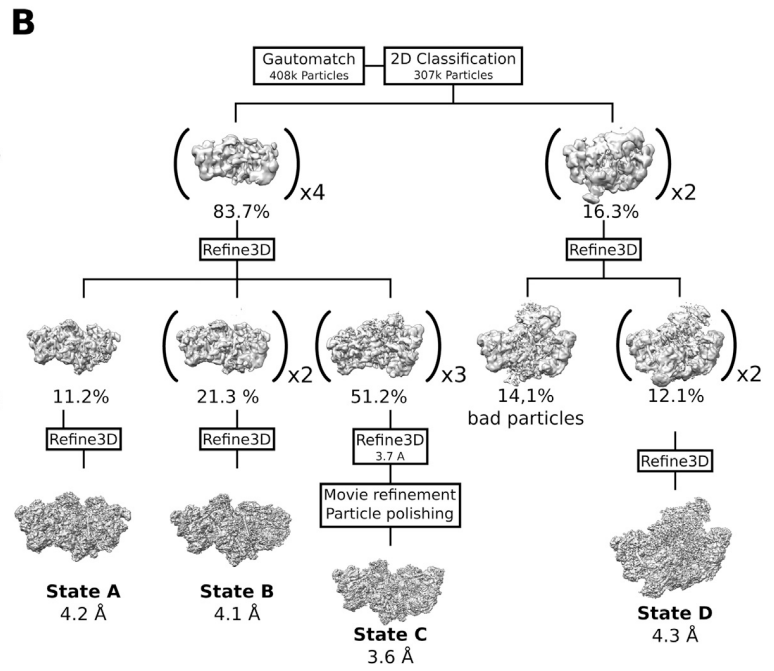
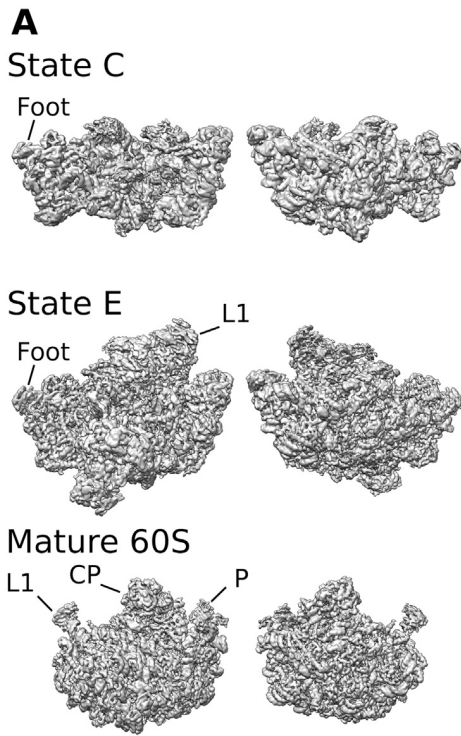


Figure S2. Comparison of States C and E to the Mature 60S and Cryo-EM Processing Schemes, Related to Figure 1

(A) Pre-60S States C and D and the mature 60S (EMDB: 6478) (Passos and Lyumkis, 2015) showing the intersubunit side (left) and the solvent exposed side (right). (B–D) Cryo-EM processing schemes for the Nsa1-TAP Flag-Ytm1 (B), Rix1-TAP Rpf2-Flag (C), and the TAP-Flag-Ytm1 E80A (D) sample. Percentages indicate the fraction of total particles after 2D classification in a class or set of classes. Brackets indicate the joining of several highly similar classes.

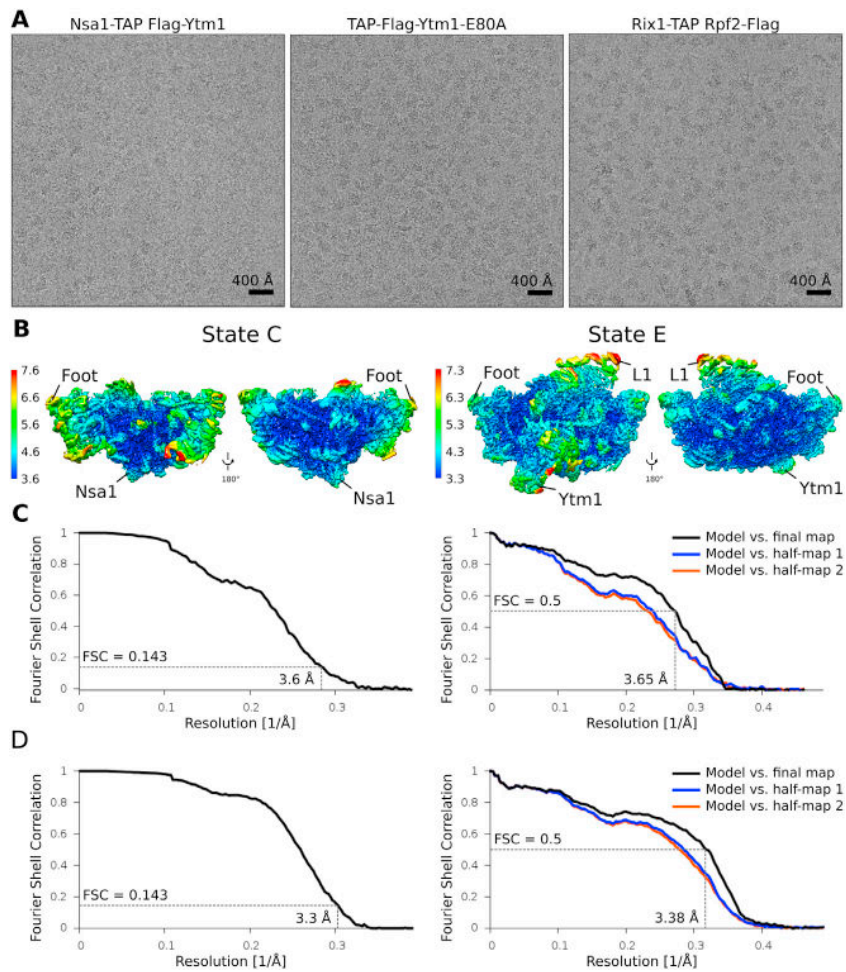


Figure S3. Resolution Estimation and Model Validation, Related to Figure 1

(A) Exemplary micrographs of the three different biochemical samples.

(B–D) Two views rotated by 180° of volumes of state C and E filtered and colored according to local resolution as provided by Relion-2.0 (Kimanius et al., 2016). Gold standard FSC-curves and FSC curves calculated between the cryo-EM maps and the models for the State C particle (C), and for the State E particle (D).

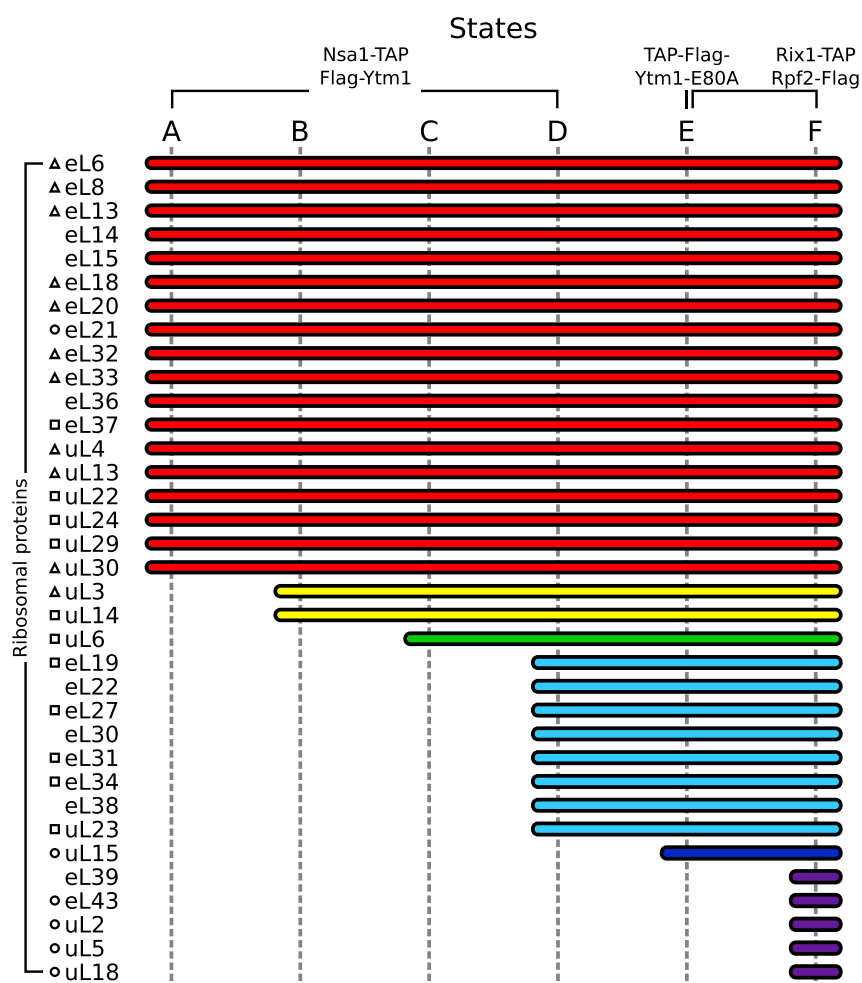


Figure S4. RP Composition of the Six Identified States, Related to Figure 1

RPs clustered and colored according to time of stable association with the core particle. RPs are marked with a triangle, square or circle according to depletion phenotypes leading to maturation arrests at early, middle, and late assembly stages, respectively (Gamalinda et al., 2014).

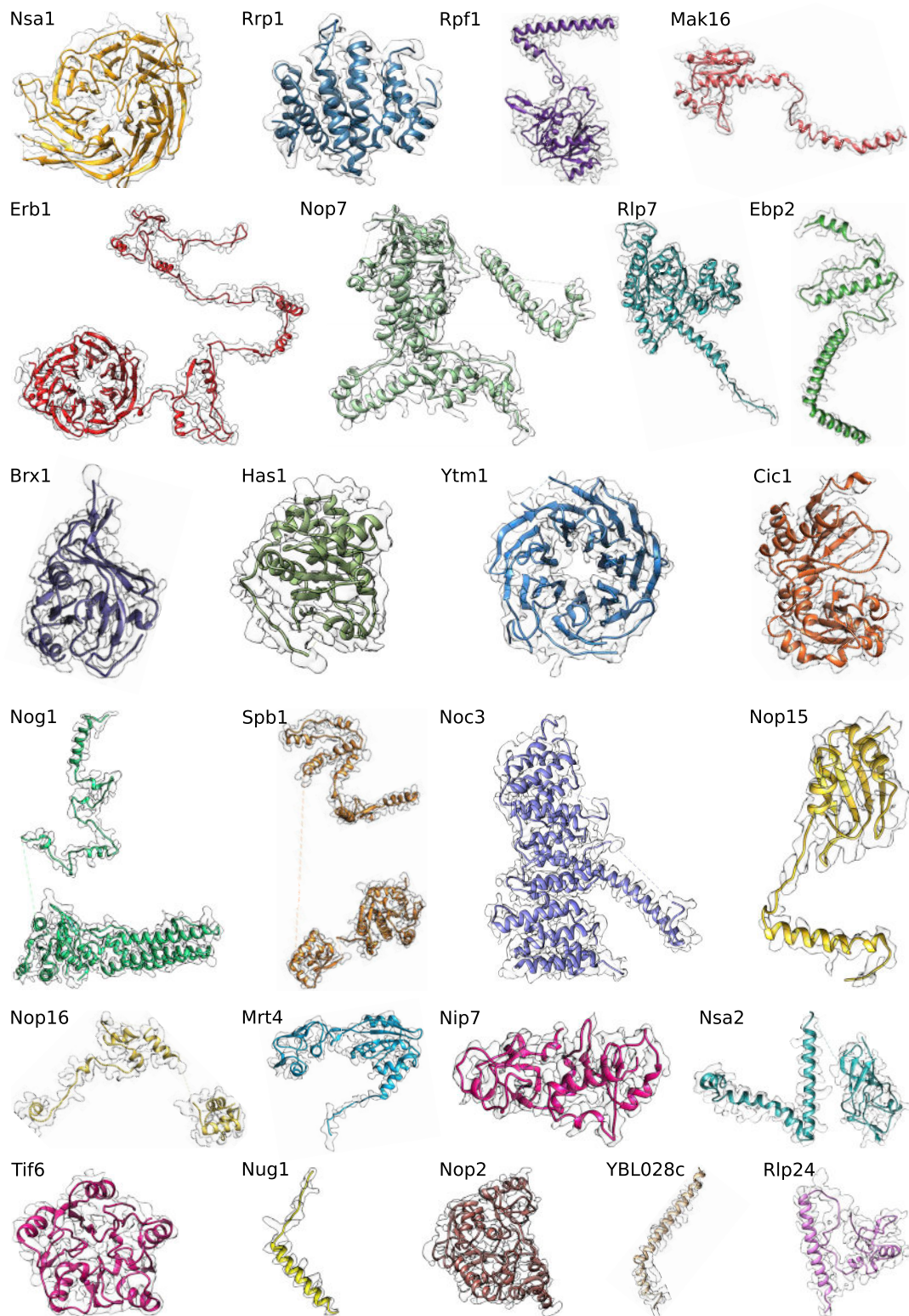
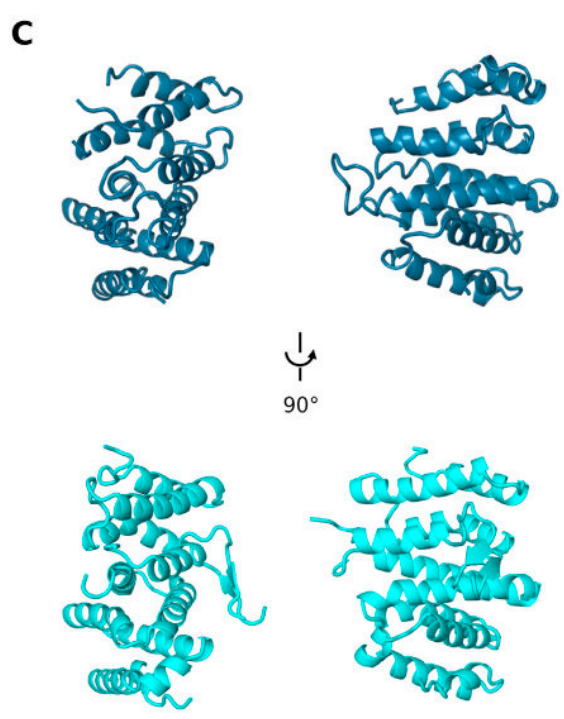
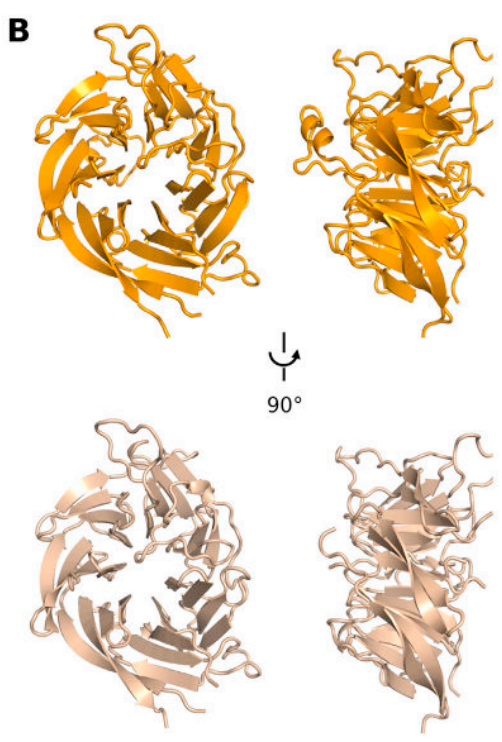
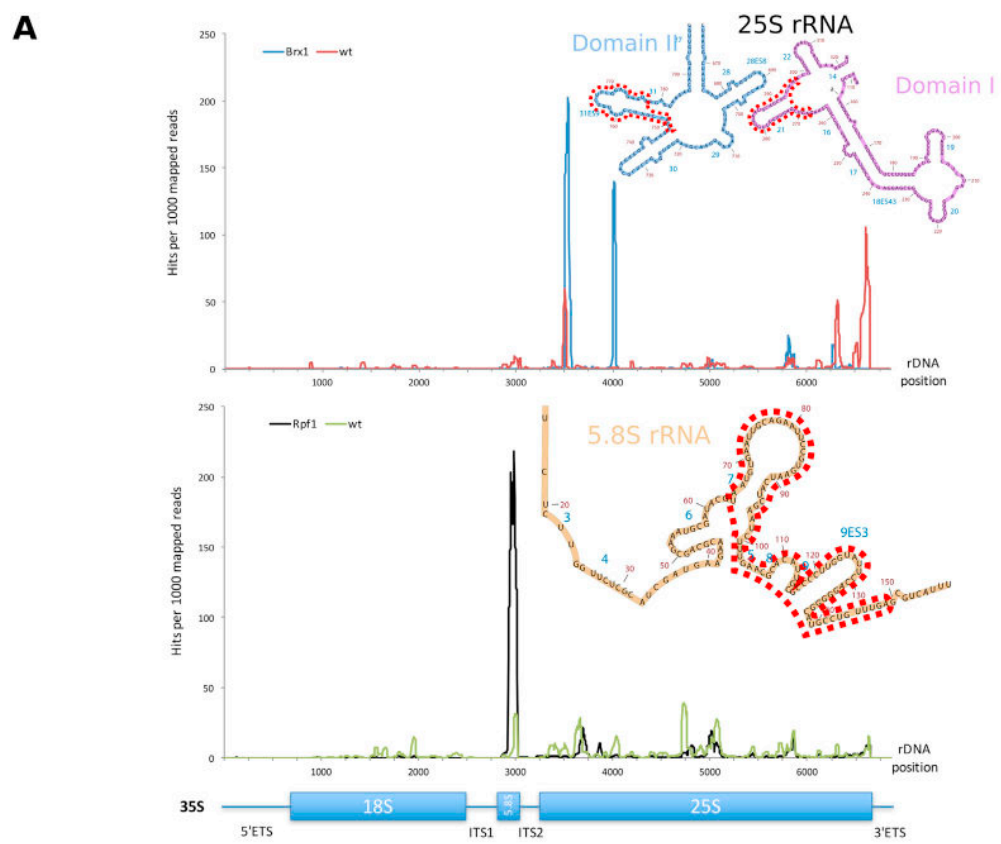


Figure S5. Gallery of All Modeled AFs, Related to Figures 1, 2, 3, and 4

AF models overlaid with the corresponding segmented map volumes. All AFs are taken from state E, except for Rrp1, Rpf1, Nsa1, and Mak16, which are taken from state C. Map densities are filtered to 3.3 Å and 3.6 Å for State E and C respectively.



(legend on next page)

Figure S6. CRAC Crosslinks and Crystal Structures, Related to Figure 2

(A) CRAC analysis hits of yeast Brx1 (blue, top plot) and untagged wild-type strain (red, top plot) as well as Rpf1 (black, bottom plot) and untagged wild-type strain (green, bottom plot). A schematic representation of the 35S pre-rRNA is drawn below the x axis. The number of hits per 1000 total mapped reads is plotted against the nucleotide position on the rDNA.

(B) Comparison of the cryo-EM model (top) of Nsa1 with its crystal structure (bottom).





(C) Comparison of the cryo-EM model (top) of Rrp1 with the crystal structure of *Chaetomium thermophilum* Rrp1 (bottom).

ARTICLE

DOI: 10.1038/s41467-018-06660-w

OPEN

Suppressor mutations in Rpf2-Rrs1 or Rpl5 bypass the Cgr1 function for pre-ribosomal 5S RNP-rotation

Matthias Thoms ¹, Valentin Mitterer¹, Lukas Kater², Laurent Falquet³, Roland Beckmann ², Dieter Kressler ³ & Ed Hurt ¹

During eukaryotic 60S biogenesis, the 5S RNP requires a large rotational movement to achieve its mature position. Cryo-EM of the Rix1-Rea1 pre-60S particle has revealed the post-rotation stage, in which a gently undulating α -helix corresponding to Cgr1 becomes wedged between Rsa4 and the relocated 5S RNP, but the purpose of this insertion was unknown. Here, we show that *cgr1* deletion in yeast causes a slow-growth phenotype and reversion of the pre-60S particle to the pre-rotation stage. However, spontaneous extragenic suppressors could be isolated, which restore growth and pre-60S biogenesis in the absence of Cgr1. Whole-genome sequencing reveals that the suppressor mutations map in the Rpf2-Rrs1 module and Rpl5, which together stabilize the unrotated stage of the 5S RNP. Thus, mutations in factors stabilizing the pre-rotation stage facilitate 5S RNP relocation upon deletion of Cgr1, but Cgr1 itself could stabilize the post-rotation stage.

¹Biochemistry Centre, University of Heidelberg, Heidelberg 69120, Germany. ²Gene Center, University of Munich, Munich 81377, Germany. ³University of Fribourg and Swiss Institute of Bioinformatics, Fribourg 1700, Switzerland. These authors contributed equally: Matthias Thoms, Valentin Mitterer. Correspondence and requests for materials should be addressed to M.T. (email: matthias.thoms@bzh.uni-heidelberg.de) or to E.H. (email: ed.hurt@bzh.uni-heidelberg.de)

Eukaryotic ribosome synthesis is a complex and highly spatially and temporally coordinated process that requires the consecutive action of more than 200 *trans*-acting assembly factors to meet the enormous cellular demand for accurately assembled mature ribosomal subunits^{1–5}. The biogenesis pathway starts in the nucleolus with RNA-polymerase-I-catalysed transcription of ribosomal DNA into a large 35S precursor rRNA, which, upon concomitant and hierarchical joining of ribosome assembly factors and ribosomal proteins, is embedded into the huge 90S particle^{6–10}. Endonucleolytic cleavage of the 35S pre-rRNA subsequently generates the pre-40S and pre-60S particles, which from that point on undergo individual maturation and quality-control steps to finally join again in the cytoplasm forming translation-competent ribosomes.

The large 60S ribosomal subunit is composed of three rRNA species (25S/28S, 5.8S and 5S rRNA) and 46 (in yeast) or 47 (in human) ribosomal proteins^{11,12}. Once separated from the pre-40S particles, the first individual precursors of the 60S subunit are formed within the nucleolus. Upon binding of ribosomal proteins, the nucleolar pre-60S maturation pathway is initiated by the appearance of the 27SA₂ pre-rRNA that is further processed to the 27SB pre-rRNA. Concomitantly, the intertwined rRNA domains are shaped into the developing 60S core in a consecutive order in which first the solvent-exposed side, followed by the polypeptide exit tunnel (PET) and finally the inter-subunit side are formed^{13–16}. At the stage of nucleolar maturation intermediates, the 5S ribonucleoprotein particle (5S RNP), consisting of the 5S rRNA and ribosomal proteins Rpl5 (also known as uL11) and Rpl11 (also known as uL18), is already recruited, and the characteristic pre-60S ‘foot’ structure surrounding the internal transcribed spacer 2 (ITS2) RNA fragment has already formed^{14,17–20}. Crucial pre-60S remodelling events, such as the removal of the Erb1–Ytm1 complex by the AAA-ATPase Rea1, facilitate the transition of the particle to the nucleoplasm^{14,21–23}. A hallmark structure on early nucleoplasmic maturation intermediates, isolated via Arx1 or Nog2 (also known as Nug2), is the twisted 5S RNP, which adopts a conformation rotated ~180° compared to mature 60S subunits^{18–20}. The recruitment of the Rix1 subcomplex, which allows stable docking of Rea1, and the removal of assembly factors Rpf2 and Rrs1 occur during the rotation of the 5S RNP into a near-mature conformation^{20,24}. Subsequently, Rea1 performs its second restructuring role by triggering the release of Rsa4²⁵. Prior to nuclear export, conformational proofreading of the particle takes place that links the removal of Rsa4 with activation and release of the GTPase Nog2, which in turn allows the recruitment of the export adaptor Nmd3²⁶. After nuclear export, the AAA-ATPase Drg1 initiates the cytoplasmic maturation cascade by releasing the placeholder protein Rlp24, thus permitting the recruitment of Rpl24 (also known as eL24)^{27,28}. Subsequent cytoplasmic pre-60S maturation steps include the Rei1–Jjj1–Ssa1-dependent dissociation of the export factor Arx1^{29,30}, assembly of the P-stalk and incorporation of Rpp0 (also known as uL10)^{31,32}, removal of Nmd3 by the GTPase Lsg1 coupled to the incorporation of Rpl10 (also known as uL16)^{33–35}, and release of the anti-association factor Tif6 promoted by Efl1 and Sdo1^{30,36}, which finally activates the 60S subunit to enter the pool of functionally translating ribosomes.

Whereas the 35S pre-rRNA is the common precursor of three of the four rRNA species (18S, 5.8S, 25S/28S), the 5S rRNA precursor is transcribed separately by RNA polymerase III. The 5S rRNA subsequently associates with the ribosomal proteins Rpl5 and Rpl11 to form the 5S RNP that is incorporated as a prefabricated complex adopting an immature conformation on the pre-60S particle^{17,19}. Nuclear import of Rpl5 and Rpl11 is coordinated by the adaptor protein Syo1, which, in a second function, chaperones the 5S RNP until its pre-ribosomal assembly

by shielding exposed RNA-binding sites on Rpl11^{37,38}. In addition, the heterodimer Rpf2–Rrs1 is thought to guide 5S RNP incorporation by providing a docking platform that anchors the 5S RNP in a network of interactions around the central protuberance (CP) involving the 25S rRNA and assembly factor Rsa4^{39–41}. Therefore, the Rpf2–Rrs1 complex has to dissociate from the pre-60S particle, a reaction that appears to be necessary for 5S RNP relocation. However, to date, the mechanistic details of the events that trigger 5S RNP rotation have remained unexplored.

Here, we show that the small and conserved protein Cgr1, which was implicated in 60S biogenesis^{20,42,43}, plays a role in the relocation of the 5S RNP during 60S biogenesis. We found that yeast cells with a chromosomal *cgr1* deletion (*cgr1Δ*)—resulting in a slow-growth phenotype—exhibit a 5S RNP maturation defect on pre-60S particles. However, specific suppressor mutations could be isolated that map in genes encoding Rpf2, its binding partner Rrs1, and the ribosomal protein Rpl5. Owing to the nature of these suppressor mutations, which bypass Cgr1’s function in this process, we were able to gain insight into the mechanism of 5S RNP rotation, revealing how untying of the twisted 5S RNP from its surrounding assembly factor network can drive 5S RNP rotation.

Results

Cgr1 marks pre-60S particles during 5S RNP rotation. Cryo-EM analysis of the Rix1–Rea1 pre-60S particle showed that the 5S RNP had already rotated ~180° to its near-mature position²⁴, whereas in the ‘upstream’ pre-60S particles, such as the early Arx1 particle or Nog2 particle, the 5S RNP was still in the unrotated topology^{19,20}. Among the many other structural peculiarities, the Rix1–Rea1 particle exhibited a 114 Å long, slightly undulating, α -helix inserted between the β -propeller domain of Rsa4 and the rotated 5S RNP, thereby clamping H38 of the 25S rRNA (A-site finger) at a new position (Fig. 1a)²⁴. We suspected that this α -helix corresponds to the small, 120-amino-acid-long protein Cgr1 (Fig. 1b), which has been suggested to perform a role in pre-60S biogenesis^{42–44}. Consistent with this interpretation, Gao and colleagues identified this long α -helix as Cgr1 in the early (unrotated 5S RNP) and late (rotated 5S RNP) states of their Nog2 pre-60S particles that resemble the early Arx1 and Rix1–Rea1 particles, respectively²⁰.

To find out with which pre-60S particles Cgr1 interacts, we first affinity purified both N- and C-terminally tagged Cgr1 from whole yeast cell lysates via TAP-Flag or Flag-TEV-ProtA (FTpA), respectively. Consistent with a predominantly nucleolar/nuclear localization of GFP-Cgr1 (Fig. 1c), the two different Cgr1 purifications were co-enriched for ribosome assembly factors that are typically present on intermediate pre-60S particles (i.e. Nog2, Rix1 and Arx1), and, accordingly, Cgr1 was not found on early nuclear (Ssf1 and Nsa1) or later cytoplasmic (Lsg1) particles (Fig. 1d, e, Supplementary Fig. 1a, b).

Cgr1 depletion stalls the pre-60S prior to 5S RNP rotation. To study the *in vivo* role of *CGR1* during 60S maturation, a *cgr1Δ* null strain was generated. Earlier data indicated that *CGR1* is either essential or non-essential for cell growth, depending on the strain background^{42,43}. In our laboratory yeast strain, W303⁴⁵, *CGR1* is a non-essential gene, but displays an extreme slow-growth phenotype at all tested temperatures (23, 30 and 37 °C) (Fig. 2a). To analyse such a near-essential phenotype in a controlled way, we generated an auxin-inducible degron (AID)⁴⁶ allele of *CGR1*, which efficiently targeted Cgr1 for proteasomal degradation within 30–45 min of auxin addition (Supplementary Fig. 2a). This *CGR1*-HA-AID strain did not display an obvious

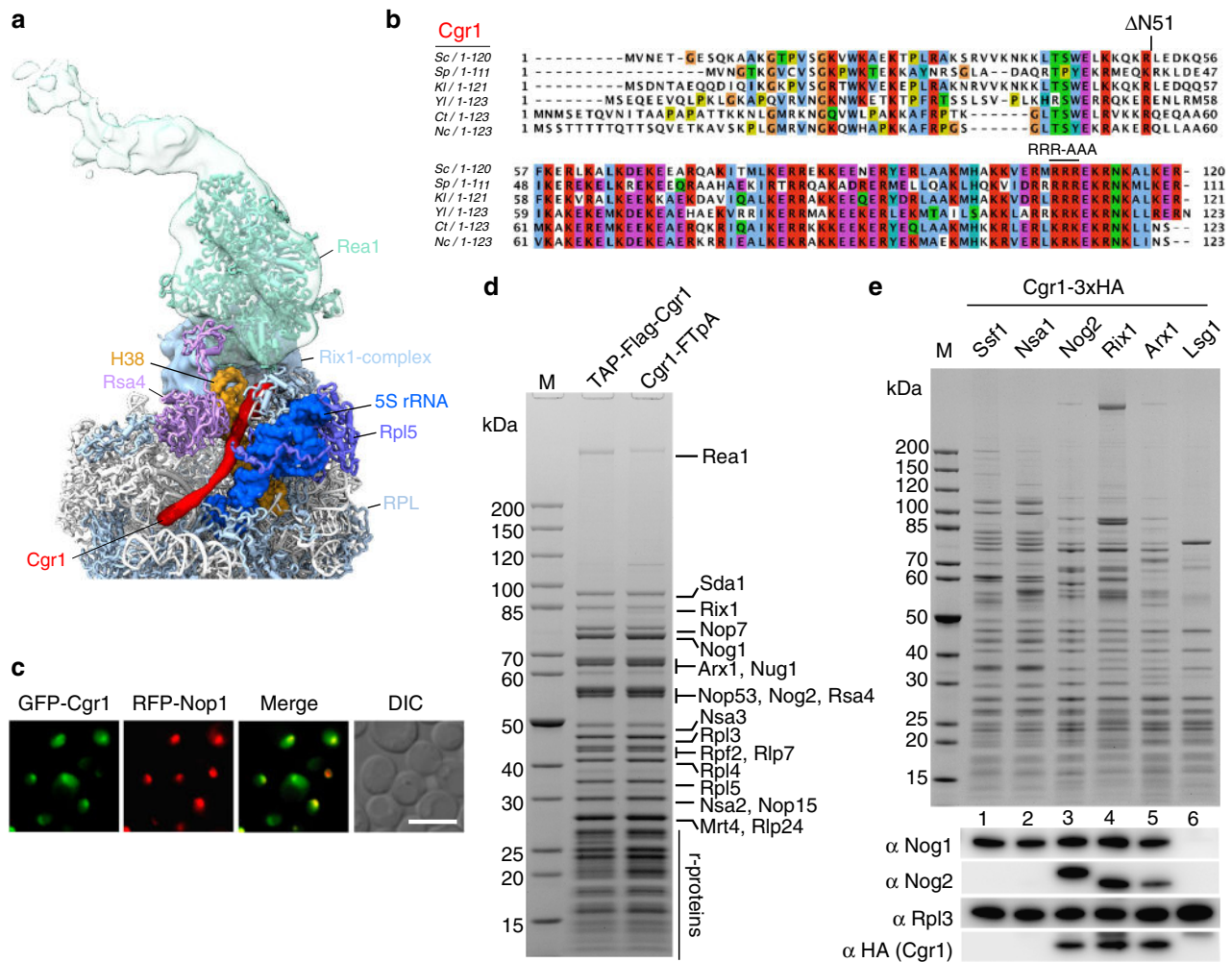
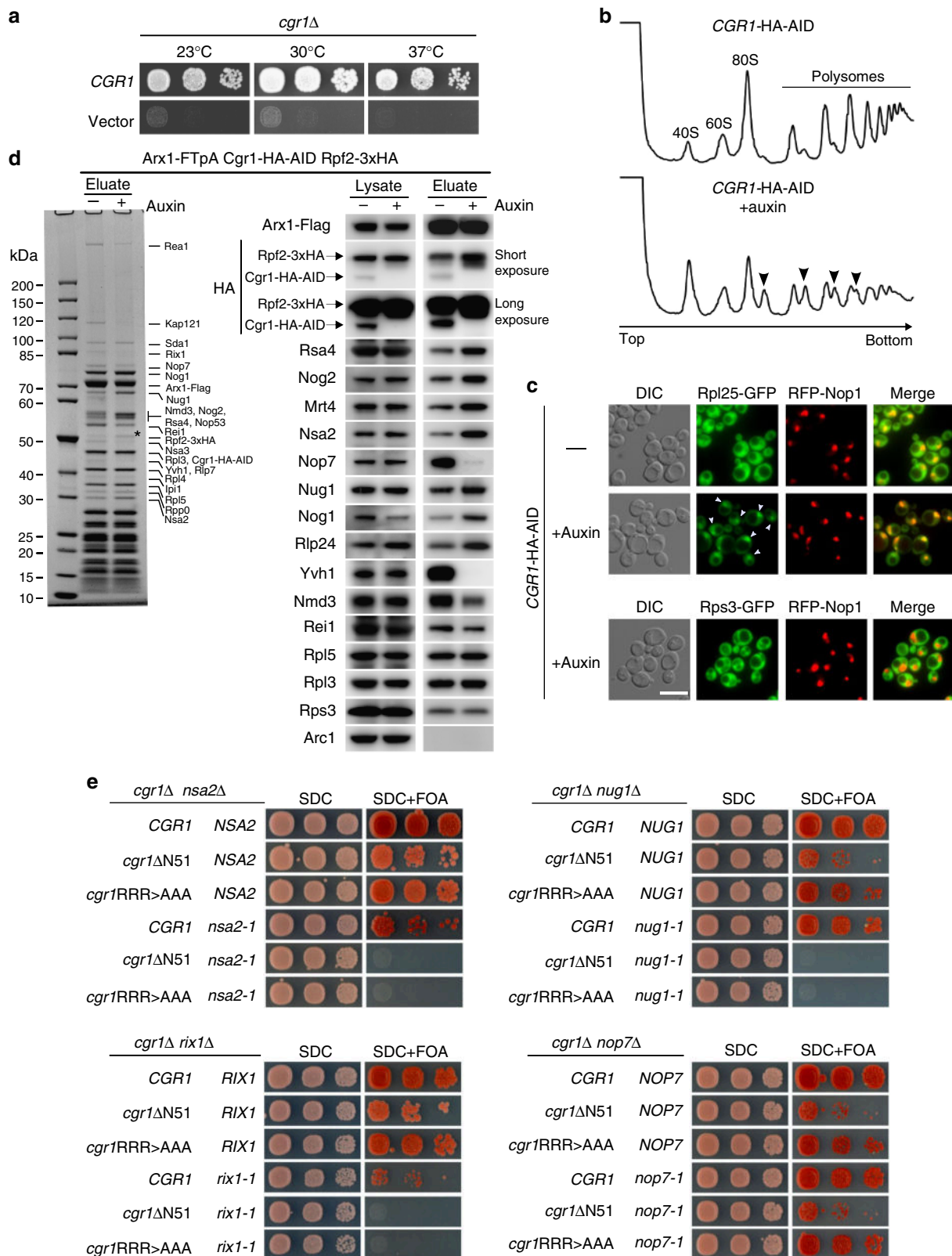


Fig. 1 The short α -helical protein Cgr1 is wedged on nucleoplasmic pre-60S particles close to the rotated 5S RNP. **a** Cryo-EM position of Cgr1 wedged between the β -propeller domain of Rsa4 and the rotated 5S RNP on the Rix1–Rea1 pre-ribosomal particle (PDB: 5jcs,²⁴). The 5S rRNA (blue) and H38 of the 25S rRNA (orange) are shown as surface models, Cgr1 (red), Rsa4 (purple), Rea1 (cyan), Rix1-complex (light blue), Rpl5 (dark blue), and other ribosomal proteins (RPL, light blue) are depicted. **b** Multiple sequence alignment of Cgr1 orthologues from different fungal species: *Saccharomyces cerevisiae* (Sc), *Schizosaccharomyces pombe* (Sp), *Kluyveromyces lactis* (Kl), *Yarrowia lipolytica* (Yl), *Chaetomium thermophilum* (Ct) and *Neurospora crassa* (Nc); for the sequence alignment with higher eukaryotic orthologues including human Cgr1, see Supplementary Fig. 9. Two mutant constructs, Cgr1 Δ N51 and Cgr1RRR > AAA, used for genetic interaction studies, are indicated above the alignment. **c** Subcellular distribution in yeast cells of GFP-Cgr1 and RFP-Nop1 was monitored by fluorescence microscopy. The localization of GFP-Cgr1 is distributed over the nucleus, with the tendency to show a slightly stronger signal in the nucleolus. Scale bar is 5 μ m. **d, e** Cgr1 is co-enriched on intermediate pre-60S particles typically found in the nucleus. **d** Cgr1 tagged either N-terminally (TAP-Flag) or C-terminally (FTpA) were isolated from yeast lysates in two affinity-purification steps. The final Flag eluates were analysed by SDS-PAGE followed by Coomassie staining. The bands identified by mass spectrometry are indicated. **e** Different pre-60S particles affinity purified via bait proteins Ssf1-FTpA (early nucleolar), Nsa1-FTpA (early nucleolar), Nog2-FTpA (intermediate nucleoplasmic), Rix1-FTpA (intermediate nucleoplasmic), Arx1-FTpA (intermediate nucleoplasmic to late cytoplasmic) and Lsg1-FTpA (late cytoplasmic) were affinity purified from yeast strains, which expressed Cgr1 carrying 3xHA (Cgr1-3xHA). Final eluates were analysed by SDS-PAGE and Coomassie staining (upper panel) or western blotting, using the indicated antibodies detecting Nog1, Nog2, Rpl3 and Cgr1 (lower panels). M: molecular weight marker

growth defect when incubated in the absence of auxin (Supplementary Fig. 2b), but exhibited a very mild half-mer phenotype, which could be due to the HA–AID-tag at the C-terminus (Fig. 2b). However, the polysome profile of the cells after auxin-dependent Cgr1–HA–AID depletion showed a drastic increase of the half-mer phenotype, consistent with previous findings⁴² and indicative of a severe 60S biogenesis defect (Fig. 2b). Moreover, robust nuclear accumulation of the 60S reporter Rpl25–GFP was observed upon Cgr1 depletion, suggesting that the 60S maturation defect occurs prior to nuclear export (Fig. 2c).

Next, we wished to find out where exactly Cgr1 participates in the nuclear pre-60S maturation pathway. Since Cgr1 is closely intertwined with the interaction network around the CP,

adopting considerably different conformations depending on the rotation state of the 5S RNP²⁰, we hypothesized that the protein could function at a maturation step during 5S RNP relocation. To assess whether 5S RNP maturation might be affected in absence of Cgr1, we compared the assembly factor profile of Arx1-derived pre-60S particles, isolated from non-depleted (–auxin) versus Cgr1-depleted (+auxin) cells (Fig. 2d). Since Arx1 is associated with a broad range of pre-60S intermediates, from nuclear to cytoplasmic particles^{18,19,47}, it can serve as a bait to define the stage of pre-60S arrest by biochemical means. To allow monitoring of the 5S RNP maturation stage of the isolated particles, we used a strain expressing a chromosomal Rpf2–3xHA fusion, which is



functional based on growth (Supplementary Fig. 1c), as it was suggested that the presence of the assembly factor Rpf2 in complex with its binding partner Rrs1 hinders 5S RNP rotation^{17,20,39–41}. Indeed, western blot analyses revealed that Rpf2-3xHA became significantly enriched on Arx1 particles isolated from Cgr1-depleted cells in comparison to non-depleted

cells (Fig. 2d), indicating Cgr1 might facilitate 5S RNP relocation. Consistent with this finding, Cgr1 depletion caused a significant reduction of late-acting pre-60S factors (e.g. Yvh1, Rei1, Nmd3), whereas earlier assembly factors (e.g. Rsa4, Nog2, Nsa2, Mrt4, Rlp24) became more enriched (Fig. 2d). In contrast, the foot factors Nop7 and Nsa3 (also known as Cic1) were reduced on

Fig. 2 Cgr1 plays a crucial role in ribosome biogenesis of pre-60S particles. **a** Chromosomal *CGR1* deletion in wild-type yeast strain W303 yields viable cells with an extreme slow-growth phenotype. The *cgr1Δ* shuffle strains transformed with empty plasmid or plasmid carrying wild-type *CGR1* were shuffled on SDC + FOA plates, before representative colonies were spotted in 10-fold serial dilutions on YPD plates. They were grown at the indicated temperatures for 2 days. **b** Cgr1 depletion impairs 60 S subunit synthesis. Polysome-profiles of *CGR1*-HA-AID (i.e. Cgr1-depletion strain) were recorded for untreated or auxin-treated (for 120 min) cells. Arrows denote ribosomal half-mers, indicating a specific 60S biogenesis defect. **c** pre-60S export is inhibited in cells depleted of Cgr1. Subcellular localization of the 60S reporter Rpl25-GFP, the 40S reporter Rps3-GFP and the nucleolar marker RFP-Nop1 was analysed in untreated or auxin-treated (for 120 min) *CGR1*-HA-AID cells. Arrows indicate nuclear accumulation of Rpl25-GFP. Scale bar is 5 μm. **d** Depletion of Cgr1 shifts Arx1 pre-60S particles to the early pool typical for the unrotated 5S RNP. Arx1-FTpA particles were affinity purified from untreated or auxin-treated (for 120 min) *CGR1*-HA-AID cells expressing a chromosomally integrated *RPF2*-3xHA variant. Lysates serving as input for the purifications and final eluates were analysed by SDS-PAGE and Coomassie staining. Indicated bands were identified by mass spectrometry (left panel, asterisk indicates Rpf2-3xHA) and western blotting based on specific antibodies (right panel). Rpf2 carries a 3xHA tag, whereas only one HA epitope is fused to Cgr1, explaining the different signal intensities of the HA western blots. **e** Synthetic lethal relationship between *cgr1* mutant alleles and distinct pre-60S assembly factors. Double-shuffle strains of *cgr1Δ* in combination with *nsa2Δ*, *rix1Δ*, *nug1Δ* and *nop7Δ*, respectively, were co-transformed with indicated plasmid-based wild type and mutant constructs. Transformants were spotted in 10-fold serial dilutions and growth on SDC-Leu-Trp (SDC) and SDC + FOA plates at 30 °C was monitored after 2 and 6 days, respectively. The *cgr1RRR* > AAA and *cgr1ΔN51* mutants are shown in Fig. 1b and Supplementary Fig. 3. Published mutant alleles *nsa2-1*, *rix1-1*, *nug1-1* and *nop7-1* are listed in Supplementary Table 3

Cgr1-depleted particles, indicating that ITS2 processing and removal of the foot structure could proceed uncoupled of 5S RNP rotation.

Genetic interactions between *cgr1* and pre-60S factors. Next, we performed genetic analyses to further elucidate the in vivo function of Cgr1. For this purpose, we generated ‘milder’ *cgr1* mutant alleles compared to the *cgr1* null by truncating either the N-terminus (*cgr1ΔN51*) or mutating a cluster of positively charged residues at the C-terminus (R108A, R109A, R110A, *cgr1RRR* > AAA). The latter motif contacts a part of the 5S rRNA in the pre-rotation state²⁰. Both of these *cgr1* mutants grew well at 30 °C compared to the *cgr1*-null, but exhibited a temperature-sensitive phenotype at 37 °C (Supplementary Fig. 3a, b). Combining *cgr1ΔN51* or *cgr1RRR* > AAA with mutant alleles of other pre-60S assembly factors revealed a synthetic lethal phenotype at 30 °C in the case of *rix1-1*, *nsa2-1* and *nug1-1*, but not with *nop7-1* (Fig. 2e). The Rix1 subcomplex is implicated in the initiation of 5S RNP rotation²⁴, and an α-helix in the Nug1 N-terminal domain is in direct contact with and the Nsa2 N-domain in close proximity to Cgr1^{19,20}, whereas Nop7 is located far away at the ‘foot’ of the pre-60S particle²⁰. Thus, the observed genetic relationships correlate well with the biochemical and cryo-EM data, reinforcing Cgr1’s role in 5S RNP relocation.

Specific suppressor mutations bypass the function of Cgr1.

During the course of growing the *cgr1Δ* strain on plates, we consistently noticed a few fast-growing colonies in the high-cell-density streak-out, which among other possibilities could be spontaneous suppressors that bypass the requirement for *CGR1* (Fig. 3a). To further elaborate on this possibility, we performed clarifying genetic tests with these putative suppressors. First, we backcrossed a few of these suppressor strains to a haploid *cgr1Δ* strain of opposite mating type, which harboured wild-type *CGR1* on a *URA3*-containing plasmid. After sporulation and tetrad dissection, the four germinated *cgr1Δ* spores containing *URA3-CGR1* plasmid showed a 2⁺:2⁻ segregation regarding slow versus fast growth on 5-fluoroorotic acid (5-FOA) plates (Fig. 3b). Apparently, the fast-growth-suppressor phenotype points to a single mutated gene locus responsible for the extragenic suppression.

This finding prompted us to perform whole-genome DNA sequencing of two selected suppressor strains that upon backcrossing showed a 2:2 segregation (see above). Strikingly, in both strains a single missense mutation (G227A and C84F) in the open reading frame of the *RPF2* gene was found. The G227A mutation

mapped to the conserved sigma-70-like motif found in all members of the Brix protein family⁴⁸, whereas the C84F mutation is found in a conserved region known to be involved in the interaction with Rrs1⁴⁰. Thus, the identified mutations, together with the observed accumulation of Rpf2 on pre-ribosomes after Cgr1 depletion, establish a direct link between Cgr1 and 5S RNP maturation.

To find out whether suppressor mutations in genes other than *RPF2* exist, we systematically analysed the remaining *cgr1Δ* suppressors in a different way. For this purpose, we expressed the wild-type allele of *RPF2* and other factors suspected to functionally interact with Cgr1 on the pre-60S particles (i.e. *RRS1*, *RPL5* and *RPL11*; all placed under *GALI-10* control) in all 41 *cgr1Δ* suppressor strains (39 remained uncharacterized) and tested for reversion of the fast-growing phenotype. Strikingly, overexpression of *RPF2* changed 30 suppressors, *RRS1* six suppressors and *RPL5* five suppressors into a slow-growth phenotype, suggesting that all of our isolated suppressor strains were hit in only three genes (Fig. 3c). Cloning and DNA sequencing of these suppressor genes revealed single point mutations in *RPF2* (25 unique exchanges), *RRS1* (four unique exchanges) and *RPL5* (four unique exchanges) (Table 1).

To confirm that the cloned suppressor alleles behave like anticipated, double-shuffle strains were generated, in which *cgr1Δ* was finally combined with the given cloned suppressor allele. This genetic analysis revealed that all identified suppressor alleles complemented the severe growth defect of *cgr1Δ* mutant cells, although wild-type growth levels were not reached (Fig. 3d-f, Supplementary Fig. 4).

cgr1Δ suppressor mutations within the pre-60S structure.

We sought to localize the suppressor mutations within the cryo-EM structure of pre-60S particles, where the 5S RNP is still unrotated and in direct contact with the Rpf2-Rrs1 heterodimer^{19,20} (Fig. 4, Supplementary Figs. 5–7 and Table 1). For Rpf2, where a total of 25 different suppressor mutations were isolated, three mutations (A10E, R14I, K18T) map in an N-terminal α-helix interacting with H83 and H87 of 25S rRNA, whereas the remaining ones are distributed throughout the Brix-fold, which broadly participates in the interaction with both the 5S RNP and Rrs1 (Fig. 4, Supplementary Fig. 5). Several of these mutations showed substitutions of surface-exposed basic residues that change the electrostatic surface potential. Notably, surface-exposed basic amino acid clusters within Rpf2 were recently analysed in vitro, demonstrating that highly conserved R236, the R62-K63 cluster and the KKR loop (residues 94–96) are important for 5S rRNA binding³⁹. Strikingly, the Rpf2 R62L/S, K63T and R236G/I

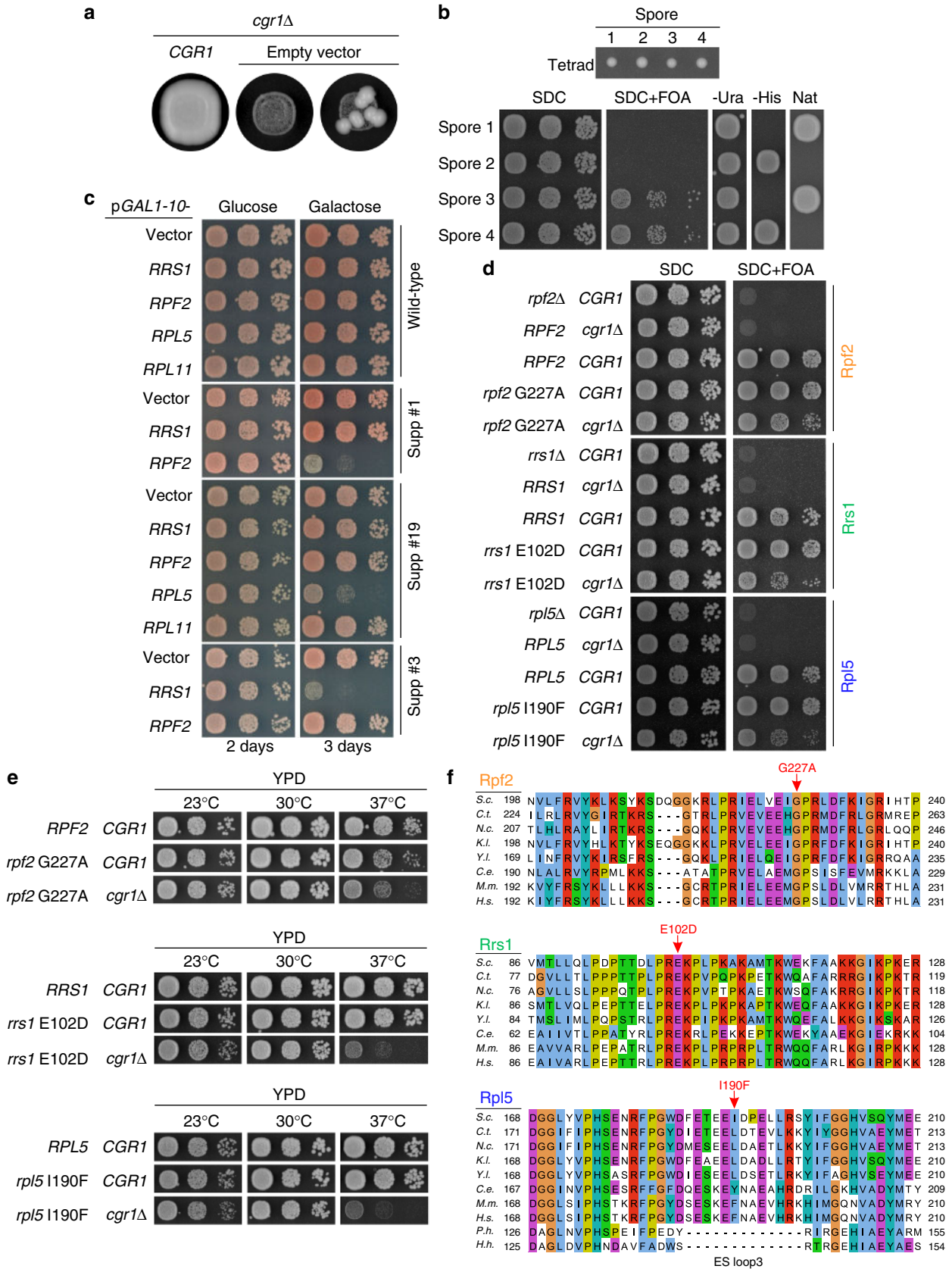


Fig. 3 Suppressor mutations in *RPF2*, *RRS1* and *RPL5* bypass the requirement for *CGR1*. **a** Dot spot growth analyses of the *cgr1Δ* strain, harbouring plasmid-borne *CGR1* (left panel) or empty plasmid (middle and right panels), incubated on YPD plates at 30 °C for 3 days. The dot spot on the right, but not the middle, exhibits faster-growing colonies, which are suppressors of *cgr1Δ*. **b** *cgr1Δ* (*cgr1::natNT2*) suppressor strain was crossed with a *cgr1Δ* (*cgr1::HIS3MX6*) strain containing *CGR1* on a *URA3* plasmid (pRS316-*CGR1*). After sporulation and tetrad dissection (upper panel shows a representative tetrad), the four haploid spores were tested for growth in the absence of pRS316-*CGR1* on SDC + FOA plates, for the presence of pRS316-*CGR1* on SDC-Ura, and for the presence of the *CGR1* gene disruption markers on SDC-His and YPD + clonNat. Cells were spotted in 10-fold serial dilutions and incubated at 30 °C for 2 days (lower panel). **c-f** Suppressor mutations are located in genes encoding *RPF2*, *RRS1* and *RPL5*. **c** Wild type and different *cgr1Δ* suppressor strains (suppressor #1, #3 and #19) were transformed with plasmids expressing *RPF2*, *RRS1*, *RPL5* or *RPL11* under the control of the galactose-inducible *GAL1-10* promoter. Representative transformants were spotted in 10-fold serial dilutions on SDC plates containing glucose (*GAL* repression) and galactose (*GAL* induction) and growth was assessed after incubation at 30 °C for 2 and 3 days, respectively. **d, e** Double-shuffle strains of *cgr1Δ* (+ *pURA3-CGR1*) combined with *rpf2Δ* (+ *pURA3-RPF2*), *rrs1Δ* (+ *pURA3-RRS1*) and *rpl5Δ* (+ *pURA3-RPL5*), respectively, were transformed with plasmids harbouring the suppressor allele or the respective wild-type gene combined with plasmids harbouring wild-type *CGR1* or empty plasmid. Transformants were spotted in 10-fold serial dilutions on SDC + FOA plates (**d**) and after plasmid shuffling on YPD plates (**e**). Growth was analysed after incubation for 2 days at the indicated temperatures. **f** Multiple sequence alignment of Rpf2, Rrs1 and Rpl5 orthologues from *Saccharomyces cerevisiae* (*S.c.*), *Chaetomium thermophilum* (*C.t.*), *Neurospora crassa* (*N.c.*), *Kluyveromyces lactis* (*K.l.*), *Yarrowia lipolytica* (*Y.l.*), *Caenorhabditis elegans* (*C.e.*), *Mus musculus* (*M.m.*), *Homo sapiens* (*H.s.*), *Pyrococcus horikoshii* (*P.h.*) and *Halobacterium hubeiense* (*H.h.*). The respective suppressor alleles analysed in **d** and **e** are indicated

Table 1 Comparison of the isolated *cgr1Δ* suppressor mutations

Protein	Point mutation	Interaction/role
<i>Rpf2</i> (30 isolated suppressor strains)	A10E (2 strains)	25S rRNA (CP H87)
	R14I (2 strains)	25S rRNA (CP H87)
	K18T	25S rRNA (CP H87)
	D48Y	Folding
	K53R	Folding
	K54E	5S rRNA
	R62L	5S rRNA/25S rRNA
	R62S	5S rRNA/25S rRNA
	K63T	5S rRNA/25S rRNA
	N64K	5S rRNA/25S rRNA
	K81N	25S rRNA
	K81T (2 strains)	25S rRNA
	C84F	Folding
	C84W	Folding
	S93F	5S rRNA (KKR loop)
	R104L	Rrs1, folding
	D112Y (3 strains)	Folding
	M117V	5S rRNA (KKR loop), folding
	G177R	Rpl5/Rrs1, folding
	H180N	Folding
	V203F	Rrs1, folding
	G227A	Rrs1 (sigma70-like motif), folding
	G227V	Rrs1 (sigma70-like motif), folding
R236G	5S rRNA	
R236I	5S rRNA	
<i>Rrs1</i> (6 isolated suppressor strains)	L92H	Rpf2
	E102D	Rpf2
	K103N (3 strains)	Rpf2
	P106Q	Rpf2
<i>Rpl5</i> (5 isolated suppressor strains)	V73F (2 strains)	5S rRNA/Rpf2
	E126K	Rsa4/Rpf2 (ES loop 2)
	E128K	Rsa4/Rpf2 (ES loop 2)
	I190F	Rsa4/5S rRNA (ES loop 3)

CP = central protuberance; ES = eukaryote-specific

mutations were all among our *cgr1Δ* suppressors. Although no mutations in the highly conserved KKR motif were found, the suppressor mutation Rpf2 S93F is within this KKR loop as well, which may be destabilized by the S93F change (Fig. 4, Supplementary Fig. 5), and hence could be the cause of a reduced interaction with the 5S rRNA. Consistent with this data, specific

point mutations in the 5S rRNA tip, mediating the interaction with the Rpf2 KKR loop, strongly impaired the interaction between Rpf2–Rrs1 and the 5S rRNA⁴¹. Other suppressor mutations in Rpf2, such as D48Y, D112Y or H180N, are found within the Brix-domain fold and eventually destabilize the Rpf2–Rrs1 interaction (Fig. 4, Supplementary Fig. 5).

In the case of Rrs1, all identified mutations are clustered in a highly conserved, proline-rich unstructured region (residues 92–108), which protrudes from the Rpf2 interaction-domain and continues into the carboxy-terminal sequence that contacts the 25S rRNA at multiple sites (Fig. 4, Supplementary Fig. 6), thereby also stabilizing the unrotated 5S RNP^{20,40}. In vitro, both the proline-rich region and the C-terminal end of Rrs1 are not required for complex formation with Rpf2³⁹, but, in the cryo-EM structure, the proline-rich region is in contact with the Brix1-fold domain of Rpf2 (Fig. 4, Supplementary Fig. 6). Therefore, it is conceivable that our identified suppressor mutations in the proline-rich Rrs1 loop might change the position of the Rrs1 C-terminus, and thereby destabilize the unrotated 5S RNP.

Interestingly, three of our discovered suppressor mutations map to the ribosomal protein Rpl5 (E126K, E128K, I190F), specifically in two of the three eukaryote-specific loop regions required for 60S biogenesis, which if deleted cause trapping of Rpf2–Rrs1 on pre-60S particles⁴⁹. In particular, the I190F mutation is located in eukaryotic-specific loop 3 (residues 185–198) that bridges Rpl5 with the Rsa4 β-propeller and the twisted 5S rRNA, whereas the mutations E126K and E128K map to the neighbouring eukaryote-specific loop 2 (residues 122–138), which is not resolved in the cryo-EM structure, but most likely connects the β-propeller of Rsa4 and Rpf2 (Fig. 4, Supplementary Fig. 7). In contrast, the fourth suppressor mutation within Rpl5 (V73F) maps to a conserved short loop motif sandwiched between the 5S rRNA and Rpf2 (Fig. 4, Supplementary Fig. 7).

Thus, considering all these different suppressor mutations in the structural context of the pre-60S particle, they likely destabilize the intricate interaction network between Rpf2–Rrs1, Rsa4 and the unrotated 5S RNP, which consequentially could allow driving the equilibrium towards the rotated state of the 5S RNP, thus compensating for the absence of *Cgr1*.

Suppressor mutants promote 5S RNP rotation in *cgr1Δ* strains.

Based on the structural interpretation of the various *cgr1Δ* suppressors, we examined the impact of a few of these mutations on pre-60S maturation. First, we determined the localization of the 60S export reporter Rpl25–GFP in the mutants *rpf2V203F*, *rrs1E102D* and *rpl5I190F*, which all confer a strong suppression

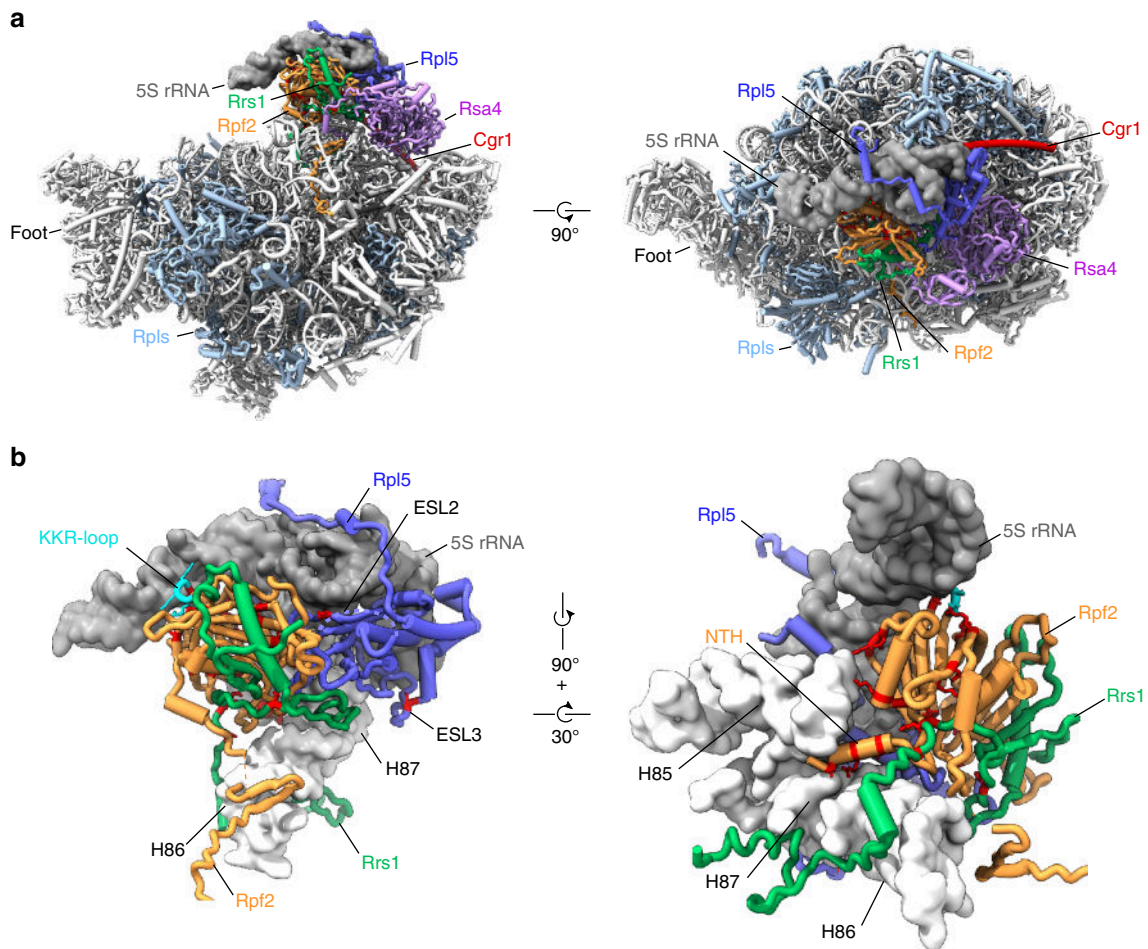


Fig. 4 *cgr1* Δ suppressor mutations in *RPF2*, *RRS1* and *RPL5* destabilize the unrotated 5S RNP on the pre-60S particle. **a** Overview of biogenesis factors Rpf2 (orange), Rrs1 (green), Rsa4 (purple), Cgr1 (red) and the ribosomal protein Rpl5 (dark blue) on the Nog2 particle (PDB: 3jct,²⁰) in the front and top view. Ribosomal proteins are shown in light blue and 5S rRNA as a dark grey surface model filtered at 6 Å resolution. **b** Positions of *cgr1* Δ null suppressor mutations (red) displayed with surface models of the 5S rRNA (dark grey) and helices H83 to H87 (nucleotides 2650–2754) of the 25S rRNA (light grey). The KKR-loop of Rpf2 is highlighted in cyan. ESL2 and ESL3 mark the eukaryotic-specific loops 2 and 3 of Rpl5, NTH marks the N-terminal helix of Rpf2

phenotype on *cgr1* Δ . In contrast to wild-type *RPF2*, *RRS1* and *RPL5* cells, which display nuclear accumulation of Rpl25–GFP after auxin-dependent Cgr1–HA–AID depletion, efficient nuclear export of Rpl25–GFP was re-established in the respective suppressor strains, which is clear-cut evidence for resuming pre-60S biogenesis (Fig. 5a). Moreover, we analysed the assembly factor composition of Arx1-affinity purified pre-60S particles derived from the *rpf2V203F*, *rrs1E102D* and *rpl5I190F* suppressor mutants, before and after Cgr1 depletion (Fig. 5b). In all cases, the pattern of factor enrichment on and removal from the Arx1 particles was consistent with our previous interpretation that nuclear export of pre-60S subunits was re-established in *cgr1* Δ cells by specific mutations in Rpf2, Rrs1 and Rpl5 (Fig. 5b). Notably, the assembly factor Rpf2, which became enriched on Arx1 pre-60S particles upon Cgr1 depletion (see also above), co-purified similar to the wild-type condition in the suppressor mutants (Fig. 5b). This finding further strengthens the hypothesis that the bypassing function of the suppressors could be specifically connected to a step in the course of 5S RNP relocation.

To directly assess whether 5S RNP rotation is inhibited in pre-60S particles when Cgr1 is depleted, but restored in the suppressor mutants, we performed cryo-EM analysis (Fig. 6, Supplementary Fig. 8 and Supplementary Table 1). This method showed that in the Cgr1 non-depleted strain (Arx1–FTpA Cgr1–

HA–AID, no auxin), which served as control, the 5S RNP was rotated in ~40% of the Arx1 particles, whereas ~60% of particles exhibited the non-rotated stage (Fig. 6a). This ratio is typical for the distribution of rotated (mature) versus non-rotated (immature) 5S RNP in Arx1 or Nog2 pre-60S particles^{19,20}. Strikingly, the 5S RNP remained to 100% non-rotated in the *cgr1*-depletion mutant (Fig. 6b; Arx1–FTpA Cgr1–HA–AID, + auxin). However, 5S RNP relocation was significantly restored in the *rrs1E102D* suppressor strain, showing 23% of the Arx1 pre-60S particles in the post-rotation stage (Fig. 6c; Arx1–FTpA Cgr1–HA–AID *rrs1E102D*, + auxin). Thus, structural analysis also supports the view that the suppressor mutations facilitate 5S RNP rotation in the absence of Cgr1, which explains well why the suppressor strains can re-export pre-60S particles and regain better cell growth. However, suppressor mutants did not reach optimal growth (see also Fig. 3e), which may correlate with the degree of the 5S RNP relocation. Notably, the cryo-EM analysis further revealed that the foot structure, carrying the ITS2 fragment of the 7S pre-rRNA and associated assembly factors, was absent from the Cgr1-depleted Arx1 particles (Fig. 6b). This finding is in line with the biochemical data demonstrating a strong decrease of foot factors Nop7 and Nsa3 on these particles (see Figs. 2d and 5b), which suggests that maturation of the foot can proceed independent of 5S RNP maturation.

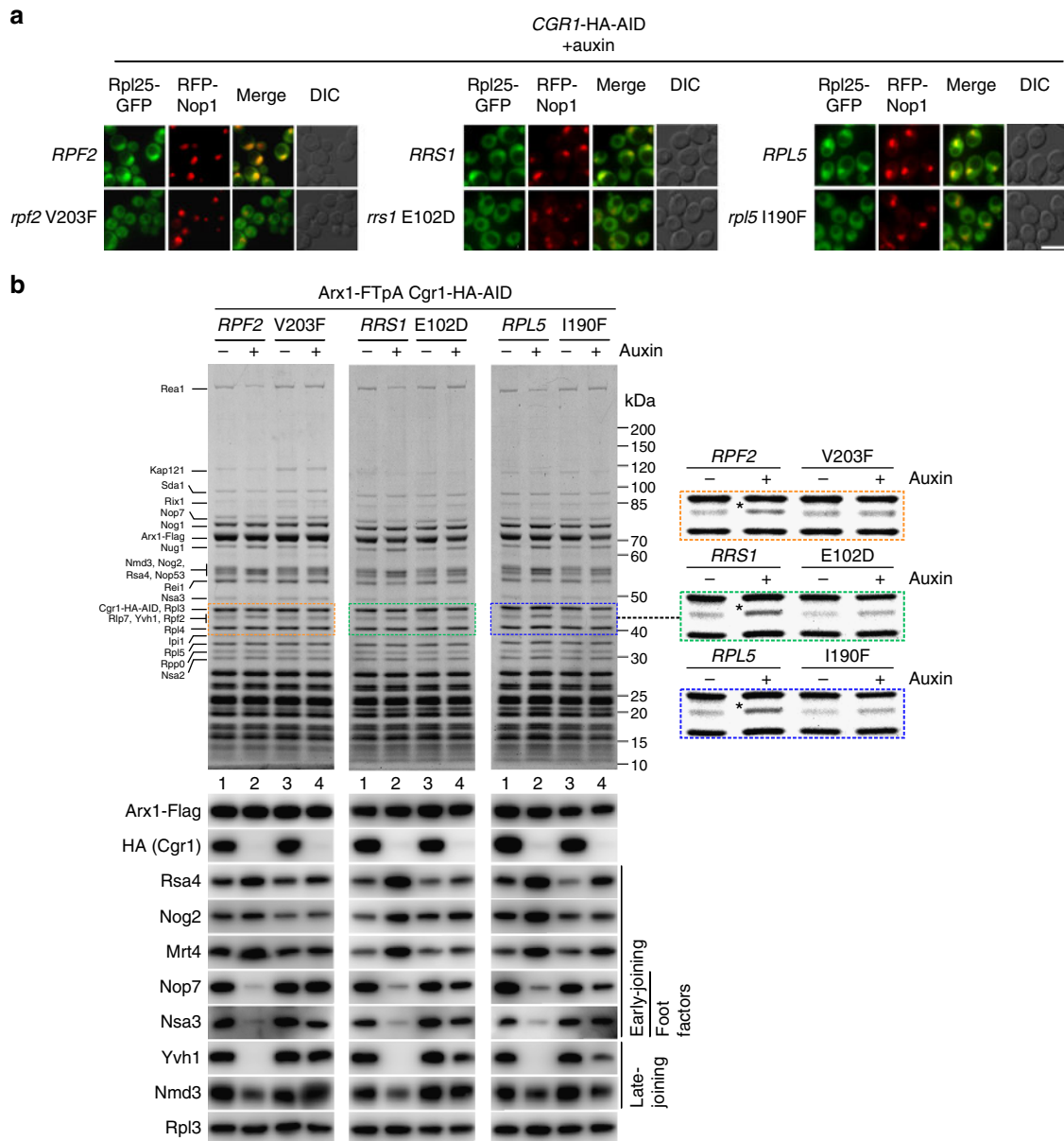


Fig. 5 Suppressor mutations in Rpf2, Rrs1 and Rpl5 rescue the 60S biogenesis defect in *Cgr1*-depleted cells. **a** Nuclear pre-60S export is restored in suppressor mutants after *Cgr1* depletion. Subcellular location of Rpl25-GFP and RFP-Nop1 (nucleolar marker) was examined in *CGR1*-HA-AID cells expressing either wild-type *RPF2*, *RRS1* and *RPL5* or the respective mutant alleles *rpf2*V203F, *rrs1*E102D and *rpl5*I190F, after incubation with auxin for 120 min. Scale bar is 5 μ m. **b** Biochemical maturation of Arx1 pre-60S particles is restored in *cgr1* Δ suppressor mutants. Arx1-FTpA particles were affinity purified from *CGR1*-HA-AID cells expressing either wild-type *RPF2*, *RRS1* or *RPL5*, or the indicated suppressor mutants before and after treatment with auxin for 120 min. Final eluates were analysed by SDS-PAGE and Coomassie staining (indicated bands were identified by mass spectrometry; upper panels) or by western blotting using the antibodies shown on the left (lower panels). The area of the Coomassie-stained SDS-polyacrylamide gel to which Rpf2 migrates is enlarged on the right to better reveal how the intensity of co-enriched Rpf2 changes, depending on *Cgr1* depletion in the various suppressor mutants

Discussion

In this study, we unveiled a function of the small conserved α -helical protein *Cgr1* (Supplementary Fig. 9) in 5S RNP rotation during 60S biogenesis, which occurs in the nucleus prior to nuclear export. Previous findings have shown that *Cgr1* decorates nuclear pre-60S particles, which are in the process of 5S RNP rotation^{20,24}. Due to its topological positioning, *Cgr1* can ideally influence progression through this maturation step, by either affecting the transition stage to overcome the rotational block or by stabilizing the rotated stage. Consistent with this interpretation, pre-60S particles are shifted back to the pre-rotational stage

in *cgr1* Δ cells, thus identifying the arrest of 60S maturation as a possible cause of the severe slow-growth phenotype of the *cgr1*-null mutant. However, this defect can be overcome by second-site revertants (i.e. extragenic suppressor mutations), which allow resumption of cell growth. Strikingly, all the isolated suppressor mutations map in only three factors—Rpf2, Rrs1 and Rpl5—which normally under wild-type conditions keep the 5S RNP on pre-60S particles in the pre-rotation stage. Thus, the identified suppressor mutations hint to the mechanism by which cells can re-locate the 5S RNP during 60S biogenesis in the absence of *Cgr1*. Accordingly, depletion of *Cgr1* results in inhibition of 5S

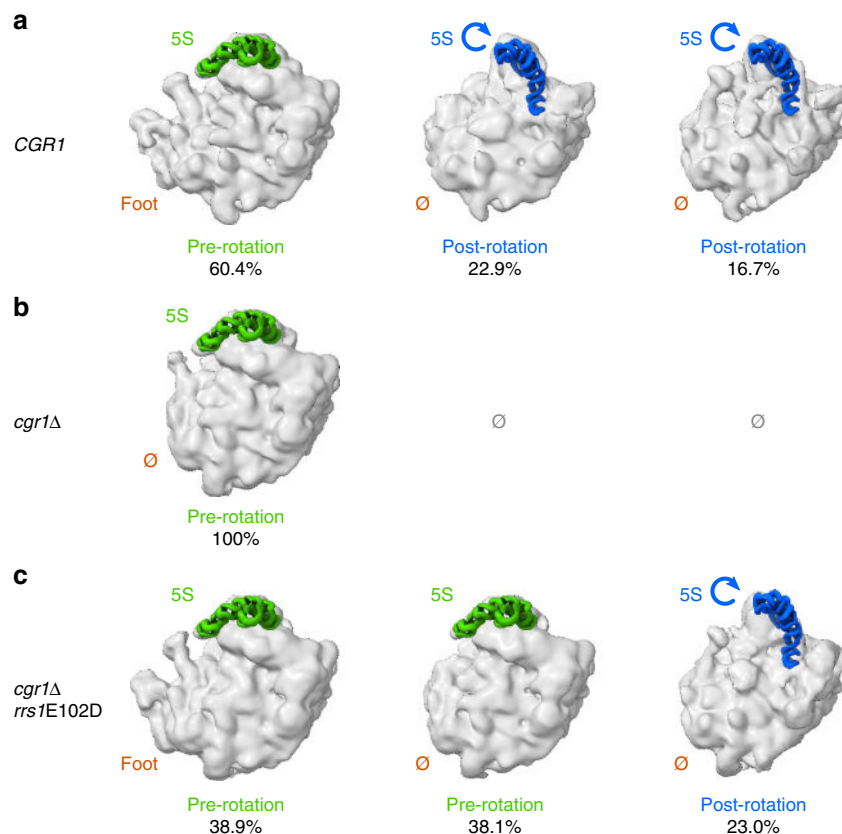


Fig. 6 Cryo-EM reveals inhibition of 5S RNP rotation in *cgr1Δ* cells but restoration in *rrs1E102D* suppressor mutant. **a–c** 3D cryo-EM reconstructions of pre-60S particles affinity purified via the Arx1 bait protein from the indicated yeast strains. **a** *CGR1* control strain: *rrs1Δ* [YCplac111-*RRS1*] Arx1-FTpA Cgr1-HA-AID; -auxin. **b** *cgr1Δ* depleted: *rrs1Δ* [YCplac111-*RRS1*] Arx1-FTpA Cgr1-HA-AID; + auxin (2 h). **c** *cgr1Δ* depleted in the presence of the *rrs1E102D* suppressor: *rrs1Δ* [YCplac111-*rrs1E102D*] Arx1-FTpA Cgr1-HA-AID + auxin (2 h). For each obtained class of the respective data set, the rotation state of the 5S is indicated by a fit model of 5S rRNA taken from PDB: 3jct (green: pre-rotation,²⁰) or PDB: 5jcs (blue: post-rotation,²⁴). Also, the presence or absence of the ITS2-harboring foot structure is indicated

RNP rotation, but suppressor mutations mapping in factors stabilizing the pre-rotational stage of the 5S RNP allow to partly overcome this defect.

As previously observed in the cryo-EM structure of the Rix1–Rea1 particle, the gently undulating C-terminal α -helix of Cgr1 is wedged between the rotated 5S RNP, the relocated A-site finger H38 and the β -propeller domain of Rsa4, thereby stabilizing the rotated 5S in a position that hinders back rotation²⁴. In the ‘early’ state 1 of Nog2 pre-60S particles (resembling the ‘early’ pool of Arx1 pre-60S particles), in which the 5S RNP is non-rotated, the binding sites for Cgr1 are very different compared to those of the rotated stage^{19,20}. Specifically, Cgr1 is located on the solvent side in the pre-rotation stage, contacting H38 as well as one tip of the unrotated 5S RNP, whereas after 5S RNP rotation, the Cgr1 α -helix adopts a more straightened conformation and is clamped between Rsa4 and the 5S RNP, thereby holding the relocated H38 in a bent position on the inter-subunit side. This rearranged topology suggests that Cgr1 accompanies or even facilitates H38 relocation from the solvent to the inter-subunit side. In addition, by snapping in after relocation, Cgr1 could stabilize the rotated 5S RNP position. It is tempting to speculate that upon initiation of the 5S RNP rotational movement, potentially induced by the recruitment of the Rix1 subcomplex²⁴, the contact between the 5S RNP and Cgr1’s C-terminal α -helix gets temporarily disconnected, which could allow H38 to slide under the detached Cgr1 C-terminus. During the subsequent 5S RNP rotation, the straightened and co-rotating Cgr1 α -helix could continuously exert pressure on H38, which helps to bring it into the new

position at the inter-subunit interface. Interestingly, in bacteria, a key role for H38 in the maturation of the CP was postulated⁵⁰. Depletion of the circularly permuted GTPase YlqF allowed the isolation of late ribosome assembly intermediates with an immature CP, which was highly disordered with no obvious structured intermediate, in contrast to the stable arrangement of the 5S RNP in the ‘early’ Arx1 particle. Nevertheless, it was shown that in these particles, H38 also adopts different orientations, and it was suggested that re-orientation of the A-site finger is a pre-requisite for stable CP formation.

In summary, this study provided mechanistic insight into the 5S RNP rotation during large subunit biogenesis and its coupling to pre-60S nuclear export. This could be achieved by combining classical yeast genetic methods with modern whole-genome high-throughput sequencing, which appears to be an effective approach to further unravel the complicated process of eukaryotic ribosome assembly.

Methods

Yeast strains and plasmids. The *Saccharomyces cerevisiae* strains used in this study were derived from W303⁴⁵ and are listed in Supplementary Table 2. Strains were constructed by using established gene disruption, genomic tagging^{51,52}, mating and tetrad dissection methods. Shuffle strains were constructed by knocking out an essential gene in a diploid yeast strain, transformation with a *URA3* plasmid containing the respective wild-type gene and sporulation to generate haploids harbouring the gene knockout and the complementing *URA3* plasmid. Subsequently, double-shuffle strains containing knockouts of *cgr1* and an essential gene (as indicated in the respective figures) complemented by two *URA3* plasmids harbouring the corresponding wild-type genes were generated by crossing

of two in the first step generated shuffle strains with opposing mating types and subsequent sporulation and identification of haploids containing both knockouts and both *URA3* plasmids (i.e. spores containing both selection markers used for the two knockouts, fast-growing on plates lacking uracil, and non-viable on 5-FOA containing plates).

The plasmids used in this study are listed in Supplementary Table 3 and were constructed according to standard DNA cloning techniques and verified by sequencing.

Identification of suppressors by high-throughput sequencing. The two suppressor mutants and the *CGRI* shuffle strain (parental control strain) were grown in YPD medium to an OD_{600} value of around 1, and cells corresponding to 20 OD_{600} units were harvested by centrifugation. Genomic DNA was extracted essentially as described in Current Protocols in Molecular Biology⁵³. After washing in dH_2O , cells were transferred to a 2.2 ml safe-seal Eppendorf tube, centrifuged again and resuspended in 200 μ l breaking buffer [100 mM NaCl, 10 mM Tris-HCl (pH 8), 1 mM EDTA (pH 8), 2% Triton X-100, 1% SDS]. After addition of 0.3 g glass beads and 200 μ l phenol-chloroform-isoamyl alcohol (49.5:49.5:1; Sigma), cells were broken by vigorous vortexing for 3 min. Then, 200 μ l of TE buffer [10 mM Tris-HCl (pH 7.5), 1 mM EDTA (pH 8)] was added and the tubes were briefly vortexed. Tubes were centrifuged for 5 min at 13,500 rpm in an Eppendorf centrifuge and the aqueous upper phase was transferred to a 1.5 ml Eppendorf tube. Then, 1 ml of absolute ethanol was added and the contents of the tubes were mixed by inversion. Following centrifugation for 3 min at 13,500 rpm, the supernatant was removed and the pellet was resuspended in 400 μ l of TE buffer. To digest the RNA, 30 μ l of a 1 mg/ml DNase-free RNase A solution (Sigma) was added and the tubes were incubated for 5 min at 37 °C. Genomic DNA was then precipitated upon addition of 10 μ l of 5 M ammonium acetate and 1 ml of absolute ethanol. After mixing by inversion, the tubes were centrifuged for 3 min at 13,500 rpm and the supernatant was discarded. Finally, the air-dried pellet was resuspended in 100 μ l of TE buffer. To estimate the integrity of the isolated genomic DNA, 2.5 μ l of the preparation was migrated on a 1% agarose gel. The concentration of the genomic DNA was determined with a Qubit 2.0 fluorimeter (Invitrogen).

Libraries were generated from 1 μ g of genomic DNA and high-throughput sequencing was performed on a HiSeq 3000 instrument (Illumina). Library preparation and Illumina sequencing were carried out by the Next Generation Sequencing (NGS) Platform of the University of Bern. The raw reads (paired-end reads of 150 bp) were processed according to the following procedure: after preparing a quality check with FastQC v0.11.2 (<https://www.bioinformatics.babraham.ac.uk/projects/fastqc/>), all the reads were filtered for quality (minimum of 20), truncated to 100 bp with Sickle v1.29⁵⁴ and then mapped with BWA-MEM v0.7.10⁵⁵ to the *S. cerevisiae* reference genome R64-1-1.79 (strain S288C) obtained from Ensembl⁵⁶. The SAM files were sorted and converted to BAM files with SAMtools v1.2⁵⁷. Single-nucleotide variants (SNVs), as well as small insertions and deletions (Indels), were identified with SAMtools and BCFtools v1.27⁵⁷. Variant annotation was added with SnpEff v4.3⁵⁸. Then, variants were filtered with SnpSift⁵⁹ to retain homozygous variants that are not found in the parental control strain and that are not 'synonymous' or 'intergenic', leading to an annotated and curated Variant Call Format (VCF) file. Results were viewed with the Integrative Genomics Viewer (IGV) software⁶⁰. Deletion of the *CGRI* gene was verified visually using IGV. Our sequence analysis revealed 13 variants for the three genomes and unambiguously identified one single-nucleotide change within the *RPF2* gene in each suppressor strain.

Yeast affinity purification. Two-step affinity purifications were performed with either N-terminally TAP-Flag- or C-terminally Flag-TEV-proteinA (FTpA)-tagged bait proteins. The respective yeast strains were grown in 2 l of YPD medium at 30 °C, harvested in the logarithmic growth phase, flash frozen in liquid nitrogen and stored at -80 °C. Where indicated in the figures, cultures were incubated in the presence of 0.5 mM auxin (3-indoleacetic acid, Sigma-Aldrich) for 120 min prior to harvesting the cells. Cell pellets were resuspended in 'lysis buffer' [50 mM Tris-HCl (pH 7.5), 100 mM NaCl, 5 mM $MgCl_2$, 0.05% NP-40, 1 mM DTT, supplemented with 1 mM PMSF, 1 \times SIGMAFAST protease inhibitor (Sigma-Aldrich)], and cells were ruptured by shaking in a bead beater (Fritsch) in the presence of glass beads. Lysates were cleared by two subsequent centrifugation steps at 4 °C for 10 and 30 min at 5000 and 14,000 rpm, respectively. Supernatants were incubated with immunoglobulin G (IgG) Sepharose 6 Fast Flow beads (GE Healthcare) on a rotating wheel at 4 °C for 90 min. Beads were transferred into Mobicol columns (Mobic) and, after washing with 10 ml of lysis buffer, cleavage with tobacco etch virus (TEV) protease was performed at 16 °C for 120 min. In a second purification step, TEV eluates were incubated with Flag agarose beads (ANTI-FlagM2 Affinity Gel, Sigma-Aldrich) for 60 min at 4 °C. After washing with 5 ml of lysis buffer, bound proteins were eluted with lysis buffer containing 300 μ g/ml Flag peptide at 4 °C for 45 min. Buffer lacking NP-40 was used for the last purification step in samples used for cryo-EM. Flag eluates were analysed by SDS-PAGE on 4-12% polyacrylamide gels (NuPAGE, Invitrogen) with colloidal Coomassie staining (Roti-blue, Roth) or by western blotting with antibodies, as indicated in the respective figures. Uncropped gel and western blot images are shown in Supplementary Fig. 10.

Cryo electron microscopy. Cryo electron microscopy was performed for three different purifications: (1) *rrs1 Δ* [YCplac111-*RRS1*] Arx1-FTpA Cgr1-HA-AID; -auxin. (2) *cgr1 Δ* depleted: *rrs1 Δ* [YCplac111-*RRS1*] Arx1-FTpA Cgr1-HA-AID; + auxin (2 h). (3) *cgr1 Δ* depleted in the presence of the *rrs1E102D* suppressor: *rrs1 Δ* [YCplac111-*rrs1E102D*] Arx1-FTpA Cgr1-HA-AID + auxin (2 h).

For each purification, Quantifoil holy carbon grids (R3/3, +2 nm carbon) were glow discharged at 2.2×10^{-1} torr for 20 s. Then for each grid, 3.5 μ l of sample concentrated to 1.8 OD_{260} /ml was applied and plunge frozen in liquid ethane using a vitrobot mark IV (FEI), operating at 5 °C and 90% humidity, blotting for 2 s after a 45 s incubation. For each sample 400 micrograph were recorded on a Tecnai Spirit (FEI) operating at 120 kV, equipped with a TEMCam F216 (TVIPS, Germany). Semi-automated micrograph acquisition was performed using the EM-Tools software suite (TVIPS, Germany).

Image processing. GCTF⁶¹ was used to estimate the contrast transfer function parameters. Micrographs with a defocus in the range of 0.8-3.2 μ m were used for further processing. Template free particle picking was performed with Gautomatch (<http://www.mrc-lmb.cam.ac.uk/kzhang>). All further image processing (classifications, refinements, and post processing) was performed using Relion-2.1⁶², analogously for all data sets as described in the following. First, the particle sets were cleaned using reference free 2D classification to eliminate falsely picked particles. Then, a consensus refinement was performed using EMD-3199²⁴ as a reference. To address structural heterogeneity, multiple subsequent steps of alignment free 3D classification was performed. After every classification step, similar classes were joined and all remaining classes were refined and subsorted to check for additional heterogeneity (see Supplementary Fig. 8). For the *cgr1 Δ* depleted sample, all classification attempts failed to separate the particles into subsets with structurally distinguishable features, resulting in one final class.

Western blotting. Western blot analysis was performed using the following antibodies: anti-Nog1 antibody (1:5000), anti-Nog2 antibody (1:20,000), anti-Arx1 antibody (1:2000), anti-Rei1 antibody (1:10,000), anti-Nsa2 antibody (1:10,000), anti-Rlp24 antibody (1:2000), provided by Micheline Fromont-Racine, anti-Nug1 antibody (1:10,000), anti-Yvh1 antibody (1:4000), provided by Vikram Panse, anti-Nmd3 antibody (1:10,000), anti-Rpl10 antibody (1:10,000), provided by Arlen Johnson, anti-Rpl3 antibody (1:5000), provided by Jonathan Warner, anti-Rpl5 antibody (1:10,000), provided by John Woolford, anti-Nop7 antibody (1:50,000), provided by Bruce Stillman, anti-Rsa4 antibody (1:10,000), provided by Miguel Remacha, anti-Mrt4 antibody (1:1000), provided by Juan Pedro Ballesta, anti-Arc1 antibody (1:5000), raised in our lab, anti-HA antibody (1:10,000, Covance Research Products, MMS-101R), horseradish-peroxidase-conjugated anti-Flag antibody (1:15,000, Sigma-Aldrich, A8592), secondary horseradish-peroxidase-conjugated goat anti-rabbit antibody (1:2000, Bio-Rad-170-6515), secondary horseradish-peroxidase-conjugated goat anti-mouse antibody (1:2000, Bio-Rad-170-6516).

Polysome profile analyses. Cells expressing chromosomal C-terminal fusions of Cgr1 tagged with HA-AID (*CGRI-HA-AID*) were grown in YPD medium to early logarithmic growth phase. Prior to harvesting, cultures were incubated with 0.5 mM auxin for 120 min to induce proteasomal degradation of Cgr1-HA-AID or left untreated. Subsequently, 100 μ g/ml cycloheximide was added and after incubation for 10 min on ice, cells were pelleted and washed once with lysis buffer [50 mM Tris-HCl (pH 7.5), 100 mM KCl, 12 mM $MgCl_2$, 100 μ g/ml cycloheximide]. After resuspension in lysis buffer and cell lysis with glass beads, 6 A_{260} units of the cell extracts were loaded onto 10-50% sucrose gradients [dissolved in 50 mM Tris-HCl (pH 7.5), 100 mM KCl, 12 mM $MgCl_2$] and centrifuged with a SW40 rotor (Beckman Coulter) at 39,000 rpm for 2 h 45 min at 4 °C. Gradients were analysed on a Foxy Jr. fraction collector (Teledyne ISCO) with continuous monitoring at 254 nm.

Fluorescence microscopy. Living yeast cells expressing GFP- or RFP-tagged proteins were grown to the logarithmic growth phase and imaged by fluorescence microscopy using a Zeiss Imager Z1 microscope. As indicated, auxin was added to a final concentration of 0.5 mM and cells were subsequently incubated for 120 min prior to imaging.

Data availability

All relevant data supporting the findings of this study can be found in the results or the supplementary information section and are available from the corresponding authors upon request. All experiments were performed at least twice with similar outcome. Cryo-EM densities of maps 1-7 of the Arx1 particles have been deposited in the Electron Microscopy Data Bank and can be retrieved using the following accession codes, respectively: EMDB-0218, EMDB-0219, EMDB-0220, EMDB-0221, EMDB-0222, EMDB-0223, EMDB-0224.

Received: 26 April 2018 Accepted: 17 September 2018

Published online: 05 October 2018

References

- de la Cruz, J., Karbstein, K. & Woolford, J. L. Functions of ribosomal proteins in assembly of eukaryotic ribosomes in vivo. *Annu. Rev. Biochem.* **84**, 93–129 (2015).
- Kressler, D., Hurt, E. & Bassler, J. Driving ribosome assembly. *Biochim. Biophys. Acta* **1803**, 673–683 (2010).
- Kressler, D., Hurt, E. & Baßler, J. A puzzle of life: crafting ribosomal subunits. *Trends Biochem. Sci.* **42**, 640–654 (2017).
- Peña, C., Hurt, E. & Panse, V. G. Eukaryotic ribosome assembly, transport and quality control. *Nat. Struct. Mol. Biol.* **24**, 689–699 (2017).
- Woolford, J. L. & Baserga, S. J. Ribosome biogenesis in the yeast *Saccharomyces cerevisiae*. *Genetics* **195**, 643–681 (2013).
- Chaker-Margot, M., Hunziker, M., Barandun, J., Dill, B. D. & Klinge, S. Stage-specific assembly events of the 6-MDa small-subunit processome initiate eukaryotic ribosome biogenesis. *Nat. Struct. Mol. Biol.* **22**, 920–923 (2015).
- Chaker-Margot, M., Barandun, J., Hunziker, M. & Klinge, S. Architecture of the yeast small subunit processome. *Science* **355**, ea11880 (2017).
- Cheng, J., Kellner, N., Berninghausen, O., Hurt, E. & Beckmann, R. 3.2-Å-resolution structure of the 90S preribosome before A1 pre-rRNA cleavage. *Nat. Struct. Mol. Biol.* **24**, 954–964 (2017).
- Kornprobst, M. et al. Architecture of the 90S pre-ribosome: a structural view on the birth of the eukaryotic ribosome. *Cell* **166**, 380–393 (2016).
- Sun, Q. et al. Molecular architecture of the 90S small subunit pre-ribosome. *Elife* **6**, e22086 (2017).
- Ben-Shem, A. et al. The structure of the eukaryotic ribosome at 3.0 Å resolution. *Science* **334**, 1524–1529 (2011).
- Khatler, H., Myasnikov, A. G., Natchiar, S. K. & Klaholz, B. P. Structure of the human 80S ribosome. *Nature* **520**, 640–645 (2015).
- Gamalinda, M. et al. A hierarchical model for assembly of eukaryotic 60S ribosomal subunit domains. *Genes Dev.* **28**, 198–210 (2014).
- Kater, L. et al. Visualizing the assembly pathway of nucleolar Pre-60S ribosomes. *Cell* **171**, 1599–1610 (2017). e14.
- Sanghai, Z. A. et al. Modular assembly of the nucleolar pre-60S ribosomal subunit. *Nature* **556**, 126–129 (2018).
- Zhou, D. et al. Cryo-EM structure of an early precursor of large ribosomal subunit reveals a half-assembled intermediate. *Protein Cell*. <https://doi.org/10.1007/s13238-018-0526-7> (2018).
- Zhang, J. et al. Assembly factors Rpf2 and Rrs1 recruit 5S rRNA and ribosomal proteins rpl5 and rpl11 into nascent ribosomes. *Genes Dev.* **21**, 2580–2592 (2007).
- Bradatsch, B. et al. Structure of the pre-60S ribosomal subunit with nuclear export factor Arx1 bound at the exit tunnel. *Nat. Struct. Mol. Biol.* **19**, 1234–1241 (2012).
- Leidig, C. et al. 60S ribosome biogenesis requires rotation of the 5S ribonucleoprotein particle. *Nat. Commun.* **5**, 3491 (2014).
- Wu, S. et al. Diverse roles of assembly factors revealed by structures of late nuclear pre-60S ribosomes. *Nature* **534**, 133–137 (2016).
- Bassler, J. et al. The AAA-ATPase Rea1 drives removal of biogenesis factors during multiple stages of 60S ribosome assembly. *Mol. Cell* **38**, 712–721 (2010).
- Thoms, M., Ahmed, Y. L., Maddi, K., Hurt, E. & Sinning, I. Concerted removal of the Erb1-Ytm1 complex in ribosome biogenesis relies on an elaborate interface. *Nucleic Acids Res.* **44**, 926–939 (2016).
- Wegrecki, M., Rodríguez-Galán, O., de la Cruz, J. & Bravo, J. The structure of Erb1-Ytm1 complex reveals the functional importance of a high-affinity binding between two β-propellers during the assembly of large ribosomal subunits in eukaryotes. *Nucleic Acids Res.* **43**, 11017–11030 (2015).
- Barrio-García, C. et al. Architecture of the Rix1-Rea1 checkpoint machinery during pre-60S-ribosome remodeling. *Nat. Struct. Mol. Biol.* **23**, 37–44 (2016).
- Ulbrich, C. et al. Mechanochemical removal of ribosome biogenesis factors from nascent 60S ribosomal subunits. *Cell* **138**, 911–922 (2009).
- Matsuo, Y. et al. Coupled GTPase and remodelling ATPase activities form a checkpoint for ribosome export. *Nature* **505**, 112–116 (2014).
- Kappel, L. et al. Rlp24 activates the AAA-ATPase Drg1 to initiate cytoplasmic pre-60S maturation. *J. Cell Biol.* **199**, 771–782 (2012).
- Pertschy, B. et al. Cytoplasmic recycling of 60S preribosomal factors depends on the AAA protein Drg1. *Mol. Cell Biol.* **27**, 6581–6592 (2007).
- Greber, B. J. et al. Insertion of the biogenesis factor Rei1 probes the ribosomal tunnel during 60S maturation. *Cell* **164**, 91–102 (2016).
- Lo, K.-Y. et al. Defining the pathway of cytoplasmic maturation of the 60S ribosomal subunit. *Mol. Cell* **39**, 196–208 (2010).
- Kemmler, S., Occhipinti, L., Veisu, M. & Panse, V. G. Yvh1 is required for a late maturation step in the 60S biogenesis pathway. *J. Cell Biol.* **186**, 863–880 (2009).
- Lo, K.-Y., Li, Z., Wang, F., Marcotte, E. M. & Johnson, A. W. Ribosome stalk assembly requires the dual-specificity phosphatase Yvh1 for the exchange of Mrt4 with P0. *J. Cell Biol.* **186**, 849–862 (2009).
- Hedges, J., West, M. & Johnson, A. W. Release of the export adapter, Nmd3p, from the 60S ribosomal subunit requires Rpl10p and the cytoplasmic GTPase Lsg1p. *EMBO J.* **24**, 567–579 (2005).
- Ma, C. et al. Structural snapshot of cytoplasmic pre-60S ribosomal particles bound by Nmd3, Lsg1, Tif6 and Reh1. *Nat. Struct. Mol. Biol.* **24**, 214–220 (2017).
- Malyutin, A. G., Musalgaonkar, S., Patchett, S., Frank, J. & Johnson, A. W. Nmd3 is a structural mimic of eIF5A, and activates the cpGTPase Lsg1 during 60S ribosome biogenesis. *EMBO J.* **36**, 854–868 (2017).
- Weis, F. et al. Mechanism of eIF6 release from the nascent 60S ribosomal subunit. *Nat. Struct. Mol. Biol.* **22**, 914–919 (2015).
- Calviño, F. R. et al. Symportin 1 chaperones 5S RNP assembly during ribosome biogenesis by occupying an essential rRNA-binding site. *Nat. Commun.* **6**, 6510 (2015).
- Kressler, D. et al. Synchronizing nuclear import of ribosomal proteins with ribosome assembly. *Science* **338**, 666–671 (2012).
- Asano, N. et al. Structural and functional analysis of the Rpf2-Rrs1 complex in ribosome biogenesis. *Nucleic Acids Res.* **43**, 4746–4757 (2015).
- Kharde, S., Calviño, F. R., Gumiero, A., Wild, K. & Sinning, I. The structure of Rpf2-Rrs1 explains its role in ribosome biogenesis. *Nucleic Acids Res.* **43**, 7083–7095 (2015).
- Madru, C. et al. Chaperoning 5S RNA assembly. *Genes Dev.* **29**, 1432–1446 (2015).
- Moy, T. I., Boettner, D., Rhodes, J. C., Silver, P. A. & Askew, D. S. Identification of a role for *Saccharomyces cerevisiae* Cgr1p in pre-rRNA processing and 60S ribosome subunit synthesis. *Microbiol. (Read., Engl.)* **148**, 1081–1090 (2002).
- Sun, J. et al. Cgr1p, a novel nucleolar protein encoded by *Saccharomyces cerevisiae* orf YGL0292w. *Curr. Microbiol.* **42**, 65–69 (2001).
- Tarassov, K. et al. An in vivo map of the yeast protein interactome. *Science* **320**, 1465–1470 (2008).
- Thomas, B. J. & Rothstein, R. Elevated recombination rates in transcriptionally active DNA. *Cell* **56**, 619–630 (1989).
- Nishimura, K., Fukagawa, T., Takisawa, H., Kakimoto, T. & Kanemaki, M. An auxin-based degron system for the rapid depletion of proteins in nonplant cells. *Nat. Methods* **6**, 917–922 (2009).
- Nissan, T. A., Bassler, J., Petfalski, E., Tollervey, D. & Hurt, E. 60S pre-ribosome formation viewed from assembly in the nucleolus until export to the cytoplasm. *EMBO J.* **21**, 5539–5547 (2002).
- Wehner, K. A. & Baserga, S. J. The sigma(70)-like motif: a eukaryotic RNA binding domain unique to a superfamily of proteins required for ribosome biogenesis. *Mol. Cell* **9**, 329–339 (2002).
- Baßler, J. et al. A network of assembly factors is involved in remodeling rRNA elements during preribosome maturation. *J. Cell Biol.* **207**, 481–498 (2014).
- Li, N. et al. Cryo-EM structures of the late-stage assembly intermediates of the bacterial 50S ribosomal subunit. *Nucleic Acids Res.* **41**, 7073–7083 (2013).
- Janke, C. et al. A versatile toolbox for PCR-based tagging of yeast genes: new fluorescent proteins, more markers and promoter substitution cassettes. *Yeast* **21**, 947–962 (2004).
- Longtine, M. S. et al. Additional modules for versatile and economical PCR-based gene deletion and modification in *Saccharomyces cerevisiae*. *Yeast* **14**, 953–961 (1998).
- Ausubel, F. M. et al. *Current Protocols in Molecular Biology* 2.13.11.1–13.11.4 (John Wiley & Sons, Inc, New York, NY, 1994).
- Joshi, N. A. and Fass, J. N. (2011). SickLe: A sliding-window, adaptive, quality-based trimming tool for FastQ files (Version 1.33) [Software]. 26 April 2018 Available at <https://github.com/najoshi/sickle>
- Li, H. & Durbin, R. Fast and accurate long-read alignment with Burrows-Wheeler transform. *Bioinformatics* **26**, 589–595 (2010).
- Yates, A. et al. Ensembl 2016. *Nucleic Acids Res.* **44**, D710–D716 (2016).
- Li, H. A statistical framework for SNP calling, mutation discovery, association mapping and population genetical parameter estimation from sequencing data. *Bioinformatics* **27**, 2987–2993 (2011).
- Cingolani, P. et al. A program for annotating and predicting the effects of single nucleotide polymorphisms, SnpEff: SNPs in the genome of *Drosophila melanogaster* strain w1118; iso-2; iso-3. *Fly. (Austin)* **6**, 80–92 (2012).
- Cingolani, P. et al. Using *Drosophila melanogaster* as a model for genotoxic chemical mutational studies with a new program, SnpSift. *Front. Genet.* **3**, 35 (2012).
- Thorvaldsdóttir, H., Robinson, J. T. & Mesirov, J. P. Integrative Genomics Viewer (IGV): high-performance genomics data visualization and exploration. *Brief. Bioinforma.* **14**, 178–192 (2013).
- Zhang, K. Gctf: Real-time CTF determination and correction. *J. Struct. Biol.* **193**, 1–12 (2016).
- Kimanius, D., Forsberg, B. O., Scheres, S. H. & Lindahl, E. Accelerated cryo-EM structure determination with parallelisation using GPUs in RELION-2. *Elife* **5**, e18722 (2016).

Acknowledgements

We would like to thank Marén Gnädig for excellent technical support. We are grateful to Micheline Fromont-Racine, Vikram Panse, Arlen Johnson, Jonathan Warner, John Woolford, Bruce Stillman, Miguel Remacha and Juan Pedro Ballesta for the generous gift of antibodies. The research was supported by the Deutsche Forschungsgemeinschaft DFG (grants HU363/10-5, HU363/12-1 to E.H.) and by the Swiss National Science Foundation (grants 31003A_156764 and 31003A_175547 to D.K.).

Author contributions

M.T. and E.H. conceived the study. M.T. and V.M. constructed yeast strains and plasmids. M.T., V.M., L.K., L.F. and D.K. performed the experiments. M.T., V.M., L.K., L.F., R.B., D.K. and E.H. analysed the data and discussed the results. M.T., V.M. and E.H. wrote the manuscript and all authors commented on the manuscript.

Additional information

Supplementary Information accompanies this paper at <https://doi.org/10.1038/s41467-018-06660-w>.

Competing interests: The authors declare no competing interests.

Reprints and permission information is available online at <http://npg.nature.com/reprintsandpermissions/>





Publisher's note: Springer Nature remains neutral with regard to jurisdictional claims in published maps and institutional affiliations.



Open Access This article is licensed under a Creative Commons Attribution 4.0 International License, which permits use, sharing, adaptation, distribution and reproduction in any medium or format, as long as you give appropriate credit to the original author(s) and the source, provide a link to the Creative Commons license, and indicate if changes were made. The images or other third party material in this article are included in the article's Creative Commons license, unless indicated otherwise in a credit line to the material. If material is not included in the article's Creative Commons license and your intended use is not permitted by statutory regulation or exceeds the permitted use, you will need to obtain permission directly from the copyright holder. To view a copy of this license, visit <http://creativecommons.org/licenses/by/4.0/>.

© The Author(s) 2018

Partially inserted nascent chain unzips the lateral gate of the Sec translocon

Lukas Kater¹, Benedikt Frieg² , Otto Berninghausen¹, Holger Gohlke^{2,3,*} , Roland Beckmann^{1,**}  & Alexej Kedrov^{1,4,***} 

Abstract

The Sec translocon provides the lipid bilayer entry for ribosome-bound nascent chains and thus facilitates membrane protein biogenesis. Despite the appreciated role of the native environment in the translocon:ribosome assembly, structural information on the complex in the lipid membrane is scarce. Here, we present a cryo-electron microscopy-based structure of bacterial translocon SecYEG in lipid nanodiscs and elucidate an early intermediate state upon insertion of the FtsQ anchor domain. Insertion of the short nascent chain causes initial displacements within the lateral gate of the translocon, where α -helices 2b, 7, and 8 tilt within the membrane core to “unzip” the gate at the cytoplasmic side. Molecular dynamics simulations demonstrate that the conformational change is reversed in the absence of the ribosome, and suggest that the accessory α -helices of SecE subunit modulate the lateral gate conformation. Site-specific cross-linking validates that the FtsQ nascent chain passes the lateral gate upon insertion. The structure and the biochemical data suggest that the partially inserted nascent chain remains highly flexible until it acquires the transmembrane topology.

Keywords membrane protein insertion; nanodisc; native environment; reconstitution; ribosome

Subject Categories Membranes & Trafficking; Structural Biology

DOI 10.15252/embr.201948191 | Received 29 March 2019 | Revised 10 July 2019 | Accepted 16 July 2019 | Published online 5 August 2019

EMBO Reports (2019) 20: e48191

See also: Y Tanaka & T Tsukazaki et al (October 2019)

Introduction

Membrane proteins constitute a large part of the cellular proteome and determine the vital functionality and identity of biological membranes. These proteins are co-translationally targeted as ribosome:

nascent chain complexes (RNCs) to the endoplasmic reticulum in eukaryotes and the cytoplasmic membrane in bacteria and archaea, where they are inserted by the dedicated and universally conserved Sec translocon (Fig 1A and B) [1]. The translocon, an integral membrane protein itself, builds a protein-conducting channel in the lipid bilayer and allows either transmembrane passage of nascent polypeptide chains or their partitioning into the lipid environment as transmembrane α -helices (TMHs). The nascent chain hydrophobicity forms a basis for the triage [2]. The central subunit of the translocon, SecY in bacteria or Sec61 α in eukaryotes, consists of 10 TMHs arranged as a pseudo-symmetric “clam-shell” with a protein-conducting pore between the N- and C-terminal parts (Fig 1) [3,4]. A bilayer-facing crevice between SecY TMHs 2b and 7 is assumed to serve as a route, or a “lateral gate”, for nascent TMHs to reach the hydrophobic membrane core. SecY is stabilized at the periphery by the essential subunit SecE/Sec61 γ that contains two α -helices, one in interfacial and one in transmembrane topologies. SecE of some Gram-negative bacteria, including *Escherichia coli*, contains also an accessory pair of N-terminal TMHs, the role and localization of which have remained largely unclear [5]. A non-essential and non-conserved SecG/Sec6 β subunit near the N-terminal half of SecY is built of either one or two TMHs and plays a stimulatory role in protein translocation [6].

The assembly of the translocon:ribosome complex at the cytoplasmic membrane interface is a key step in membrane protein biogenesis, as it allows the hydrophobic nascent chain to egress into the lipid bilayer via the translocon, while not being exposed to the polar aqueous environment [1,7]. The architecture of the complex has been extensively studied by structural methods, first of all cryo-electron microscopy (cryo-EM) [8–11]. Binding of a ribosome results in minor rearrangements within the translocon and brings it to a pre-open or “primed” state [11]. The following insertion of a sufficiently hydrophobic helical domain, such as a signal sequence or signal anchor domain, shifts the complete N-terminal domain of SecY/Sec61 α by 22° and also tilts TMH 7, so the lateral gate of the translocon acquires an open state (Fig 1B) [12,13]. The folded signal

1 Gene Center Munich, Ludwig-Maximilians-University, Munich, Germany

2 John von Neumann Institute for Computing, Jülich Supercomputing Centre, Institute for Complex Systems - Structural Biochemistry (ICS-6), Forschungszentrum Jülich GmbH, Jülich, Germany

3 Institute for Pharmaceutical and Medicinal Chemistry, Heinrich Heine University Düsseldorf, Düsseldorf, Germany

4 Synthetic Membrane Systems, Institute for Biochemistry, Heinrich Heine University Düsseldorf, Düsseldorf, Germany

*Corresponding author. Tel: +49 211 81 13662; E-mail: gohlke@hhu.de

**Corresponding author. Tel: +40 89 2180 76900; E-mail: beckmann@genzentrum.lmu.de

***Corresponding author. Tel: +49 211 81 13731; E-mail: kedrov@hhu.de

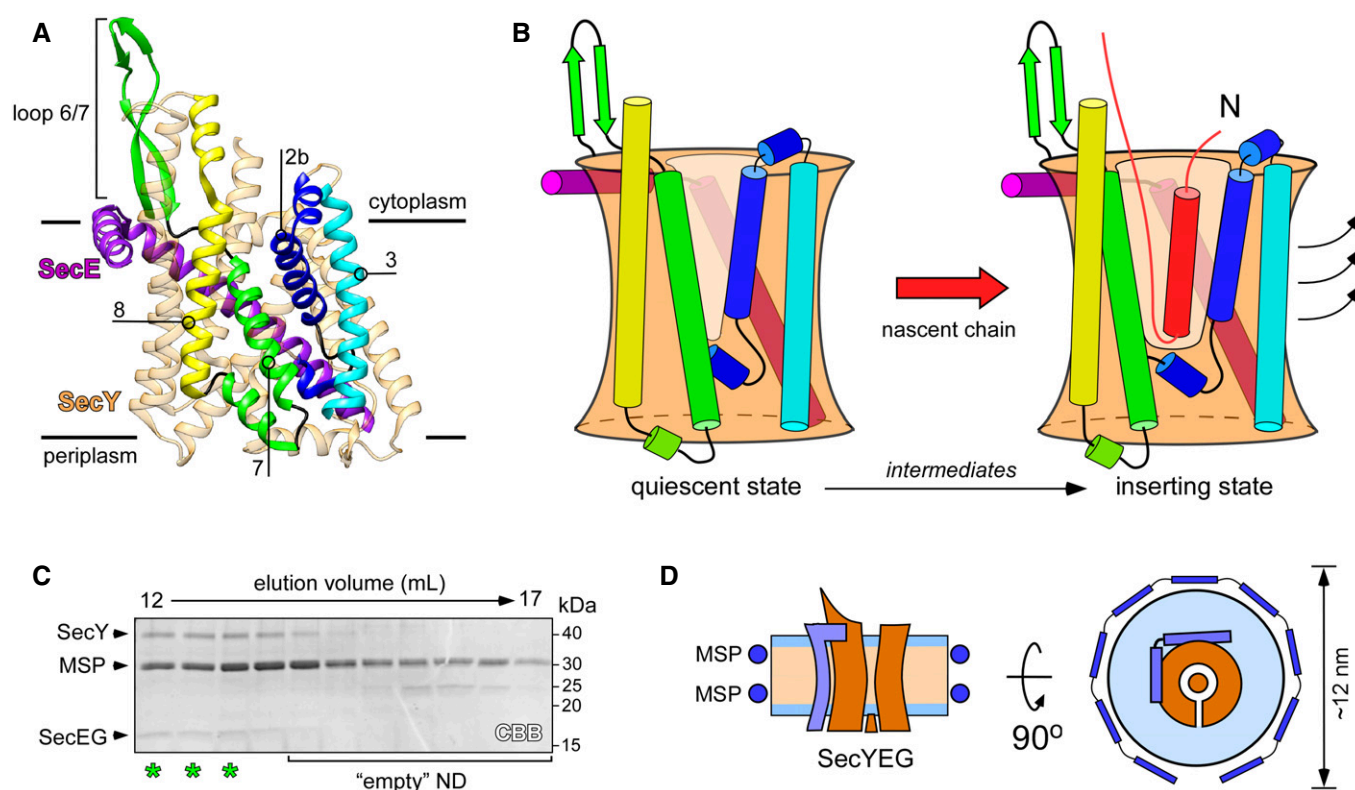


Figure 1. Structure and dynamics of SecYEG translocon.

- A Structure of quiescent SecYEG of *Thermus thermophilus* in the lipid cubic phase (PDB ID: 5AWW). TMHs 2b, 3, 7, and 8 of the lateral gate, as well as the proximate loop 6/7 involved in ribosome binding are indicated. The non-essential SecG subunit is omitted for clarity.
- B Model of the SecY lateral gate opening upon inserting a nascent chain (red) in the lipid bilayer. The color-coding of SecYE TMHs is as in panel (A). In the presence of the completely inserted and folded nascent chain, TMHs 2b and 3 of the N-terminal domain of SecY are displaced (arrows) thus opening a broad passage for the nascent TMH toward the lipid moiety.
- C SDS-PAGE of SecYEG-ND sample after size-exclusion chromatography. Asterisks indicate translocon-enriched fractions used for forming the RNC FtsQ:SecYEG-ND complex. Lipid-loaded “empty” nanodiscs elute at larger volumes and so can be separated.
- D Schematic drawing of a SecYEG-ND particle. Lateral dimensions of the nanodisc should be appropriate to accommodate a single SecYEG with surrounding lipids, thus mimicking the naturally occurring environment.

sequence in a transbilayer topology may occupy the lateral gate where it replaces TMH 2b. Upon the further elongation of the nascent polypeptide chain, the newly inserted α -helix leaves the lateral gate and egresses into the lipid bilayer, and the translocon undergoes a reverse transition from a widely opened [14] to a compact, pre-closed state [15].

Although the dynamics of the lateral gate have been commonly acknowledged [16,17], the mechanism of the nascent chain insertion remains unclear. First, existing structures reflect rather late insertion stages, where the signal sequence has been fully inserted in the transmembrane topology, while early intermediates have been barely addressed [4,18]. Second, a vast majority of available ribosome:translocon structures represent detergent-solubilized complexes; however, the non-physiological environment and extensive downstream purification schemes may significantly affect the conformation and the interaction properties of membrane proteins, including the translocon [19–21]. The variations in detergent-based solubilization protocols may explain contradictory results on the translocon dynamics, where either a local displacement of helices within the lateral gate or an extensive movement of the complete

N-terminal half was observed upon the nascent chain insertion, and also the conformation of the central “plug” domain has been disputed [12,13,22]. Furthermore, a compact “primed” state has been described for detergent-solubilized translocons in the absence of hydrophobic nascent chains [11], while a recent cryo-electron tomography analysis has revealed a predominantly open conformation of the ribosome-bound Sec61 within native ER membranes and so suggested a crucial effect of the molecular environment on protein dynamics [23].

Up to date, the only structure of the translocon:ribosome complex at the lipid interface was obtained by cryo-EM when using nanodisc-reconstituted SecYEG (SecYEG-ND) bound to a translation-stalled RNC [14]. Although demonstrating an advance compared to detergent-solubilized systems, the structure offers only limited resolution and also illustrates a rather late stage of the TMH insertion, with the translocon lateral gate widely open and the inserted anchor domain de-localized within the membrane. Here, we set out to determine the structure of the SecYEG:RNC complex that would describe an early stage of a transmembrane domain insertion into the lipid bilayer. Using cryo-EM and single-particle

analysis, we resolved for the first time all three subunits of SecYEG in nanodiscs and described a novel conformation, where SecY TMHs 2b and 7 were apart at the cytoplasmic side to form a V-shaped lateral gate that is pre-opened for the nascent chain insertion, while accessory SecE TMHs 1 and 2 interacted with the gate at the periplasmic side. The RNC-induced dynamics within the translocon was validated by atomistic molecular dynamics simulations, which also described the interactions of SecYEG with anionic lipids. Cryo-EM data and site-specific chemical cross-linking further suggested that the FtsQ anchor domain is inserted via the lateral gate, where it forms close contacts with SecY TMH 7, but remains highly flexible before leaving the translocon.

Results and Discussion

Functional reconstitution of *E. coli* SecYEG in nanodiscs has been previously performed by several groups for biochemical, biophysical, and structural studies and allowed probing of the translocon interactions with the motor protein SecA, targeting factors, and ribosomes [14,20,24,25]. The diameter of formed nanodiscs is essentially determined by the length of the major scaffold protein (MSP) that girdles the lipid bilayer [26,27]. Translocon molecules have been initially embedded into nanodiscs as small as 9 nm in diameter [16,20,24]. However, a follow-up functional analysis demonstrated that larger nanodisc dimensions are beneficial for facilitating the translocation activity, likely due to the increased amount of co-reconstituted lipids [25,28]. Thus, we used an extended scaffold protein MSP1E3D1 and POPG/POPC lipids to reconstitute SecYEG into nanodiscs with a diameter of approximately 12 nm. A large excess of MSPs and lipids ensured that translocons were reconstituted predominantly as monomers [25], as those have been shown to be the principle functional form both in bacteria and in eukaryotes [9,29,30]. Due to solvent-exposed loops of SecYEG, which contributed to the hydrodynamic radius, SecYEG-ND could be separated from “empty” nanodiscs containing only lipids by means of size-exclusion chromatography (Fig 1C). Within formed nanodiscs, SecYEG would occupy ~30% of the surface area (Fig 1D) [25,26,28], thus providing sufficient space for the conformational dynamics, and for insertion of nascent TMHs upon interactions with RNCs.

We have previously demonstrated that SecYEG:ribosome assembly is strongly enhanced by hydrophobic nascent chains, such as a TMH of FtsQ, a model protein for studying the SecYEG-mediated insertion pathway [20]. The hydrophobic polypeptide exposed from a ribosome exit tunnel is sufficient to mediate SecYEG:ribosome binding in native and model membranes, even in the absence of targeting factors [20,31], but unlikely to undergo the complete insertion due to its short ribosome-bound linker. Thus, to investigate an early stage of the TMH insertion, we prepared translation-stalled ribosomes, which exposed the first 48 amino acids of FtsQ, including the TMH within the nascent chain (Fig EV1), and incubated those with a 10-fold excess of SecYEG-ND to achieve complex formation. After vitrification, samples were subjected to cryo-EM imaging and single-particle analysis. RNCs could be readily seen in raw micrographs, and a discoidal density of SecYEG-ND bound to RNCs was observed in projection groups of two-dimensional (2D) classification and in 3D reconstructions (Fig 2A–C). After sorting and refinement steps (Fig EV2), the ribosome structure was resolved at 3.3 Å, and

independent refinement of the SecYEG-ND:RNC complex elements led to 3.2 and 3.1 Å resolution for the small (30S) and large (50S) ribosomal subunits, respectively (Appendix Fig S1), and was limited to 6 Å for the lipid-embedded SecYEG due to its small size and apparent dynamics relative to the 50S ribosomal subunit (Movie EV1). The local resolution within the SecYEG-ND particle ranged from 3.5 Å at the ribosome contact sites to 6–7 Å within the transmembrane core and above 10 Å for the surrounding MSP1E3D1 and lipid head groups, which could be visualized at lower threshold levels (Fig 2D and E).

In agreement with the initial prediction, the nanodisc dimensions were sufficiently large to accommodate a single copy of SecYEG. As SecYEG was positioned in the center of the nanodisc and contacts with edges of the lipid bilayer or MSP were not observed, it is likely that the translocon conformation was not affected by the confined environment. As electron densities of the centrally positioned translocon and the MSP were well-separated (Fig 2E), it facilitated the assignment of rod-shaped densities to TMHs of SecYEG and building the molecular model based on the structure of the quiescent translocon [4]. Both TMHs and extramembrane domains of SecY, SecE, and SecG subunits could be unambiguously fitted into the cryo-EM density (Figs 2E and 3A). The translocon:ribosome complex was established via the well-known canonical interactions [9,11,14]: Two structured cytoplasmic loops between TMHs 6/7 and 8/9 of SecY extended toward the ribosomal tunnel to interact with rRNA helices H6, H24, and H50, and the uL23 protein. Additionally, the ribosomal protein uL24 approached the C-terminal end of the SecY TMH 10, and the ribosomal protein uL23 formed two contacts within the essential amphipathic helix of SecE. Differently to earlier findings [14], we did not observe the contact between the rRNA helix H59 and the lipid head groups, although the H59 helix was displaced toward the bilayer (Fig 3B). It seems plausible that those contacts are established at a later stage of membrane protein insertion, when one or more nascent TMHs egress the lipid bilayer and the H59 helix “screens” the charge of connecting loops, and so participates in the topology determination [15,32]. When evaluating other known structures of bacterial and eukaryotic translocons in complex with ribosomes (Appendix Fig S2), we noted a close agreement between our model and the detergent-solubilized *E. coli* SecYEG bound to a translation-stalled ribosome [18]. Interestingly, although the SecYEG structures in both environments were highly similar, the relative orientation of the ribosome and SecYEG differed substantially: While being bound to the RNC via its C-terminal domain, the detergent-solubilized translocon rotated as a rigid body away from the rRNA helix H59, so the displacement was most pronounced for its N-terminal half (Fig EV3). It is tempting to speculate that the altered SecYEG:ribosome binding geometry, as well as the enhanced affinity of the complex in detergent [20], arose from the lack of electrostatic interactions between the rRNA and the polar moiety of lipid head groups.

In spite of the loose binding of SecYEG to the RNC and its higher flexibility, the complete architecture of essential SecY and SecE subunits was resolved, and a single-helix density proximate to the SecY N-terminal domain was assigned to TMH 2 of the SecG subunit, while TMH 1 could not be reliably detected (Figs 2E and 3A). No SecG subunit could be resolved in the earlier structure of SecYEG-ND [14], and the crystal structure of the quiescent SecYEG revealed that SecG TMH 1 faces away from the translocon core, so its periplasmic tip is separated by ~10 Å from the nearest TMH 4 of SecY, with a

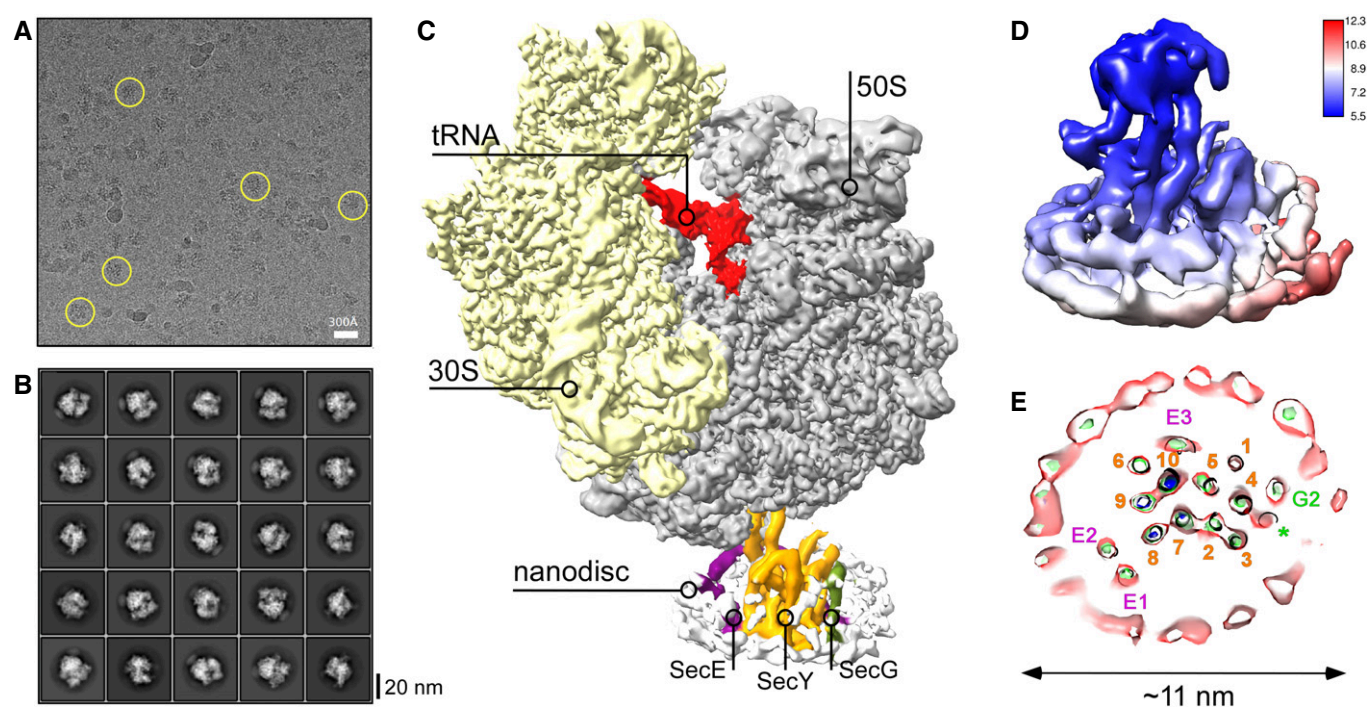


Figure 2. Cryo-EM of the RNC FtsQ:SecYEG-ND complex.

- A Representative cryo-EM micrograph of RNC FtsQ:SecYEG-ND. Exemplary individual ribosomes are encircled.
 B Examples of two-dimensional classes of imaged particles. RNC:nanodisc assemblies can be seen at different view angles.
 C Three-dimensional reconstruction of RNC FtsQ:SecYEG-ND complex. Primary structural elements of the ribosome and SecYEG-ND are indicated.
 D Local resolution map of SecYEG-ND sub-particle. The cytoplasmic side of the translocon demonstrates higher resolution due to stabilization by the bound ribosome, while high resolution at the periplasmic side is hindered by the SecYEG-ND dynamics within the complex. The associated ribosome is not shown for clarity.
 E A planar slice through the SecYEG-ND core at different signal levels (blue/green/red) with indicated positions of SecYEG TMHs (SecY indicated in orange, SecE in purple, and SecG in green). A single helical turn could be fitted in a density in the area where SecG TMH 1 was expected (green asterisk).

lipid molecule filling the void [4]. Thus, weak protein:protein inter-subunit interactions in the lipid environment likely favor spatial dynamics of SecG, up to a complete topology inversion [33], and the dynamics might be modulated by the ribosome binding. Remarkably, within the SecYEG-ND complex we could clearly observe accessory TMHs 1 and 2 of SecE, which were either absent or only poorly resolved in previous translocon structures [14,15,18]. Earlier models placed the SecE TMHs either distanced from the translocon by 20 Å, or near SecY TMH 9, i.e., at the back of the translocon [14,15] (Appendix Fig S2). However, our structure revealed a very different organization of the complex, as SecE TMHs formed a helical hairpin in close proximity to SecY C-terminal domain, and the hairpin was tilted within the lipid bilayer by ~30° (Fig 3A). Such a tilted orientation of the SecE TMHs could also be recognized in densely packed 2D crystals of SecYEG [34,35], but has not been reported for either free-standing or ribosome-bound translocons. Surprisingly, the periplasmic loop of the SecE helical hairpin reached TMH 8 and a short helix connecting TMHs 7 and 8 of SecY, and so appeared in direct contact with the lateral gate of the translocon, thus suggesting a potential role of SecE in the translocon gating mechanism but also explaining interactions of SecE with nascent TMHs soon after their membrane partitioning [36].

We further examined whether the early interactions with the RNC were sufficient to trigger a conformational change within

SecYEG, as it would be required for the nascent chain insertion into the lipid bilayer. SecY TMH 2a, known as a plug domain [37,38], resided in the central position, thus keeping the SecY pore sealed upon RNC binding [12,31], and only minor shifts could be seen for most TMHs in comparison with the quiescent state or detergent-solubilized SecYEG:RNC complex [4,18] (Fig 3C and Appendix Fig S2). Interestingly though, substantial rearrangements were observed within the lateral gate of the translocon, when compared both to the quiescent and to RNC-bound detergent-solubilized states (Fig 3D): TMH 2b was displaced toward the central pore of the translocon, and SecY TMH 7 underwent a tilting of ~5°, so its cytoplasmic and the periplasmic ends approached TMH 8 and TMH 3, respectively [3,4]. This tilting of TMH 7 was coupled to a displacement of TMH 8, as they are connected via a short rigid helix at the periplasmic side (Fig 3D). The resulting conformation of the ribosome-bound translocon manifested a V-shaped crevice at the cytoplasmic side of the lateral gate that differed from the rather closed conformation of the detergent-solubilized SecYEG [18], but also from “primed” and fully opened post-insertion states of the eukaryotic homolog [10,11,13]. Thus, the observed conformation likely reflected a novel early stage in the gate opening. Such dynamics are in agreement with a previous fluorescence-based study on SecYEG-ND:RNC [16], but, to our knowledge, represent the first direct visualization of the pre-opened translocon in the lipid environment.

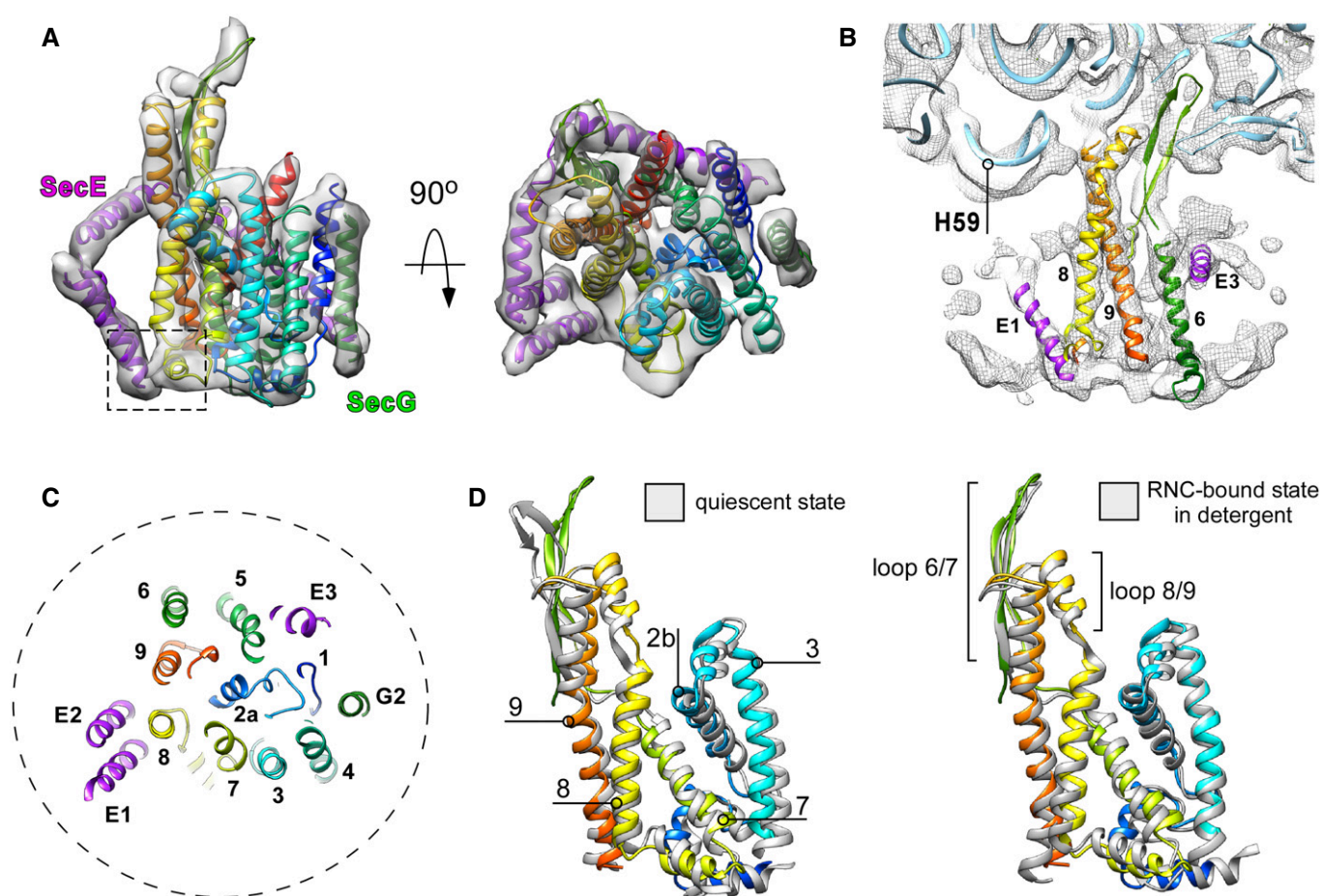


Figure 3. Structural dynamics of the translocon and ribosome upon the nascent chain insertion.

A Isolated cryo-EM density of SecYEG with the fitted molecular model of the translocon in front and the cytoplasmic views. SecY is displayed in rainbow pattern, SecE in purple, and SecG in green. Dashed box: a contact site between tilted SecE TMHs 1/2 and SecY TMH 8.

B Cryo-EM density corresponding to the ribosomal RNA helix 59 ("H59") is displaced toward the nanodisc. No contact with the lipid bilayer could be detected. Blue ribbon: structure of the translocon-free 50S ribosomal subunit (PDB ID: 4UY8).

C Central cross-section through the SecYEG model. The "plug" TMH 2a occupies the central position, thus keeping the translocon sealed. The nanodisc perimeter is indicated as a dashed circle.

D The lateral gate of nanodisc-embedded translocon undergoes rearrangements relatively to a quiescent conformation (left, PDB ID 5AWW) and an RNC-bound detergent-solubilized state (right, PDB ID 5GAE).

To investigate whether the observed translocon conformation was a result of RNC FtsQ binding, we employed microsecond-long molecular dynamics (MD) simulations of SecYEG in explicit solvent and an explicit membrane, which allows to study the behavior of lipid-embedded SecYEG in full atomic detail [39]. From the projection of MD conformations of SecY onto the plane spanned by the first two principal components (PC; both PCs together describe ~50% of the total variance of motions during the simulations), a configurational free energy landscape was computed (equation 1). In this landscape, the SecY conformation from the SecYEG-ND:RNC complex lies in an area of slightly elevated free energy ($\Delta G_{conf,i} \approx 2$ kcal/mol, Appendix Fig S3A), suggesting that this conformation was stabilized by the bound RNC and/or the nascent chain. The mechanism of structural adaptation of the translocon was then probed in a reverse direction, as the MD simulations started from the RNC-bound SecYEG conformation, but without

RNC FtsQ. That way, the adaptation toward a non-disturbed quiescent state could be followed, as has previously been shown for membrane protein complexes [40,41]. The cytoplasmic loop 6/7 of SecY was highly mobile (mean root-mean-square fluctuations (RMSF) > 5 Å; Fig 4A), likely due to the absent ribosome that otherwise recruits the loop as a docking site. The TMHs were substantially less dynamic (RMSF < 3 Å), except for the lateral gate and the cytoplasmic part of TMH 2b. Structural differences upon reaching the free energy minimum were the most substantial for loop 6/7 and were followed by the lateral gate (Fig 4B). We measured internal distances within the lateral gate (TMHs 2, 7, and 8), between TMH 7 and the adjacent TMH 3, as well as the angle η between TMH 7 and TMH 8 (Fig EV4, panels A and C). The cryo-EM structure implied that binding of RNC FtsQ to SecY induced tilting of TMH 7, such that its periplasmic end approached TMH 3, while TMH 2b shifted toward the pore. This effect was completely

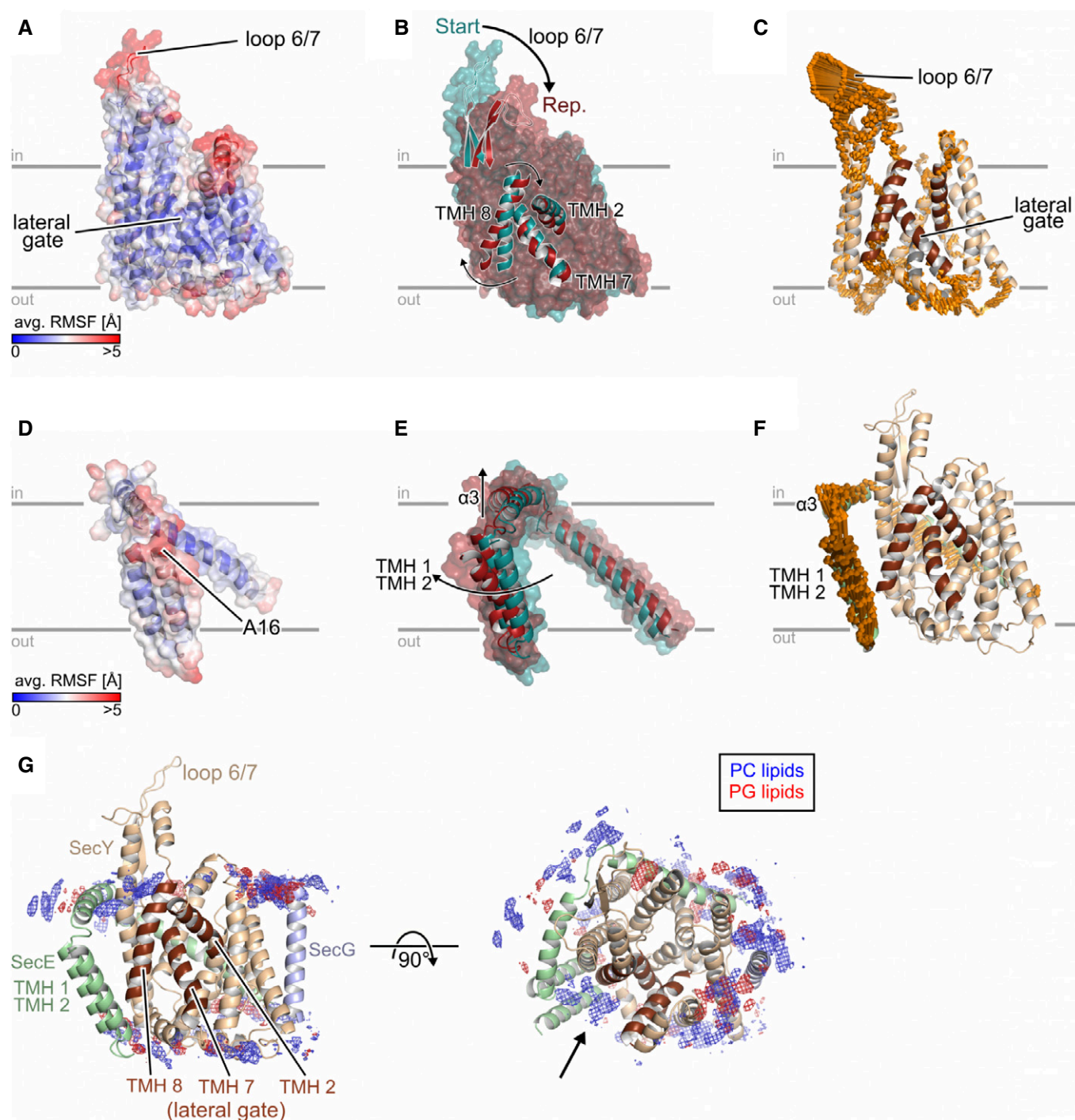


Figure 4. Analysis of molecular dynamics simulations of SecYEG in the lipid bilayer.

A–F (A, D): Average all-atom atomic fluctuations (RMSF; root-mean-square fluctuations) for SecY (A) and SecE (D). The mean RMSFs are projected onto the 3D structures of SecY/SecE and colored according to the color scales starting from blue (low mobility) to red (highly mobile). (B, E): Overlay of the SecY (B) or SecE (E) representative structure (red) onto the corresponding starting structure (dark cyan). Parts that show a pronounced structural change are explicitly shown as cartoon representation, and the movements are highlighted by arrows. (C, F): Visualization of displacements along the 1st (golden arrows) principal component computed for the joint, five 1 μ s long MD simulations for SecY (C) and SecE (F). The amplitudes of the motions were scaled, and a cutoff for small displacements was applied for best graphical representation.

G Distribution of lipids during MD simulations. Grids represent the 3D density of phosphatidylcholine (PC; blue) and phosphatidylglycerol (PG; red) groups from the lipid bilayer. The densities were normalized to the number of considered conformations, which are identical in both cases.

reversed in the absence of the RNC, as both the distance between TMHs 3 and 7 and the angle η increased (Fig EV4, panels B and D). Compared to the initial conformation, the distances between TMHs 2b and 7, and between TMHs 2 and 8, decreased over the course of the simulations, while the distance between TMHs 7 and 8 increased, which led to a closing of the observed V-shaped crevice (Fig EV4, panel B). Interestingly, the PC analysis also suggested that the movements of TMHs 7 and 8 were connected to the dynamics of the cytoplasmic loop 6/7 (Fig 4C, Appendix Fig S3B), such that the ribosome binding likely also influences the structural dynamics within the lateral gate, in agreement with an earlier structure of the ribosome-bound Sec61 translocon [11] and the recent biochemical data [42]. In the absence of a ribosome, binding of a short signal peptide causes an outward displacement of TMH 2b but not TMH 7 [4], so the enhanced structural dynamics at the cytoplasmic side of the lateral gate likely allows a range of pre-opened translocon conformations.

Differently to SecY, the SecE conformation from the SecYEG-ND:RNC complex corresponded to a low free energy region ($\Delta G_{conf.,i} \approx 0.16$ kcal/mol; Appendix Fig S8A), indicating that it was similar to predominant SecE conformations in MD simulations. Accordingly, structural differences upon reaching the free energy minimum were small, as all residues in SecE, except the termini, show a RMSF < 3 Å (Fig 4D). Notably though, a small upward motion of TMHs 1 and 2 (Fig 4E and F, and Appendix Fig S4B) caused a loss of initial contacts between SecE TMH 1 and the SecY periplasmic helix (Appendix Fig S5, panel A), while new ionic interactions were formed on the periplasmic side between R44 on SecE TMH 2 and D393 on SecY TMH 9 (Appendix Fig S5, panel B). This change in the interaction pattern supports the hypothesis that the RNC-induced structural re-arrangement in SecE can be transferred toward the periplasmic part of TMHs 7, 8, and 9 in SecY and further modulates the lateral gate dynamics.

The MD simulations also revealed that the lateral gate area was enriched with zwitterionic lipids (POPC) (Fig 4G). Assuming that the phosphatidylcholine lipids used in the simulations adequately resemble the distribution of naturally occurring phosphatidylethanolamine lipids, this uneven distribution suggests that anionic lipids (POPG) are not an essential factor in the lateral gate dynamics, while the overall neutral charge in the lipid head group region may be beneficial for the insertion of hydrophobic nascent chains. The simulations furthermore indicated that anionic POPG lipids were also unevenly distributed within the nanodisc and preferentially clustered proximate to TMHs 3 and 4 of SecY (Fig 4G). Remarkably, the same regions of SecYEG have been recently described to recruit negatively charged cardiolipin lipids via interactions with lysine residues at the cytoplasmic interface of SecY, such as those in positions 115 (TMH 3) and 181 (TMH 4) [43]. Our data suggest that the SecYEG:lipid interaction is purely charge-determined, and the functionality of the translocon can be ensured either by cardiolipin or by phosphatidylglycerol lipids, while cardiolipin is not essential for the translocon functioning *in vivo* and *in vitro* [29].

As RNC FtsQ contained a hydrophobic anchor domain, we focused on locating that domain within the SecYEG-ND:RNC complex. The nascent chain could be traced along the whole ribosomal tunnel, and it was followed by a free-standing density aligned with the tunnel exit and the central cavity of SecY (Figs 5A and EV5, panel A), suggesting that the nascent chain was loaded into

the translocon. The pronounced density of TMH 2b and 7 displayed the V-shaped conformation of the partially opened lateral gate, with an additional connecting density possibly indicating the presence of a flexible or partially folded FtsQ TMH in proximity of the gate in the bilayer (Fig 5B). Finally, a short rod-like density within the nanodisc interior pointed toward the lateral gate (Fig EV5, panel A), thus suggesting that the short FtsQ TMH emerged into the bilayer via the lateral gate and acquired a stable helical conformation. As the resolution of the map alone was insufficient for unambiguous attribution of the flexible FtsQ TMH, we performed site-specific chemical cross-linking of the nascent chain and the translocon lateral gate. For this purpose, RNC variants which contained single cysteines at positions 40–43 within the FtsQ anchor domain, thus covering one helical turn, were examined. Complementary, cysteines were introduced within TMH 2b (residues 83 and 87) and TMH 7 (residues 282 and 283) of the SecY lateral gate (Fig 5B), and the cross-linking was catalyzed by copper phenanthroline. In the presence of SecY^{C282}EG-ND or SecY^{C283}EG-ND, a cross-linking product of ~80 kDa was detected for RNC FtsQ^{C40} in Western blots when using antibodies against the hemagglutinin-tagged nascent chain (Fig 5C). As the molecular weight matched closely that of the putative tRNA-FtsQ:SecY adduct, we further investigated the involvement of SecY in the cross-linking products. We have found that the solvent-exposed cysteine within the periplasmic loop 3/4 of SecY (residue 148; Fig EV5, panel B) could be efficiently conjugated to CF488A-maleimide [29], but the fluorophore could not access cysteines within the lateral gate (Fig EV5, panel C). Thus, double-cysteine translocon SecY^{C148/C283}EG could be fluorescently labeled and used for cross-linking experiments, and presence of SecY in cross-linking adducts could be determined by in-gel fluorescence. If no ribosomes were added, only weak cross-linking products of SecY were observed at ~85 kDa that likely represented occasional translocon dimers co-reconstituted into a single nanodisc (Fig 5D). If either non-translating ribosomes or cysteine-free RNC FtsQ were added, three cross-linking bands at molecular weights between 40 and 60 kDa were observed. Those bands diminished if the sample was treated with N-ethylmaleimide prior adding the SDS-containing sample buffer (Figs 5E and EV5, panel E), so they were assigned to cross-linking of SDS-denatured SecY with ribosomal proteins. However, in the presence of RNC FtsQ^{C40}, a specific cross-linking product of 80 kDa was formed that agreed with the observation from Western blotting experiments (Fig 5D). Thus, we concluded that the FtsQ nascent chain indeed resided within the lateral gate and could reach the core of the translocon, but did not partition the bilayer via the cytoplasmic crevice. Interestingly, we also observed cross-linking products between SecY^{C283}EG-ND and the nascent chains that contained cysteines in proximate positions 41 and 42, but not the upstream position 35 (Fig 5E), thus suggesting that the N-terminal part of FtsQ TMH has been released into the lipid bilayer. The SecYEG:FtsQ cross-linking was equally efficient in the presence and absence of phosphatidylethanolamine (POPE), a major component of the bacterial membrane (Fig 5D). PE lipids are known to stimulate the SecA-mediated post-translational translocation through SecYEG [44], but seemingly have little effect on the SecYEG-ND:RNC assembly, and the translocon:ribosome complex was also visualized by cryo-EM, although at substantially lower resolution (Appendix Fig S6).

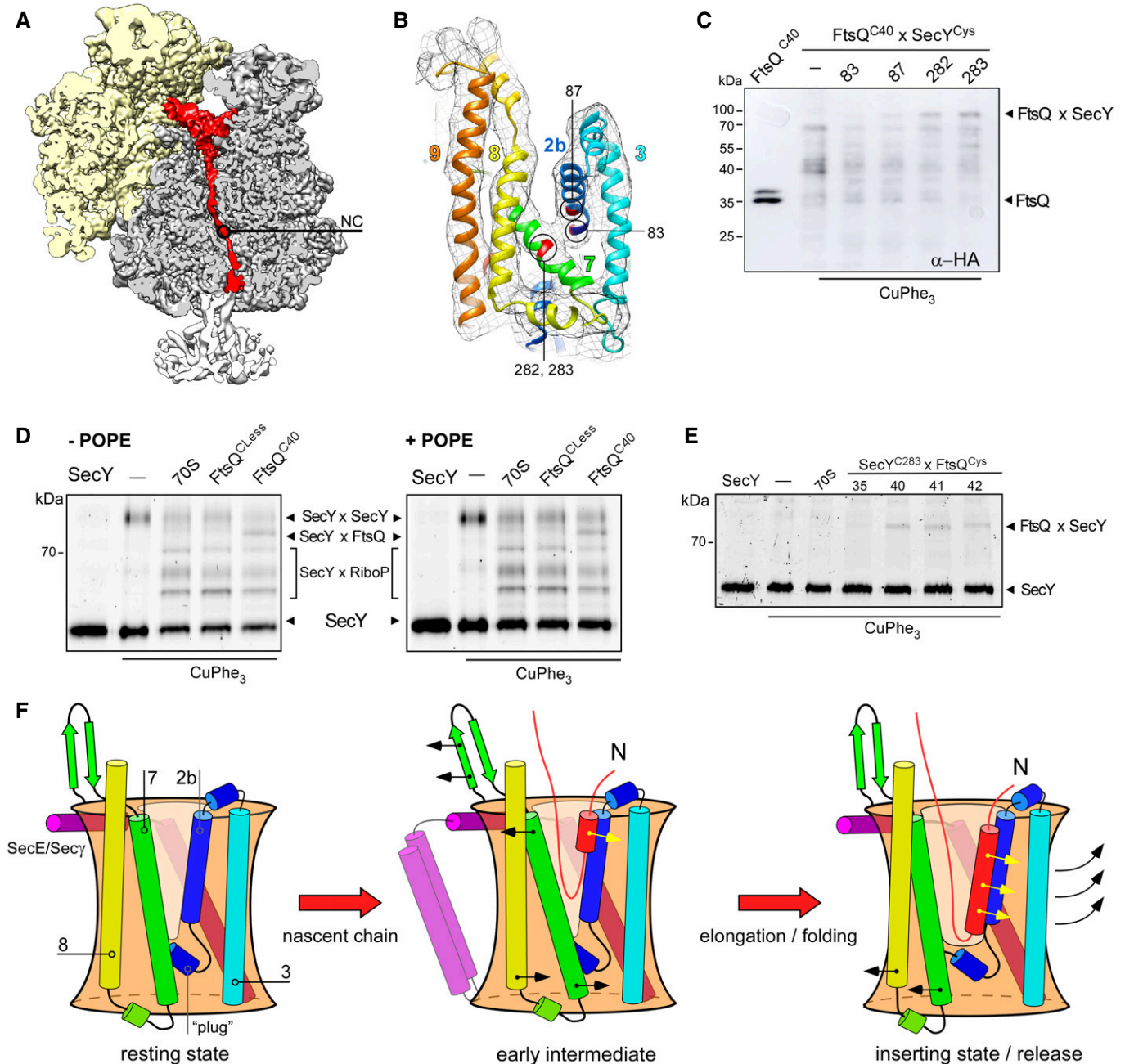


Figure 5. FtsQ nascent chain occupies the lateral gate of the translocon.

- A, B** Cryo-EM visualizes tRNA-bound nascent chain (red, NC) within the ribosomal tunnel (A) and a density between separated TMHs 2b and 7 of the lateral gate (B, shown in mesh). The proximate cysteine positions within SecY used for cross-linking are indicated and highlighted in red.
- C** Western blot against the hemagglutinin tag within the nascent chain FtsQ^{C40} reveals a cross-linking product of ~80 kDa in presence of nanodisc-reconstituted SecY^{C282EG} and SecY^{C283EG}, presumably assigned to FtsQxSecY adduct. The double band for FtsQ^{C40} likely indicates the incomplete cleavage of the hexa-histidine tag by 3C protease.
- D** In-gel fluorescence imaging of SecY^{CF488A} reveals a cross-linking product of ~80 kDa assigned to the FtsQ^{C40}xSecY^{C283} adduct ("SecYxFtsQ"). Bands for covalently cross-linked SecY dimer ("SecYxSecY"), and adducts of SecY and ribosomal proteins ("SecYxRiboP") are indicated. The nascent chain-specific adduct "SecYxFtsQ" does not depend on the presence of PE lipids.
- E** FtsQ:SecY cross-linking is position specific. FtsQ TMH C-terminal residues 40–42 could be cross-linked to the lateral gate (SecY residue 283), while no adduct could be detected at the upstream position 35.
- F** A refined scheme of the nascent chain insertion via the translocon. In the early intermediate state, the ribosome binding to the loop 6/7 and the emerging nascent chain cause displacements of SecY TMHs 2b and 7 at the cytoplasmic interface and "unzip" the lateral gate. The rigid-body tilt of TMH 7 leads to a close contact between TMHs 3 and 7 at the periplasmic side, so the V-shaped crevice is formed. The flexible nascent chain reaches the core of the lateral gate and gradually egresses the lipid moiety, where the helical fold is stabilized by hydrophobic interactions. Upon further nascent chain elongation and movements of SecY TMHs 2b, 3, 7, and 8, the widely open "inserting" state of the translocon is formed, with the complete nascent TMH at the lateral gate prior the release into the membrane.

Membrane protein biogenesis occurs in a highly complex and anisotropic environment of a lipid bilayer, and lipid:protein interactions are known to mediate the structure and functionality of inserted proteins [45–47]. Here, we have revealed the most complete structure of the lipid-embedded SecYEG translocon in complex with RNC at the early stage of the nascent chain insertion. The accessory TMHs of SecE were found to interact with the lateral gate, so they potentially mediate the gate dynamics, but may also be involved in nascent chain release or interactions with the YidC insertase [48,49] and the membrane-anchored chaperones PpiD and YfgM [50,51]. Supported by the MD simulations, the structure evidenced that the opening of the translocon lateral gate was induced at the cytoplasmic interface upon the RNC binding. TMH 2b underwent a displacement of up to ~ 5 Å toward the central pore, and TMH 7 tilted toward TMH 8 at the cytoplasmic side that resulted in a V-shaped crevice open for the nascent chain loading (Fig 5F). When compared to other visualized translocon:ribosome complexes, the observed translocon conformation could be readily placed between the “primed” and “inserting” states reported for the eukaryotic Sec61 complex [11,13]. Differently to the complex in its “inserting” state, the translated and exposed part of the FtsQ nascent chain was not sufficiently long to form a TMH in an $N^{\text{in}}\text{-}C^{\text{out}}$ topology. The cross-linking results and the weak densities observed in the cryo-EM map imply that at this early insertion stage the short nascent chain remains flexible within the lateral gate of the translocon. One can envision that the elongation of the nascent chain would cause a further displacement of SecY TMHs 2b and 7 and results in the open “inserting” state of the lateral gate, so complete folding and insertion of the TMH can be achieved in a downstream event [13]. As a bimodal profile has been observed when studying the translocon-mediated insertion of TMHs in $N^{\text{out}}\text{-}C^{\text{in}}$ topology, and two distinct insertion steps have been detected *in vivo* [52,53], the presented intermediate state of the translocon that allows for partial membrane partitioning and folding of a nascent TMH may potentially explain the experimental data.

Materials and Methods

Materials

All chemicals used were purchased from Merck/Sigma-Aldrich and Carl Roth in p.a. grade quality. Detergents were purchased from Anatrace and lipids from Otto Nordwald GmbH/Avanti Polar Lipids, Inc. Fluorophores were purchased from Thermo Fisher Scientific, Lumiprobe GmbH, and Atto-Tec GmbH.

SecYEG purification and labeling and reconstitution

Escherichia coli SecYEG translocons containing an N-terminal decahistidine tag followed by a flexible linker and the 3C protease cleavage site were overexpressed in *E. coli* strain ER2566 (New England Biolabs) and isolated as previously described [25] with minor modifications. Briefly, after the lysis (Microfluidizer M-110P, Microfluidics Corp.) bacterial membranes were pelleted upon centrifugation for 1 h at 125,000 g (rotor Ti45, Beckman Coulter) and resuspended in 50 mM HEPES pH 7.4, 150 mM KCl. Membranes were solubilized with 1% DDM in presence of 500 mM KCl, 50 mM HEPES pH 7.4,

200 μM TCEP, and protease inhibitors (cOmplete Protease inhibitor cocktail, Roche). Histidine-tagged translocons were isolated on Ni^{2+} -NTA-sepharose resin (Macherey-Nagel GmbH) following standard procedures. Optionally, labeling with 200 μM fluorophore-maleimide conjugates was carried out for 2 h prior eluting the protein from the Ni^{2+} -NTA resin, and the labeling efficiency was determined spectrophotometrically [29]. After the elution in presence of 300 mM imidazole, the buffer was exchanged for 50 mM HEPES pH 7.4, 150 mM KCl, 0.1% DDM, and 5% glycerol using PD SpinTrap or MiniTrap G-25 columns (GE Healthcare Life Sciences). The homogeneity of the purified translocons was controlled by size-exclusion chromatography using Superdex 200 10/300 column connected to the AKTA Purifier (GE Healthcare Life Sciences) and the protein concentrations were determined spectrophotometrically. Samples were aliquoted, flash-frozen in liquid nitrogen, and stored at -80°C .

Reconstitution of SecYEG into nanodiscs using MSP1E3D1 scaffold protein and either 30 mol % POPG, 70 mol % POPC or 30 mol % POPG, 30 mol % POPE, and 40 mol % POPC was carried out at the SecYEG:MSP:lipid molar ratio 1:10:500, as previously described [25]. SecYEG-loaded and empty nanodiscs could be separated via size-exclusion chromatography using Superdex 200 10/300 GL column.

RNC preparation

To form SecYEG-ND:ribosome complexes, *in vivo* translation-stalled RNCs bearing FtsQ nascent chains were prepared, as previously described [15,54]. The nascent chain consisted of an N-terminal histidine tag (eight residues) linked to a 3C protease cleavage site (17 residues), FtsQ residues 4–51, hemagglutinin tag (11 residues), and the TnaC stalling motif (23 residues) (Fig EV1). For site-specific cross-linking experiments, single cysteines were introduced within the FtsQ TMH via mutations L35C, V40C, S41C, G42C, and W43C via Quick-change PCR and the mutations were confirmed by sequencing (Eurofins Genomics). The stalled nascent chain was detected via Western blot using monoclonal antibodies against the hemagglutinin tag (SC-7392) and polyclonal HRP-conjugated antibodies (SC-2005, both Santa Cruz Biotechnology).

Cryo-EM experiments

For cryo-EM experiments, the SecYEG-ND-enriched fractions from size-exclusion chromatography were concentrated to ~ 1 μM by using Amicon Ultra 0.5-ml tubes (MWCO 30 kDa, Merck/Millipore), and 100 nM RNC FtsQ was added and incubated at least 15 min at room temperature. Prior to sample vitrification, fluorinated octyl-maltoside was added to the reaction to the concentration 0.2% to promote random orientation of particles on cryo-EM grids [54,55]. Vitrification was achieved using a Vitrobot mark IV (FEI). For each grid, 3.5 μl of sample was applied onto a glow discharged (20 s, 0.22 Torr) Quantifoil holey carbon grid coated with 2 nm carbon (R 3/3). After 45-s incubation, surplus sample was blotted away (2 s) and the grid was plunged into liquid ethane. From these grids, two separate datasets with a total of 13,098 micrograph movies with each 16 frames and an exposure of $2.5 \text{ e}^-/\text{\AA}^2/\text{frame}$ were collected on a Titan Krios 300 keV cryo-electron microscope (FEI) using a Falcon II direct electron detector and the EM-Tools software (TVIPS GmbH). Magnification was set to result in a pixel size of 1,084 Å.

Cryo-EM data analysis

Anisotropic motion correction of the micrographs was performed using MotionCor2 [56], initially using the first ten frames only. The contrast transfer function (CTF) parameters were estimated using Gctf v1.06 [57], and particles were picked using Gautomatch v0.53 (www.mrc-lmb.cam.ac.uk/kzhang/Gautomatch/). All subsequent data analysis was carried out in Relion 2.1 [58]. At first, both datasets were processed individually but identically. Two rounds of unsupervised 2D classification of all particles were performed to eliminate false positives of the particle picking step (Fig EV2). In the following step, a 3D refinement was performed to align all particles to a *E. coli* 70S ribosome reference without the translocon. All following 3D classifications were performed with fixed alignment parameters. An initial round of 3D classification with five classes was used to select for 70S particles bearing the SecYEG translocon. The resulting particles of both data sets were joined for further processing with Relion 3.0 [59]. After a further 3D refinement of the joined set, beam tilt and per particle CTF refinement was performed. Using the resulting improved CTF parameters, all particles were re-extracted with 2× binning. Multi-body refinement was used to refine the ribosomal small subunit (SSU) and ribosomal large subunit including the SecYEG-ND (LSU:SecYEG-ND) as two independent rigid bodies. Following this step, the `relion_flex_analyse` tool was used to subtract the signal of the SSU from the particle images and re-center these on the LSU:SecYEG-ND moiety. This process of multi-body refinement and extraction of sub-particles was then repeated for the LSU and SecYEG-ND to finally obtain a stack of particle images containing only SecYEG-ND signal. These final sub-particles were used for a further round of 3D classification. Refinement of the final subset of SecYEG-ND sub-particles resulted in an average resolution of 6.0 Å. To obtain high-resolution reconstructions of the ribosomal density, the particles of the final class were re-extracted from the motion-corrected micrographs and subjected to un-binned refinement. Again using multi-body refinement, the SSU and LSU:SecYEG-ND moieties were refined as independent rigid bodies to obtain optimal reconstructions of the ribosome, yielding resolutions of 3.3 and 3.1 Å for SSU and LSU:SecYEG-ND, respectively.

Model building

As a starting model, we used both a crystal structure of quiescent *Thermus thermophilus* SecYEG solved in the lipid cubic phase (PDB ID: 5AWW) [4], as well as the cryo-EM structure of *Escherichia coli* SecYEG together with the 70S ribosome (PDB ID: 5GAE) [18]. Rigid-body docking was performed with UCSF Chimera [60], and the positions of individual helices were adjusted using `coot` [61]. To obtain reasonable geometry, real space model refinement was performed using the `phenix` suite [62]. To complement the intermediary resolution of the SecYEG map, the aforementioned models 5AWW and 5GAE were used to provide external reference restraints for refinement. In a final step, side chains were pruned to alanine length. Mutual orientation of SecE TMHs 1 and 2 was derived from a co-evolution pattern of residues within TMHs (<http://gremlin.bakerlab.org/ecoli.php?uni=P0AG96>). Strong correlations (probability score threshold 0.8) were found for residue pairs: A24:I50, L25:A54, L25:

V58, V28:L51, and A29:V48, which formed a defined interaction interface.

Molecular dynamics simulations

In order to investigate the structural dynamics of the SecYEG complex in the absence of the ribosome and the nascent peptide, MD simulations of the SecYEG complex in an explicit membrane and explicit solvent were carried out, which used the cryo-EM-based structure as a starting conformation. ACE and NME groups were connected to the N-terminal and C-terminal residues, respectively, to avoid artificially charged termini. The SecYEG complex was prepared for pH 7 using EpiK [63] distributed with Schrodinger's Maestro® suite of programs [64], which led to deprotonated residues E176 and E389 in SecY, and a protonated K81 in SecE. Furthermore, H99 in SecY was assigned to the HIE state, while the remaining histidine residues are in the HID state. We used the in-house software `packmol_memgen`, now also distributed with the Amber 18 suite of programs [65], to embed the SecYEG complex into a POPC:POPG (ratio 2:1) bilayer that mimics the nanodisc composition, to add 0.15 M of KCl, and to solvate the bilayer system with TIP3P water [66]. All relevant system files for subsequent MD simulations were generated using the `Leap` program of the Amber 17 suite of programs [67]. The Amber ff14SB force field [68] was used to parameterize the protein, adaptations by Joung and Cheatham [69] were applied to treat K^+ and Cl^- , and the lipid 17 force field distributed with Amber 17 to treat the lipid bilayer.

For subsequent MD simulations, we used the simulation protocol as described by us previously [70,71]. In order to set up five independent MD production simulations, the target temperature during thermalization varied from 299.8 to 300.2 K in 0.1 K intervals, so that we obtained five different configurations for subsequent MD production runs. These production simulations were performed at 300.0 K for 1.0 μs. Coordinates were saved in a trajectory file every 200 ps. The particle mesh Ewald method was applied to treat long-range electrostatic interactions. Structural relaxation, thermalization, and production runs of MD simulations were conducted with `pmemd.cuda` [72] of Amber 17 [67].

We used the `cpptraj` program [73] to analyze the trajectories with respect to distances, root-mean-square fluctuations (RMSF), a measure for atomic mobility, angles, and lipid distributions. If not reported differently, all results are expressed as mean value ± standard error of mean over $n = 5$ independent simulations. Additionally, we performed a principal component analysis to extract the essential motions displayed by the systems, after superimposing each snapshot onto the ten transmembrane helices in SecY of the overall average coordinates in order to remove global rotational and translational motions. Mapping SecY and SecE along the trajectories onto a plane spanned by the 1st and 2nd principal components yielded a 2D histogram, from which we estimated the relative configurational free energy $\Delta G_{conf.,i}$ of the state of the protein in bin i using equation (1)

$$\Delta G_{conf.,i} = -RT \ln \frac{N_i}{N_{max}} \quad (1)$$

where R is the universal gas constant, $T = 300$ K, N_i the population of bin i , and N_{max} the population of the most populated bin [74].

The representative conformations of SecY and SecE were extracted from the MD trajectories and analyzed toward their structural features relative to the initial 3D structure.

In vitro cross-linking

To probe potential SecYEG:FtsQ contacts, 100 nM RNC FtsQ variants bearing single cysteines (mutations V40C, S41C, G42C, and W43C) in the FtsQ TMH were incubated with $\sim 1 \mu\text{M}$ SecYEG-ND, which contained single cysteines within the translocon lateral gate (M83C, S87C, I282C, and I283C). After 15-min incubation at the ambient temperature, copper phenanthroline was added to the concentration of 1 mM, and the cross-linking reaction was conducted for 30 min at the ambient temperature. Cross-linking products containing the nascent chain were detected via Western blotting [75]. Western blots were developed using ECL Western blotting substrate (Pierce) and imaged using LAS-4000 Mini imager (GE Life Sciences). To detect SecYEG-based cross-linking products, the cysteines within the lateral gate were combined with a cysteine at the translocon periplasmic interface (mutation L148C), which was labeled with CF488A-maleimide (Sigma/Merck), as previously described [29]. For the cross-linking experiments, 100 nM SecY^{CF488A}EG-ND variants was mixed with 200 nM non-translating ribosomes or RNCs, and the cross-linking with copper phenanthroline was conducted as described above. Where indicated, samples were treated with *N*-ethylmaleimide prior loading on SDS-PAGE. In-gel fluorescence was recorded using Typhoon FLA 7000 imaging system (GE Life Sciences).

Data availability

The datasets produced in this study are available in the following databases:

- cryo-EM map: Electron Microscopy Data Bank (EMDB, www.ebi.ac.uk/pdbe/emdb), accession code 4743.
- SecYEG molecular model: Protein Data Bank (PDB, www.rcsb.org), accession code 6R7L.

Expanded View for this article is available online.

Acknowledgements

We would like to acknowledge Susanne Rieder for the assistance with the cryo-EM sample preparation; Bertrand Beckert and André Heuer for the support with the data processing; and Eli van der Sluis for fruitful discussions. L.K. is a scholar of the QBM Graduate School. The research was supported by the Deutsche Forschungsgemeinschaft (DFG) via the Research grant KE1879/3-1 to A.K. and projects A10 (A.K.) and A03 (H.G.) within the CRC 1208 “Identity and dynamics of biological membranes” (project number 267205415), and European Research Council (ERC, Advanced Investigator grant “Cryotranslation” to R.B.). The computational support and infrastructure for MD simulations were provided by the Centre for Information and Media Technology (ZIM) at Heinrich Heine University Düsseldorf. We are grateful to the John von Neumann Institute for Computing (NIC) and the Jülich Supercomputing Centre for computing time on the supercomputer JURECA (NIC project HKF7, H.G. and B.F.). Financial support by DFG for funds (INST 208/704-1 FUGG) to purchase

the hybrid computer cluster used in this study is gratefully acknowledged by H.G.

Author contributions

LK: cryo-EM data analysis and structure modeling. BF: molecular dynamics simulations and free energy calculations. OB: cryo-EM data acquisition and analysis. HG: data analysis of molecular dynamics simulations, project design, and supervision. RB: data analysis, project design, and supervision. AK: biochemical preparations and experiments, cryo-EM data analysis, project design, and supervision. All authors contributed to the manuscript preparation.

Conflict of interest

The authors declare that they have no conflict of interest.

References

1. Shao S, Hegde RS (2011) Membrane protein insertion at the endoplasmic reticulum. *Annu Rev Cell Dev Biol* 27: 25–56
2. Hessa T, Meindl-Beinker NM, Bernsel A, Kim H, Sato Y, Lerch-Bader M, Nilsson I, White SH, Von Heijne G (2007) Molecular code for transmembrane-helix recognition by the Sec61 translocon. *Nature* 450: 1026–1030
3. Van Den Berg B, Clemons WM, Collinson I, Modis Y, Hartmann E, Harrison SC, Rapoport TA (2004) X-ray structure of a protein-conducting channel. *Nature* 427: 36–44
4. Tanaka Y, Sugano Y, Takemoto M, Mori T, Furukawa A, Kusakizako T, Kumazaki K, Kashima A, Ishitani R, Sugita Y et al (2015) Crystal structures of SecYEG in lipidic cubic phase elucidate a precise resting and a peptide-bound state. *Cell Rep* 13: 1561–1568
5. Nishiyama KI, Suzuki H, Tokuda H (2000) Role of the non-essential region encompassing the N-terminal two transmembrane stretches of *Escherichia coli* SecE. *Biosci Biotechnol Biochem* 64: 2121–2127
6. Belin D, Plaia G, Boulfekhar Y, Silva F (2015) *Escherichia coli* SecG is required for residual export mediated by mutant signal sequences and for SecY-SecE complex stability. *J Bacteriol* 197: 542–552
7. Pfeffer S, Dudek J, Zimmermann R, Förster F (2016) Organization of the native ribosome-translocon complex at the mammalian endoplasmic reticulum membrane. *Biochim Biophys Acta* 1860: 2122–2129
8. Beckmann R, Bubeck D, Grassucci R, Penczek PA, Verschoor A, Blobel G, Frank J (1997) Alignment of conduits for the nascent polypeptide chain in the ribosome-Sec61 complex. *Science* 278: 2123–2126
9. Becker T, Bhushan S, Jarasch A, Armache JP, Funes S, Jossinet F, Gumbart JC, Mielke T, Berninghausen O, Schulten K et al (2009) Structure of monomeric yeast and mammalian Sec61 complexes interacting with the translating ribosome. *Science* 326: 1369–1373
10. Park E, Ménétret JF, Gumbart JC, Ludtke SJ, Li W, Whynot A, Rapoport TA, Akey CW (2014) Structure of the SecY channel during initiation of protein translocation. *Nature* 506: 102–106
11. Voorhees RM, Fernández IS, Scheres SHW, Hegde RS (2014) Structure of the mammalian ribosome-Sec61 complex to 3.4 Å resolution. *Cell* 157: 1632–1643
12. Gogala M, Becker T, Beatrix B, Armache JP, Barrio-García C, Berninghausen O, Beckmann R (2014) Structures of the Sec61 complex engaged in nascent peptide translocation or membrane insertion. *Nature* 506: 107–110

13. Voorhees RM, Hegde RS (2016) Structure of the SecE1 channel opened by a signal sequence. *Science* 351: 88–89
14. Frauenfeld J, Gumbart JC, van der Sluis EO, Funes S, Gartmann M, Beatrix B, Mielke T, Berninghausen O, Becker T, Schulten K *et al* (2011) Cryo-EM structure of the ribosome-SecYE complex in the membrane environment. *Nat Struct Mol Biol* 18: 614–621
15. Bischoff L, Wickles S, Berninghausen O, Van Der Sluis EO, Beckmann R (2014) Visualization of a polytopic membrane protein during SecY-mediated membrane insertion. *Nat Commun* 5: 1–8
16. Ge Y, Draycheva A, Bornemann T, Rodnina MV, Wintermeyer W (2014) Lateral opening of the bacterial translocon on ribosome binding and signal peptide insertion. *Nat Commun* 5: 1–6
17. Gouridis G, Karamanou S, Gelis I, Kalodimos CG, Economou A (2009) Signal peptides are allosteric activators of the protein translocase. *Nature* 462: 363–367
18. Jomaa A, Boehringer D, Leibundgut M, Ban N (2016) Structures of the *E. coli* translating ribosome with SRP and its receptor and with the translocon. *Nat Commun* 7: 1–9
19. Cross TA, Murray DT, Watts A (2013) Helical membrane protein conformations and their environment. *Eur Biophys J* 42: 731–755
20. Wu ZC, De Keyser J, Kedrov A, Driessen AJM (2012) Competitive binding of the SecA ATPase and ribosomes to the SecYEG translocon. *J Biol Chem* 287: 7885–7895
21. Kedrov A, Sustarsic M, De Keyser J, Caumanns JJ, Wu ZC, Driessen AJM (2013) Elucidating the native architecture of the YidC: ribosome complex. *J Mol Biol* 425: 4112–4124
22. Egea PF, Stroud RM (2010) Lateral opening of a translocon upon entry of protein suggests the mechanism of insertion into membranes. *Proc Natl Acad Sci USA* 107: 17182–17187
23. Pfeffer S, Burbaum L, Unverdorben P, Pech M, Chen Y, Zimmermann R, Beckmann R, Förster F (2015) Structure of the native SecE1 protein-conducting channel. *Nat Commun* 6: 1–7
24. Alami M, Dalal K, Lej-Garolla B, Sligar SG, Duong F (2007) Nanodiscs unravel the interaction between the SecYEG channel and its cytosolic partner SecA. *EMBO J* 26: 1995–2004
25. Taufik I, Kedrov A, Exterkate M, Driessen AJM (2013) Monitoring the activity of single translocons. *J Mol Biol* 425: 4145–4153
26. Ritchie TK, Grinkova YV, Bayburt TH, Denisov IG, Zolnerciks JK, Atkins WM, Sligar SG (2009) Reconstitution of membrane proteins in phospholipid bilayer nanodiscs. *Methods Enzymol* 464: 211–231
27. Hagn F, Eitzkorn M, Raschle T, Wagner G (2013) Optimized phospholipid bilayer nanodiscs facilitate high-resolution structure determination of membrane proteins. *J Am Chem Soc* 135: 1919–1925
28. Koch S, De Wit JG, Vos I, Birkner JP, Gordiichuk P, Herrmann A, Van Oijen AM, Driessen AJM (2016) Lipids activate SecA for high affinity binding to the SecYEG complex. *J Biol Chem* 291: 22534–22543
29. Kedrov A, Kusters I, Krasnikov VV, Driessen AJM (2011) A single copy of SecYEG is sufficient for preprotein translocation. *EMBO J* 30: 4387–4397
30. Park E, Rapoport TA (2012) Bacterial protein translocation requires only one copy of the SecY complex *in vivo*. *J Cell Biol* 198: 881–893
31. Lycklama A, Nijeholt JA, Wu ZC, Driessen AJM (2011) Conformational dynamics of the plug domain of the SecYEG protein-conducting channel. *J Biol Chem* 286: 43881–43890
32. Cymer F, Von Heijne G, White SH (2015) Mechanisms of integral membrane protein insertion and folding. *J Mol Biol* 427: 999–1022
33. Sugai R, Takemae K, Tokuda H, Nishiyama KI (2007) Topology inversion of SecE is essential for cytosolic SecA-dependent stimulation of protein translocation. *J Biol Chem* 282: 29540–29548
34. Bostina M, Mohsin B, Kühlbrandt W, Collinson I (2005) Atomic model of the *E. coli* membrane-bound protein translocation complex SecYEG. *J Mol Biol* 352: 1035–1043
35. Hizlan D, Robson A, Whitehouse S, Gold VAM, Vonck J, Mills D, Kühlbrandt W, Collinson I (2012) Structure of the SecY complex unlocked by a preprotein mimic. *Cell Rep* 1: 21–28
36. Houben ENG, ten Hagen-Jongman CM, Brunner J, Oudega B, Luirink J (2004) The two membrane segments of leader peptidase partition one by one into the lipid bilayer via a SecYidC interface. *EMBO Rep* 5: 970–975
37. Tam PCK, Maillard AP, Chan KKY, Duong F (2005) Investigating the SecY plug movement at the SecYEG translocation channel. *EMBO J* 24: 3380–3388
38. Li W, Schulman S, Boyd D, Erlandson K, Beckwith J, Rapoport TA (2007) The plug domain of the SecY protein stabilizes the closed state of the translocation channel and maintains a membrane seal. *Mol Cell* 26: 511–521
39. Dror RO, Dirks RM, Grossman JP, Xu H, Shaw DE (2012) Biomolecular simulation: a computational microscope for molecular biology. *Annu Rev Biophys* 41: 429–452
40. Dror RO, Arlow DH, Maragakis P, Mildorf TJ, Pan AC, Xu H, Borhani DW, Shaw DE (2011) Activation mechanism of the β_2 -adrenergic receptor. *Proc Natl Acad Sci USA* 108: 18684–18689
41. Shan Y, Arkhipov A, Kim ET, Pan AC, Shaw DE (2013) Transitions to catalytically inactive conformations in EGFR kinase. *Proc Natl Acad Sci USA* 110: 7270–7275
42. Mandon EC, Butova C, Lachapelle A, Gilmore R (2018) Conserved motifs on the cytoplasmic face of the protein translocation channel are critical for the transition between resting and active conformations. *J Biol Chem* 293: 13662–13672
43. Corey RA, Pyle E, Allen WJ, Watkins DW, Casiraghi M, Miroux B, Arechaga I, Politis A, Collinson I (2018) Specific cardiolipin–SecY interactions are required for proton-motive force stimulation of protein secretion. *Proc Natl Acad Sci USA* 115: 7967–7972
44. Van Der Does C, Swaving J, Van Klompenburg W, Driessen AJM (2000) Non-bilayer lipids stimulate the activity of the reconstituted bacterial protein translocase. *J Biol Chem* 275: 2472–2478
45. Dowhan W, Bogdanov M (2009) Lipid-dependent membrane protein topogenesis. *Annu Rev Biochem* 78: 515–540
46. Pliotas C, Dahl ACE, Rasmussen T, Mahendran KR, Smith TK, Marius P, Gault J, Banda T, Rasmussen A, Miller S *et al* (2015) The role of lipids in mechanosensation. *Nat Struct Mol Biol* 22: 991–998
47. Harris NJ, Charalambous K, Findlay HE, Booth PJ (2018) Lipids modulate the insertion and folding of the nascent chains of alpha helical membrane proteins. *Biochem Soc Trans* 46: 1355–1366
48. Van Der Laan M, Houben ENG, Nouwen N, Luirink J, Driessen AJM (2001) Reconstitution of Sec-dependent membrane protein insertion: nascent FtsQ interacts with YidC in a Sec YEG-dependent manner. *EMBO Rep* 2: 519–523
49. Petriman NA, Jauß B, Hufnagel A, Franz L, Sachelar I, Drepper F, Warscheid B, Koch HG (2018) The interaction network of the YidC insertase with the SecYEG translocon, SRP and the SRP receptor FtsY. *Sci Rep* 8: 1–16
50. Sachelar I, Petriman NA, Kudva R, Koch HG (2014) Dynamic interaction of the Sec translocon with the chaperone PpiD. *J Biol Chem* 289: 21706–21715
51. Götzke H, Palombo I, Muheim C, Perrody E, Genevaux P, Kudva R, Müller M, Daley DO (2014) YfgM is an ancillary subunit of the SecYEG translocon in *Escherichia coli*. *J Biol Chem* 289: 19089–19097

52. Ismail N, Hedman R, Schiller N, von Heijne G (2012) A biphasic pulling force acts on transmembrane helices during translocon-mediated membrane integration. *Nat Struct Mol Biol* 19: 1018–1022
53. Niesen MJM, Müller-lucks A, Hedman R, von Heijne G, Miller TFI (2018) Forces on nascent polypeptides during membrane insertion and translocation via the sec translocon. *Biophys J* 115: 1885–1894
54. Kedrov A, Wickles S, Crevenna AH, van der Sluis EO, Buschauer R, Berninghausen O, Lamb DC, Beckmann R (2016) Structural dynamics of the YidC: ribosome complex during membrane protein biogenesis. *Cell Rep* 17: 2943–2954
55. Efremov RG, Leitner A, Aebersold R, Raunser S (2015) Architecture and conformational switch mechanism of the ryanodine receptor. *Nature* 517: 39–43
56. Zheng SQ, Palovcak E, Armache J-P, Verba KA, Cheng Y, Agard DA (2017) MotionCor2: anisotropic correction of beam-induced motion for improved cryo-electron microscopy. *Nat Methods* 14: 331
57. Zhang K (2016) Gctf: real-time CTF determination and correction. *J Struct Biol* 193: 1–12
58. Kimanius D, Forsberg BO, Scheres SHW, Lindahl E (2016) Accelerated cryo-EM structure determination with parallelisation using GPUS in RELION-2. *Elife* 5: 1–21
59. Zivanov J, Nakane T, Forsberg B, Kimanius D, Hagen WJH, Lindahl E, Scheres SHW (2018) RELION-3: new tools for automated high-resolution cryo-EM structure determination. *Elife* 7: e42166
60. Pettersen EF, Goddard TD, Huang CC, Couch GS, Greenblatt DM, Meng EC, Ferrin TE (2004) UCSF Chimera - A visualization system for exploratory research and analysis. *J Comput Chem* 25: 1605–1612
61. Emsley P, Cowtan K (2004) Coot: model-building tools for molecular graphics. *Acta Crystallogr Sect D Biol Crystallogr* 60: 2126–2132
62. Wang Z, Hryc CF, Bammes B, Afonine PV, Jakana J, Chen DH, Liu X, Baker ML, Kao C, Ludtke SJ et al (2014) An atomic model of brome mosaic virus using direct electron detection and real-space optimization. *Nat Commun* 5: 1–12
63. Shelley JC, Cholleti A, Frye LL, Greenwood JR, Timlin MR, Uchimaya M (2007) Epik: a software program for pKa prediction and protonation state generation for drug-like molecules. *J Comput Aided Mol Des* 21: 681–691
64. Schrödinger, LLC, New York N Schrödinger Release 2017-2: Maestro.
65. Case DA, Ben-Shalom IY, Brozell SR, Cerutti DS, Cheatham TE III, Cruzeiro VWD, Darden TA, Duke RE, Ghoreishi D, Gilson MK et al Amber 18. University of California San Francisco
66. Jorgensen WL, Chandrasekhar J, Madura JD, Impey RW, Klein ML (1983) Comparison of simple potential functions for simulating liquid water. *J Chem Phys* 79: 926–935
67. Case DA, Cerutti DS, Cheatham TE III, Darden TA, Duke RE, Giese TJ, Gohlke H, Goetz AW, Greene D, Homeyer N et al Amber17. University of California San Francisco
68. Maier JA, Martinez C, Kasavajhala K, Wickstrom L, Hauser KE, Simmerling C (2015) ff14SB: improving the accuracy of protein side chain and backbone parameters from ff99SB. *J Chem Theory Comput* 11: 3696–3713
69. Joung IS, Cheatham TE III (2008) Determination of alkali and halide monovalent ion parameters for use in explicitly solvated biomolecular simulations. *J Phys Chem B* 112: 9020–9041
70. Frieg B, Görg B, Homeyer N, Keitel V, Häussinger D, Gohlke H (2016) Molecular mechanisms of glutamine synthetase mutations that lead to clinically relevant pathologies. *PLoS Comput Biol* 12: e1004693
71. Diedrich D, Moita AJR, Rütger A, Frieg B, Reiss GJ, Hoepfner A, Kurz T, Gohlke H, Lüdeke S, Kassack MU et al (2016) α -Aminoxy oligopeptides: synthesis, secondary structure, and cytotoxicity of a new class of anti-cancer foldamers. *Chemistry* 22: 17600–17611
72. Salomon-Ferrer R, Götz AW, Poole D, Le Grand S, Walker RC (2013) Routine microsecond molecular dynamics simulations with Amber on GPUs. 2. Explicit solvent particle mesh Ewald. *J Chem Theory Comput* 9: 3878–3888
73. Roe DR, Cheatham TE III (2013) PTRAJ and CPPTRAJ: software for processing and analysis of molecular dynamics trajectory data. *J Chem Theory Comput* 9: 3084–3095
74. Pierce LCT, Salomon-Ferrer R, Augusto F de Oliveira C, McCammon JA, Walker RC (2012) Routine access to millisecond time scale events with accelerated molecular dynamics. *J Chem Theory Comput* 8: 2997–3002
75. Wickles S, Singharoy A, Andreani J, Seemayer S, Bischoff L, Berninghausen O, Soeding J, Schulten K, van der Sluis EO, Beckmann R (2014) A structural model of the active ribosome-bound membrane protein insertase YidC. *Elife* 3: 1–17



License: This is an open access article under the terms of the Creative Commons Attribution 4.0 License, which permits use, distribution and reproduction in any medium, provided the original work is properly cited.

Structure of the Bcs1 AAA-ATPase suggests an airlock-like translocation mechanism for folded proteins

Lukas Kater¹, Nikola Wagener², Otto Berninghausen¹,
Thomas Becker¹, Walter Neupert³ and Roland Beckmann^{1,4}

Abstract

Some proteins require completion of folding before translocation across a membrane into another cellular compartment. Yet the permeability barrier of the membrane should not be compromised and mechanisms have remained mostly enigmatic. Here, we present the structure of Bcs1, an AAA-ATPase of the inner mitochondrial membrane. Bcs1 facilitates the translocation of the Rieske protein, Rip1, which requires folding and incorporation of a Fe₂-S₂ cluster before translocation and subsequent integration into the bc1 complex. Surprisingly, Bcs1 assembles into exclusively heptameric homo-oligomers, with each protomer consisting of an amphipathic transmembrane helix, a middle domain and an ATPase domain. Together, they form two aqueous vestibules, the first accessible from the mitochondrial matrix and the second positioned in the inner membrane, both separated by the seal forming middle domain. Based on this unique architecture, we propose an airlock-like translocation mechanism for folded Rip1.

Introduction

Proteins are translocated across membranes mostly in an unfolded state. In this mode, canonical protein-conducting channels such as the Sec61 complex of the endoplasmic reticulum (ER) and the TOM and TIM23 complexes (mitochondria) can handle a plethora of different soluble and membrane proteins as mostly uniform extended peptide chains. In case of the Sec61 complex, these chains are guided through a relatively small and easy to seal pore, which also allows for lateral release of sufficiently hydrophobic peptide chains into the lipid phase¹. In contrast, when protein maturation is manda-

tory before translocation, a limited number of such proteins can be transported in a fully folded state, for example across the bacterial plasma membrane or into the peroxisomal compartment of eukaryotes. Several specialized bacterial secretion systems have evolved, often associated with self-defense or virulence². However, the main machinery for translocation of folded proteins is provided by the Tat (twin arginine translocator) system in bacteria³, employing a so far enigmatic transport mechanism. Curiously, during evolution chloroplasts have kept, but most mitochondria have lost their Tat system despite the presence of a universally conserved folded substrate for translocation, the Rieske protein (Rip1 in yeast).

Rip1 is a key component of the ubiquinol-cytochrome c reductase, the bc1 complex (or complex III). It consists of a C-terminal globular iron-sulfur cluster domain (FeS-domain) exposed to the inter-membrane space (IMS) and a single, rather mildly hydrophobic transmembrane helix spanning the inner mitochondrial membrane (IM)⁴. After import of Rip1 as a precursor from the cytoplasm into the mitochondria by the TOM-TIM23 complex, the 2Fe-2S cluster is added to the apoprotein in the mitochondrial matrix^{5,6}, followed by selective back-translocation across and insertion into the IM in a folded state⁷. Notably, in bacteria and chloroplasts the Rieske Fe-S protein is transported to the periplasmic space and to the intrathylakoid space, respectively, by the canonical Tat system^{8,9}. In contrast, in most mitochondria the AAA-ATPase Bcs1 has replaced the Tat system as an export machinery for the folded Rieske protein^{7,10,11}.

BCS1 (ubiquinol-cytochrome c reductase (bc1) synthesis) genes are present in most eukaryotic organisms and represent an outlying clade of the large family of AAA proteins (ATPases associated with diverse cellular activities)¹². These ATPases mainly function in unfolding and disaggregation of proteins, but also in protein extraction from membranes, both processes often coupled to processing and degradation^{13,14}. AAA proteins usually assemble into hexameric ring-like complexes with each subunit comprising one or two highly conserved ATP-binding domains. Together they form a central pore-like channel lined by protruding loops (the pore loops), which function in ATP hydrolysis dependent substrate transport through this central pore¹⁵. AAA pro-

¹Gene Center and Center for Integrated Protein Science Munich, Department of Biochemistry, University of Munich, Munich, Germany.

²Department of Biology, University of Munich, Munich, Germany.

³Biomedical Center, University of Munich, Munich, Germany

⁴e-mail:beckmann@genzentrum.lmu.de

teins in mitochondria are involved in crucial processes like organelle fusion, protein quality control, mitochondrial protein translation and degradation¹⁶. The hexameric Msp1 for example is anchored via its N-terminal transmembrane helix (TMH) to the outer mitochondrial membrane (OM) and facilitates extraction of wrongly targeted tail anchored proteins from the OM into the cytoplasm^{17–19}. Moreover, similar to the FtsH machinery in bacteria, the AAA protein Yme1 is anchored to the mitochondrial IM but facing the IMS, and recent structures have revealed how its ATPases form a closed spiral staircase on an unfolded substrate, thereby directing substrate transport toward a protease ring for degradation²⁰. Importantly, most recent structural studies indicate a general hand-over-hand mechanism for these hexameric AAA proteins: coexisting nucleotide states in the hexamer trigger distinct staircase-like positioning of substrate engaging pore loops in the central channel. The ATPase domains perform a sequential, around-the-ring ATP hydrolysis cycle that results in stepwise substrate translocation^{21–24}. Similar to Msp1 and Yme1 the Bcs1 AAA protein is also anchored to the IM via a single N-terminal transmembrane domain, however, the large C-terminal (ATPase) domain faces the mitochondrial matrix^{10,25}. Moreover, in contrast to classical AAA proteins characteristic pore loop sequences are not conserved in Bcs1²⁶. This raises the question of what mechanism Bcs1 employs for the translocation of the folded Rieske protein, and how an AAA protein can display Tat-like activity without substantially compromising the critical permeability barrier of the inner mitochondrial membrane.

We determined three cryo-EM structures of Bcs1, an ADP-bound state and two distinct apo states. Contrary to most other hexameric AAA proteins, Bcs1 exclusively forms a homo-heptameric ring. This heptameric assembly of Bcs1 results in the formation of two large aqueous vestibules, one on the matrix side (matrix vestibule) and a smaller second one in the inner membrane (IM vestibule). The AAA domains and amphipathic transmembrane helices (TMHs) delineate the matrix and IM vestibules (respectively), with the middle domain forming a seal-like structure in-between. The architecture of Bcs1 together with the conformational differences between apo and ADP states indicate an airlock like mechanism for Rip1 translocation.

Results

Cryo-EM reveals a heptameric assembly of Bcs1.

We used affinity purification to prepare Bcs1 complex from a crude mitochondrial fraction of a *S. cerevisiae* strain expressing His-tagged Bcs1 essentially as described before (Extended Data Fig. 1)⁷. The purified Bcs1 oligomers were incubated with ATP and subsequently subjected to single particle cryo-electron mi-

croscopy (cryo-EM). After classification and 3D reconstruction we unexpectedly observed heptameric but not hexameric Bcs1 oligomers. At an overall resolution of 4 Å for C1 symmetry and 3.4 Å after applying C7 symmetry (Fig. 1a, b; Extended Data Fig. 2–4; Table 1; Supplementary Movie 1) a near complete molecular model for Bcs1 was built for the residues N49 to L449. It comprises the N-terminal transmembrane helix (TMH, aa53-83), the seal forming middle domain (aa84-202) and the typical small and large AAA domains (LD, aa203-387; SD, aa388-449) (Fig. 1c). The N-terminal TMHs measure about 50 Å in length and pass the membrane in an angle of about 35°. They contact each other in the leaflet of the membrane facing the intermembrane space (IMS), but at the opposite leaflet at the base of the middle domain two neighboring helices are separated by a 25 Å gap. As a result, the TMHs of Bcs1 form a highly unusual basket-like arrangement in the membrane. The middle domain consists of a β -sheet with four antiparallel strands stabilized by a peripheral α -helix and a C-terminal α -helix connecting it with the LD. In addition, a loop of the middle domain, we termed seal loop, protrudes towards the central axis of the heptamer and a long α -hairpin (connector hairpin, CH) establishes an additional connection with the neighboring LD (Fig. 1c). The Bcs1 LD and SD together form the typical nucleotide-binding pocket. In contrast to other AAA proteins, however, Bcs1 has two additional β -strands (β -a1 and β -a2), which augment the canonical β -sheet of the AAA LD (Fig. 1c). Notably, these additional β -strands connect the ATPase domain with the middle domain, and an arginine (R223) in the loop between the strand β -a2 and the helix α 0 of the AAA LD protrudes towards the nucleotide-binding pocket where it possibly monitors nucleotide presence. The AAA domain of Bcs1 also features two loops corresponding to the pore loops in classical AAA proteins (Extended Data Fig. 5). These loops (henceforth also referred to as pore loops) are flexible and thus not well resolved. However, while the longer pore loop 2 features a phenylalanine (F336), the shorter pore loop 1 lacks aromatic residues, a key component of the characteristic pore loop motif. Moreover, in contrast to what is observed classical hexameric AAA protein structures, these loops do not protrude into the central pore, but rather point away from the ring plane (Extended Data Fig. 5).

ADP uniformly occupies the binding pocket of the AAA domain (Fig. 1c). Apparently, incubation with ATP during the preparation resulted in binding and hydrolysis of all seven ATPs, yielding a uniform symmetric conformation. This is likely to represent an ADP-bound post-hydrolysis ground state of the protomers, since preparation and visualization of Bcs1 without any added ATP resulted in the observation of two distinct apo states (see below). We cannot conclude if the apo state represents the physiological state in the mitochondrial matrix or whether bound nucleotides were lost during purification.

Table 1: Cryo-EM data collection, refinement and validation statistics

	#1 ADP EMD-10192 PDB 6SH3	#2 Apo1 EMD-10193 PDB 6SH4	#3 Apo2 EMD-10194 PDB 6SH5
Data collection and processing			
Magnification	130	130	130
Voltage (kV)	300	300	300
Electron exposure (e ⁻ /Å ²)	65	58	58
Defocus range (μm)	0.8 – 2.8	0.8 – 2.8	0.8 – 2.8
Pixel size (Å)	1.059	1.059	1.059
Symmetry imposed	C7	C7	C7
Initial particle images (no.)	1,101,692	1,389,762	1,389,762
Final particle images (no.)	271,736	36,141	38,934
Map resolution (Å)	3.4	4.4	4.6
FSC threshold	0.143	0.143	0.143
Map resolution range (Å)	3.2 – 5.5	4.3 – 7.3	4.4 – 8.5
Refinement			
Initial model used	De novo	PDB 6SH3	PDB 6SH3
Model resolution (Å)	3.4	4.5	6.5
FSC threshold	0.5	0.5	0.5
Model resolution range (Å)	3.4 – 5.5	4.4 – 7.3	4.6 – 8.5
Map sharpening B factor (Å ²)	-173	-225	-235
Model composition			
Nonhydrogen atoms	21,042	12,957	11,774
Protein residues	2,632	2,632	2,387
Ligands	7	0	0
B factors (Å ²)			
Protein	79.35	357	419
Ligand	47.72	-	-
R.m.s. deviations			
Bond lengths (Å)	0.005	0.004	0.004
Bond angles (°)	0.831	1.068	0.915
Validation			
MolProbity score	1.56	0.79	0.77
Clashscore	3.45	2.61	1.06
Poor rotamers (%)	0.62	0	0
Ramachandran plot			
Favored (%)	93.5	91.6	91.8
Allowed (%)	6.5	7.31	8.2
Disallowed (%)	0	1.09	0

Bcs1 forms two separate aqueous vestibules.

The heptameric AAA domains of Bcs1 together with the middle domains form a large vestibule (matrix vestibule) with lateral window-like openings of a 10-15 Å diameter (Fig. 2a, b). It has a depth of about 45 Å and an opening to the matrix with a diameter of about 40 Å. Towards the membrane it is sealed by the middle domains. A second vestibule is located within the IM, referred to as the IM vestibule. It is confined by the basket shaped TMHs and the middle domains (Fig. 2a, b). Notably, both of these vestibules are sufficiently large to accommodate the folded FeS domain of Rip1 (Fig 2c). The middle domains separate the matrix and the IM vestibule but

leave a small pore in the center of about 10 Å diameter (seal pore). In all reconstructions (C1 and C7 symmetric), this pore was occluded by an extra density on the membrane side, which lacked structural detail. While partially connecting with the pore loop region in unsymmetrized maps, it is not part of the Bcs1 protein (Fig. 2 a, d). Lipids or a mixture of lipids and detergent are possible candidates explaining this amorphous density, which could not be further resolved by classification and refinement preventing identification. The interaction between the CH and the AAA LD is established by stacking interactions between H123 and R313 and hydrogen bonds between N125 and N287 (Fig. 2e, f). In contrast, the seal pore of the middle domain is

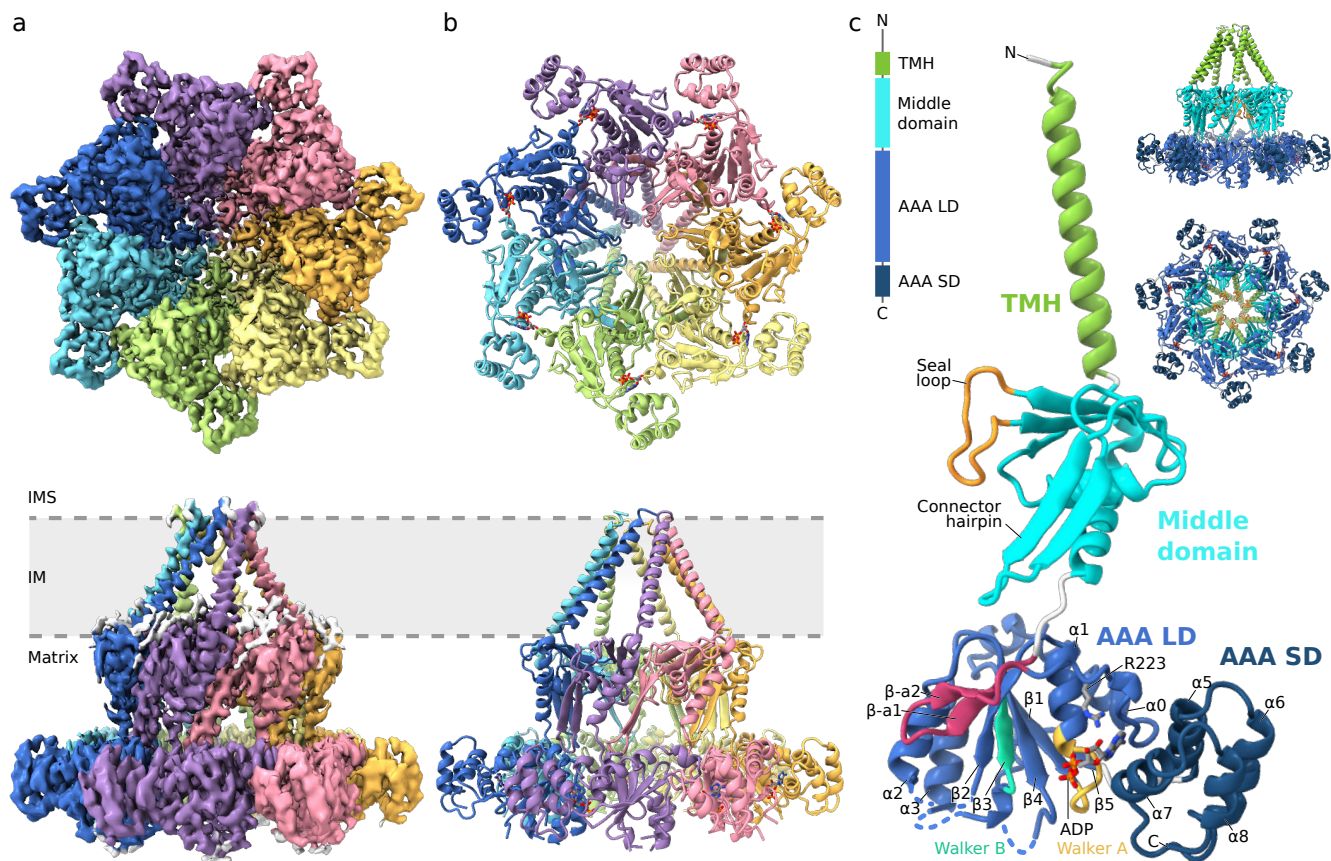


Figure 1: Bcs1 structure and domain organization in the ADP state. Top and side views on the cryo-EM structure (a) and the molecular model (b) of the Bcs1 heptamer. Single Bcs1 protomers are shown in different colours. For orientation, in lower panels, a schematic of the inner mitochondrial membrane is shown. IMS = inter-membrane space; IM inner membrane. (c) Model of a Bcs1-ADP protomer highlighting individual domains, their structural features and their location within the heptamer. TMH = transmembrane helix; AAA LD and AAA SD: large and small AAA domains.

formed by the seal loops mainly employing hydrophobic interactions by M160, I161 and I163. This results in a highly hydrophobic character of the seal pore towards the matrix side, which is contrasted by the highly hydrophilic character of a collar formed by lysines (K159 of each protomer) on the membrane facing side (Fig. 2g). The IM vestibule formed by the middle domains and the N-terminal TMHs creates an unusual aqueous environment spanning almost the entire membrane. On the matrix side it is as wide as the matrix vestibule, but it tapers towards the IMS side where the TMHs contact each other and form an iris-like short hydrophobic bundle. In the matrix leaflet of the bilayer, the helices create a gap of up to 25 Å between each other, thereby allowing direct access from the interior of the IM vestibule to the lipid environment of the membrane (Fig. 2a, 3a). The amphipathic character of the TMHs supports the notion that an aqueous environment is formed in the membrane (Fig. 3): on the outside, they are uniformly hydrophobic, but hydrophilic amino acids are exposed to the inside. Only the N-terminal region of the helices on the IMS side is more uniformly hydrophobic, which may allow them to dynamically dissociate and emerge

in the lipids of the IMS leaflet. It may also facilitate a situation in which only the wider part of the basket supports an aqueous milieu, and the narrower part, which is exposed to the IMS leaflet of the inner membrane and is more uniformly hydrophobic, could coordinate lipids inside the basket.

Two Bcs1 apo states illustrate opening of the seal pore.

Classification and 3D reconstruction of Bcs1 prepared without addition of nucleotides yielded two distinct states termed Apo1 and Apo2 (Fig. 4). The overall resolution for both states was 6.3 and 6.8 Å for C1 and 4.4 and 4.6 Å when applying C7 symmetry (Extended Data Fig. 2, 3). Using these preparation conditions, all nucleotide-binding pockets were empty. The two apo states were also exclusively heptameric, but displayed significantly different conformations when compared to the ADP state and to each other (Fig. 4). Compared to the ADP state, both apo states presented a smaller opening of the matrix vestibule (27 Å vs. 40 Å diameter) as a result of an inward rolling movement of the

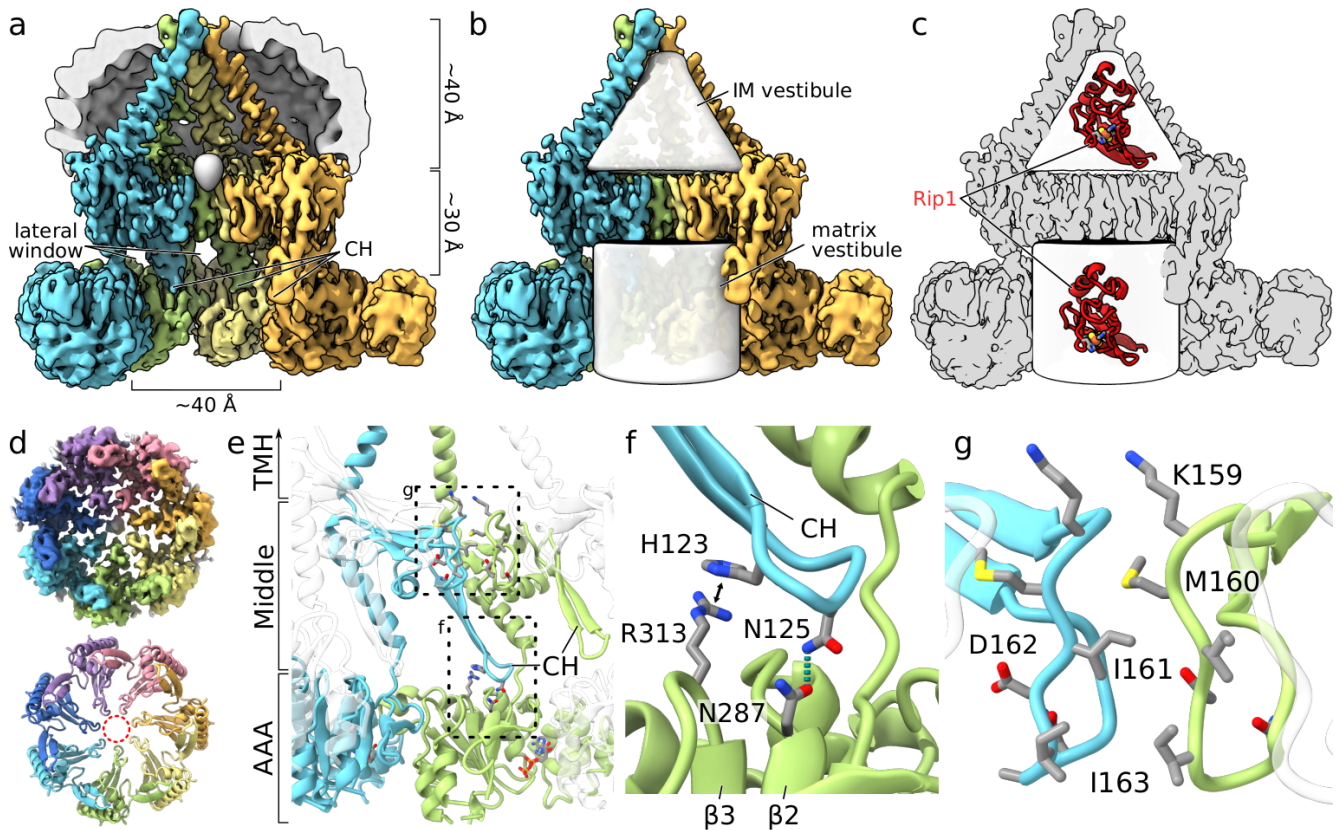


Figure 2: Bcs1 vestibules and protomer interactions. (a) Cut side view showing four protomers of Bcs1 embedded in the micelle (grey outer shell) and unaccounted density near the seal loop. Segmented maps for the micelle and the unaccounted density were lowpass filtered to 7.5 Å. (b) view of Bcs1 as in (a) but showing a cone shaped and a cylindrical volume representing the IM and matrix vestibules. (c) View as in (b) with Bcs1 in grey and an additional ribbon representation of the globular domain of Rip1 (PDB: 1KB9) fitted into the two vestibules. (d) Top views of the isolated middle domains (map and model) highlighting the pore. (e) View highlighting inter-domain connections with zooms (f) and (g) showing the CH interacting with the neighbouring large AAA domain (f) and two neighbouring seal loops (g).

ATPase domains (Fig. 5). Moreover, a significant difference was apparent between the Apo1 and the Apo2 state regarding the middle domain, which resulted in an opening of the seal pore otherwise separating the matrix vestibule from the IM vestibule (Fig. 4c, cut view). In more detail, the ATPase domains in the heptameric ring undergo an inward rotation of about 20° when measured relative to their interface at the nucleotide-binding pocket (Fig. 5a). In general, in all AAA proteins, a reorganization of their AAA domains is caused by conformational changes of dynamic trans-acting elements at their interfaces. Here, most important are the Arg-finger (the loop between $\alpha 4$ and $\beta 5$ second region of homology; SRH) and the intersubunit sensing (ISS) motif (located at the end of $\alpha 3$ and the following loop towards $\beta 4$ and characterized by a conserved aspartate, D350)²⁷. We find that the Arg-fingers of Bcs1, R376 and R379 present in the respective loop, moved about 7 Å towards the nucleotide-binding pocket of the neighboring subunit when comparing the ADP- to the Apo states (Fig. 5b). We also identified an ISS-like region (ILR) with an aspar-

tate in an identical position as observed in the classical clades of AAA proteins. In the ADP- and Apo2 state, the ILR loop is rather elongated, but in the Apo1 state, it bulges out towards the nucleotide-binding pocket (Fig. 5b). When comparing the two apo states, the main conformational changes occur on the middle domain and its CH. In the ADP and Apo1 states, the relative conformation of the middle domains is very similar and the states mainly differ by the rolling movement of the AAA domains narrowing the matrix vestibule (Fig. 5c). In contrast, the Apo2 state displayed a more dramatic difference (Fig. 5d): we observe a tilt of the middle domain away from the membrane plane, thus, separating the seal loops and creating a widened pore opening between the vestibules (Fig. 4 c, 5d). Whereas in the ADP and Apo1 state, the seven seal loops are tightly packed together to form the closed seal, these loops are separated in the Apo2 state, which results in increased flexibility and disorder as indicated by reduced local resolution (Extended Data Fig. 2). As a consequence, the widened pore appears to provide sufficient space for Rip1 to translocate

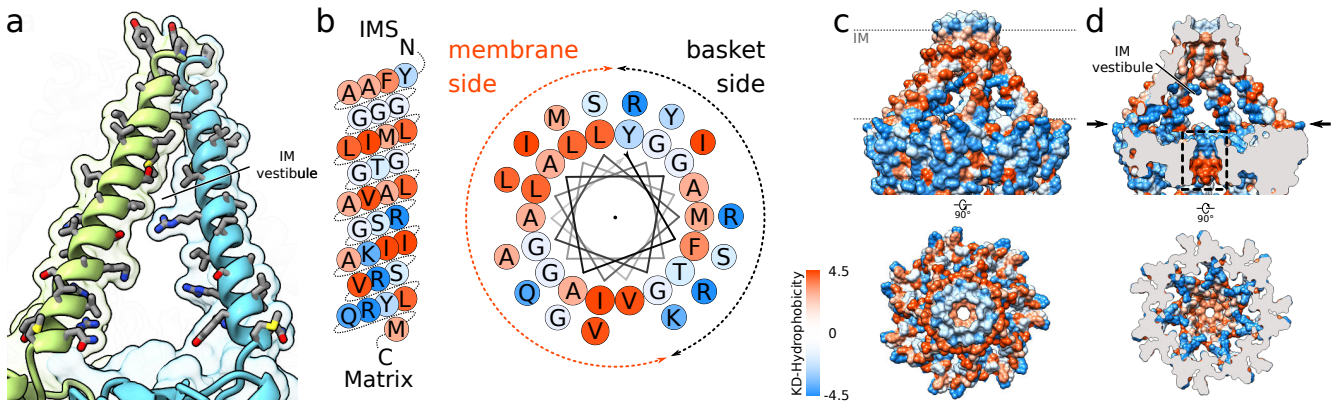


Figure 3: The IM vestibule and TMH surface hydrophobicity. (a) View highlighting the basket-like arrangement of the TMHs; a surface representation and side chains of two adjacent TMHs are shown. (b) Schematic and helical wheel representation of the Bcs1 TMH indicating its amphipathic/hydrophobic character on the C-/N-terminal sides. (c) and (d) Surface representations of Bcs1-ADP coloured according to the hydrophobicity scale of Kyte and Doolittle³³. (c) Two views (side and bottom) showing the hydrophobic character of the membrane-facing side of the TMHs; (d) two views (cut side view and cut top view) showing the hydrophobic character of the seal ring towards the matrix side and the hydrophilic character of the IM vestibule; note the highly amphiphilic character of the pore (dashed black box).

from the matrix to the IM vestibule in the Apo2 state. A further structural difference distinguishing the Apo2 from both other structures is the conformation of the CH (Fig. 5d). While the CH points inwards to the matrix vestibule of Bcs1 in the ADP and Apo1 state, the Apo2 state displays a flipped out conformation, i.e. the CH points away from the matrix vestibule. This outward movement may be a direct result of the inward rolling of the AAA domains. Therefore, the tilt of the middle domain may be triggered by this relocation of the CH. Thus opening of the seal could be a direct result of the Bcs1 ATPase activity. Notably, a N125D mutation at the tip of the CH (Fig. 2f) results in complete loss of respiratory growth capability²⁸ supporting the functional relevance of the CH dynamics in Bcs1 activity.

Discussion

In this work, we present the structure of Bcs1, a molecular machine that is able to translocate the fully folded Rip1 protein from the mitochondrial matrix to the IMS. We found that in contrast to most AAA proteins Bcs1 assembles into heptamers and not hexamers. This allows formation of two sizable cavities that are large enough to accommodate the folded Rieske protein without extensive conformational remodeling: the matrix vestibule and the inner membrane vestibule. These two vestibules are separated by the seal forming middle domain of Bcs1, and conformational differences between the Apo2 state and Apo1 or ADP state indicate that outward rolling of the middle domains can result in an opening of the seal, allowing passage between the two vestibules. Based on these structures, we propose an airlock-like mechanism for translocation of the folded Rieske protein (Fig. 6).

Similar to an airlock, which enables passage between two different atmospheric conditions without mixing them via two alternately used doors, we envision that Bcs1 follows a conceptually similar mechanism: it allows the Rieske protein to translocate from the matrix into the IMS / IM while essentially maintaining the vital permeability barrier of the IM.

As a prerequisite, Rip1 needs to be targeted from the mitochondrial matrix to Bcs1, a poorly understood process, which involves the chaperone Mzm1 that protects matrix located Rip1 prior to Bcs1 mediated topogenesis from aggregation²⁹. Once targeting has occurred, we suggest that Rieske translocation happens in three steps: i) Rip1 loading into the Bcs1 matrix vestibule, ii) gating of the seal and transition of Rip1 into the IM vestibule through the widened pore similar to that observed in the Apo2 state and iii) release of the Rieske protein to the IMS accompanied by lateral release of its TMH (Fig. 6). The detailed mechanism of release from the IM vestibule remains unclear but is likely to involve rearrangement of the Bcs1 TMHs to allow release of the globular Rip1-FeS domain and lateral partitioning of the Rip1 TMH into the IM. Here, the mild hydrophobicity of the Rip1 TMH and a nucleotide dependent interaction between Bcs1 and specific assembly intermediates of the bc1-complex point towards a pathway, in which Rip1 is directly handed over to and incorporated into the bc1-precomplex^{11,26}.

The question remains, how Bcs1 couples ATP-hydrolysis with substrate transport. All AAA proteins are mechanochemical machines that are driven by their ATPase cycle, during which binding and hydrolysis of ATP is coupled to conformational changes. Thereby, classical hexameric AAA proteins such as Yme1 or Cdc48 utilize ATP hydrolysis to induce a

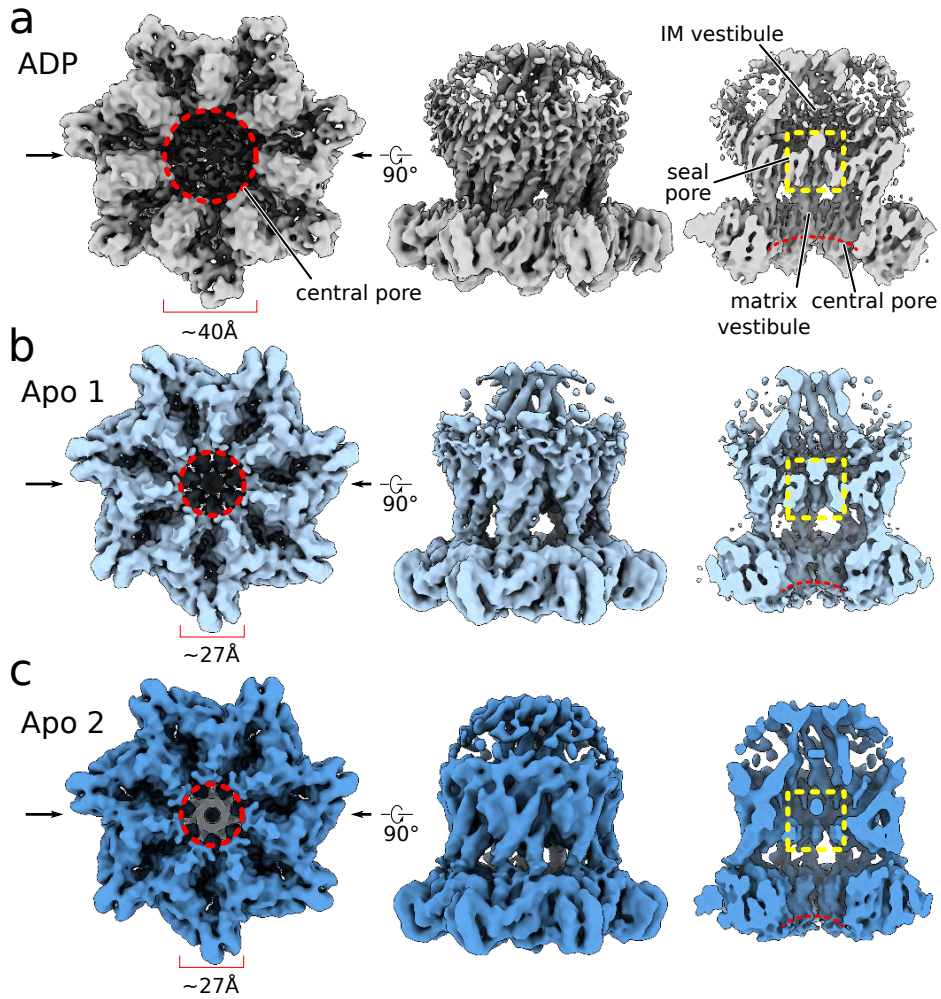


Figure 4: Overview of the Bcs1 ADP and apo states. (a) – (c) Top, side and cut side views of cryo-EM maps of the Bcs1 ADP, Apo1 and Apo2 states. The pore formed by the ring of AAA domains (central pore) is indicated by a dashed red circle (left column) and the pore formed by the middle domains (seal pore) by a dashed yellow box in the cut views (right column).

pulling force on a substrate peptide chain, and recent high-resolution cryo-EM structures revealed that individual protomers usually have different states in the active assembly (ATP-bound, ADP-bound or apo). Here ATP binding enables substrate binding via conserved pore loops, which are arranged in a staircase-like manner, whereas ATP-hydrolysis triggers substrate release. Conformational changes within the protomer and relative to the assembly enable a so-called hand-over-hand mechanism, that gives rise to a unidirectional force on the substrate^{20–22,24,30,31}. In case of Bcs1, we, unfortunately, could not obtain a structure with a bound substrate and either ATP or a non-hydrolysable ATP analogon present. Yet, our structures still reveal possible conformational rearrangements that may happen during the ATPase cycle. The Bcs1 pore loops do not point towards the central axis of the heptameric assembly but rather away from the plane of the AAA ring, distinguishing these loops from what is observed in classical hexameric AAA proteins engaging a substrate. Nevertheless, one or both of these loops could transiently bind to Rip1

and thus, ATP hydrolysis could generate a translocation force in a mechanism similar to what is known from other hexameric AAA proteins. Notably, in classical AAA proteins such as Cdc48, Yme1 or AFG3L2^{20,22,32}, the substrate first engages with pore loop 1 and then pore loop 2. In contrast, the unique architecture and orientation of the heptameric Bcs1 AAA ring would require the substrate to first engage pore loop 2 and then possibly pore loop 1 for translocation (Extended Data Fig. 5). Thus, the translocation direction is indeed reversed with respect to the AAA ring compared to canonical AAA proteins. These findings may indicate distinct mechanistic adaptations of Bcs1 to its much larger and folded translocation substrate.

The linked conformational dynamics of the middle domain and the ATPase domain in particular in state Apo2 show that the seal pore can substantially widen. Thus, one possibility is that ATP-hydrolysis can trigger the conformational change in the middle domain that leads to opening of the seal. Yet, considering the observed structures it is not clear whether this transition occurs

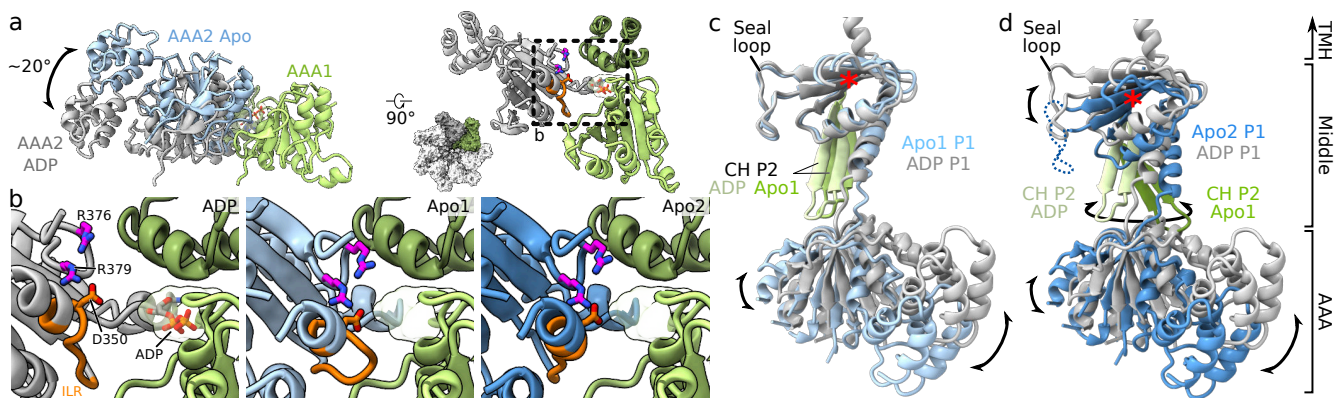


Figure 5: Conformational dynamics of Bcs1 between ADP and apo states. (a) Conformational rearrangement of the AAA domains within the heptamer. Left half: The AAA domain of the neighbouring subunit (AAA2) undergoes an inward rotation of approximately 20° relative to the first AAA domain (AAA1) from the ADP- to both apo states. Right half: an orthogonal view highlighting the region around the nucleotide binding pocket of the AAA domains between two adjacent protomers. A thumbnail of the Bcs1 complex indicates the orientation. (b) Zoom on the dashed box shown in (a) comparing nucleotide-binding pockets in the ADP, Apo1 and Apo2 states. Arginines in the Arg-finger (magenta) as well as the ISS-like region (ILR; orange) with a conserved aspartate are highlighted; the transparent surface indicates the location of the nucleotide-binding pocket. (c), (d), Conformational rearrangements of the middle domain and AAA domain of Apo1 (c) and Apo2 (d) compared with the ADP state. (c) A rolling movement of the AAA domains is observed when superimposing the middle domains of the ADP- with the Apo1 state. (d) Same view as (c), but highlighting the tilt of the middle domain away from the membrane plane and the relocation of the connector hairpin (green) of the neighbouring subunit. P1 and P2: protomer 1 and 2, the red asterisk indicates the location of the CH of P1 which is not displayed for clarity.

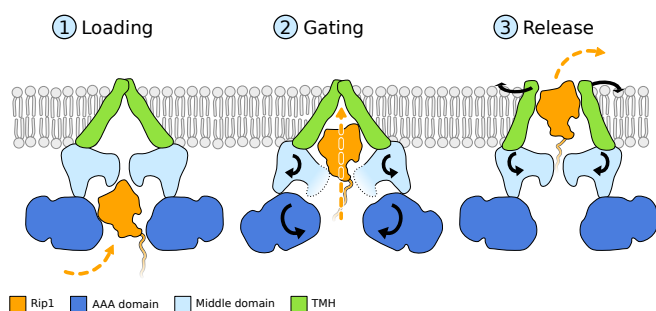


Figure 6: Model for translocation of folded Rip1 protein by Bcs1. We propose a mechanism, by which the Rip1 passes through both Bcs1 vestibules in an airlock-like mechanism. The model involves three steps: i) loading of Rip1 into the matrix vestibule of Bcs1, ii) Opening of the seal pore to allow gating of Rip1 for its translocation into the IM vestibule, and iii) Closure of the seal pore and release of the Rip1 globular domain into the IMS as well as lateral integration of the N-terminal TMH into the IM. The likely flexible N-terminus of Rip1 is only partially displayed.

subsequently in each individual protomer or whether all protomers act in a concerted way. Subsequent transitions would more closely reflect the mechanism described for classical AAA proteins performing hand-over-hand translocation with a split-washer like conformation. Al-

ternatively, a concerted action resulting in a synchronous opening of all seal loops may be important to facilitate an opening of the seal pore wide enough for the Rieske protein to traverse from the matrix vestibule to IM vestibule. To elucidate these questions, future studies, for example using a slowly hydrolyzing walker B mutant of Bcs1 with and without cargo may bring novel insight into the Bcs1-ATPase cycle and its coupling to substrate translocation. Of particular interest will be to understand the role and functional dynamics of the unique TMHs arrangement of Bcs1 that forms the basket-like IM vestibule and may function similar to the enigmatic TAT system in membrane translocation of folded proteins.

Acknowledgments

We thank Susanne Rieder, Charlotte Ungewickell and Sandra Esser for technical assistance and help with experiments and Michael Ameisemeier for support with electron microscopy. This work was supported by funding from the Deutsche Forschungsgemeinschaft (DFG) through the GRK1721 to R.B., a DFG fellowship through the QBM (Quantitative Biosciences Munich) graduate school to L.K. and the DFG grant WA3802/1-1 and the LMUexcellent program of the Bundesexzellenzinitiative to N.W. and W.N.

Author Contributions

R.B. and W.N. designed the study and L.K., N.W., T.B. and R.B. wrote the manuscript. N.W. purified and characterized Bcs1 complexes, L.K. prepared cryo-EM samples and together with O.B. collected data. L.K. processed cryo-EM maps, built molecular models and together with T.B. and R.B. interpreted the structures.

Competing Interests Statement

The authors declare no competing interests.

References

1. Rapoport, T.A., Li, L. & Park, E. Structural and Mechanistic Insights into Protein Translocation. *Annu Rev Cell Dev Biol* 33, 369-390 (2017).
2. Green, E.R. & Meccas, J. Bacterial Secretion Systems: An Overview. *Microbiol Spectr* 4(2016).
3. Berks, B.C. The twin-arginine protein translocation pathway. *Annu Rev Biochem* 84, 843-64 (2015).
4. Hunte, C., Koepke, J., Lange, C., Rossmann, T. & Michel, H. Structure at 2.3 Å resolution of the cytochrome bc₁ complex from the yeast *Saccharomyces cerevisiae* co-crystallized with an antibody Fv fragment. *Structure* 8, 669-84 (2000).
5. Kispal, G., Csere, P., Guiard, B. & Lill, R. The ABC transporter Atm1p is required for mitochondrial iron homeostasis. *FEBS Lett* 418, 346-50 (1997).
6. Kispal, G., Csere, P., Prohl, C. & Lill, R. The mitochondrial proteins Atm1p and Nfs1p are essential for biogenesis of cytosolic Fe/S proteins. *EMBO J* 18, 3981-9 (1999).
7. Wagener, N., Ackermann, M., Funes, S. & Neupert, W. A pathway of protein translocation in mitochondria mediated by the AAA-ATPase Bcs1. *Mol Cell* 44, 191-202 (2011).
8. Molik, S., Karnauchoy, I., Weidlich, C., Herrmann, R.G. & Klosgen, R.B. The Rieske Fe/S protein of the cytochrome b₆/f complex in chloroplasts: missing link in the evolution of protein transport pathways in chloroplasts? *J Biol Chem* 276, 42761-6 (2001).
9. Aldridge, C., Spence, E., Kirkilionis, M.A., Frigerio, L. & Robinson, C. Tat-dependent targeting of Rieske iron-sulphur proteins to both the plasma and thylakoid membranes in the cyanobacterium *Synechocystis* PCC6803. *Mol Microbiol* 70, 140-50 (2008).
10. Nobrega, F.G., Nobrega, M.P. & Tzagoloff, A. BCS1, a novel gene required for the expression of functional Rieske iron-sulfur protein in *Saccharomyces cerevisiae*. *EMBO J* 11, 3821-9 (1992).
11. Cruciat, C.M., Hell, K., Folsch, H., Neupert, W. & Stuart, R.A. Bcs1p, an AAA-family member, is a chaperone for the assembly of the cytochrome bc₁ complex. *EMBO J* 18, 5226-33 (1999).
12. Frickey, T. & Lupas, A.N. Phylogenetic analysis of AAA proteins. *J Struct Biol* 146, 2-10 (2004).
13. Sauer, R.T. et al. Sculpting the proteome with AAA(+) proteases and disassembly machines. *Cell* 119, 9-18 (2004).
14. Truscott, K.N., Lowth, B.R., Strack, P.R. & Dougan, D.A. Diverse functions of mitochondrial AAA+ proteins: protein activation, disaggregation, and degradation. *Biochem Cell Biol* 88, 97-108 (2010).
15. Zolkiewski, M. A camel passes through the eye of a needle: protein unfolding activity of Clp ATPases. *Mol Microbiol* 61, 1094-100 (2006).
16. Tatsuta, T. & Langer, T. AAA proteases in mitochondria: diverse functions of membrane-bound proteolytic machines. *Res Microbiol* 160, 711-7 (2009).
17. Chen, Y.C. et al. Msp1/ATAD1 maintains mitochondrial function by facilitating the degradation of mislocalized tail-anchored proteins. *EMBO J* 33, 1548-64 (2014).
18. Okreglak, V. & Walter, P. The conserved AAA-ATPase Msp1 confers organelle specificity to tail-anchored proteins. *Proc Natl Acad Sci U S A* 111, 8019-24 (2014).
19. Wohlever, M.L., Mateja, A., McGilvray, P.T., Day, K.J. & Keenan, R.J. Msp1 is a membrane protein dislocase for tail-anchored proteins. *Molecular cell* 67, 194-202 (2017).
20. Puchades, C. et al. Structure of the mitochondrial inner membrane AAA+ protease YME1 gives insight into substrate processing. *Science* 358(2017).
21. Lee, S. et al. Cryo-EM Structures of the Hsp104 Protein Disaggregase Captured in the ATP Conformation. *Cell Rep* 26, 29-36 e3 (2019).
22. Twomey, E.C. et al. Substrate processing by the Cdc48 ATPase complex is initiated by ubiquitin unfolding. *Science* (2019).
23. Majumder, P. et al. Cryo-EM structures of the archaeal PAN-proteasome reveal an around-the-ring ATPase cycle. *Proc Natl Acad Sci U S A* 116, 534-539 (2019).

24. White, K.I., Zhao, M., Choi, U.B., Pfuetzner, R.A. & Brunger, A.T. Structural principles of SNARE complex recognition by the AAA+ protein NSF. *Elife* 7(2018).
 25. Folsch, H., Guiard, B., Neupert, W. & Stuart, R.A. Internal targeting signal of the BCS1 protein: a novel mechanism of import into mitochondria. *EMBO J* 15, 479-87 (1996).
 26. Wagener, N. & Neupert, W. Bcs1, a AAA protein of the mitochondria with a role in the biogenesis of the respiratory chain. *J Struct Biol* 179, 121-5 (2012).
 27. Miller, J.M. & Enemark, E.J. Fundamental Characteristics of AAA+ Protein Family Structure and Function. *Archaea* 2016, 9294307 (2016).
 28. Nouet, C., Truan, G., Mathieu, L. & Dujardin, G. Functional analysis of yeast *bcs1* mutants highlights the role of Bcs1p-specific amino acids in the AAA domain. *J Mol Biol* 388, 252-61 (2009).
 29. Atkinson, A. et al. The LYR protein Mzm1 functions in the insertion of the Rieske Fe/S protein in yeast mitochondria. *Mol Cell Biol* 31, 3988-96 (2011).
 30. de la Pena, A.H., Goodall, E.A., Gates, S.N., Lander, G.C. & Martin, A. Substrate-engaged 26S proteasome structures reveal mechanisms for ATP-hydrolysis-driven translocation. *Science* 362(2018).
 31. Monroe, N., Han, H., Shen, P.S., Sundquist, W.I. & Hill, C.P. Structural basis of protein translocation by the Vps4-Vta1 AAA ATPase. *Elife* 6(2017).
 32. Puchades, C. et al. Unique Structural Features of the Mitochondrial AAA+ Protease AFG3L2 Reveal the Molecular Basis for Activity in Health and Disease. *Mol Cell* 75, 1073-1085 e6 (2019).
 33. Kyte, J. & Doolittle, R.F. A simple method for displaying the hydropathic character of a protein. *J Mol Biol* 157, 105-32 (1982).
- lysate was diluted 1:1 with 50 mM Na phosphate pH 8.0, 100 mM NaCl, 10 mM imidazole, 5% glycerol and incubated with NiNTA agarose beads for 1 h at 4°C. After washing, Bcs1 was eluted from the beads by addition of 50 mM Na phosphate pH 8.0, 100 mM NaCl, 400 mM imidazole, 5% glycerol, 0.1% digitonin. The buffer of the eluate was exchanged via a NAP-5 column (GE healthcare, fisher Scientific) to 50 mM Na phosphate pH 8.0, 100 mM NaCl, 0.1% digitonin. Using an Amicon Ultra concentrator (MW CO 100K) oligomeric BCS1 complex was concentrated to 0.5 mg/ml. In case of ADP-bound Bcs1 ATP was added to 1 mM final concentration to the purified Bcs1 complex and incubated on ice for 1h prior to cryo-EM sample preparation.

Grid making and data acquisition

Samples were applied on Quantifoil carbon coated R 1.2/1.3 (for Bcs1 Apo) or R2/2 (for Bcs1 ADP) UltrAu-Foil grids. The grids were first plasma cleaned (2.2×10^{-1} torr, 20s), then $3.5 \mu\text{l}$ of sample (0.5 mg/ml) were spotted onto the grids, incubated for 45 s, blotted (2.5 s; blot force 0, 95% humidity, 5°C) and then flash frozen in liquid ethane using a Vitrobot Mark IV (FEI / Thermo Fisher).

Data for both samples were collected on a Titan Krios G3 (FEI / ThermoFisher) using a K2 (Gatan) detector and GIF energy filter. Using EPU (FEI / ThermoFisher), 2919 (for Bcs1 Apo) and 7092 (for Bcs1 ADP) dose fractionated movies with 48 frames, an exposure of $1.2 \text{ e}^-/\text{frame}$ and $1.35 \text{ e}^-/\text{frame}$, respectively, and a magnification resulting in an image pixel size of $1.059 \text{ \AA}/\text{px}$ were collected.

Image Processing

First, anisotropic motion correction (4x4 patches, grouping of 3 frames) and dose weighting was achieved utilizing MotionCor2³⁴. Then CTF parameters were estimated using CTFFIND4³⁵. The dose weighted micrograph sums were visually inspected and bad micrographs showing aggregates, contamination or bad ice were discarded.

After pre-processing, single particle analysis was performed as outlined in Extended Data Fig. 3. In brief, for the Bcs1 Apo dataset 1829 micrographs were imported into CRRYOSPARC v2³⁶ to generate an initial reference model. 2D projections generated from the cryo-EM structure of the Vps4 hexamer (EMD-8588)³⁷ via the `relion_project` command served as templates to pick 481,514 particles in CRYOSPARC v2. After extraction, particles were subjected to 2D classification with 100 classes. Good 2D classes were selected and the resulting 36,489 particles were used as input for *ab initio* reconstruction of three classes, of which one clearly showed the heptameric ring of AAA domains and a micelle. Further processing was conducted in RELION-3 (version 3.0.4)^{38,39}. Selected particles were subjected to 3D auto-refinement using C1 symmetry using the *ab*

Methods

Ni-NTA affinity purification of native BCS1 complex.

A mitochondrial crude fraction was isolated from a *S. cerevisiae* strain (W303) expressing N-terminally His-tagged Bcs1 from the YEp51 plasmid in the *bcs1* Δ background. 5 mg of this mitochondrial fraction were resuspended in 50 mM Na phosphate pH 8.0, 100 mM NaCl, 10 mM imidazole, 5% glycerol, 1:100 diluted protease inhibitor without EDTA (Calbiochem). Afterwards digitonin was added to a final concentration of 3% (w/v) and incubated for 10 min on ice. Undissolved membranes were pelleted at 15000xg for 10 min at 4°C. The clear

initio map as reference. The resulting map was then used as a reference for auto-picking, yielding 1,389,762 particles. They were extracted and down-sampled to 2.12 Å/pixel and subsequently classified into 100 2D classes. 2D classes were selected based on visual inspection and the provided alignment statistics, giving a set of 223,580 particles. Using 3D classification with particle alignment, these particles were grouped into four classes, with the largest class (44%) giving good resolution. Unbinned particles of this class were re-extracted and subjected to 3D auto-refinement with applied C7 symmetry yielding a map with 4.4 Å resolution. Further 3D sub-classification of this class with C1 symmetry yielded two distinct states, Apo1 and Apo2, which by applying C7 symmetry could be refined to 4.4 Å and 4.6 Å, respectively. Additional classification, CTF-refinement or Bayesian polishing could not further improve the resolution.

The Bcs1 ADP dataset was processed as described in Extended Data Fig. 4 using RELION-3 (version 3.0.4). To start, 2000 micrographs were used for initial particle picking using the RELION AutoPick Laplacian of Gaussian (LoG) method³⁹ yielding 1,101,692 particles. These particles were extracted, down-sampled to 4.14 Å/pixel and subjected to 2D classification (100 classes). The resulting 730,699 good particles were re-extracted (2.12 Å/pixel) and refined against a 45 Å low-pass filtered map obtained from the Bcs1 Apo dataset (see above; Bcs1 Apo). The resulting map was used as a 3D reference for particle picking of the complete set of 7092 micrographs, yielding 3,479,264 particles. These were extracted, down-sampled to 4.14 Å/pixel and subjected to 2D classification (100 classes), yielding 1,549,306 good particles. Using the reference generated from the initial subset of 2000 micrographs, a 3D classification with five classes and global particle alignment was performed. Apart from four classes showing low resolution, miss-picked particles and in one case very strong orientation bias, one class showed clear features similar to the Bcs1 Apo states. The particles were re-extracted unbinned, refined with C7 symmetry and the resulting 3.5 Å map was used to perform refinement of the CTF parameters (beam tilt and per particle CTF parameters), increasing the resolution to 3.4 Å and 4.0 Å for C7 and C1 symmetry refinements, respectively.

Model building and refinement

First, a model was built for the C7 symmetrized Bcs1-ADP map at 3.4 Å. A homology model for the Bcs1 AAA domains was generated using HHPred⁴⁰ and Modeller⁴¹. Based on this model adjustments to the AAA domain and de novo building of the middle and TMH domain was conducted using COOT⁴². The model was refined using MDFF and PHENIX real space refinement as provided by the NAMDINATOR server⁴³. To obtain models for the Apo states, the ADP model was fit into the maps of states Apo1 and Apo2 using COOT and re-

fined in a further round of real space refinement using PHENIX⁴⁴. PHENIX PDB tools was then used to trim the sidechains. Models and maps were visualized and figures were made using UCSF ChimeraX⁴⁵.

Data Availability Statement

The cryo-EM density maps and corresponding atomic models reported in this paper have been deposited in the EM Data Bank and Protein Data Bank with the accession codes EMD-10192, EMD-10193 and EMD-10194 as well as PDB 6SH3, 6SH4 and 6SH5 for the Bcs1-ADP, Bcs1-Apo1 and Bcs1-Apo2 states.

Methods-only References

34. Zheng, S.Q. et al. MotionCor2: anisotropic correction of beam-induced motion for improved cryo-electron microscopy. *Nat Methods* 14, 331-332 (2017).
35. Rohou, A. & Grigorieff, N. CTFFIND4: Fast and accurate defocus estimation from electron micrographs. *J Struct Biol* 192, 216-21 (2015).
36. Punjani, A., Rubinstein, J.L., Fleet, D.J. & Brubaker, M.A. cryoSPARC: algorithms for rapid unsupervised cryo-EM structure determination. *Nat Methods* 14, 290-296 (2017).
37. Su, M. et al. Mechanism of Vps4 hexamer function revealed by cryo-EM. *Sci Adv* 3, e1700325 (2017).
38. Fernandez-Leiro, R. & Scheres, S.H.W. A pipeline approach to single-particle processing in RELION. *Acta Crystallogr D Struct Biol* 73, 496-502 (2017).
39. Zivanov, J. et al. New tools for automated high-resolution cryo-EM structure determination in RELION-3. *Elife* 7(2018).
40. Hildebrand, A., Remmert, M., Biegert, A. & Sodring, J. Fast and accurate automatic structure prediction with HHpred. *Proteins* 77 Suppl 9, 128-32 (2009).
41. Webb, B. & Sali, A. Protein Structure Modeling with MODELLER. *Methods Mol Biol* 1654, 39-54 (2017).
42. Emsley, P. & Cowtan, K. Coot: model-building tools for molecular graphics. *Acta Crystallogr D Biol Crystallogr* 60, 2126-32 (2004).
43. Kidmose, R.T. et al. Namdinator - automatic molecular dynamics flexible fitting of structural models into cryo-EM and crystallography experimental maps. *IUCrJ* 6, 526-531 (2019).
44. Afonine, P.V. et al. Real-space refinement in PHENIX for cryo-EM and crystallography. *Acta Crystallogr D Struct Biol* 74, 531-544 (2018).

45. Goddard, T.D. et al. UCSF ChimeraX: Meeting modern challenges in visualization and analysis. *Protein Sci* 27, 14-25 (2018).

Extended Data

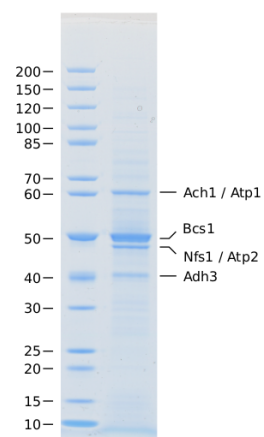


Figure 7: SDS-PAGE gel of purified Bcs1. The concentrated Bcs1-His eluate (see Materials and Methods) was loaded on a 4-10% gradient gel and bands were analyzed by mass spectrometry. This mild and fast one-step affinity purification yields Bcs1 assemblies active in nucleotide and substrate binding⁷; remaining background proteins represent abundant mitochondrial proteins that unspecifically interact with Ni-NTA resin.

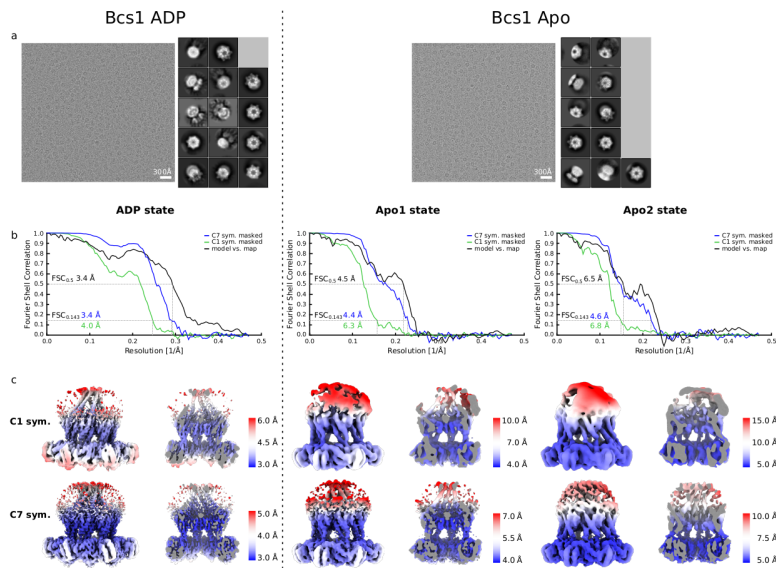


Figure 8: Cryo-EM data processing of the Bcs1 complex with and without ADP. (a) Representative original micrograph and 2D class averages for the ADP (left) and the Apo (right) datasets. (b) “Gold standard” Fourier-Shell correlation (FSC) curves when applying C1 and C7 symmetry during refinement. The final resolutions were 3.4 Å (C7) and 4.0 Å (C1). (c) Final C1 and C7 symmetrized maps filtered and colored according to local resolution as calculated with RELION-3.

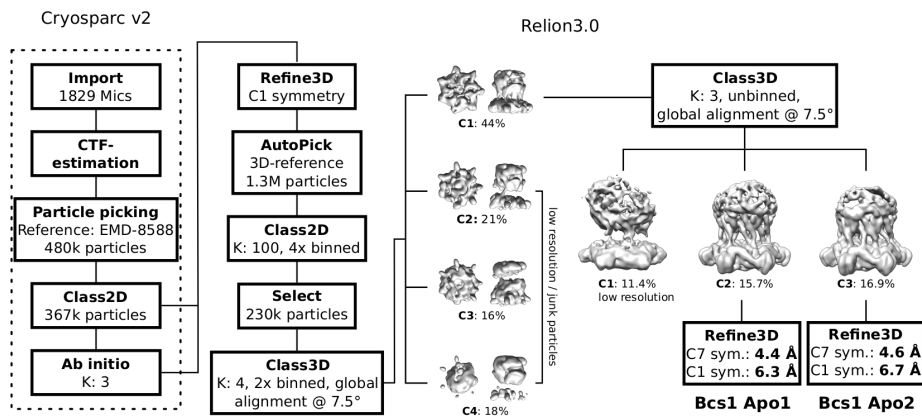


Figure 9: 3D classification scheme for the Bcs1 apo data set. The classification regiment is described in detail in the Methods section. In brief, after import and CTF-estimation, particles were first picked using the structure of the Vps4 AAA-ATPase hexamer as a template (EMD-8588)³⁷. Particles were 2D classified and an ab initio model was obtained using cryoSPARC v.2. From the refined map, a better reference for RELION autopicking was obtained and resulting particles were again 2D classified. Good classes were subjected to 3D classification yielding one stable feature-containing class that could be sub-classified further. Two stable classes were then 3D refined using either C1 or C7 symmetry yielding the final Bcs1 Apo1 and Bcs1 Apo2 maps. K: number of classes.

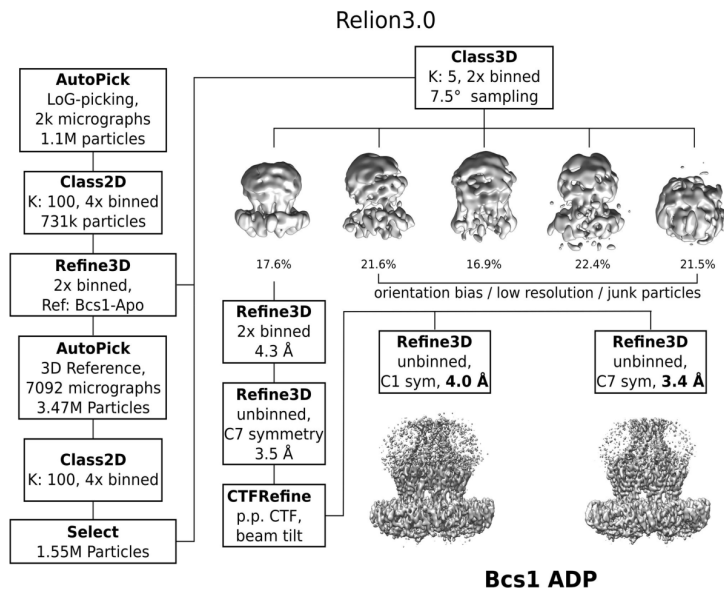


Figure 10: 3D classification scheme for the Bcs1 ADP dataset. The classification regiment is described in detail in the Methods section. In brief, autopicking in RELION-3 (Laplacian of Gaussian (LoG) method)³⁸ was performed using the previously obtained structure of Bcs1 Apo1 as a reference. 2D classification and 3D refinement were performed and auto-picking repeated using the refined map to optimize the quality and yield of good Bcs1 complex particles. After a second round of 2D classification and refinement, 3D classification yielded in one class that could be refined including per particle CTF correction and beam tilt correction in RELION-3 using C1 and C7 symmetry to a final resolution of and 3.4 Å and 4.0 Å, respectively. K: number of classes.

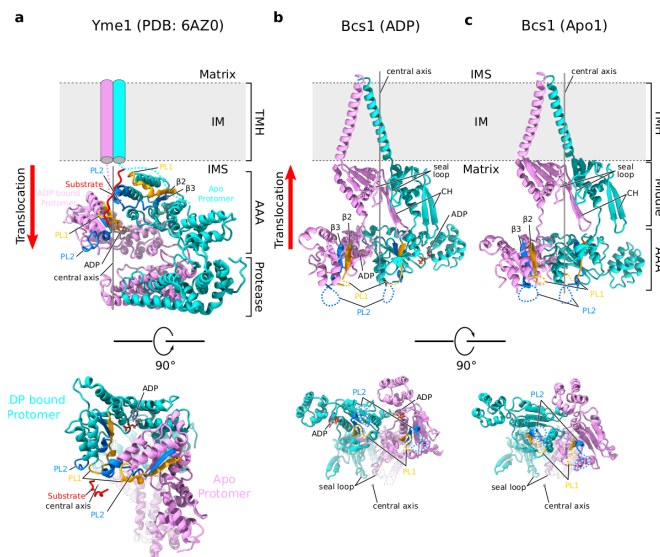
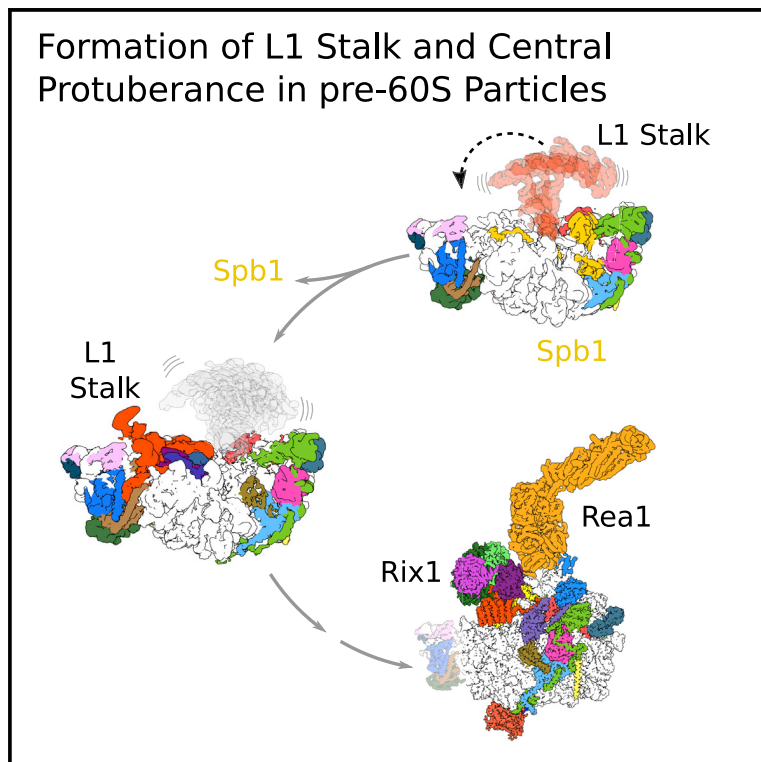


Figure 11: Comparison of two membrane bound mitochondrial AAA proteins Yme1 and Bcs1. Shown are two protomers of both Yme1 (a) (PDB: 6AZ0) 20 and Bcs1 either in the ADP state (b) or the Apo1 state (c). The pore loops and preceding beta strands are shown in orange (PL1, $\beta 2$) and blue (PL2, $\beta 3$). The six AAA domains of Yme1 form a spiral staircase configuration. Displayed here are the ADP-bound (purple) and Apo (cyan) protomers, which constitute the bottom and top end of this spiral. The two pore loops of every AAA domain protrude towards the central axis of this complex, where they can interact with the peptide backbone of the substrate (red) via the conserved tyrosine residues. In this configuration, the beta strands $\beta 2$ and $\beta 3$, which precede the two pore loops point towards the central axis. Conversely, in Bcs1, these loops and the corresponding preceding beta strands do not point towards the opening of the ring of AAA domains, but rather point away from the ring plane in both displayed conformations. In the ADP state these loops are oriented approximately parallel to the central axis, in the apo states they are slightly tilted towards the central axis.

Construction of the Central Protuberance and L1 Stalk during 60S Subunit Biogenesis

Graphical Abstract



Authors

Lukas Kater, Valentin Mitterer, Matthias Thoms, Jingdong Cheng, Otto Berninghausen, Roland Beckmann, Ed Hurt

Correspondence

beckmann@genzentrum.lmu.de (R.B.), ed.hurt@bzh.uni-heidelberg.de (E.H.)

In Brief

Kater et al. show structures of pre-60S assembly intermediates, revealing how two Rix1-Rea1 machinery-dependent transitions result in L1 stalk formation and construction of the central protuberance. A molecular model of the Rix1 complex shows how its Ipi1 subunit anchors it to the pre-60S subunit, in turn permitting Rea1 recruitment.

Highlights

- Pre-60S cryo-EM structures show L1 stalk formation after Erb1-Ytm1 release
- L1 stalk maturation sets the basis for central protuberance construction
- Nucleoplasmic Rix1-Rea1 pre-60S particle reveals architecture of the Rix1 complex
- Ipi1 serves as anchor of the Rix1 complex to the pre-60S particle

Article

Construction of the Central Protuberance and L1 Stalk during 60S Subunit Biogenesis

Lukas Kater,¹ Valentin Mitterer,² Matthias Thoms,^{1,2} Jingdong Cheng,¹ Otto Berninghausen,¹ Roland Beckmann,^{1,3,*} and Ed Hurt^{2,*}

¹Gene Center Munich and Center of Integrated Protein Science-Munich (CiPS-M), Department of Biochemistry, Feodor-Lynen-Str. 25, University of Munich, 81377 Munich, Germany

²Biochemie-Zentrum der Universität Heidelberg, 69120 Heidelberg, Germany

³Lead Contact

*Correspondence: beckmann@genzentrum.lmu.de (R.B.), ed.hurt@bzh.uni-heidelberg.de (E.H.)

<https://doi.org/10.1016/j.molcel.2020.06.032>

SUMMARY

Ribosome assembly is driven by numerous assembly factors, including the Rix1 complex and the AAA ATPase Rea1. These two assembly factors catalyze 60S maturation at two distinct states, triggering poorly understood large-scale structural transitions that we analyzed by cryo-electron microscopy. Two nuclear pre-60S intermediates were discovered that represent previously unknown states after Rea1-mediated removal of the Ytm1-Erb1 complex and reveal how the L1 stalk develops from a pre-mature nucleolar to a mature-like nucleoplasmic state. A later pre-60S intermediate shows how the central protuberance arises, assisted by the nearby Rix1-Rea1 machinery, which was solved in its pre-ribosomal context to molecular resolution. This revealed a Rix1₂-Ipi3₂ tetramer anchored to the pre-60S via Ipi1, strategically positioned to monitor this decisive remodeling. These results are consistent with a general underlying principle that temporarily stabilized immature RNA domains are successively remodeled by assembly factors, thereby ensuring failsafe assembly progression.

INTRODUCTION

To generate functional ribosomes, eukaryotic cells produce and assemble four ribosomal RNA (rRNA) species (18S, 5.8S, 25S, and 5S rRNA in yeast) and about 80 ribosomal proteins into two ribonucleoprotein particles (RNPs), the 60S large ribosomal subunits (LSUs) and the 40S small ribosomal subunits (SSUs). These processes occur in a highly orchestrated and regulated assembly line, which is coordinated by more than 200 assembly factors, also known as biogenesis factors (Baßler and Hurt, 2019; Klinge and Woolford, 2019; Woolford and Baserga, 2013). Cryo-electron microscopy (cryo-EM) studies have revealed the structural details underpinning a three-phase hierarchical model of LSU assembly first proposed after a biochemical analysis by Gamalinda et al. (2014). These phases are (1) formation of the solvent-exposed outer shell and peptide exit tunnel in the nucleolus (Kater et al., 2017; Sanghai et al., 2018; Zhou et al., 2019a), (2) construction of the central protuberance (CP) and initial formation of the inter-subunit surface (ISS) in the nucleoplasm (Barrio-Garcia et al., 2016; Wu et al., 2016), and (3) maturation of the ISS and the peptidyl transferase center (PTC), which is the active site of the ribosome, in the cytoplasm (Kargas et al., 2019; Ma et al., 2017; Malyutin et al., 2017; Zhou et al., 2019b).

Toward the end of the first phase, after construction of the solvent-exposed back and formation of the peptide exit tunnel, late

nucleolar particles (states D and E) (Kater et al., 2017) stabilize the L1 stalk rRNA (helices 75–78 of the 25S rRNA) in a pre-mature conformation with an array of assembly factors (Ebp2, Nip7, Noc3, and Nop2) (Kater et al., 2017). In this conformation, the stalk blocks the site that would be occupied by the mature CP. Thus, to construct the CP during phase 2, extensive restructuring at the site of the yet-to-form ISS is required, allowing the assembly and stable incorporation of helices 80–88 of the 25S rRNA and the 5S RNP into the pre-60S particle (Figure 1A) (Kater et al., 2017). During this restructuring, several assembly factors (among these, Brx1, Ebp2, Erb1-Ytm1, Noc3, Nip7, Nop2, Nop16, and Spb1) must be released from the maturing LSU (Kater et al., 2017). Furthermore, the L1 stalk must be repositioned by a rotation at its base to adopt a mature position (Kater et al., 2017). Initial formation of the CP and ISS ultimately results in the well-known nucleoplasmic pre-60S Arx1/Nog2 particle (Bradatsch et al., 2012; Leidig et al., 2014; Wu et al., 2016).

Both major structural transitions of the nuclear assembly phase, restructuring of the L1 stalk and rotation of the CP, depend on the activity of the ATPase Rea1. First, the Erb1-Ytm1 heterodimer of the early nucleolar pre-60S particle is released by Rea1 (Bassler et al., 2010; Thoms et al., 2016; Wegrecki et al., 2015). Many previously mentioned assembly factors, which are located at the site of the yet-to-form ISS, interact with the long N-terminal tail of Erb1 (Kater et al., 2017). Furthermore, inhibition of the Rea1-mediated

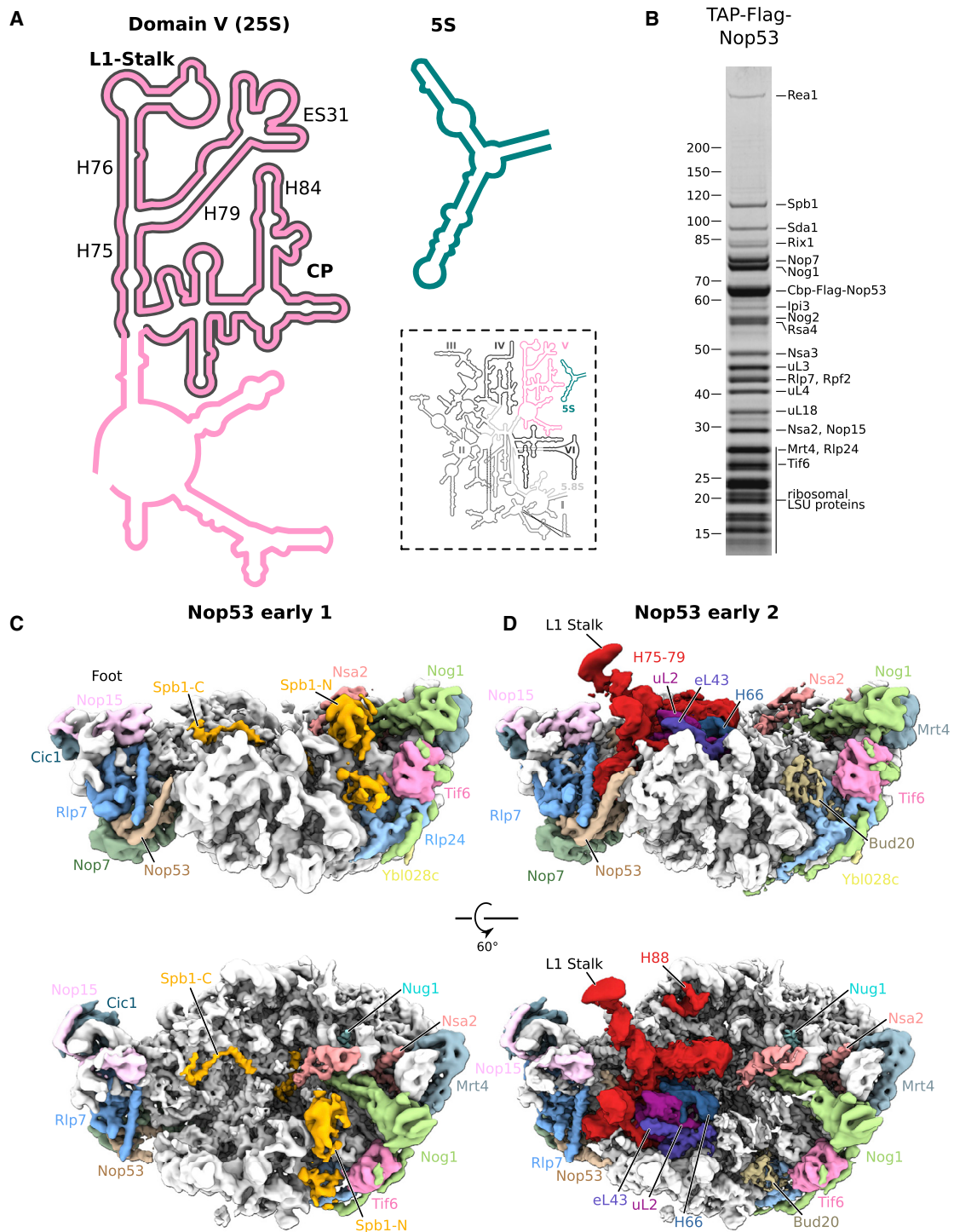


Figure 1. Nop53-Purified Particles Reveal Two Novel Early States *En Route* to Forming the CP

(A) Secondary structure plot of 25S domain V with the rRNA of the L1 stalk and CP highlighted. Inset: secondary structure diagram of the entire mature rRNA (Petrov et al., 2014).

(B) SDS-PAGE analysis of pre-60S particles purified using TAP-FLAG-Nop53.

(C and D) Front and top views of the cryo-EM maps of NE1 (C) and NE2 (D) states with assembly factors, relevant rRNA segments, and ribosomal proteins highlighted.

release of Ytm1 stalls pre-ribosomes at a nucleolar stage with all these factors bound (Kater et al., 2017). Altogether, these findings let us propose that this series of dismantling steps is triggered by the Rea1-mediated release of the Erb1-Ytm1 module (Bassler et al., 2010; Kater et al., 2017). Release of Erb1 finally allows binding of the exosome-interacting factor Nop53, because they share a common binding site on the internal transcribed spacer 2 (ITS2)-containing foot structure (Kater et al., 2017; Sanghai et al., 2018; Wu et al., 2016). The methyltransferase Spb1 also interacts with the meandering tail of Erb1, and its removal is required to form the pre-mature ISS of the Arx1/Nog2 particle, because its binding site overlaps with that of Nog2 (Kater et al., 2017; Leidig et al., 2014; Wu et al., 2016). Spb1 is found on both nucleolar Erb1 and later Nop53-containing particles (Kater et al., 2017; Thoms et al., 2015), indicating the presence of distinct 60S assembly intermediates between release of Erb1 and assembly of the CP.

Second, the 5S RNP initially binds the pre-60S particle in the nucleolus but remains flexible and unresolved in nucleolar pre-60S intermediates (Kater et al., 2017; Kressler et al., 2008; Sanghai et al., 2018; Zhang et al., 2007; Zhou et al., 2019a). Later, when the 5S RNP and CP are stably incorporated within the Arx1/Nog2 pre-60S particle, a rigid but pre-mature conformation is adopted, with the 5S rRNA rotated by 180° with respect to its mature orientation (Leidig et al., 2014; Wu et al., 2016). To drive the CP closer to maturity, a further major remodeling step is required that is induced by the second binding of Rea1, an ATPase associated with diverse cellular activity (AAA), together with the Rix1-Ipi1-Ipi3 complex (Barrio-Garcia et al., 2016). Similar to the release of Ytm1, upon ATP hydrolysis, Rsa4 is extracted by Rea1 from the pre-60S, from which the Rix1 complex, Rea1, and Sda1 then dissociate (Ulbrich et al., 2009).

After these two major nuclear remodeling steps, release of the guanosine triphosphatase (GTPase) Nog2/Nug2 allows binding of the nuclear export factor Nmd3 (Matsuo et al., 2014; Trotta et al., 2003). After transport into the cytoplasm, the pre-60S particle undergoes final maturation, which includes formation of the mature PTC and dissociation of the remaining assembly factors (Kargas et al., 2019; Lo et al., 2010; Zhou et al., 2019b).

Although the final stages of 60S maturation can be visualized as several highly resolved assembly intermediates (Kargas et al., 2019; Zhou et al., 2019b), the preceding steps that initiate the formation of the CP and ISS are poorly understood. To better understand these earlier steps of nucleolar and nuclear 60S maturation, we sought to biochemically and structurally characterize additional pre-60S intermediates that allow us to trace the formation and maturation of the CP. We also disclose the first high-resolution structure of the Rix1-Rea1 machinery docked to the late nucleoplasmic pre-60S particle, which affords a more accurate description of the remodeling processes driving CP formation.

RESULTS

Two-Step Rearrangement of the L1 Stalk during the Pre-60S Nucleolar-Nucleoplasmic Transition

To study the formation of the CP and its adjacent L1 stalk (see Figure 1A for an overview of the rRNA elements), we used the tandem affinity purification tag and FLAG tagged (TAP-FLAG-

tagged) exosome recruiting factor Nop53 for affinity purification from yeast (Figure 1B) (Thoms et al., 2015). By performing single-particle cryo-EM of the obtained pre-60S particles, we identified several Nop53-associated intermediates, of which two termed Nop53 early 1 (NE1) and Nop53 early 2 (NE2) were novel and could be resolved at 3.9 and 3.8 Å resolution, respectively (Figures 1C, 1D, and S1–S3; Table 1). Both intermediates (NE1 and NE2, classes C4C1 and C4C2 in Figure S2) possess the typical ITS2-harboring foot structure in which the nucleolar Erb1 has been replaced by Nop53, suggesting that the Rea1-mediated release of Ytm1-Erb1 had already occurred. Notably, Erb1 release and replacement by Nop53 in the foot structure coincides with a conformational change of the Rlp7 N terminus, which is a prerequisite for accommodation of the L1 stalk and expansion segment (ES) 31 (Kater et al., 2017). In contrast to the preceding nucleolar pre-60S states D and E, neither of the two novel intermediates shows density for the assembly factors Brx1, Ebp2, Has1, Noc3, Nop16, Spb4, or an unknown α -soleinoid (Kater et al., 2017; Sanghai et al., 2018). However, NE1 particles retain the Spb1 methyltransferase (Kressler et al., 1999; Lapeyre and Purushothaman, 2004), which detaches during the transition from state NE1 to state NE2, upon which it is replaced in part by Bud20. In addition to this change, the L1 stalk rRNA, which was already rigidly positioned in state D/E particles, albeit in a pre-mature conformation (Kater et al., 2017), became flexible and mostly delocalized in NE1 particles, only visible at low resolution (Figure S3E). However, in NE2 particles, enabled by the dissociation of Sbp1, the L1 stalk rRNA for the first time adopts its typical mature-like conformation (Figures 1C and 1D). The peptide exit tunnel of both NE1 and NE2 particles remained empty, as it does in state E (Kater et al., 2017), Arx1-Alb1, eL39, and the C terminus of Nog1 were not yet recruited to the tunnel.

We sought to more closely investigate the composition of state NE1 by purifying this specific particle via subsequent affinity purifications targeting first Nop53 and then Spb1 (split-affinity purification). To do so, we generated two Spb1 constructs with FLAG tags inserted into the extended, unstructured section of the C terminus of Spb1 (after amino acids 437 and 516) and performed split-affinity purifications of the ProtA-(His)₆-Nop53 and Spb1-FLAG-tagged particles (Figure S3C). We chose to use an internal FLAG tag, because both the N terminus and the C terminus of Spb1 are buried in state E particles (Kater et al., 2017). Mass spectrometry analysis of these particles showed that the methyl-transferase Nop2 and its binding partner Nip7 remained bound to these particles or a subpopulation thereof, presumably still bound to the flexible L1 stalk rRNA. Cryo-EM analysis of these particles shows almost exclusively the particles corresponding to the previously described state NE1 derived from TAP-FLAG-Nop53 purification (Figures S2B, S3E, and S3F). Nog2 and Rsa4, assembly factors associated with the pre-mature CP and the ISS in Arx1/Nog2 particles, were not yet associated with these particles and likely require the stable incorporation of the CP and 5S RNP.

Thus, given the absence of the Ytm1-Erb1 complex in these two particles and the still missing CP and Arx1-Alb1, hallmarks of Arx1/Nog2 particles, we can place the pre-60S states NE1 and NE2 between the known nucleolar state E and the

Table 1. Model and Map Statistics

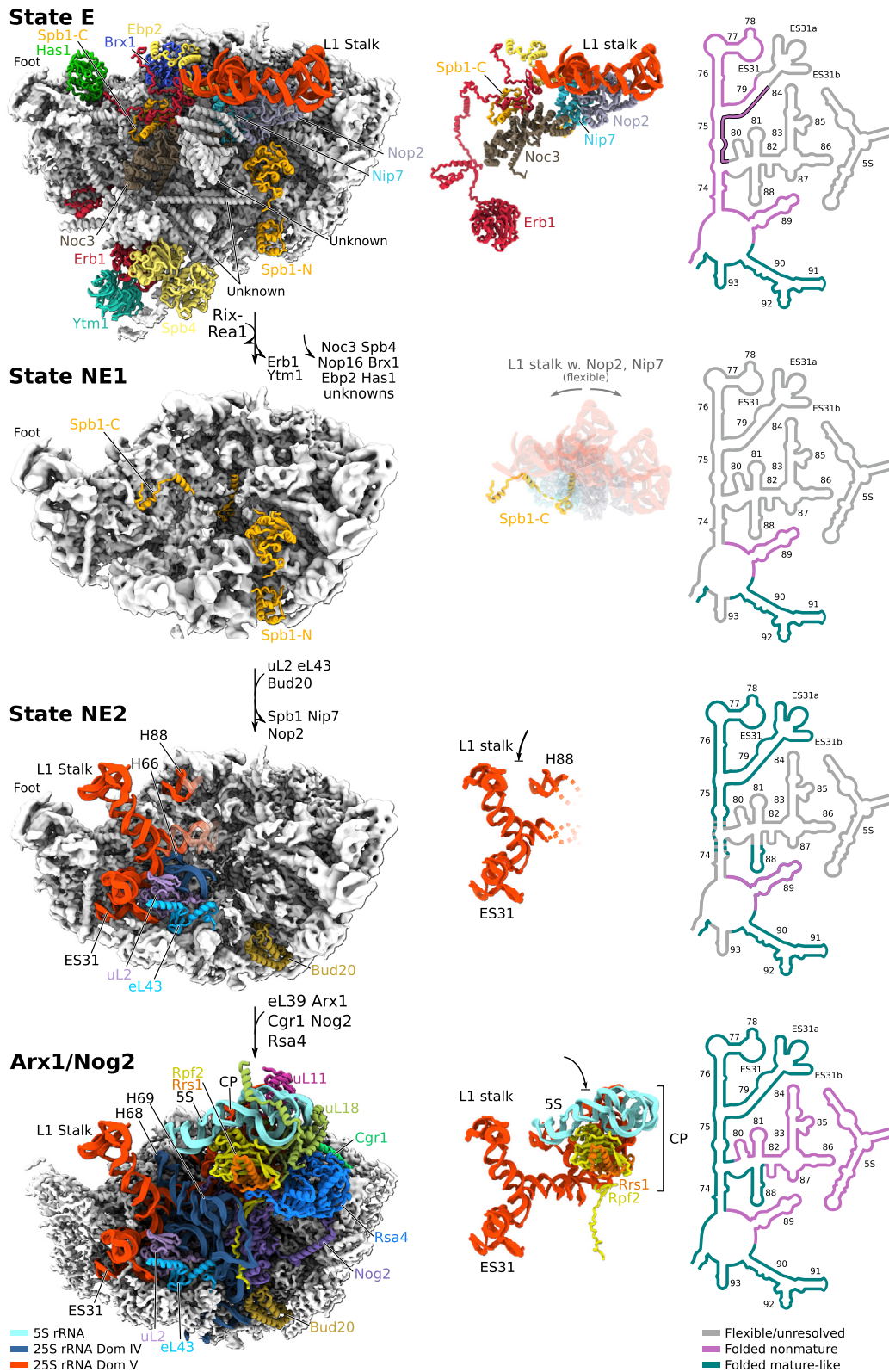
Data Collection and Processing					
Dataset	Nop53		Rix1-Rea1		
Model	NE1	NE2	60S core	Rix12-Ipi32	Rea1
Magnification	75,000×	75,000×	130,000×	130,000×	130,000×
Voltage (kV)	300	300	300	300	300
Electron exposure (e ⁻ /Å ²)	28	28	75	75	75
Defocus range (mm)	-1.0 to -3.0	-1.0 to -3.0	-0.8 to -2.5	-0.8 to -2.5	-0.8 to -2.5
Pixel size (Å)	1.084	1.084	1.059	1.059	1.059
Symmetry imposed	C ₁	C ₁	C ₁	C ₁	C ₁
No. initial particle images	499,748	499,748	273,799	273,799	273,799
No. final particle images	29,163	30,364	114,398	114,398	55,397
Map resolution (Å)	3.9	3.8	3.0	3.3	4.2
FSC threshold	0.143	0.143	0.143	0.143	0.143
Refinement					
Initial model(s) used (PDB ID)	3JCT, 6N8J, 6ELZ	3JCT, 6N8J	3JCT, 4V88, 4WJV, 6N8J	<i>de novo</i>	6EES
Map sharpening B factor (Å ²)	-60	-70	-36	-67	-85
Model Composition					
Nonhydrogen atoms	118,882	120,663	147,190	15,372	18,362
Protein residues	7,493	7,352	9,666	1,930	3,700
Nucleotide residues	2,757	2,899	3,310	0	0
B Factors (Å ²)					
Protein	96	85	57	74	128
Nucleotide	104	98	58	N/A	N/A
Ligand	N/A	109	58	N/A	N/A
RMSD					
Bond lengths (Å)	0.019	0.013	0.004	0.010	0.005
Bond angles (°)	1.666	1.314	0.997	1.352	1.264
Validation					
MolProbity score	1.58	1.47	1.71	1.19	1.34
Clashscore	6.5	6.8	4.8	4.0	1.1
Rotamer outliers (%)	0.65	0.11	0.16	0.34	0.00
Ramachandran Plot					
Favored (%)	96.6	97.5	92.8	98.5	91.1
Allowed (%)	3.4	2.4	6.8	1.5	8.9
Disfavored (%)	0	0	0.4	0	0.1

RMSD, root-mean-square deviation; FSC, Fourier shell correlation.

nucleoplasmic Arx1/Nog2 particles. Hence, we suggest the following pre-60S assembly steps (Figure 2). First, assembly factors that stabilize the pre-mature L1 stalk are released from state E, rendering the L1 rRNA flexible and unresolved in NE1. At the same time, the Spb1 C-terminal domain prevents accommodation of the L1 stalk in its mature-like conformation. Next, Spb1 dissociates, enabling the L1 stalk and ES31 to adopt mature-like conformations; concomitant with this remodeling, stable incorporation of ribosomal proteins uL2 and eL43 and positioning of rRNA helix 66 (domain IV) occur, fixing the L1 stalk at its base and priming ISS maturation. After L1 stalk formation in NE2 particles, CP formation can begin because helix 88 (see also Figure 1D) and the L1 stalk rRNA provide two anchoring points for the compaction and accommodation of the CP

rRNA, along with fixation of the 5S RNP. As a result, the prominent CP structure becomes visible for the first time in the Arx1/Nog2 particle (Figure 2). Apart from the formation of the pre-mature CP, the transition from the NE2 particle to the Arx1/Nog2 particle coincides with maturation of the peptide exit tunnel through binding of ribosomal protein eL39, together with the Nog1 C domain and Arx1-Alb1. The ISS can further mature by compaction and assembly of rRNA domain IV (i.e., ES27 and rRNA helices 67–70), accompanied by the binding of assembly factors Cgr1, Nog2, and Rsa4 (Figure 2).

In conclusion, the transition from the pre-60S nucleolar state E to the Arx1/Nog2 particles could be visualized as the two novel intermediates NE1 and NE2 that represent stages after Erb1-Ytm1 removal. This process is coupled to the release of



(legend on next page)

assembly factors that are predominantly associated with the Erb1-meandering tail and stepwise maturation of helices 75–79 of the 25S rRNA, including ES31.

Molecular Architecture of the Rix1-Rea1 Machinery on Nucleoplasmic Pre-60S Particles

To obtain insight into the next transition, that is, the Rix1-Rea1-dependent CP formation and 5S rotation, we analyzed particles obtained by split-tag-affinity purification based on Rix1-TAP as first bait and FLAG-Rea1 as second bait (Figures 3A and S3D). Performing successive affinity purifications allowed us to target the small subset of all pre-60S particles that are simultaneously associated with both the Rix1 complex and Rea1. These pre-60S particles could be separated into two distinct cryo-EM classes, with average resolutions of 6.8 and 3.0 Å, respectively (Figures 3B, 3C, and S4; Table 1). The first class (class C8 in Figure S4; 1% of all particles) exhibits an early pre-60S state before the release of Ytm1, which apparently lacks rigidly bound Rix1-Rea1 (Figure S4). This class corresponds to particles of state E, which have also been obtained by split-affinity purification using Rix1-TAP and Rpf2-FLAG (Kater et al., 2017). A second class represents a later pre-60S state (class C2 in Figure S4; 41.8% of all particles) carrying Rix1-Rea1, together with Rsa4 and Arx1, and resembles the previous Rix1-Rea1 particle, which was solved only at lower resolution (Barrio-Garcia et al., 2016; Wu et al., 2016). We noticed that the Rix1-Rea1 particles are compositionally heterogeneous, because approximately half of the particles contain the ITS2-harboring foot structure, whereas the other half had already undergone foot removal (Figure S4). Using multibody refinement (Nakane et al., 2018), we overcame the conformational variability imposed by the flexible Rix1-Rea1 machinery, yielding a final resolution of 3.0 Å for the 60S core, 3.4 Å for the Rix1 subcomplex, and 4.2 Å each for the Rea1 tail and AAA ring (Figure S1 and S4A). Altogether, this allowed us to generate molecular models for the entire Rix1-Rea1 particle, including *de novo* models for Alb1, Ipi1, Ipi3, Rix1, and Sda1 (Figures 3B and 3C).

The initially limited resolution of Rea1 on the particle indicated flexibility caused by movement of the AAA domains relative to each other and the tail relative to the Rea1 ring (Figures S1J and S4). To overcome this problem, we performed multibody refinement on Rea1 segmented into two bodies: the Rea1 tail and the Rea1 ring including the MIDAS and Rsa4-UBL domains (Figure S4). Principal-component analysis (PCA) of the rigid-body motions (Nakane et al., 2018) indicated a prominent up-and-down movement of the Rea1 tail with respect to the Rea1 ring and 60S subunit (Figure S5A). However, neither the PCA of the rigid-body motions nor further 3D classification or 2D class averages revealed a particle state in which the Rea1 tail contacts the Rsa4-UBL, as previously suggested by negative-stain elec-

tron microscopy (EM) (Ulbrich et al., 2009). All Rea1-associated pre-60S particles featured the Rea1-MIDAS bound to the Rsa4-UBL and docked onto the Rea1 AAA ring (Figures 3B, 4, and S5B). This is consistent with previous structural studies of isolated Rea1 derived from either *Saccharomyces cerevisiae* or *Schizosaccharomyces pombe* (Chen et al., 2018; Sosnowski et al., 2018). The mode of interaction between Rea1-MIDAS and Rsa4-UBL is similar to that between integrin α subunits bound to extracellular ligands but is augmented by an additional β -hairpin of the MIDAS domain (Figure 4B) (Ahmed et al., 2019). The two other Rea1-specific elements of the MIDAS domain are an N-terminal α helix (α 1) and the adjacent loop (N loop), the density of which can be traced into the central pore of the AAA ring in our map (Figure 4B). Although the cryo-EM Rea1-MIDAS/Rsa4-UBL structure is similar to the corresponding *Chaetomium thermophilum* crystal structure, the α 1 and α 9 helices adopt conformations that are more similar to the structure of the unbound MIDAS domain (MIDAS-Apo) (Figure S5C).

Additional interactions between the Rea1 MIDAS domain and the lower part of the Rea1 AAA ring could be observed in our cryo-EM structure (Figures 4C–4F and S5D), such as (1) AAA2 and AAA3 small domain loops interacting with MIDAS α 5 and the loop between MIDAS α 8 and β 8 (Figures 4C and 4E); (2) AAA3 and AAA5 large domain loops, which correspond to the pore loops in classical AAA proteins, contacting MIDAS β 5 and α 9 and the MIDAS α 1 helix (Figures 4D and 4F; for functional importance, see also Chen et al., 2018); and (3) the AAA5 helix 2 insertion element reaching the end of the N loop protruding from the Rea1 central pore (Figure 4F). These observations indicate that the AAA pore loops might play a role in the mechanism of Rsa4 release (and that of Ytm1). Altogether, these findings are reminiscent of other AAA ATPases (e.g., Cdc48 and Yme1) that thread substrates through their central pore via their pore loops (Puchades et al., 2017; Twomey et al., 2019).

The spherical density identified as the Rix1-Ipi1-Ipi3 complex on the previously reported low-resolution Rix1-Rea1 particle (Barrio-Garcia et al., 2016) can be described in atomic detail based on our new cryo-EM structure. Accordingly, the Rix1-Rea1 particle harbors two copies of Rix1 and Ipi3 that form a tetrameric complex with an apparent C_2 symmetry, but surprisingly, only a small loop segment from the Ipi1 C terminus (residues 245–268) is incorporated into this assembly (Figure 5A). The two Rix1 monomers each form α -solenoids, which are capped toward the C terminus, by one of the two Ipi3 β propellers. Consistent with cross-linking mass spectrometry studies (Barrio-Garcia et al., 2016), an additional interaction between Ipi3 and Rix1 is formed via the C-terminal α helix (residues 472–489) of Ipi3, sandwiched between the two copies of Rix1. Ipi1, the fifth member of the heteropentameric Rix1 complex, only contributes to the globular part

Figure 2. NE1 and NE2 Represent Two Distinct States in the Transition from Late Nucleolar to Early Cytoplasmic Particles

Left: combined model and map representations highlighting the transition of pre-60S particles from the nucleolar state E particle (PDB: 6ELZ, EMD: 3891) (Kater et al., 2017) via states NE1 and NE2 to the early nucleoplasmic Arx1/Nog2 particle (PDB: 3JCT, EMD: 6615) (Wu et al., 2016). The cores of the particles are shown as gray volumes; moieties relevant to the maturation of the CP are shown as colored ribbon representations of the respective models. Center: isolated view of the L1 stalk rRNA and associated factors; views correspond to left column. Right: segments of pre-25S rRNA domain V, with conformations that are either mature-like (green) or stably folded, but not mature-like (pink) or flexible and/or unfolded, and hence not resolved in the maps (gray). Unknown proteins in state E were fit as polyalanine helices, and a homology model of Spb4 was fit as suggested by Sanghai et al. (2018).

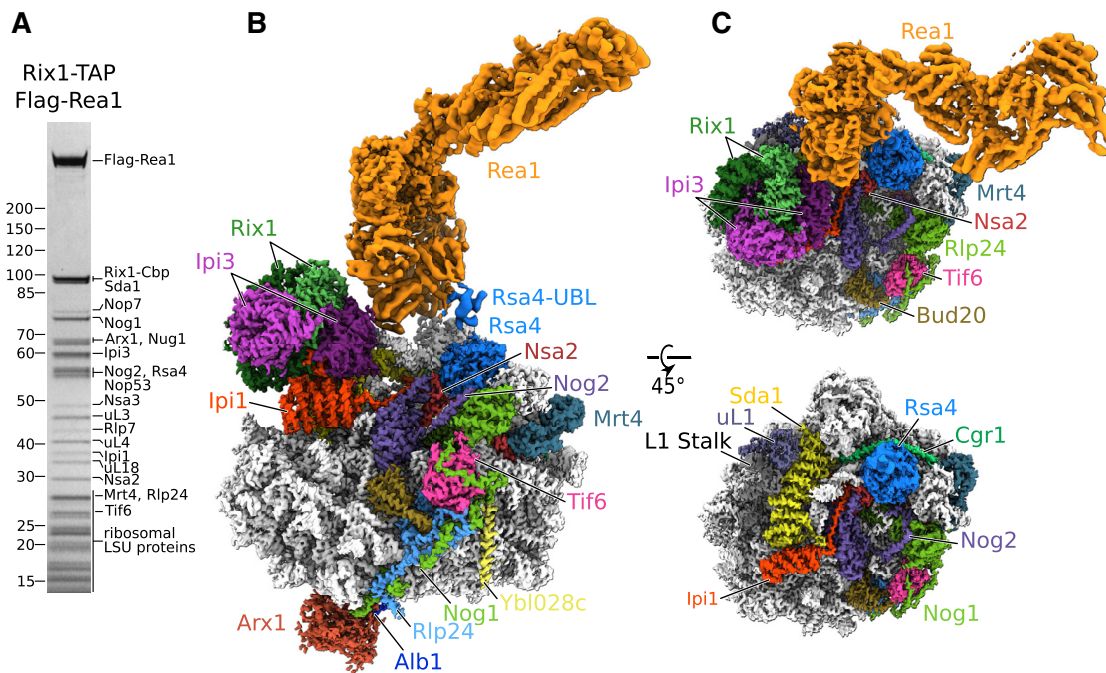


Figure 3. High-Resolution Structure of the Rix1-Rea1 Remodeling Machinery on the Nucleoplasmic Arx1/Nog2 Particles

(A) SDS-PAGE analysis of pre-60S particles split-tag-affinity purified using Rix1-TAP and FLAG-Rea1.

(B) Front view of the composite structure of the nucleoplasmic Rix1-Rea1 particle with assembly factors highlighted. The map is a composite of the individual multibody refined rigid bodies (60S core, Rea1 ring, Rea1 tail, and Rix1 complex).

(C) Top views of (B) showing all assembly factors (top) and with Rea1 and the Rix1-Ipi3 subcomplex omitted (bottom).

The ITS2-containing foot structure present in ~50% of the particles was masked out for clarity in these depictions.

of this complex, with a C-terminal loop wedged into the crevice formed between one of the Ipi3 β -propeller domains and Rix1 proteins (Figures 5A and 5B). The α -solenoid domains of Ipi1 and Sda1 are placed on top of helices 69 and 81 and between the L1 stalk and the rotated CP. Altogether, this forms the binding platform of the Rix1₂-Ipi3₂ heterotetramer (Figures 3C and 5B–5G). Thus, in contrast to what was previously thought (Barrio-Garcia et al., 2016), Ipi3 and Rix1 contribute the bulk of the spherical Rix1 complex density, whereas Ipi1 appears to anchor the Rix1 complex onto the ISS of the pre-60S particle.

Based on the newly determined architecture of the Rix1-Ipi1-Ipi3 pentamer, we performed complementary biochemical studies. Split-tag-affinity purification of overexpressed Rix1-TEV-ProtA and Ipi3-FLAG (in the absence of Ipi1) yielded a stable Rix1-Ipi3 complex that could be well separated by size-exclusion chromatography (Figures 6A and 6B) and exhibited the typical globular form in negative-stain EM (Figure 6C). This structure greatly resembles the tetrameric Rix1₂-Ipi3₂ assembly on the pre-60S particle solved by cryo-EM. Thus, Rix1 and Ipi3 can self-assemble in the absence of Ipi1 to form a hetero-tetramer. To elucidate the *in vivo* role of Ipi1 for recruiting the Rix1₂-Ipi3₂ tetramer to pre-60S particles, we depleted Ipi1 via an auxin-induced degron (Figure S6A) (Nishimura et al., 2009). As anticipated, neither Ipi3 nor Rix1 co-purified pre-60S particles after Ipi1 depletion (Figure 6D) or a specific deletion of the flexible Ipi1 loop harboring

the Rix1₂-Ipi3₂ interaction segment (Figures 6E, 6F, and S6B). Because Rix1 and Ipi3 are still imported into the nucleus in the absence of Ipi1 (Figure S6C), the Ipi1 C-terminal loop provides a principal site for binding the Rix1₂-Ipi3₂ tetramer to the pre-60S particle, which is fully consistent with our cryo-EM data.

Finally, recruitment and positioning of the Rix1-Rea1 machinery on the Arx1/Nog2 particle is a prerequisite for the 180° rotation of the CP and 5S RNP toward their mature conformations (Barrio-Garcia et al., 2016; Wu et al., 2016). At this state of maturation, Rpf2 and Rrs1, which are associated at the nonrotated 5S RNP, leave the pre-60S particle, allowing the Ipi1 N terminus to replace the Rpf2 C terminus that interacted with Nog2 (Figures 5D–5G). Furthermore, rotation of the CP allows Sda1 to be accommodated in its observed conformation. Stabilized by Sda1, only helices 80 and 81 of the CP remain in a pre-mature configuration. After Rea1-mediated release of Rsa4 and subsequent dissociation of the Rix1-Rea1 remodeling machinery, together with Sda1, the ribosomal proteins eL29 and eL42 stabilize rRNA ES12 and helices 80 and 81 in their mature conformations. These changes coincide with a minor shift of the entire CP, resulting in a mature conformation, as previously observed in the late nuclear or early cytoplasmic particle (Zhou et al., 2019b) (Figure S7). These steps thus pave the way toward the third and last major maturation phase (see Introduction): the formation of the PTC at the matured ISS.

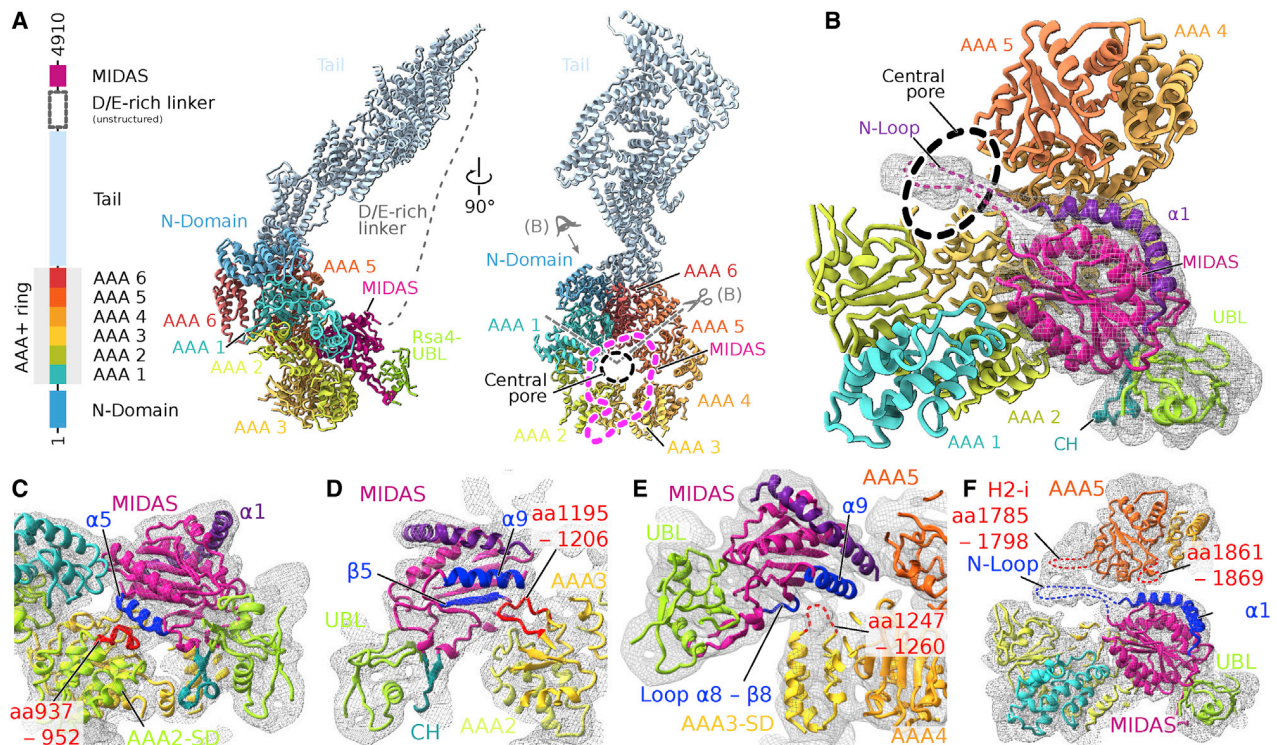


Figure 4. Rea1-MIDAS Is Bound to Rsa4-UBL and Shows Multiple Interactions with the Rea1 AAA Ring

(A) Domain organization of Rea1 and the corresponding model in equivalent colors shown in side and front views. In the front view, the MIDAS domain of Rea1 is indicated by a dashed magenta line and the central pore of Rea1 is indicated as a dashed black circle. The gray arrow and gray dashed line indicate the viewing direction and crop of (B).

(B) Overview of the Rea1-MIDAS domain bound to Rsa4-UBL. The bottom half of the Rea1 ring is shown as viewed from the N domain toward the center of the ring. The density of the MIDAS and UBL domains is depicted as a mesh. The Rea1-MIDAS-specific elements connector hairpin (CH) and helix $\alpha 1$ are highlighted in purple and turquoise, respectively. The central pore is indicated as a dashed black ellipse.

(C-F) Different viewing angles highlighting interactions between the Rea1-MIDAS and the AAA2-AAA5 domains (C-F, respectively) of the Rea1 ring shown as models and maps (mesh). The ring interaction sites are highlighted in red, and the corresponding MIDAS interaction sites are shown in blue. AAA-SD, AAA small domain.

See also Figure S5.

DISCUSSION

This study has unveiled two previously unknown intermediates of the pre-60S assembly pathway, giving insight into the large-scale remodeling of the nascent LSU upon transiting from a late nucleolar state to an early nucleoplasmic state. Moreover, we provide a molecular-resolution intermediate of a subsequent pre-60S particle that reveals for the first time the architecture of the unusual Rix1 subcomplex, with implications for Rix1-Rea1-driven pre-60S remodeling. Based on these data, we propose a sequence of maturation events for these transitions (Figure 7). The late nucleolar pre-60S particle that is state E, which awaits the ATPase Rea1 to bind to the Ytm1-UBL domain, represents the starting point of this series. However, the expected intermediate with Rea1 bound has yet to be captured by cryo-EM, and this remains a challenge for future studies because of its apparently highly dynamic mode of interaction. Regardless, the Rea1-mediated release of Ytm1-Erb1 triggers a cascade of restructuring events, including the release of a series of 60S assembly factors that were previously associated with the

meandering N terminus of Erb1. This dissociation event culminates in the delocalization of the L1 stalk and binding of the exosome recruitment factor Nop53 in state NE1. Subsequent release of Spb1 allows accommodation of the L1 stalk and its fixation in a mature-like conformation (state NE2); it and helix 88 (domain V) provide two nucleation seeds in which compaction and assembly of the residual domain V rRNA (helices 80–87, the rRNA of the CP) (Figure 1A) and 5S RNP are initiated. Subsequently, recruitment of Cgr1, Nog2, and Rsa4 and incorporation of ISS rRNA lead to the well-known Arx1/Nog2 particle (Bradatsch et al., 2012; Leidig et al., 2014; Wu et al., 2016). This is primed for the Rix1-Rea1 recruitment that is suggested to trigger 5S RNP rotation with release of Rpf2 and Rrs1 (Barrio-Garcia et al., 2016; Wu et al., 2016). In a final step, Rea1 ATPase activity causes the dissociation of Rsa4 and the Rix1-Rea1 remodeling machinery (Barrio-Garcia et al., 2016; Baßler et al., 2014). Stable incorporation of uL2 and eL43 and maturation of rRNA helices 81 and 82 eventually conclude this cascade, leading to the appearance of the typical CP structure as known from mature 60S subunits.

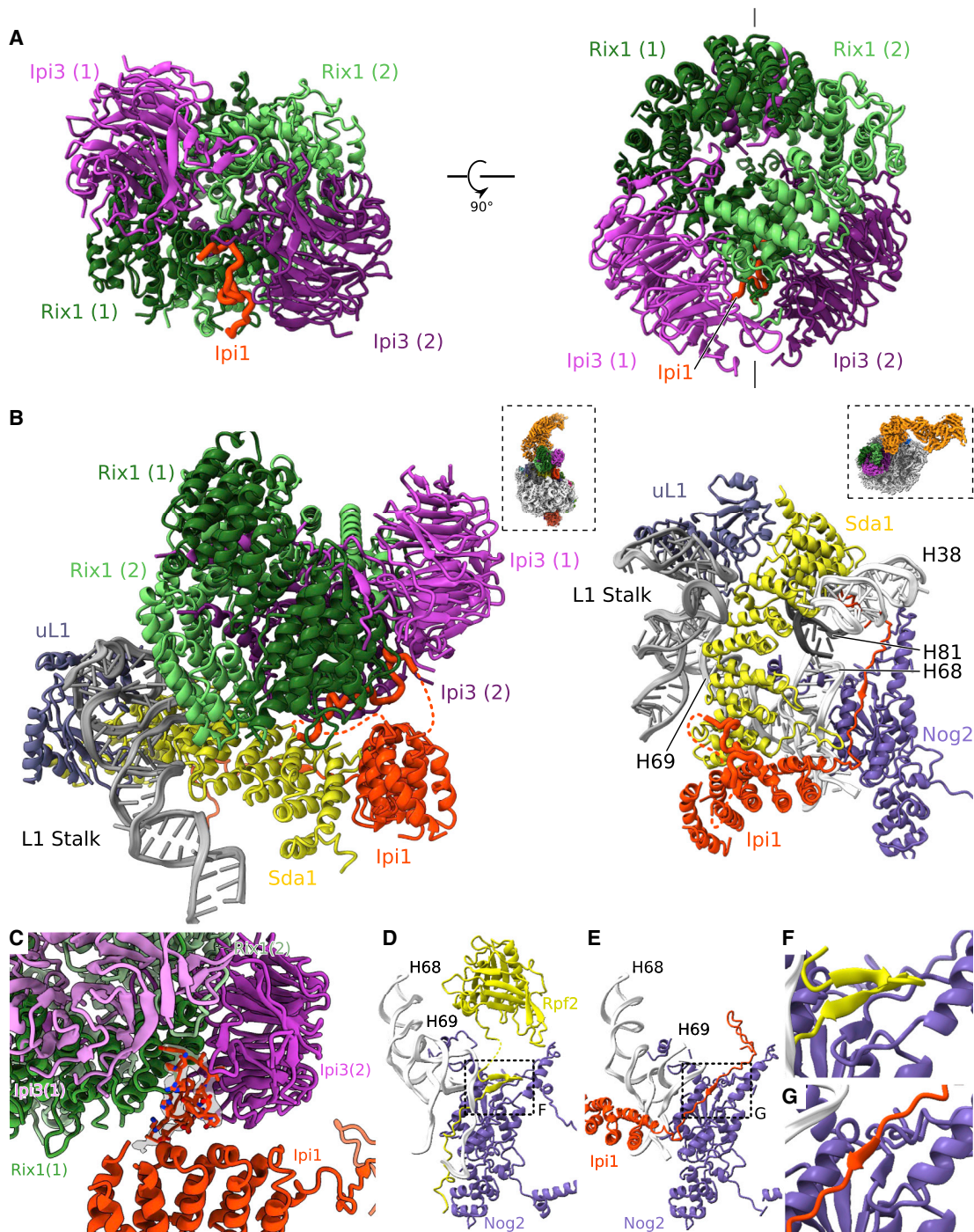


Figure 5. Ipi1 Anchors the Rix1-Ipi3 Hetero-tetramer to the ISS of the Maturing Pre-60S Particle

(A) Architecture of the globular domain of the Rix1-Ipi3-Ipi1 subcomplex depicted as ribbons shown in two views. The black lines centered at the top and bottom of the right view indicate the axis of the apparent C_2 symmetry.

(B) Two views showing the interaction of the Rix1 subcomplex with the pre-60S particle. Left: viewed from the L1 side, including the Rix1-Ipi3 tetramer. Right: viewed from the top without showing the Rix1-Ipi3 tetramer. The volume insets indicate the respective views of the two depictions.

(C) Close up of the Ipi1 C-terminal loop binding to the Rix1-Ipi3 tetramer.

(D and E) β sheet augmentations formed between Nog2 and Rpf2 (D) and between Nog2 and Ipi1 (E).

(F and G) Close-up views of the areas outlined in (D) (shown in F) and (E) (shown in G).

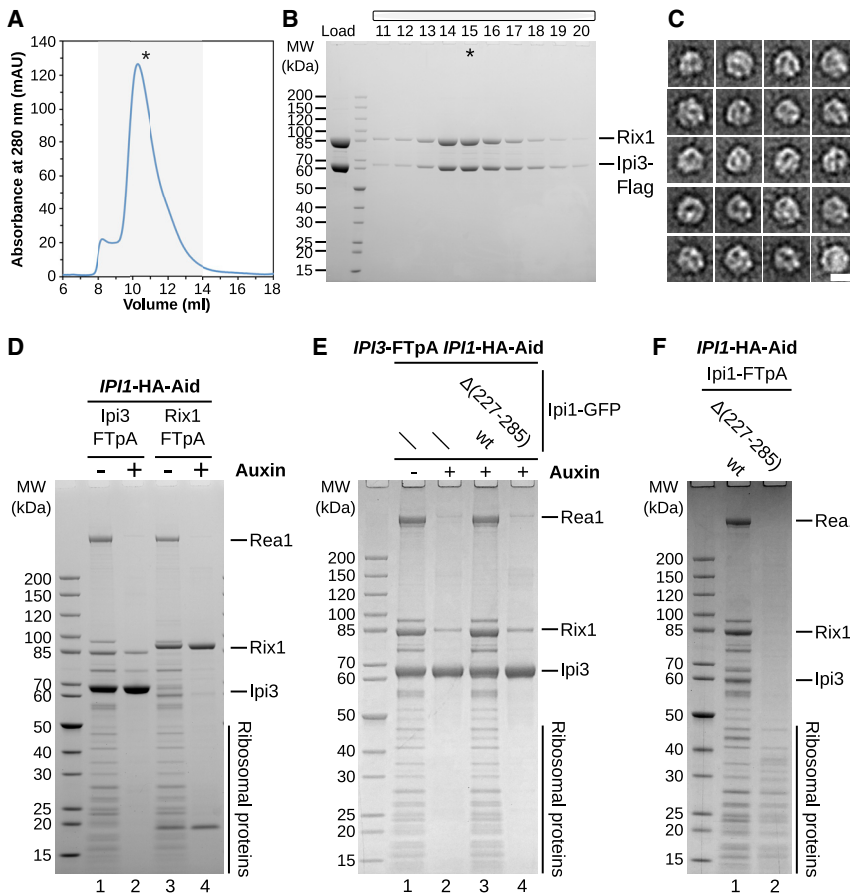


Figure 6. Biochemical Analysis of the Rix1-Ipi3 Complex

(A–C) Split-tag-affinity purification of Rix1-TEV-pA/Ipi3-FLAG overexpressed in *S. cerevisiae*. (A) Size-exclusion chromatography analysis (absorbance versus elution volume) of the Rix1-Ipi3 complex. The fractions marked in gray in (A) were analyzed by SDS-PAGE and Coomassie staining (B). The fraction labeled with an asterisk in (A) was used for negative-stain EM analysis (C). Representative class averages of the Rix1-Ipi3 complex are shown. Scale bar, 10 nm.

(D) Affinity purifications of Ipi3 and Rix1 from an *IPI1*-HA-Aid strain (lanes 1–4). Each combination was purified under expression (– auxin, lanes 1 and 3) or depletion (+ auxin, lanes 2 and 4) conditions of Ipi1-HA-Aid. Final eluates were analyzed by SDS-PAGE and Coomassie staining. The band around 18 kDa (lane 4) is a C-terminal Rix1 degradation product.

(E) Affinity purification of Ipi3-FTpA from an *IPI1*-HA-Aid degen strain. The *IPI3*-FTpA *IPI1*-HA-Aid strain was transformed with an empty plasmid (lanes 1 and 2), a plasmid containing *IPI1*-GFP wild type (lane 3), or the *ipi1* $\Delta(227-285)$ -GFP mutant (lane 4). The purifications were performed under expression (– auxin, lane 1) or depletion (+ auxin, lanes 2–4) conditions of Ipi1-HA-Aid. The final eluates were analyzed by SDS-PAGE and Coomassie staining. Ipi3 failed to co-purify pre-60S subunits under Ipi1-depletion conditions (lane 2) and if Ipi1 $\Delta(227-285)$ is expressed (lane 4).

(F) Plasmids harboring either the *IPI1* wild type or the *ipi1* $\Delta(227-285)$ mutant fused to a C-terminal FTpA tag were transformed in an *IPI1*-HA-Aid degen strain. The endogenous HA-Aid-tagged Ipi1 was degraded by the addition of auxin. Ipi1-FTpA and Ipi1 $\Delta(227-285)$ -FTpA were affinity purified and analyzed by SDS-PAGE and Coomassie staining. See also Figure S6.

The formation and maturation of the CP occurs via two large-scale remodeling steps involving the L1 stalk and the CP/5S RNP region, both of which are initially in pre-mature but distinct and stable conformations. To mature further, these entities undergo extensive restructuring, involving the successive action of the dynein-related AAA motor protein, Rea1, in conjunction with the Rix1 complex. These steps require the energy released by ATP hydrolysis, driven by the ATPase Rea1, and thus are irreversible. Both successive remodeling steps are distinct in multiple ways. First, the different locations of the Rea1 substrates Ytm1 and Rsa4 on the pre-60S particles imply dramatically different docking sites for this AAA ATPase. Second, the Rea1-mediated Ytm1-dissociation step appears to be fast *in vivo* and difficult to catch in structural terms but could be recapitulated biochemically by *in vitro* reconstitution (Bassler et al., 2010). Conversely, pre-60S particles involved in the second Rea1 step, in which Rea1 is stably bound to Rsa4, can be readily purified and studied by structural means. Thus, it is possible that during the second step, the Rix1-Rea1 remodeling machinery has an additional role in triggering the correct timing of ITS2 processing, which requires complicated machinery (Fromm et al., 2017) and therefore might be more easily trapped. Complete

processing of the ITS2 harboring foot before CP/5S RNP rotation was observed so far only in mutants that cannot undergo this rotation (Thoms et al., 2018), but in all other cases, CP/5S RNP rotation strictly precedes ITS2 processing and disassembly of the foot. In this context, the human ortholog of Las1, which performs C₂ cleavage in the ITS2, is part of the human Rix1 complex (called the PELP1 complex) (Castle et al., 2012, 2013; Fromm et al., 2017). Conversely, processing of the foot structure in yeast is not strictly coupled to the maturation of the CP, and foot-containing pre-60S particles under mutant conditions are known to be exported into the cytoplasm, where they enter translation (Biedka et al., 2018; Rodríguez-Galán et al., 2015; Sarkar et al., 2017) (see also above and Figure S2).

The structural and biochemical data presented here imply an important role for Ipi1 in tethering the Rix1₂-Ipi3₂ tetramer to the pre-60S particle. As shown by the multibody refinement, this tethering allows the tetramer to be flexibly bound to the pre-60S, whereas Ipi1 is part of the rigid pre-60S core. As shown by the biochemical analysis, binding via Ipi1 is necessary, but not sufficient, for specific targeting of the Rix1-Ipi3 subcomplex to the pre-60S. It is likely that further interactions are required, probably provided by the L1 stalk and/or Sda1. The presence of

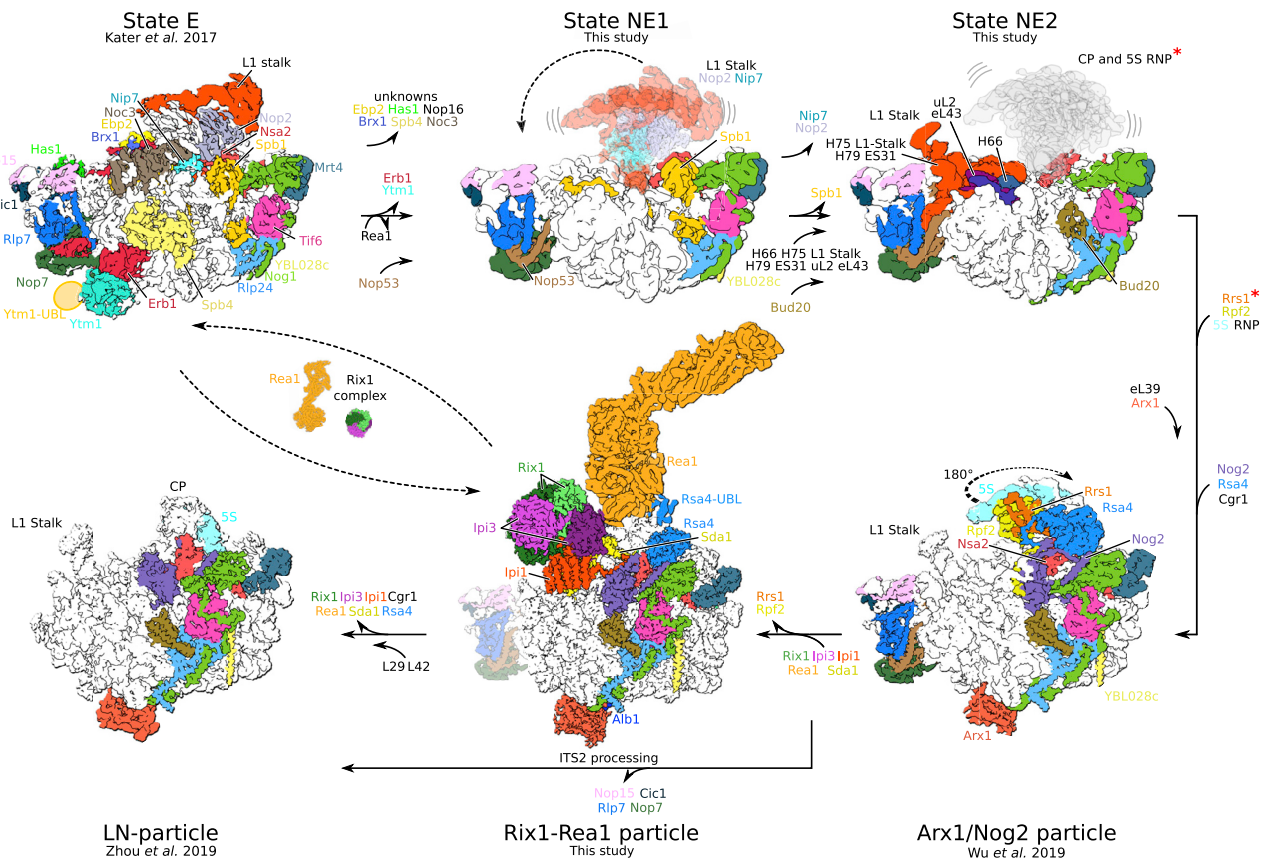


Figure 7. Assembly Sequence of the L1 Stalk and CP

Two Rea1-mediated dissociation events frame the major remodeling events leading from a late nucleolar particle (state E, PDB: 6ELZ, EMDB: 3891; Kater et al., 2017) via the Arx1/Nog2 particle (PDB: 3JCT, EMDB: 6615; Wu et al., 2016) to a particle with a mature CP ready for export (PDB: 6N8J, EMDB: 0369). *5S RNP, Rrs1, and Rpf2 bind to nucleolar particles such as state E or earlier but are not stably incorporated into the core particle (Kater et al., 2017; Kressler et al., 2008). See also Figure S7.

Sda1 is characteristic for this assembly intermediate, and together with the L1 stalk, it forms part of the binding platform of the Rix1-Ipi3 tetramer. This might explain why structures of particles purified via Nop53 show no stably bound Rix1 complex, although its presence is clearly shown biochemically (Figures 1B and S2). Structures of the same Nop53 particles, which have been reconstituted with the nuclear exosome *in vitro*, display density for the Rix1 complex, which is apparently rigidly bound under these sterically more constrained conditions (Schuller et al., 2018). Thus, we speculate that initially the Rix1 complex is bound flexibly to the pre-60S particles, resulting in state F (Kater et al., 2017) or a subpopulation of the Nop53 pre-60S intermediates that contain the Rix1 subcomplex but do not show a clear density for it. Upon construction of the complete binding platform, Ipi1 can reach deeply into the pre-60S ISS region, which stabilizes the overall binding of the Rix1 complex. The interaction between the Rix1 C terminus and the helix 2 insertion element of the Rea1 AAA2 domain could then facilitate targeting of Rea1 to the correct site on the maturing pre-60S (Barrio-Garcia et al., 2016).

Even though structures of Rea1, its MIDAS domain, and its interaction with the Rsa4-UBL and Ytm1-UBL domains have

been reported previously (Ahmed et al., 2019; Chen et al., 2018; Sosnowski et al., 2018), the exact mechanism of how Rea1 contributes to the release of its substrate proteins remains unclear. A previous model based on negative-stain EM studies suggested that the MIDAS domain is located at the tip of the Rea1 tail, which—stimulated by the AAA ring—acts like an arm, first grabbing the substrate protein and then exerting force on it by reverting to its extended conformation (Ulbrich et al., 2009). However, it has become clear only recently that the MIDAS domain is not an intrinsic part of the structurally visible Rea1 tail (Ahmed et al., 2019; Chen et al., 2018; Sosnowski et al., 2018). Our cryo-EM data do not indicate substantial rearrangements of the Rea1 tail, as indicated by negative staining (Ulbrich et al., 2009). Thus, the functional relevance of the tail, including a possible role in release of the Rea1 target proteins Rsa4 and Ytm1, remains unclear. Conversely, the interaction of the MIDAS domain with the ring, especially the loops of the AAA large domains (Figure 4), suggests the possibility of direct force transmission from the AAA domains onto the substrate protein via the MIDAS domain. In classical AAA proteins such as Cdc48, these so-called pore loops act as the main drivers

for the translation of a peptide through the central pore (Twomey et al., 2019). Similar to classical unfolding AAA proteins, such as Cdc48, Rea1 displays two connected linear polypeptide chains in its central pore, representing its own N loop connecting the MIDAS domain to the unstructured D/E-rich linker and tail via the α 1 helix. One possibility is that Rea1 functions similarly to canonical AAA proteins and possibly moves the N loop and/or the substrate-bound MIDAS through its pore. Alternatively, the ATP-hydrolysis-driven conformational change of the AAA ring may be directly transmitted to the MIDAS domain via the previously discussed MIDAS ring interactions. Whereas these scenarios might explain how Rea1 generates force to remove its substrates, the function of the conserved massive Rea1 tail domain has yet to be discovered. To this end, it would be helpful to solve structures of the full Rea1 catalyzed ATPase hydrolysis cycle in the context of the pre-60S particle.

The results of this study provide molecular insight into two major rearrangement steps that take place in 60S biogenesis, which result in the formation of the L1 stalk, the CP, and large parts of the ISS, all essential regions for the later functioning of the subunit in translation. The observed rearrangements are characterized by transitions from distinct and stable, yet pre-mature, rRNA conformations, to a more matured architecture and by the requirement of the ATP-dependent Rix1-Rea1 remodeling machinery, which renders these steps irreversible.

STAR★METHODS

Detailed methods are provided in the online version of this paper and include the following:

- **KEY RESOURCES TABLE**
- **RESOURCE AVAILABILITY**
 - Lead Contact
 - Materials Availability
 - Data and Code Availability
- **EXPERIMENTAL MODEL AND SUBJECT DETAILS**
 - Yeast strains
 - Bacterial Strains
- **METHOD DETAILS**
 - Plasmid and strains
 - Affinity purification of pre-60S particles from *S. cerevisiae*
 - Negative-stain electron microscopy and image processing
 - Grid preparation and cryogenic electron microscopy
 - Image processing
 - Nop53 dataset
 - Nop53-Spb1 dataset
 - Rix1-Rea1 dataset
 - Model building and refinement
 - Visual analysis and depiction of structures and maps

SUPPLEMENTAL INFORMATION

Supplemental Information can be found online at <https://doi.org/10.1016/j.molcel.2020.06.032>.

ACKNOWLEDGMENTS

We thank Charlotte Ungewickell and Susanne Rieder for their support with EM sample preparation and data collection. We thank Dr. Thomas Fröhlich for performing mass spectrometry analysis. We thank Dr. Dirk Flemming (BZH, University of Heidelberg) for his support with negative stain EM collection and data analysis. This work was supported by grants from the German Research Council (QBM, GRK1721 to R.B., and DFG, HU363/15-2 to E.H.).

AUTHOR CONTRIBUTIONS

R.B., E.H., L.K., V.M., and M.T. designed this study and its experiments. Preparation of cryo-EM samples was performed by V.M. and M.T. Cryo-EM data were collected by O.B. and L.K. Data processing was performed by L.K. Molecular model building was performed by L.K. and assisted by J.C. Additional biochemical experiments were performed by M.T. The results were interpreted by R.B., E.H., L.K., V.M., and M.T. The manuscript was written by R.B., E.H., and L.K. All authors discussed the results and commented on the manuscript.

DECLARATION OF INTERESTS

The authors declare no competing interests.

Received: January 21, 2020

Revised: May 13, 2020

Accepted: June 18, 2020

Published: July 14, 2020

REFERENCES

- Adams, P.D., Afonine, P.V., Bunkóczi, G., Chen, V.B., Davis, I.W., Echols, N., Headd, J.J., Hung, L.W., Kapral, G.J., Grosse-Kunstleve, R.W., et al. (2010). PHENIX: a comprehensive Python-based system for macromolecular structure solution. *Acta Crystallogr. D Biol. Crystallogr.* **66**, 213–221.
- Ahmed, Y.L., Thoms, M., Mitterer, V., Sinning, I., and Hurt, E. (2019). Crystal structures of Rea1-MIDAS bound to its ribosome assembly factor ligands resembling integrin-ligand-type complexes. *Nat. Commun.* **10**, 3050.
- Barrio-Garcia, C., Thoms, M., Flemming, D., Kater, L., Berninghausen, O., Baßler, J., Beckmann, R., and Hurt, E. (2016). Architecture of the Rix1-Rea1 checkpoint machinery during pre-60S-ribosome remodeling. *Nat. Struct. Mol. Biol.* **23**, 37–44.
- Bassler, J., Kallas, M., Pertschy, B., Ulbrich, C., Thoms, M., and Hurt, E. (2010). The AAA-ATPase Rea1 drives removal of biogenesis factors during multiple stages of 60S ribosome assembly. *Mol. Cell* **38**, 712–721.
- Baßler, J., and Hurt, E. (2019). Eukaryotic Ribosome Assembly. *Annu. Rev. Biochem.* **88**, 281–306.
- Baßler, J., Paternoga, H., Holdermann, I., Thoms, M., Granneman, S., Barrio-Garcia, C., Nyarko, A., Lee, W., Stier, G., Clark, S.A., et al. (2014). A network of assembly factors is involved in remodeling rRNA elements during preribosome maturation. *J. Cell Biol.* **207**, 481–498.
- Ben-Shem, A., Garreau de Loubresse, N., Melnikov, S., Jenner, L., Yusupova, G., and Yusupov, M. (2011). The structure of the eukaryotic ribosome at 3.0 Å resolution. *Science* **334**, 1524–1529.
- Biedka, S., Micic, J., Wilson, D., Brown, H., Diorio-Toth, L., and Woolford, J.L., Jr. (2018). Hierarchical recruitment of ribosomal proteins and assembly factors remodels nucleolar pre-60S ribosomes. *J. Cell Biol.* **217**, 2503–2518.
- Bradatsch, B., Leidig, C., Granneman, S., Gnädig, M., Tollervy, D., Böttcher, B., Beckmann, R., and Hurt, E. (2012). Structure of the pre-60S ribosomal subunit with nuclear export factor Arx1 bound at the exit tunnel. *Nat. Struct. Mol. Biol.* **19**, 1234–1241.
- Castle, C.D., Cassimere, E.K., and Denicourt, C. (2012). LAS1L interacts with the mammalian Rix1 complex to regulate ribosome biogenesis. *Mol. Biol. Cell* **23**, 716–728.
- Castle, C.D., Sardana, R., Dandekar, V., Borgiani, V., Johnson, A.W., and Denicourt, C. (2013). Las1 interacts with Grc3 polynucleotide kinase and is

- required for ribosome synthesis in *Saccharomyces cerevisiae*. *Nucleic Acids Res.* **41**, 1135–1150.
- Chen, Z., Suzuki, H., Kobayashi, Y., Wang, A.C., DiMaio, F., Kawashima, S.A., Walz, T., and Kapoor, T.M. (2018). Structural Insights into Mdn1, an Essential AAA Protein Required for Ribosome Biogenesis. *Cell* **175**, 822–834.e18.
- Emsley, P., Lohkamp, B., Scott, W.G., and Cowtan, K. (2010). Features and development of Coot. *Acta Crystallogr. D Biol. Crystallogr.* **66**, 486–501.
- Fromm, L., Falk, S., Flemming, D., Schuller, J.M., Thoms, M., Conti, E., and Hurt, E. (2017). Reconstitution of the complete pathway of ITS2 processing at the pre-ribosome. *Nat. Commun.* **8**, 1787.
- Gamalinda, M., Ohmayer, U., Jakovljevic, J., Kumcuoglu, B., Woolford, J., Mbom, B., Lin, L., and Woolford, J.L., Jr. (2014). A hierarchical model for assembly of eukaryotic 60S ribosomal subunit domains. *Genes Dev.* **28**, 198–210.
- Goddard, T.D., Huang, C.C., Meng, E.C., Pettersen, E.F., Couch, G.S., Morris, J.H., and Ferrin, T.E. (2018). UCSF ChimeraX: Meeting modern challenges in visualization and analysis. *Protein Sci.* **27**, 14–25.
- Janke, C., Magiera, M.M., Rathfelder, N., Taxis, C., Reber, S., Maekawa, H., Moreno-Borchart, A., Doenges, G., Schwob, E., Schiebel, E., and Knop, M. (2004). A versatile toolbox for PCR-based tagging of yeast genes: new fluorescent proteins, more markers and promoter substitution cassettes. *Yeast* **21**, 947–962.
- Kargas, V., Castro-Hartmann, P., Escudero-Urquijo, N., Dent, K., Hilcenko, C., Sailer, C., Zisser, G., Marques-Carvalho, M.J., Pellegrino, S., Wawiórka, L., et al. (2019). Mechanism of completion of peptidyltransferase centre assembly in eukaryotes. *eLife* **8**, e44904.
- Kater, L., Thoms, M., Barrio-Garcia, C., Cheng, J., Ismail, S., Ahmed, Y.L., Bange, G., Kressler, D., Berninghausen, O., Sinning, I., et al. (2017). Visualizing the Assembly Pathway of Nucleolar Pre-60S Ribosomes. *Cell* **171**, 1599–1610.e14.
- Kidmose, R.T., Juhl, J., Nissen, P., Boesen, T., Karlsen, J.L., and Pedersen, B.P. (2019). *Namdinator*—automatic molecular dynamics flexible fitting of structural models into cryo-EM and crystallography experimental maps. *IUCr* **6**, 526–531.
- Klinge, S., and Woolford, J.L., Jr. (2019). Ribosome assembly coming into focus. *Nat. Rev. Mol. Cell Biol.* **20**, 116–131.
- Kressler, D., Rojo, M., Linder, P., and Cruz, J. (1999). Spb1p is a putative methyltransferase required for 60S ribosomal subunit biogenesis in *Saccharomyces cerevisiae*. *Nucleic Acids Res.* **27**, 4598–4608.
- Kressler, D., Roser, D., Pertschy, B., and Hurt, E. (2008). The AAAATPase Rix7 powers progression of ribosome biogenesis by stripping Nsa1 from pre-60S particles. *J. Cell Biol.* **181**, 935–944.
- Lapeyre, B., and Purushothaman, S.K. (2004). Spb1p-directed formation of Gm2922 in the ribosome catalytic center occurs at a late processing stage. *Mol. Cell* **16**, 663–669.
- Leidig, C., Thoms, M., Holdermann, I., Bradatsch, B., Berninghausen, O., Bange, G., Sinning, I., Hurt, E., and Beckmann, R. (2014). 60S ribosome biogenesis requires rotation of the 5S ribonucleoprotein particle. *Nat. Commun.* **5**, 3491.
- Liu, X., and Wang, H.W. (2011). Single particle electron microscopy reconstruction of the exosome complex using the random conical tilt method. *J. Vis. Exp.* **49**, 2574.
- Lo, K.-Y., Li, Z., Bussiere, C., Bresson, S., Marcotte, E.M., and Johnson, A.W. (2010). Defining the pathway of cytoplasmic maturation of the 60S ribosomal subunit. *Mol. Cell* **39**, 196–208.
- Longtine, M.S., McKenzie, A., 3rd, Demarini, D.J., Shah, N.G., Wach, A., Brachat, A., Philippsen, P., and Pringle, J.R. (1998). Additional modules for versatile and economical PCR-based gene deletion and modification in *Saccharomyces cerevisiae*. *Yeast* **14**, 953–961.
- Ludtke, S.J., Baldwin, P.R., and Chiu, W. (1999). EMAN: semiautomated software for high-resolution single-particle reconstructions. *J. Struct. Biol.* **128**, 82–97.
- Ma, C., Wu, S., Li, N., Chen, Y., Yan, K., Li, Z., Zheng, L., Lei, J., Woolford, J.L., and Gao, N. (2017). Structural snapshot of cytoplasmic pre-60S ribosomal particles bound by Nmd3, Lsg1, Tif6 and Reh1. *Nat Struct Mol Biol.* **24**, 214–220.
- Malyutin, A.G., Musalgaonkar, S., Patchett, S., Frank, J., and Johnson, A.W. (2017). Nmd3 is a structural mimic of eIF5A, and activates the cpGTPase Lsg1 during 60S ribosome biogenesis. *EMBO J.* **36**, 854–868.
- Matsuo, Y., Granneman, S., Thoms, M., Manikas, R.G., Tollervey, D., and Hurt, E. (2014). Coupled GTPase and remodelling ATPase activities form a checkpoint for ribosome export. *Nature* **505**, 112–116.
- McGuffin, L.J., Bryson, K., and Jones, D.T. (2000). The PSIPRED protein structure prediction server. *Bioinformatics* **16**, 404–405.
- Nakane, T., Kimanius, D., Lindahl, E., and Scheres, S.H.W. (2018). Characterisation of molecular motions in cryo-EM single-particle data by multi-body refinement in RELION. *eLife* **7**, e36861.
- Nishimura, K., Fukagawa, T., Takisawa, H., Kakimoto, T., and Kanemaki, M. (2009). An auxin-based degron system for the rapid depletion of proteins in nonplant cells. *Nat. Methods* **6**, 917–922.
- Parks, T.D., Leuther, K.K., Howard, E.D., Johnston, S.A., and Dougherty, W.G. (1994). Release of Proteins and Peptides From Fusion Proteins Using a Recombinant Plant Virus Proteinase. *Anal Biochem.* **216**, 413–417.
- Petrov, A.S., Bernier, C.R., Gulen, B., Waterbury, C.C., Hershkovits, E., Hsiao, C., Harvey, S.C., Hud, N.V., Fox, G.E., Wartell, R.M., and Williams, L.D. (2014). Secondary structures of rRNAs from all three domains of life. *PLoS ONE* **9**, e88222.
- Pettersen, E.F., Goddard, T.D., Huang, C.C., Couch, G.S., Greenblatt, D.M., Meng, E.C., and Ferrin, T.E. (2004). UCSF Chimera—a visualization system for exploratory research and analysis. *J. Comput. Chem.* **25**, 1605–1612.
- Puchades, C., Rampello, A.J., Shin, M., Giuliano, C.J., Wiseman, R.L., Glynn, S.E., and Lander, G.C. (2017). Structure of the mitochondrial inner membrane AAA+ protease YME1 gives insight into substrate processing. *Science* **358**, eaao0464.
- Rodríguez-Galán, O., García-Gómez, J.J., Kressler, D., and de la Cruz, J. (2015). Immature large ribosomal subunits containing the 7S pre-rRNA can engage in translation in *Saccharomyces cerevisiae*. *RNA Biol.* **12**, 838–846.
- Sanghai, Z.A., Miller, L., Molloy, K.R., Barandun, J., Hunziker, M., Chaker-Margot, M., Wang, J., Chait, B.T., and Klinge, S. (2018). Modular assembly of the nucleolar pre-60S ribosomal subunit. *Nature* **556**, 126–129.
- Sarkar, A., Thoms, M., Barrio-Garcia, C., Thomson, E., Flemming, D., Beckmann, R., and Hurt, E. (2017). Preribosomes escaping from the nucleus are caught during translation by cytoplasmic quality control. *Nat. Struct. Mol. Biol.* **24**, 1107–1115.
- Schuller, J.M., Falk, S., Fromm, L., Hurt, E., and Conti, E. (2018). Structure of the nuclear exosome captured on a maturing preribosome. *Science* **360**, 219–222.
- Sosnowski, P., Urnavicius, L., Boland, A., Fagiewicz, R., Busselez, J., Papai, G., and Schmidt, H. (2018). The CryoEM structure of the *Saccharomyces cerevisiae* ribosome maturation factor Rea1. *eLife* **7**, e39163.
- Thoms, M., Thomson, E., Baßler, J., Gnädig, M., Griesel, S., and Hurt, E. (2015). The Exosome Is Recruited to RNA Substrates through Specific Adaptor Proteins. *Cell* **162**, 1029–1038.
- Taylor, R.G., Walker, D.C., and McInnes, R.R. (1993). *E. coli* host strains significantly affect the quality of small scale plasmid DNA preparations used for sequencing. *Nucleic Acids Research* **21**, 1677–1678.
- Thomas, B.J., and Rothstein, R. (1989). Elevated Recombination Rates in Transcriptionally Active DNA. *Cell* **56**, 619–630.
- Thoms, M., Ahmed, Y.L., Maddi, K., Hurt, E., and Sinning, I. (2016). Concerted removal of the Erb1-Ytm1 complex in ribosome biogenesis relies on an elaborate interface. *Nucleic Acids Res.* **44**, 926–939.
- Thoms, M., Mitterer, V., Kater, L., Falquet, L., Beckmann, R., Kressler, D., and Hurt, E. (2018). Suppressor mutations in Rpf2-Rrs1 or Rpl5 bypass the Cgr1 function for pre-ribosomal 5S RNP-rotation. *Nat. Commun.* **9**, 4094.

- Trotta, C.R., Lund, E., Kahan, L., Johnson, A.W., and Dahlberg, J.E. (2003). Coordinated nuclear export of 60S ribosomal subunits and NMD3 in vertebrates. *EMBO J.* *22*, 2841–2851.
- Twomey, E.C., Ji, Z., Wales, T.E., Bodnar, N.O., Ficarro, S.B., Marto, J.A., Engen, J.R., and Rapoport, T.A. (2019). Substrate processing by the Cdc48 ATPase complex is initiated by ubiquitin unfolding. *Science* *365*, eaax1033.
- Ulbrich, C., Diepholz, M., Bassler, J., Kressler, D., Pertschy, B., Galani, K., Böttcher, B., and Hurt, E. (2009). Mechanochemical removal of ribosome biogenesis factors from nascent 60S ribosomal subunits. *Cell* *138*, 911–922.
- van Heel, M., Harauz, G., Orlova, E.V., Schmidt, R., and Schatz, M. (1996). A new generation of the IMAGIC image processing system. *J. Struct. Biol.* *116*, 17–24.
- Wegrecki, M., Rodríguez-Galán, O., de la Cruz, J., and Bravo, J. (2015). The structure of Erb1-Ytm1 complex reveals the functional importance of a high-affinity binding between two β -propellers during the assembly of large ribosomal subunits in eukaryotes. *Nucleic Acids Res.* *43*, 11017–11030.
- Woolford, J.L., Jr., and Baserga, S.J. (2013). Ribosome biogenesis in the yeast *Saccharomyces cerevisiae*. *Genetics* *195*, 643–681.
- Wu, S., Tutuncuoglu, B., Yan, K., Brown, H., Zhang, Y., Tan, D., Gamalinda, M., Yuan, Y., Li, Z., Jakovljevic, J., et al. (2016). Diverse roles of assembly factors revealed by structures of late nuclear pre-60S ribosomes. *Nature* *534*, 133–137.
- Zhang, K. (2016). Gctf: Real-time CTF determination and correction. *J. Struct. Biol.* *193*, 1–12.
- Zhang, J., Hampicharnchai, P., Jakovljevic, J., Tang, L., Guo, Y., Oeffinger, M., Rout, M.P., Hiley, S.L., Hughes, T., and Woolford, J.L., Jr. (2007). Assembly factors Rpf2 and Rrs1 recruit 5S rRNA and ribosomal proteins rpL5 and rpL11 into nascent ribosomes. *Genes Dev.* *21*, 2580–2592.
- Zheng, S.Q., Palovcak, E., Armache, J.-P., Verba, K.A., Cheng, Y., and Agard, D.A. (2017). MotionCor2: anisotropic correction of beam-induced motion for improved cryo-electron microscopy. *Nat. Methods* *14*, 331–332.
- Zhou, D., Zhu, X., Zheng, S., Tan, D., Dong, M.Q., and Ye, K. (2019a). Cryo-EM structure of an early precursor of large ribosomal subunit reveals a half-assembled intermediate. *Protein Cell* *10*, 120–130.
- Zhou, Y., Musalgaonkar, S., Johnson, A.W., and Taylor, D.W. (2019b). Tightly-orchestrated rearrangements govern catalytic center assembly of the ribosome. *Nat. Commun.* *10*, 958.
- Zivanov, J., Nakane, T., Forsberg, B.O., Kimanius, D., Hagen, W.J.H., Lindahl, E., and Scheres, S.H.W. (2018). New tools for automated high-resolution cryo-EM structure determination in RELION-3. *eLife* *7*, e42166.

STAR★METHODS

KEY RESOURCES TABLE

REAGENT or RESOURCE	SOURCE	IDENTIFIER
Chemicals, Peptides, and Recombinant Proteins		
FLAG Peptide	SIGMA-Aldrich	Cat#F3290
TEV protease	Parks et al., 1994	N/A
3-Indoleacetic acid	SIGMA-Aldrich	Cat#I2886
Dodecyloctaglycol	SIGMA-Aldrich	Cat#P8925
SIGMAFAST protease inhibitor	SIGMA-Aldrich	Cat#S8830
Critical Commercial Assays		
IgG-Sepharose 6 Fast Flow	GE Healthcare	Cat#17096902
ANTI-FlagM2 Affinity Gel	SIGMA-Aldrich	Cat#A2220
Deposited Data		
Cryo-EM map: State NE1	This paper	EMDB: EMD-10841
Cryo-EM map: State NE2	This paper	EMDB: EMD-10842
Cryo-EM map: Rix1-Rea1 particle - combined map	This paper	EMDB: EMD-10839
Cryo-EM map: Rix1-Rea1 particle - rigid body 1: 60S core	This paper	EMDB: EMD-10838
Cryo-EM map: Rix1-Rea1 particle - rigid body 2: Rea1 and Rsa4-UBL	This paper	EMDB: EMD-10837
Cryo-EM map: Rix1-Rea1 particle - rigid body 3: Rix1-subcomplex	This paper	EMDB: EMD-10836
Atomic model: State NE1	This paper	PDB: 6YLX
Atomic model: State NE2	This paper	PDB: 6YLY
Atomic model: Rix1-Rea1 particle - combined model	This paper	PDB: 6YLH
Atomic model: Rix1-Rea1 particle - rigid body 1: 60S core	This paper	PDB: 6YLG
Atomic model: Rix1-Rea1 particle - rigid body 2: Rea1 and Rsa4-UBL	This paper	PDB: 6YLF
Atomic model: Rix1-Rea1 particle - rigid body 3: Rix1-subcomplex	This paper	PDB: 6YLE
Experimental Models: Organisms/Strains		
<i>E. coli</i> DH5 α	Taylor et al., 1993	N/A
<i>S. cerevisiae</i> : W303: <i>ade2-1, trp1-1, leu2-3,112, his3-11,15, ura3-1, can1-100</i>	Thomas and Rothstein, 1989	N/A
<i>S. cerevisiae</i> : TAP-Flag-NOP53: W303, P _{NOP53} ⁻ -TAP-Flag-NOP53::natNT2	Thoms et al., 2015	N/A
<i>S. cerevisiae</i> : RIX1-TAP Flag-REA1: W303, RIX1-TAP::HIS3MX6 <i>rea1</i> ::kanMX6 [YCplac111-P _{REA1} -Flag-REA1]	This paper	N/A
<i>S. cerevisiae</i> : ProtA-(His) ₆ -NOP53 <i>spb1</i> Δ shuffle: W303, P _{NOP53} ⁻ -ProtA-TEV-(His) ₆ -NOP53::natNT2, <i>spb1</i> ::HIS3MX4, pRS316-SPB1	This paper	N/A
<i>S. cerevisiae</i> : <i>ipi1</i> Δ shuffle: W303, IPI1::natNT2, pRS316-IPI1	This paper	N/A
<i>S. cerevisiae</i> : IPI1-HA-Aid: W303, IPI1-HA-Aid::HIS3MX6, P _{ADH1} ⁻ -OsTIR1-9xmyc::TRP1	This paper	N/A
<i>S. cerevisiae</i> : IPI3-FTpA IPI1-HA-Aid: W303, IPI3-FTpA::natNT2, IPI1-HA-Aid::HIS3MX6, P _{ADH1} ⁻ -OsTIR1-9xmyc::TRP1	This paper	N/A

(Continued on next page)

Continued

REAGENT or RESOURCE	SOURCE	IDENTIFIER
<i>S. cerevisiae</i> : RIX1-FTpA IPI1-HA-Aid: W303, RIX1-FTpA::natNT2, IPI1-HA-Aid::HIS3MX6, P _{ADH1} -OsTIR1-9xmyc::TRP1	This paper	N/A
<i>S. cerevisiae</i> : IPI3-GFP IPI1-HA-Aid: W303, IPI3-GFP::natNT2, IPI1-HA-Aid::HIS3MX6, P _{ADH1} -OsTIR1-9xmyc::TRP1	This paper	N/A
<i>S. cerevisiae</i> : RIX1-GFP IPI1-HA-Aid: W303, RIX1-GFP::natNT2, IPI1-HA-Aid::HIS3MX6, P _{ADH1} -OsTIR1-9xmyc::TRP1	This paper	N/A
Recombinant DNA		
YCplac111-IPI1-FTpA: CEN, LEU2, PIP1, TADH1, C-term. Flag-TEV cleavage site-ProteinA tag	This paper	N/A
YCplac111- <i>ipi1</i> Δ(aa227-285)-GFP: CEN, LEU2, PIP1, TADH1, C-term. GFP tag	This paper	N/A
YCplac111- <i>ipi1</i> Δ(aa227-285)-FTpA: CEN, LEU2, PIP1, TADH1, C-term. Flag-TEV cleavage site-ProteinA tag	This paper	N/A
YCplac111-SPB1: CEN, LEU2, PSPB1, TADH1	This paper	N/A
YCplac111-SPB1 aa437-Flag: CEN, LEU2, PSPB1, TADH1, internal Flag tag after residue 437	This paper	N/A
YCplac111-SPB1 aa516-Flag: CEN, LEU2, PSPB1, TADH1, internal Flag tag after residue 516	This paper	N/A
YEplac112-PGAL1-10-RIX1-TEV-ProtA: 2μ, TRP1, PGAL1-10, TADH1, C-term. TEV-cleavage site-Protein A tag	Barrio-Garcia et al., 2016	N/A
YEplac181-PGAL1-10-IPI3-Flag: 2μ, LEU2, PGAL1-10, TADH1, C-term. Flag tag	This paper	N/A
YCplac111-IPI1-GFP: CEN, LEU2, PIP1, TADH1, C-term. GFP tag	This paper	N/A
Software and Algorithms		
EPU	Thermo Fisher Scientific	https://www.thermofisher.com/us/en/home/electron-microscopy/products/software-em-3d-vis/eput-software.html
MotionCor2 v1.0.4	Zheng et al., 2017	https://emcore.ucsf.edu/ucsf-motioncor2
gCTF v1.06	Zhang, 2016	https://www2.mrc-lmb.cam.ac.uk/research/locally-developed-software/zhang-software/
Gautomatch v0.53	Jack Kai Zhang, Division of structural studies, MRC Laboratory of Molecular Biology	https://www2.mrc-lmb.cam.ac.uk/research/locally-developed-software/zhang-software/
Relion 3.0.7	Nakane et al., 2018 ; Zivanov et al., 2018	https://github.com/3dem/relion
Coot v0.89	Pettersen et al., 2004	https://www.ccpem.ac.uk/download.php
UCSF Chimera	Pettersen et al., 2004	https://www.cgl.ucsf.edu/chimera/
UCSF ChimeraX	Goddard et al., 2018	https://www.cgl.ucsf.edu/chimerax/
PSIPRED	McGuffin et al., 2000	http://bioinf.cs.ucl.ac.uk/psipred/
Namdinator	Kidmose et al., 2019	https://namdinator.au.dk/
Phenix suite	Adams et al., 2010	https://www.phenix-online.org/
Other		
Quantifoil holey carbon R3/3 with 3nm continuous carbon support	Quantifoil	https://www.emsdiasum.com/microscopy/products/grids/quantifoil.aspx

RESOURCE AVAILABILITY

Lead Contact

Further information and requests for resources and reagents should be directed to and will be fulfilled by the Lead Contact, Roland Beckmann (beckmann@genzentrum.lmu.de).

Materials Availability

All unique/stable reagents generated in this study are available from the Lead Contact without restriction.

Data and Code Availability

The accession codes of the atomic models reported in this paper are: State NE1: PDB: 6YLX, State NE2: PDB: 6YLY, composite Rix1-Rea1 pre-60S structure: PDB: 6YLH, Rix1-Rea1 pre60S - 60S core (rigid body 1): PDB: 6YLG, Rix1-Rea1 pre60S - Rea1 and Rsa4-UBL (rigid body 2): PDB: 6YLF, Rix1-Rea1 pre60S - Rix1-subcomplex (rigid body3): PDB: 6YLE. The accession codes of the cryo-EM densities are: State NE1: EMDB: 10841, State NE2: EMDB: 10842, composite Rix1-Rea1 pre-60S structure: EMDB: 10839, Rix1-Rea1 pre60S - 60S core (rigid body 1): EMDB: 10838, Rix1-Rea1 pre60S - Rea1 and Rsa4-UBL (rigid body 2): EMDB: 10837, Rix1-Rea1 pre60S - Rix1-subcomplex (rigid body3): EMDB: 10836.

EXPERIMENTAL MODEL AND SUBJECT DETAILS

Yeast strains

The genotypes of used *Saccharomyces cerevisiae* strains are listed in the [Key Resources Table](#).

Bacterial Strains

DNA recombinant work was done in *Escherichia coli* DH5 α .

METHOD DETAILS

Plasmid and strains

The plasmids used in this study were generated using standard recombinant DNA protocols. The methods used for genomic tagging and gene disruption in *S. cerevisiae* were described previously ([Janke et al., 2004](#); [Longtine et al., 1998](#)). All the strains used in this study are derived from the W303 background.

Affinity purification of pre-60S particles from *S. cerevisiae*

The TAP-Flag-NOP53 and RIX1-TAP Flag-REA1 strains, expressing the endogenously tagged proteins under control of their native promoters, were grown in YPD medium at 30°C and harvested at an OD₆₀₀ value of approximately 2.0. Cell pellets were flash-frozen in liquid nitrogen and stored at -80°C. Cell pellets were resuspended in lysis buffer [50 mM Tris-HCl (pH 7.5), 100 mM NaCl, 5 mM MgCl₂, 0.05% NP-40, 1 mM DTT, supplemented with 1 mM PMSF, 1 × SIGMAFAST protease inhibitor (Sigma-Aldrich)], and cells were ruptured by shaking in a bead-beater (Fritsch) in the presence of glass beads. Lysates were cleared with two subsequent centrifugation steps at 4°C for 10 and 30 min, at 5,000 and 15,000 rpm, respectively. Supernatants were incubated with IgG Sepharose 6 Fast Flow beads (GE Healthcare) on a rotating wheel at 4°C for 90 min. Beads were transferred into Mobicol columns (Mobictec) and, after extensive washing with lysis buffer, cleavage with tobacco etch virus (TEV) protease was performed at 16°C for 100 min. In a second purification step, the TEV eluates were incubated with Flag-agarose beads (ANTI-FlagM2 Affinity Gel, Sigma-Aldrich) for 80 min at 4°C. After washing with 5 mL of lysis buffer, bound particles were eluted with Flag elution buffer [50 mM Tris-HCl (pH 7.5), 100 mM NaCl, 5 mM MgCl₂, 0.01% dodecylglycol (Sigma-Aldrich), 1 mM DTT, 300 μg/ml Flag peptide (Sigma-Aldrich)] at 4°C for 60 min. Flag eluates were analyzed by SDS-PAGE on 4%–12% polyacrylamide gels (NuPAGE, Invitrogen) with colloidal Coomassie staining (Roti-blue, Roth). The ProtA-(His)₆-Nop53 Spb1-Flag and TAP-Flag-Nop53 purifications described in [Figures S3B](#) and [S3C](#) were purified as described above in buffer containing [50 mM Tris-HCl (pH 7.5), 100 mM NaCl, 5 mM MgCl₂, 0.1% NP-40, 5% glycerol and 1 mM DTT]. For the ProtA-(His)₆-Nop53 Spb1 aa437-Flag purification shown in [Figure S3C](#) the buffer was changed to [50 mM Tris-HCl (pH 7.5), 100 mM NaCl, 5 mM MgCl₂, 0.05% dodecylglycol (Sigma-Aldrich) and 1 mM DTT] for the Flag-agarose beads wash and Flag peptide elution step. For the elution 250 μg/ml Flag peptide (Sigma-Aldrich) was added.

The IPI3-FTpA IPI1-HA-Aid and IPI1-HA-Aid strains transformed with the respective plasmid-based constructs were grown overnight at 30°C in SDC-Leu medium. Cells were transferred to YPD medium for 6 h and depletion of Ipi1-HA-Aid was induced by the addition of indole-3-acetic acid (final concentration 500 μM) 2 h before cell harvesting. The affinity purifications were performed as described above in buffer containing 50 mM Tris-HCl (pH 7.5), 100 mM NaCl, 1.5 mM MgCl₂, 0.1% NP-40, 5% glycerol, and 1 mM DTT.

For expression and purification of the Rix1₂-Ipi3₂ tetramer, 2 μ plasmids harboring *RIX1*-TEV-ProtA and *IPI3*-FLAG were transformed under control of the inducible *GAL1-10* promoter into a W303 wild-type strain. The cells were grown overnight at 30°C in SRC-Leu-Trp medium and shifted to YPG medium for a further 6 h. The purification was performed as previously described for the Rix1-Ipi1-Ipi3 complex (Barrio-Garcia et al., 2016).

Negative-stain electron microscopy and image processing

For negative-stain EM, 5 μL of affinity-purified Rix1-Ipi3 subcomplex was applied to a freshly glow-discharged carbon-coated grid for 1 min, washed three times with water, stained with 2% (w/v) uranyl acetate, and dried. Micrographs were recorded with a Tecnai F20 electron microscope (FEI) operating at 200 kV with an Eagle bottom-mounted 4k, HS CCD camera (Tecnai) at a nominal magnification of 62,000 × (calibrated pixel size, 1.7 Å/pixel). Particles were selected manually with the interactive program BOXER (Ludtke et al., 1999), and image processing was carried out with the IMAGIC-4D package (van Heel et al., 1996). Particles were band-pass filtered and mass centered. Two-dimensional alignment, classification and iterative refinement of class averages were performed as described previously (Liu and Wang, 2011).

Grid preparation and cryogenic electron microscopy

To perform single-particle experiments, EM grids of vitrified pre-60S particles were prepared. Accordingly, Quantifoil grids (holey carbon R3/3 with a 3 nm carbon support) were glow-discharge treated at 2.2×10^{-1} Torr for 20 s. Vitrification was achieved using a Vitrobot Mark IV (FEI), 3.5 μL of sample was applied, and after 45 s of incubation at 4°C and 90% humidity, excess sample was blotted and the grids were plunged into liquid ethane. For the Rix1-Rea1 particle, 9,747 micrographs were collected using EPU (Thermo Fisher Scientific) on a Titan Krios G3 electron microscope (Thermo Fisher Scientific) operating at 300kV and equipped with a GIF and a K2 summit detector (Thermo Fisher Scientific). Micrographs were recorded in super-resolution mode as dose-fractionated movies of 40 frames at approximately 1.83 e⁻ per frame per physical pixel. A defocus spread of 0.5–3 μm and a magnification resulting in a physical pixel size of 0.5295 Å were used. For the Nop53 particle, 4,913 micrographs were collected using EPU (Thermo Fisher Scientific) on a Titan Krios G1 electron microscope operating at 300kV and equipped with a Falcon II detector upgraded with a Falcon III chip. Micrographs were recorded as dose-fractionated movies of 10 frames at approximately 2.5 e⁻ per frame per pixel. A defocus spread of 1–3.5 μm and a magnification resulting in a physical pixel size of 1.084 Å were used.

For the Nop53-Spb1 dataset, 390 micrographs were recorded on a TVIPS TemCam F216 on a Tecnai Spirit operating at 120 kV using EM-Tools software. A defocus spread of 1–3 μm and a magnification resulting in a physical pixel size of 2.55 Å were used.

Image processing

Anisotropic motion was corrected using MotionCor2 (Zheng et al., 2017) with 5 × 5 patches. In this step, the super-resolution Rix1-Rea1 data was binned by a factor of 2. Gctf (Zhang, 2016) was used to determine the CTF parameters of the micrographs. Micrographs were curated by visual inspection. Gautomatch (<https://www2.mrc-lmb.cam.ac.uk/research/locally-developed-software/zhang-software/>) was used for particle picking. All further processing was performed using the Relion 3.0 software collection (Nakane et al., 2018; Zivanov et al., 2018).

Nop53 dataset

Data processing was performed as described in Figure S2. In brief, after 747,594 particles were picked, 2D classification was performed in two equal-sized batches with 100 classes each. After manual inspection of the classes, 499,748 particles were retained for further analysis. These particles were binned by a factor of 3 and refined against EMDB-3892 (Kater et al., 2017). Subsequent alignment-free 3D classification using four classes yielded two classes resembling an Arx1-like particle (classes 1 and 2) (Bradatsch et al., 2012). Class 3 was a low-resolution particle with a mature-like rotated 5S RNP containing the foot and ITS2 moiety. This class was further sorted into three subclasses. Apparently, although not showing a prominent growth phenotype (Figure S3), hinting at aberrant 60S biogenesis, the purification here using TAP-Flag-tagged Nop53 also afforded a set of particles displaying an ITS2 processing defect, likely introduced by the N-terminal tag on Nop53. The particles of these three classes show a mature-like CP and represent cytoplasmic intermediates as they lack Nog1 and partially lack Arx1 (Figure S2). As previously shown, maturation of the CP and ISS is decoupled in such particles, allowing these to be exported to the cytoplasm and interact with mature 40S subunits to engage in translation (Sarkar et al., 2017). Thus, these particles were not further considered. Class 4 was first refined with unbinned particles and then CTF parameters (per particle defocus and per micrograph astigmatism) were refined. Using the improved CTF parameters, a further round of refinement was performed. This class showed heterogeneity around the L1 region and with respect to the presence of Spb1. Thus, a further 3D classification step using a mask around these regions was performed. The particles were separated into three classes, one of which converged to < 1% of the particles giving two effective classes: the Nop53-early 1 state with Spb1 bound but with the L1 stalk, ES31 and ribosomal proteins uL2, eL43 not stably incorporated, and the Nop53-early 2 state with these moieties present but lacking Spb1. The particles of these two classes were each subjected to a final refinement, post-processing, and local resolution estimation.

Nop53-Spb1 dataset

Data processing was performed as described in [Figure S2B](#). In brief, after picking 68,105 particles using the RELION LoG AutoPicking feature, 2D classification was performed yielding 57,211 ribosomal particles. These were initially refined against EMDB-3892 ([Kater et al., 2017](#)) and then separated into 4 classes using Relion Class3D without alignment. Four classes (98.2% of the particles after 2D classification) correspond to the Nop53 NE1 state ([Figures S3E and S3F](#)) whereas the remaining particles (1.8% of particles after 2D classification) correspond to an Arx1/Nog2 particle. The four classes corresponding to the Nop53 NE1 state were combined and subjected to a final round of Refine3D resulting in 14 Å resolution. These particles could not be further subsorted.

Rix1-Rea1 dataset

Data processing was performed as described in [Figure S4](#). In brief, after 303,723 particles were picked, 2D classification yielded 273,799 good particles. These were binned by a factor of 3 and refined against EMDB-3199 ([Barrio-Garcia et al., 2016](#)). Subsequent alignment-free 3D classification using eight classes yielded multiple low-resolution and junk classes (classes 1, 3, 5, 6, and 7), and a class for which Ipi1 and Sda1 were bound to the 60S core but the L1 was in an outward conformation, Rea1 was not bound and the Rix1-Ipi3 complex was only loosely and very flexibly associated. A further small class displayed a low-resolution equivalent of the state-E nucleolar particle ([Barrio-Garcia et al., 2016](#)), corresponding to a particle prior to the Rea1-mediated release of Ytm1-Erb1. Class 2 contained a particle similar to EMDB-3199, with the Rix1 complex and Rea1 stably bound to a 60S particle having the ITS2-harboring foot structure. These particles were further subclassified using a mask around the foot structure, revealing a 48% occupancy of the foot. As foot processing seems to be independent of the rest of the particle, the presence or absence of the foot structure in the individual particle images was subsequently ignored for further processing. The entire set of particles from class 2 was then subjected to unbinned 3D refinement, refinement of CTF parameters (per particle defocus and per micrograph astigmatism) followed by a further round of 3D refinement. To address the independent motion of the Rix1-Ipi3 complex and Rea1 density with respect to the 60S core structure, a round of multibody refinement was performed on these three bodies, resulting in 3.0, 3.3 and 6.6 Å resolution for the 60S core, the Rix1-Ipi3 complex and Rea1, respectively. To further improve the Rea1 density, the *relion_flex_analyse* tool was used to subtract the individual bodies of Rix1-Ipi3 and the core-60S, recenter and crop the particles to only fit Rea1. Masked classification using three classes revealed one class with distinct secondary structure features. This class was then refined, yielding an overall resolution of 4.6 Å. Using a further round of multibody refinement, the ring and tail sections of Rea1 were independently refined to yield final resolutions of 4.2 Å each. All final volumes were post-processed and local resolution maps were calculated.

Model building and refinement

Models were fit and built using UCSF Chimera ([Pettersen et al., 2004](#)) and Coot molecular modeling software ([Emsley et al., 2010](#)). The initial models for the Nop53-derived states NE1 and NE2 were created by combining previously published structures using rigid body fitting. To that end, Cic1, the ITS2 rRNA, Nop7, Nop15, Nop53, and Rlp7 of the foot structure were taken from the Nog2 particle (PDB: 3JCT; [Wu et al., 2016](#)) for both NE1 and NE2. To generate the core of these 60S particles, the “late nuclear” pre-60S particle (PDB: 6N8J; [Zhou et al., 2019b](#)) was rigid-body fit into the remaining density, and chains and segments not supported by the EM density were removed. Finally, Spb1 was derived from the late nucleolar state E (PDB: PDB 6ELZ; [Kater et al., 2017](#)). The model for the Rix1-Rea1 particle was derived in a similar way. An initial model was derived from PDB 3JCT for the core 60S particle excluding the CP but including the assembly factors Mrt4, Rlp24, Nog2, Nsa2, Nug1, and Tif6. The CP including the 5S RNP is based on PDB 4V88 ([Ben-Shem et al., 2011](#)); PDB 4WJV ([Baßler et al., 2014](#)) was used for Rsa4 and parts of Nsa2; PDB structures 6OR5, 6HYP, 6HYD and 6QTA ([Ahmed et al., 2019](#); [Chen et al., 2018](#); [Sosnowski et al., 2018](#)) were used for Rea1. The components of the Rix1 complex (Rix1, Ipi1, and Ipi3) and Sda1 were modeled *de novo* based on secondary structure predictions by PSIPRED ([McGuffin et al., 2000](#)). Coot was used to validate the fit and, if necessary, further adjust the models and for the *de novo* building of Rix1, Ipi3, and Sda1 ([Emsley et al., 2010](#)). Both the Rea1-Rsa4-UBL body, as well as the Rix1-body, consisting of the Rix1₂-Ipi3₂-tetramer and the loop segment of Ipi1, were initially refined using the Namdinator web server ([Kidmose et al., 2019](#)). The resulting models were then subjected to the real-space refinement tool of the PHENIX suite, using the respective segments of the initial reference models (as mentioned above) to provide external reference restraints ([Adams et al., 2010](#)).

Visual analysis and depiction of structures and maps

Visual analysis and depiction of structures for figures was performed using UCSF Chimera and UCSF ChimeraX ([Goddard et al., 2018](#); [Pettersen et al., 2004](#)).

Molecular Cell, Volume 79

Supplemental Information

**Construction of the Central Protuberance
and L1 Stalk during 60S Subunit Biogenesis**

**Lukas Kater, Valentin Mitterer, Matthias Thoms, Jingdong Cheng, Otto
Berninghausen, Roland Beckmann, and Ed Hurt**

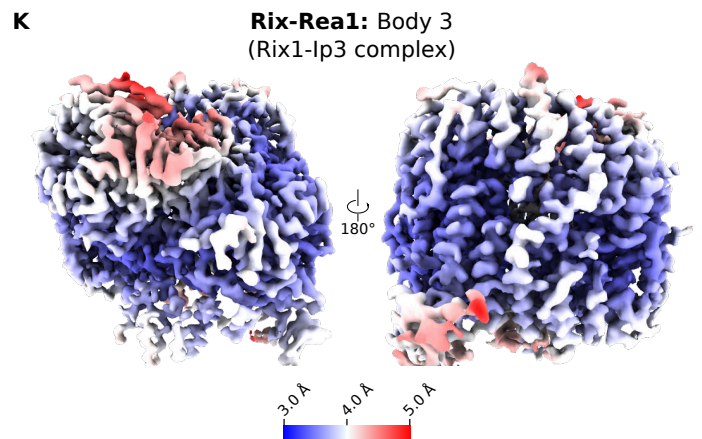
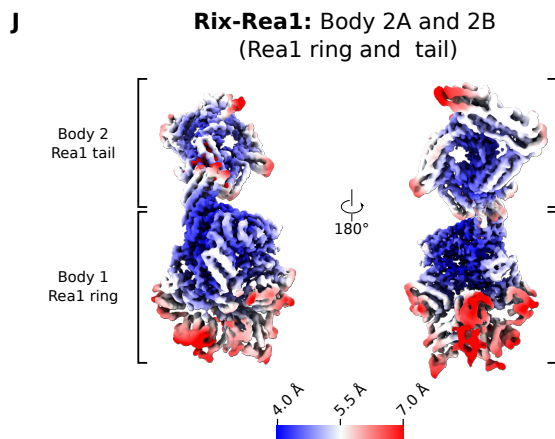
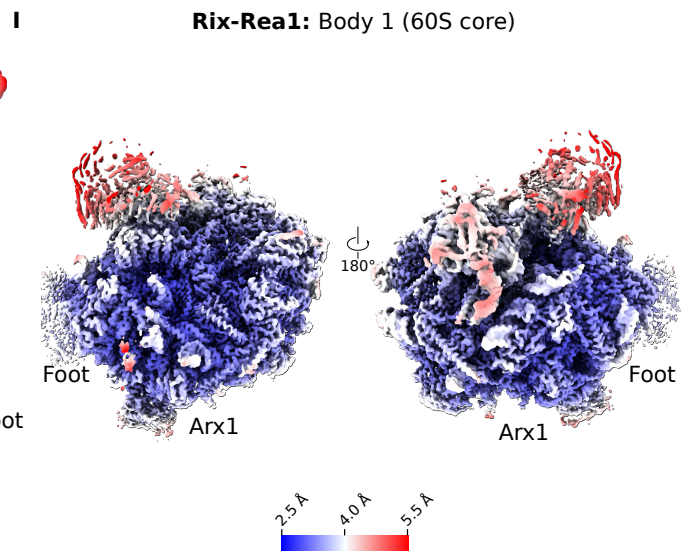
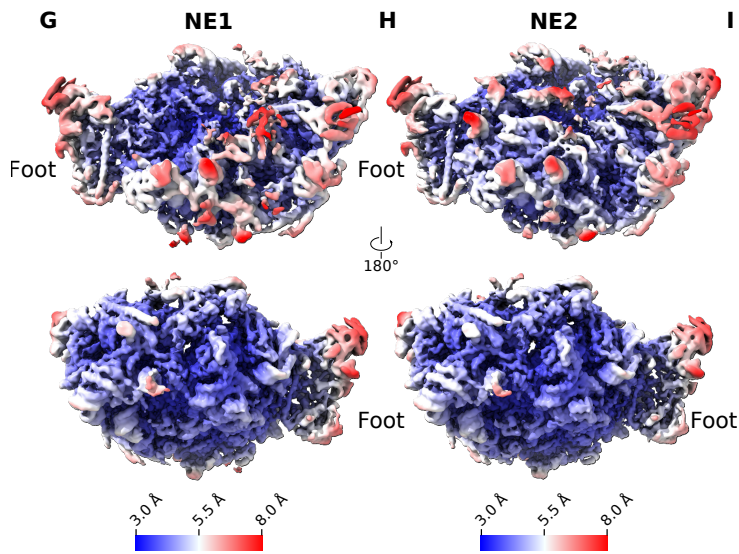
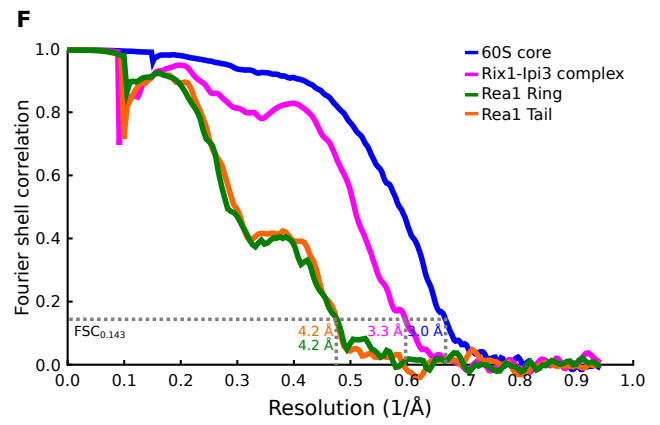
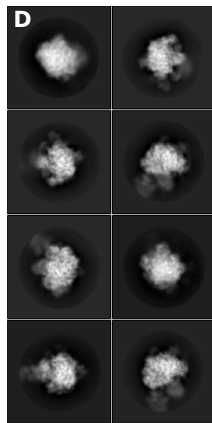
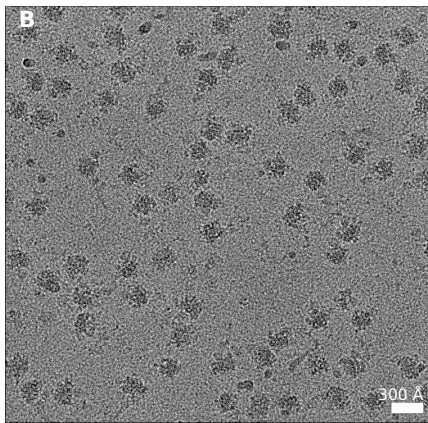
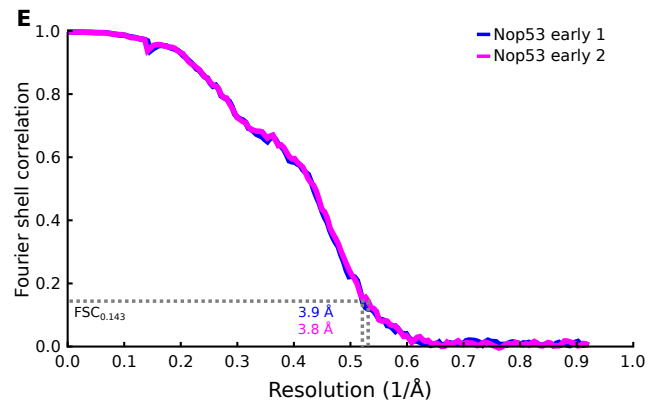
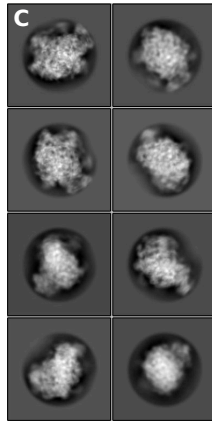
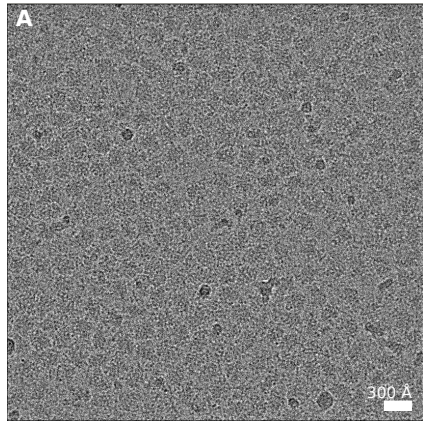


Figure S1. Electron Microscopy of the Nop53 and Rix1–Rea1 Datasets and Local Resolution of the Reconstructions, Related to STAR-Methods

(A and B) Representative electron micrographs of TAP-Flag-Nop53 particles (A) and Rix-TAP–Flag-Rea1 (B; data sets 1 and 2, respectively).

(C and D) Representative 2D class averages of datasets 1 and 2, respectively.

(E) Fourier shell correlation (FSC) curves of the two states NE1 and NE2 of data set 1.

(F) FSC curves of the individually refined rigid bodies of the late Rix1–Rea1 particle (body 1: 60S core, bodies 2A and 2B: Rea1 ring and tail, body 3: Rix1–Ipi3 subcomplex).

FSC curves shown in (E) and (F) are derived from 3D refinements of independent half-sets of particles.

(G–K) Local-resolution-filtered maps of the aforementioned states and rigid bodies thereof. Maps are colored according to local resolution, see corresponding color scales.

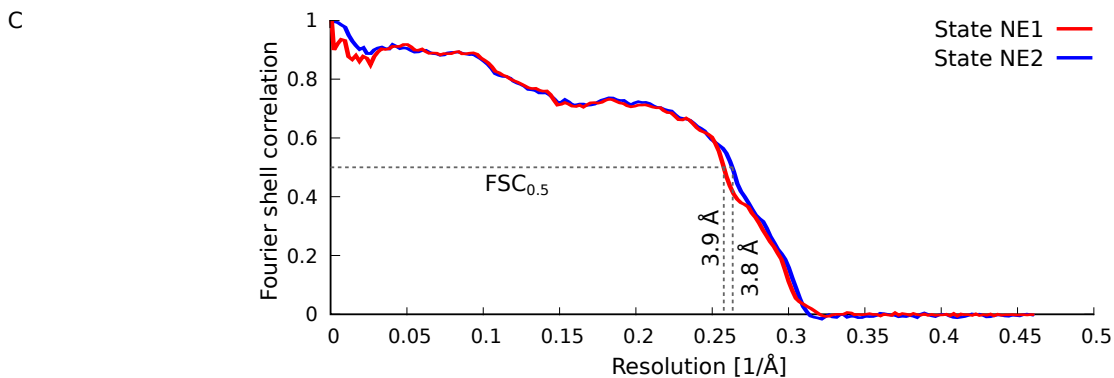
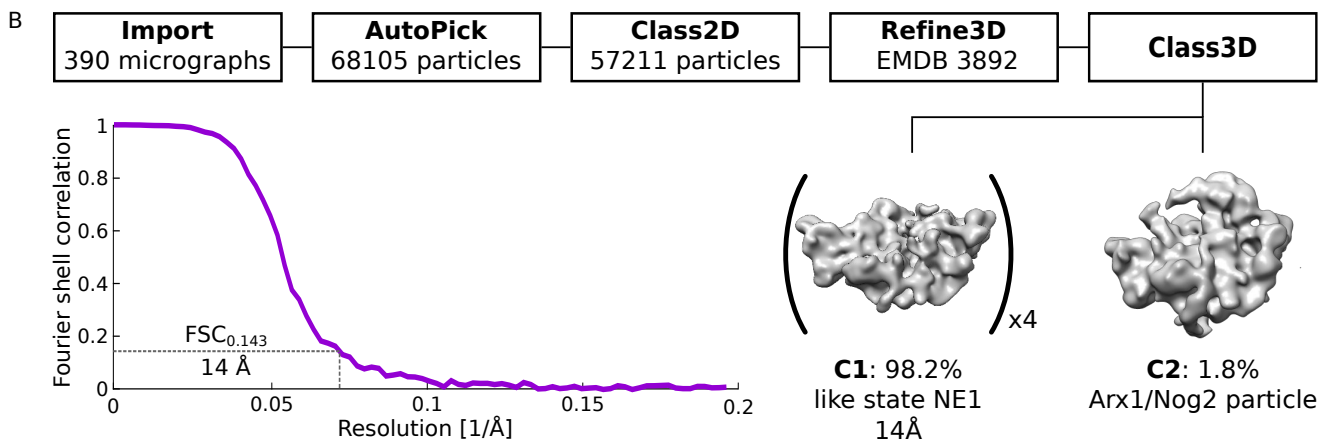
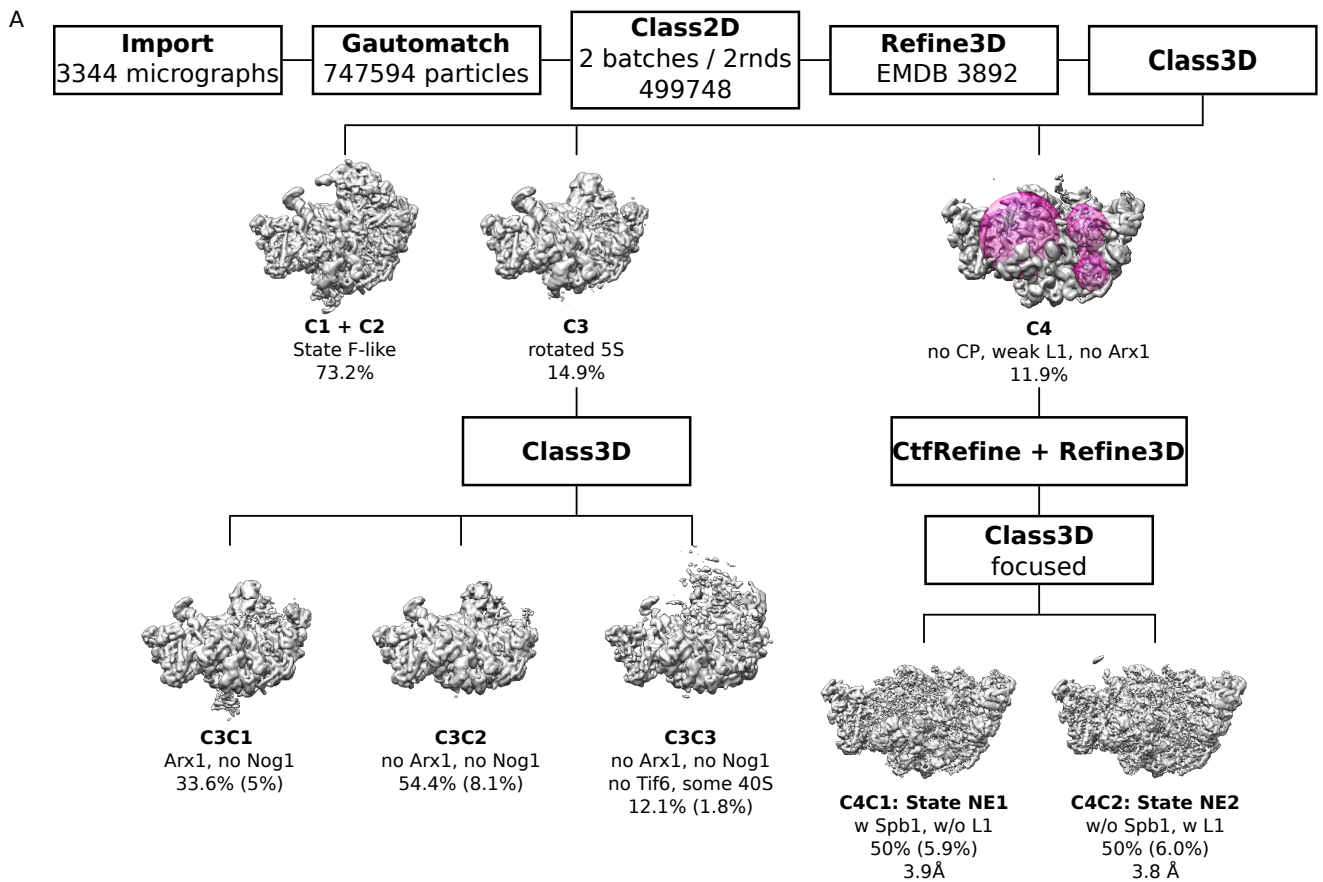


Figure S2. Data Processing, Sorting Scheme and Model Validation of the TAP-Flag-Nop53 and ProtA-(His)₆-Nop53 Spb1-aa437-Flag Data Sets, Related to STAR-Methods

(A and B) Work flow of data processing showing the volumes at relevant steps. Class sizes are given as percentage relative to the respective classification step and relative to all good particles after 2D classifications (in parentheses). Masks used for focusing specific sorting steps are indicated as semi-transparent magenta volumes. Resolutions at FSC=0.143 are shown after final 3D refinement using fully independent particle half-sets.

(C) Model to map FSC curves for the 60S core particle, the Rix1₂-Ipi3₂ tetramer and the Rea1 Rsa4-UBL bodies.

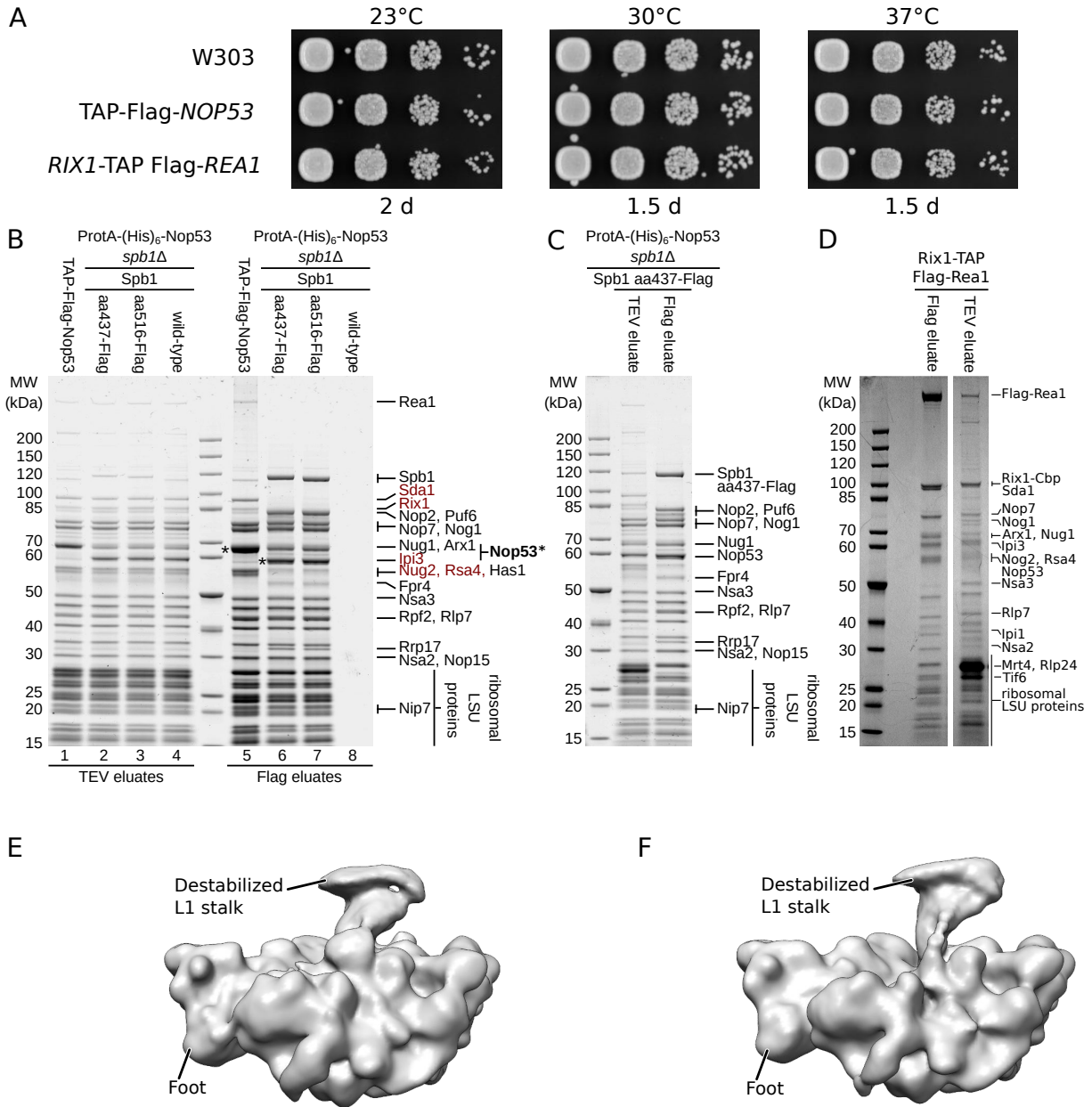


Figure S3. Growth Analysis and Affinity Purifications of Yeast Strains Used for Cryo-EM, Related to STAR-Methods

(A) Growth analysis of yeast strains used for cryo-EM sample preparation in comparison to wild-type W303 yeast. Cells were spotted in 10-fold serial dilution on YPD plates and cell growth was monitored at the indicated temperatures and times.

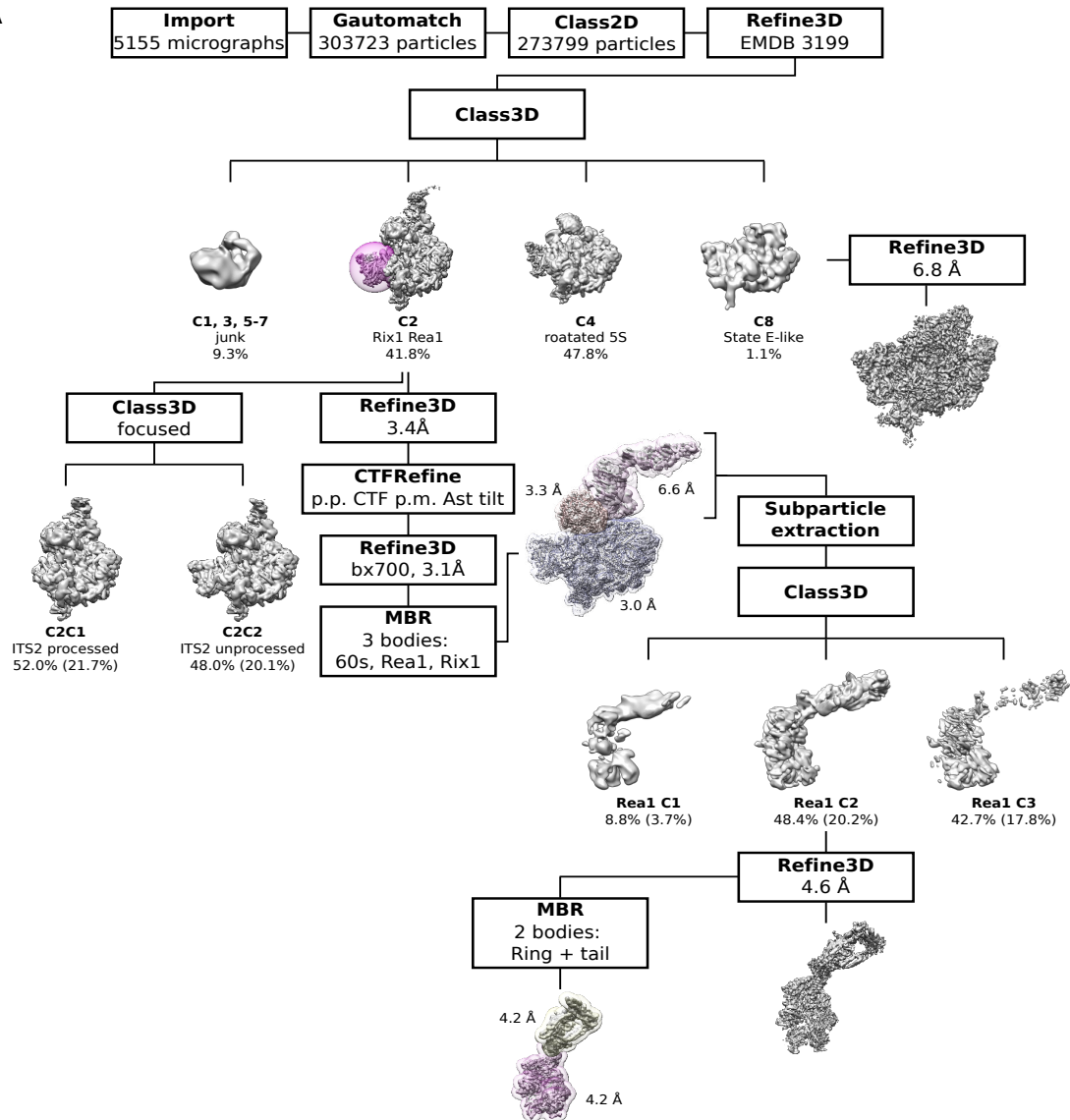
(B) Split affinity purifications from ProtA-(His)₆-Nop53 *spb1*Δ shuffle strains complemented with plasmid based Spb1 constructs with either an internal Flag tag (lane 2, 3 and 6, 7) or an untagged wild-type control (lane 4, 8) were compared with the affinity purification of the TAP-Flag-Nop53 strain (lane 1, 5). The TEV eluates (lane 1-4) and final Flag eluates (lane 5-8) were analyzed by SDS-PAGE and Coomassie staining. Proteins identified by mass spectrometry are labeled on the right side of the gel and the Nop53 baits are marked with an asterisk. Factors which were reduced in the Nop53-Spb1 split-affinity purifications (lane 6, 7) are indicated in red.

(C) Coomassie stained SDS-PAGE of the ProtA-(His)₆-Nop53 Spb1 aa437-Flag split affinity purification used for Cryo-EM analysis (F). The TEV eluate and final Flag eluate are shown and copurifying proteins were labeled on the right side of the gel.

(D) Coomassie stained SDS-PAGE of a Rix1-TAP Flag-Rea1 split affinity purification. The TEV eluate and final Flag eluate are shown and copurifying proteins were labeled on the right side of the gel.

(E and F) Comparison of state NE1 map of the TAP-Flag-Nop53 purification and the Nop53 Spb1 split purification map (C). To achieve comparable filtering and to visualize the highly flexible and thus low-resolution L1 stalk in (E), the powerspectrum of the state NE1 map was adjusted to match that of the Nop53-Spb1 split purification map using `reliion_imag_handler` with the `--adjust_power` option.

A



B

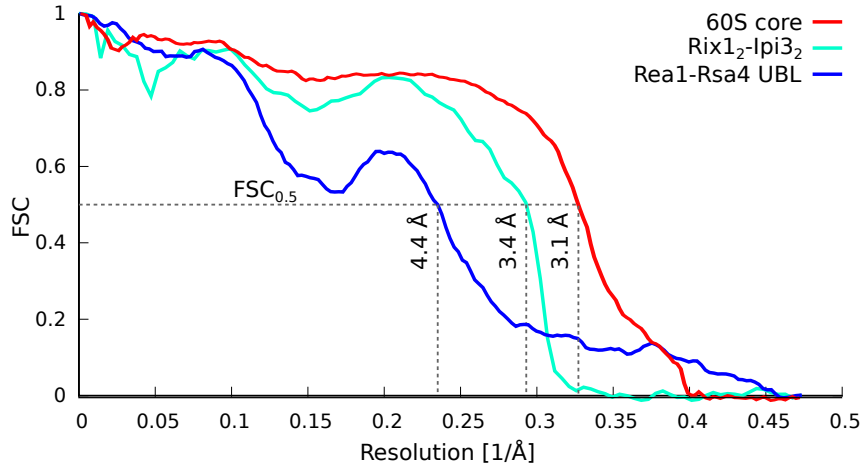


Figure S4. Data Processing, Sorting Scheme and Model Validation of the Rix1-TAP Flag-Rea1 Data Set, Related to STAR-Methods

(A) Work flow of data processing showing the volumes at relevant steps. Class sizes are given as percentage relative to the respective classification step and relative to all good particles after 2D classifications (in parentheses). Masks used for focusing specific sorting steps and to define individual rigid bodies of multibody refinement steps are indicated as semi-transparent colored volumes. Resolutions at FSC=0.143 are provided after final 3D refinement using fully independent particle half-sets.

(B) Model to map FSC curves for the 60S core particle, the Rix1₂-Ipi3₂ tetramer and the Rea1 Rsa4-UBL bodies.

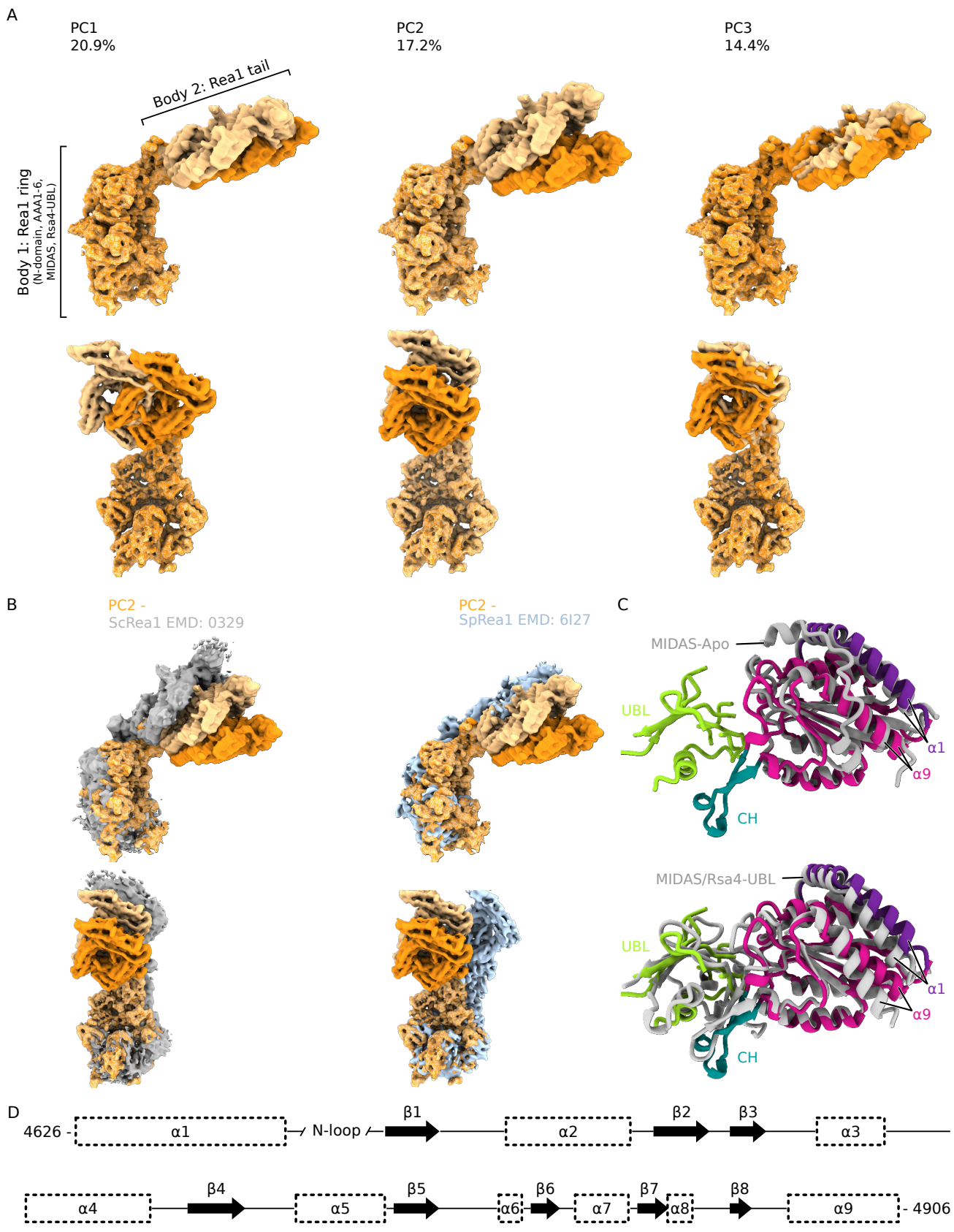


Figure S5. Flexibility Analysis of Rea1 Ring and Rea1 Tail and Architecture of the Rea1-MIDAS Domain, Related to Figure 4

(A) Side and front views of the three principal components explaining the largest amount of variance in the relative motion of the Rea1 ring relative to the Rea1 tail as provided by *relion_flex_analyse*. Percentages indicate the variance exhibited by the individual components.

(B) Comparison of principal component 2 (see panel A) and the standalone MIDAS-bound Rea1 structures from *Saccharomyces cerevisiae* (left) and *Schizosaccharomyces pombe* (right) (Chen et al., 2018; Sosnowski et al., 2018).

(C) Comparison of the Rea1-MIDAS–Rsa4-UBL complex from this study with the *Chaetomium thermophilum* MIDAS-Apo and MIDAS–Rsa4-UBL crystal structures (top: 6QT8, apo; bottom: 6QTA, Rsa4-UBL bound)(Ahmed et al., 2019). The published structures are shown in gray, overlaid with the structures from this study colored as in **Figure 4B**.

(D) Secondary structure diagram of the Rea1-MIDAS domain.

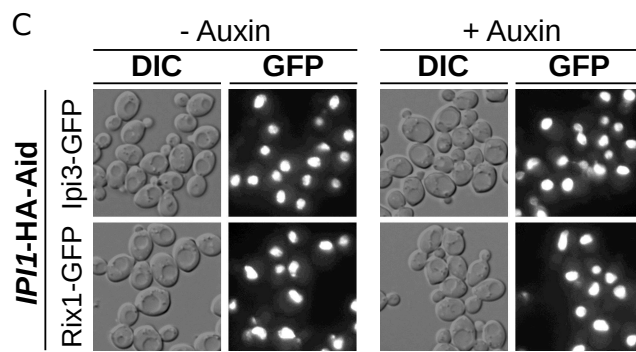
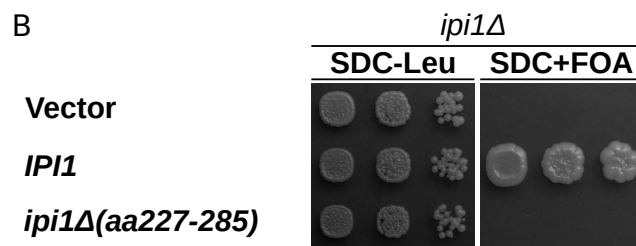
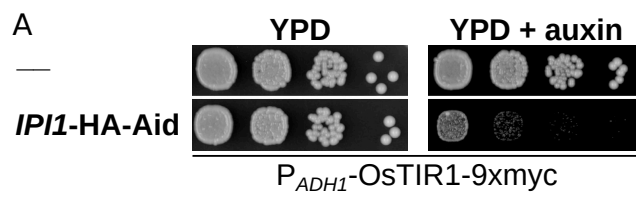


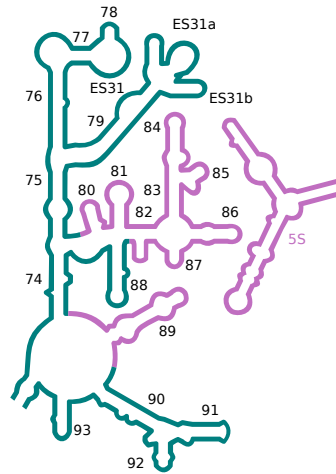
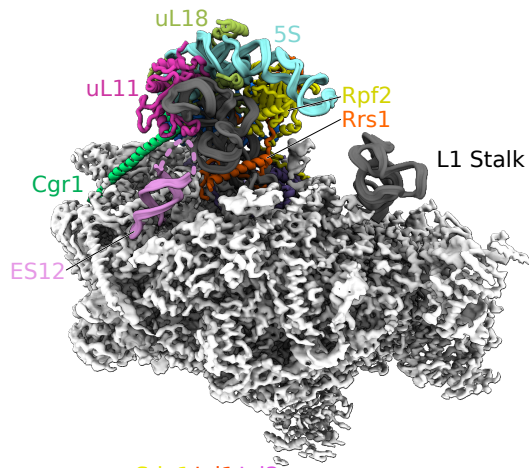
Figure S6. Growth Analysis and Subcellular Localization of Ipi3 and Rix1 of the Ipi1-HA-Aid-Depleted Strain, Related to Figure 6

(A) Growth of the *IPI1*-HA-Aid degron strain on YPD plates and YPD plates supplemented with auxin (final concentration 500 μ M). Cells were spotted in 10-fold serial dilutions and growth at 30°C was monitored after 2 days.

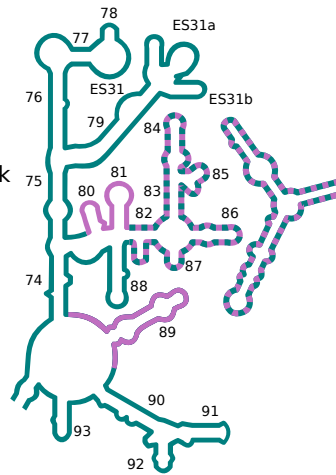
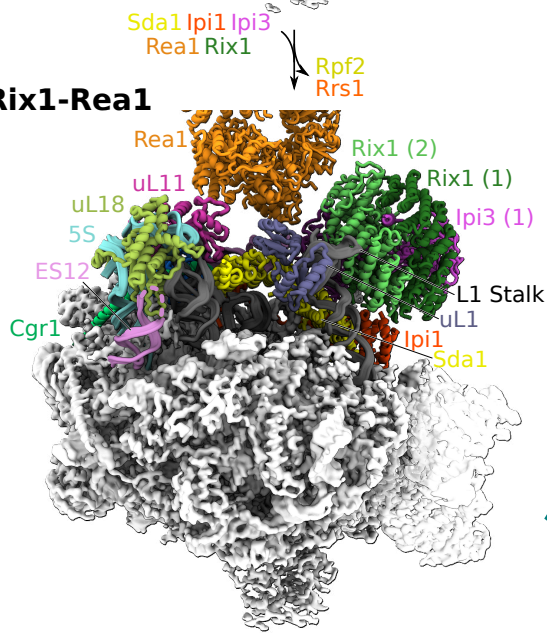
(B) The *ipi1* Δ shuffle strain was transformed with an empty vector control or plasmids containing either the *IPI1* wild type or the *ipi1* Δ (aa227–285) mutant under control of the endogenous promoter. Cells were spotted on SDC–Leu and SDC+FOA plates in 10-fold serial dilutions and cell growth at 30°C was monitored after 2 and 4 days respectively.

(C) Subcellular localization of GFP-tagged Ipi3 and Rix1, in the *IPI1*-HA-Aid degron strain, analyzed by fluorescence microscopy. The subcellular location was analyzed under expression (– auxin) or depletion (+ auxin, 500 μ M final concentration for 90 min) conditions of *IPI1*-HA-Aid, and Nomarski (DIC) and GFP channel images are shown.

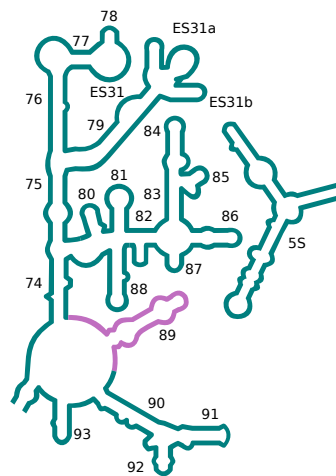
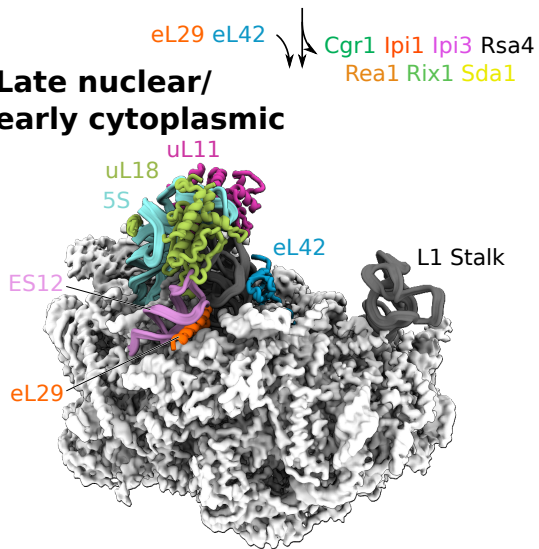
Arx1/Nog2



Rix1-Rea1



Late nuclear/ early cytoplasmic



— 5S rRNA
— 25S rRNA Dom II
— 25S rRNA Dom V

— Folded nonmature
— Folded mature-like

Figure S7. The Transition from the Arx1/Nog2 Particle to a Particle Competent for Nuclear Export, Related to Figure 7

Left: A combined model and map depicting the transition of pre-60S particles from the Arx1/Nog2 particle (PDB: 3JCT, EMDB: 6615)(Wu et al., 2016) via the late nucleoplasmic Rix1–Rea1 particle to the export-competent late nuclear/early cytoplasmic particle (PDB: 6N8J, EMDB: 0369) (Zhou et al., 2019b). The cores of the particles are displayed as gray volumes, and moieties relevant to the individual transitions of the CP are highlighted as colored ribbon representations of the respective models. Right: Segments of the pre-25S rRNA domain V, having conformations that are either mature-like (green), stably folded but not mature-like (pink), or close to mature but slightly displaced (dashed green and pink).